

UNIVERSITY OF OKLAHOMA

GRADUATE COLLEGE

NOVEL ANNEXIN A5 - NANOPARTICLES CONJUGATES FOR TARGETED CANCER
THERAPY

A DISSERTATION
SUBMITTED TO THE GRADUATE FACULTY
in partial fulfillment of the requirements for the

Degree of
DOCTOR OF PHILOSOPHY

By
GABRIELA NOGUEIRA FURTADO E FARIA
Norman, Oklahoma
2022

NOVEL ANNEXIN A5 - NANOPARTICLES CONJUGATES FOR TARGETED CANCER
THERAPY

A DISSERTATION APPROVED FOR THE
SCHOOL OF CHEMICAL, BIOLOGICAL AND MATERIALS ENGINEERING

BY THE COMMITTEE CONSISTING OF

Dr. Roger Harrison, Chair

Dr. Vassilios Sikavitsas

Dr. Daniel Resasco

Dr. Dimitrios Papavassiliou

Dr. Lacey McNally

Dr. Wajeeha Razaq

This dissertation is dedicated to
my parents, Iracema e Carlos,
my brother, Mateus,
and my husband JR.

Mamis, obrigada por me permitir sonhar alto.
Hubby, you reminded me of my strength.

Thank you. Amo vocês.

Acknowledgements

I would like to thank my committee, Dr. Vassilios Sikavitsas, Dr. Daniel Resasco, Dr. Dimitrios Papavassiliou, Dr. Lacey McNally, Dr. Wajeeha Razaq, and Dr. Roger Harrison, for their support and guidance during the Ph.D. program. A special thanks is dedicated to Dr. Harrison for his instruction and support during every day of this journey, in which he was patient and caring for my development as a scientist.

I'd like to thank our collaborators at the University of Oklahoma, Dr. Caleb Fulton, and Dr. Kieran Mullen, for sharing their knowledge and empowering such enriching and interdisciplinary projects. I also want to thank Dr. Ricardo Prada Silvy and Dr. Sathish Lageshetty from CHASM™ for sharing their expertise and supplying carbon nanotubes; the IACUC at the University of Oklahoma and the animal facilities management; all the veterinarian technicians monitored the mice daily, including Sandra Doan, Gail Goodson, Madison Vakulik, and Baylee Bahm; the veterinarians Dr. Wendy Williams and Dr. Leeza Birdwell for their insights on the animal care; Dr. Amy Burke for animal training.

I thank all my funding sources: Universidad Nacional de San Agustin de Arequipa, Peru, and the Oklahoma Center for the Advancement of Science and Technology.

I am very grateful to my colleagues in the Harrison laboratory, Alexis Woodward, Clement Karch, Adam Aissanou, Sampurna Chakraborti, and Ben Southard, who have provided significant assistance in this work. Alexis Woodward is owed a special thanks for being present and encouraging throughout my four and a half years at the University of Oklahoma.

I would also like to thank all the staff and graduate students who have been part of the Chemical, Biological, and Materials Engineering departments, especially Andrew D'Amico, Terri Colliver, Madena McGinnis, Nicole Palmeter, Rett Norman, and Donna King. The ChEGS officers, Elton Correa, Mason Rhue, Lucas Condes, Kylie Foster, Hesham Aboukeila, Luis Trevisi, and Thomas Salas, for making the experience of leading ChEGS easier and more pleasant; Kylie, for the help with flow cytometry and Daniel Karami and Parker Bryant for sharing equipment. I'd like to thank all my friends at

the University of Oklahoma, especially Aishwarya Krishnaswamy, Sanjana Mudduluru, and Gabriela Chaves.

I need to acknowledge the mice that gave their lives for this project. I believe that their deaths were not in vain. Without them, little could we do for the advancement of health sciences.

Lastly, I would like to thank my family: my husband, Joseph Shaw, for the hugs and for being present no matter what; parents, Iracema Rodrigues Furtado and Carlos Nogueira de Faria; my brother Matheus Furtado e Faria; and my parents-in-law, Megan FitzGerald and Daniel Roman, for all the love, attention, encouragement, inspiration, and prayers. Also, my aunts and uncles, especially Irene Furtado Moreira, my cousins, and my friends in Brazil, for always being supportive, encouraging, and loving. I would not be getting a Ph.D. without the love and support of everyone mentioned here.

Thank you.

Table of Contents

<i>CHAPTER 1 - INTRODUCTION</i>	1
1.1 The cell and its plasma membrane	2
1.1.1 Plasma membrane asymmetry: the default state of cells.....	4
1.1.2 Scramblase Activation and Phosphatidylserine Exposure	8
1.1.3 PS externalization on cancer cells and tumor vasculature.....	12
1.2 Annexin A5 binds to externalized phosphatidylserine	14
1.3. Perspectives on Cancer	20
1.3.1 Cancer and its relevance worldwide	20
1.3.2 What's cancer? The hallmarks	21
1.3.3 Breast cancer	29
1.3.4 Breast cancer classifications and available therapies.....	31
1.3.5 Triple negative breast cancer.....	36
1.4 Novel strategies for cancer treatment.....	42
1.4.1 Photothermal therapy.....	42
1.4.2 Immunotherapy.....	50
1.4.4 Radiofrequency ablation	54
1.4.5 Targeted single-walled carbon nanotubes as photosensitizer and radiofrequency responsive material	56
1.4.6 Theranostic platform composed of protein-drug conjugate linked to gold nanoparticles	59
<i>CHAPTER 2 - MATERIALS AND METHODS</i>	63
2.1 Materials.....	64
2.1.1 Protein production and purification	64
2.1.2 SWCNT-ANXA5 conjugation	64
2.1.3 Cell culture	65
2.1.4 <i>In vivo</i> studies	65

2.1.5 Gold nanoparticle conjugation-----	65
2.2 SWCNT-ANXA5 conjugate -----	67
2.2.1 ANXA5 conjugation to SWCNT -----	67
2.2.2 SWCNT standard curve-----	68
2.2.3 SWCNT-ANXA5 characterization-----	68
2.2.4 SWCNT-ANXA5 sterilization-----	69
2.3 Cell culture -----	69
2.4 <i>In vitro</i> studies with SWCNT-ANXA5-mediated PTT -----	70
2.5 <i>In vivo</i> studies with SWCNT-ANXA5-mediated PTT -----	72
2.5.1 Tumor implantation in BALB/cJ mice -----	72
2.5.2 Mice health and tumor volume assessment -----	73
2.5.3 Cytokine release in EMT6 tumors treated with combination therapy of PTT and anti-CTLA-4 -----	73
2.5.4 Cytokine release related to intravenous versus intratumoral injection in EMT6 tumor bearing mice -----	74
2.5.5 Cytokine release related to tumor surface temperature in EMT6 tumor bearing mice-----	75
2.5.6 Survival of EMT6 tumor bearing mice in combination therapy of PTT at 45°C and anti-PD-1 -----	76
2.5.7 Immune response of in combination therapy of PTT at 45°C and anti-PD-1 in EMT6 tumor-bearing mice. -----	77
2.5.8 Tumor control with PTT treatment keeping tumor surface temperature at 45°C for longer period of time -----	79
2.5.9 Long-term survival of combination therapy of anti-PD-1 and PTT at 45°C for 5 min in mice bearing EMT6 and 4T1 tumors -----	80
2.5.10 Carbon nanotube biodistribution after intratumoral injection SWCNT-ANXA5 -----	81
2.5.11 Long-term survival of combination therapy of anti-PD-1, immunoadjuvant imiquimod and PTT in 4T1 tumor-bearing mice -----	81

2.5.12 Immune response mechanistic analysis of combination therapy of anti-PD-1, immunoadjuvant imiquimod and PTT in 4T1 tumor-bearing mice -----	83
2.5.13 Statistical Analysis -----	84
2.6 Preliminary, <i>in vitro</i> and <i>in vivo</i> studies with SWCNT-ANXA5 mediated radiofrequency ablation -----	84
2.6.1 Analysis of responsiveness to radiofrequency irradiation of (6,5) SWCNT and few walled carbon nanotubes in different surfactants -----	84
2.6.2 Assessment of surfactant effect on radiofrequency responsivity of (6,5) SWCNT -----	86
2.6.3 Analysis of suspension of SWCNT in solvent ethanol -----	87
2.6.4 Analysis of SWCNT-ANXA5 response to radiofrequency irradiation -----	88
2.6.5 Assessment of radiofrequency responsivity of CNT samples with different chiralities -----	88
2.6.6 Effect of geometry of liquid phase on the responsivity to radiofrequency field -----	89
2.6.7 Analysis of interface heating and ionization of (6,5) SWCNT in radiofrequency field -----	90
2.6.8 Study of resonant frequency of (6,5) SWCNT in radiofrequency field in 15 W power output regenerator coupled with matching network -----	90
2.6.9 Statistical Analysis -----	91
2.7 Gold nanoparticle – annexin A5 – DM1 conjugate -----	91
2.7.1 Conjugation -----	91
2.7.2 Characterization -----	94
2.7.3 <i>In vitro</i> studies -----	95
CHAPTER 3 – RESULTS AND DISCUSSION -----	96
3.1 <i>In vitro</i> studies with SWCNT-ANXA5-mediated PTT -----	97
3.2 <i>In vivo</i> studies with SWCNT-ANXA5-mediated PTT -----	108
3.2.1 EMT6 tumor model treated with SWCNT-ANXA5 mediated PTT -----	108
3.2.2 4T1 tumor model treated with SWCNT-ANXA5-mediated PTT -----	125

3.3 Preliminary <i>in vitro</i> and <i>in vivo</i> studies with SWCNT-ANXA5 mediated radiofrequency ablation-----	142
3.3.1 Preliminary studies with SWCNT-ANXA5 mediated radiofrequency ablation -----	142
3.3.2 SWCNT-ANXA5-mediated radiofrequency ablation in biological system ---	159
3.4 Gold nanoparticle – annexin A5 – DM1 conjugate-----	164
<i>CHAPTER 4 – CONCLUSIONS AND FUTURE DIRECTIONS</i> -----	172
<i>REFERENCES</i> -----	175
<i>APPENDIX A – Supplemental data</i> -----	206
<i>APPENDIX B – Protein Protocols</i> -----	226
B1. Annexin production using LB media -----	226
B2. Annexin production using TB media -----	232
B3. Bradford protein assay -----	237
B4. SDS-page electrophoresis-----	238
B5. SWCNT-ANXA5 conjugation-----	240
B6. SWCNT standard curve preparation -----	241
B7. AuNP-annexin A5-DM1 conjugation -----	243
B8. Nanoparticle protein conjugates sterilization and assessment of sterility -----	245
B9. AuNP-ANXA5-DM1 conjugate quantification -----	246
<i>APPENDIX C – Cell Culture Protocols</i> -----	248
C1. Aseptic technique in vertical laminar flow -----	248
C2. Feeding a monolayer culture in flasks-----	250
C3. Subculture of monolayer cells -----	251
C4. Endothelial cell culture -----	254
C5. Counting cells with hemocytometer-----	256

C6. Freezing cells -----	259
C7. Alamar Blue assay -----	260
C8. SWCNT-annexin A5 laser treatment with temperature measurement -----	261
<i>APPENDIX D – Protocols for in vivo studies</i> -----	264
D1. EMT6 tumor induction in mice -----	264
D2. NIR-irradiation of mice -----	265
D3. RF irradiation of mice -----	266
D4. Euthanasia for blood collection -----	266
D5. Spleen collection and splenic cells staining for flow cytometry -----	267
D6. Preparation of tissue lysate for SWCNT detection after biodistribution study ---	269
D7. Preparation of injectable hydrogel -----	270
<i>APPENDIX E – Other Protocols</i> -----	271
E1. RF measurements using network analyser -----	271
E2. Agarose gel casting and running horizontal electrophoresis -----	272

List of Figures

Figure 1: The phospholipid bilayer.	2
Figure 2: Updated fluid—mosaic membrane model (2014)..	4
Figure 3: Lipid steady-state composition of the plasma membrane.	5
Figure 4: Distribution of phospholipids on each leaflet of the red blood cell plasma membrane.	6
Figure 5: The three classes of phospholipid translocases: flippases, floppases, and scramblases..	7
Figure 6: The credit card model for the mechanism of protein-mediated lipid transport..	10
Figure 7: Pathways phospholipid scrambling during blood coagulation and apoptosis.	11
Figure 8: Three-dimensional model of human annexin A5.	15
Figure 9: Three-dimensional model of Ca ²⁺ -dependent binding of Annexin A5 to membrane model showing.	16
Figure 10: Annexin A5 domains and trimerization:	17
Figure 11: Annexin A5 binding to phosphatidylserine induces endocytosis.	19
Figure 12: Global map ranking cancer as a leading cause of death at ages below 70 years in 2019 for each country.	20
Figure 13: The hallmarks of cancer as of 2022.	22
Figure 14: Model for the multistep metastatic process.	27
Figure 15: Incidence and mortality age-standardized rates in high/very-high human development index (HDI) regions versus low/medium HDI regions among women in 2018.	29
Figure 16: Histological classification of breast cancer subtypes shows the heterogeneity in breast cancer due to growth patterns and architectural features.	32
Figure 17: Targetable pathways of oncogenic signaling pathways in TNBC.	39
Figure 18: Mechanisms of photothermal effect during PTT.	44
Figure 19: Comparison of water and hemoglobin absorbance to carbon nanotubes.	47
Figure 20: Immunogenicity of cell death.	49

Figure 21: Interactions between PD-1 and PD-L1 on T cells and cancer cells and checkpoint inhibition.	53
Figure 22: SWCNT helicity map	57
Figure 23: Schematic representation of the state of the catalyst components before and during the production of SWCNT.	58
Figure 24: Mertansine Chemical Structure.....	61
Figure 25: Treatment schedule for the combination therapy of EMT6 tumor models with SWCNT-ANXA5 mediated photothermal therapy until 45°C and anti-PD-1.	77
Figure 26: Treatment schedule for the combination therapy of 4T1 tumor models with SWCNT-ANXA5 mediated photothermal therapy until 55°C, anti-PD-1 and immunoadjuvant imiquimod.	82
Figure 27: Matching network loading plates.....	86
Figure 28: Scheme of AuNP-ANXA5-DM1 conjugation.	94
Figure 29: Temperature elevation of different solutions and SWCNT-ANXA5 conjugate suspension after NIR laser irradiation at room temperature.	98
Figure 30: Cell viability of EMT6 cells after NIR laser at treatment room temperature.	100
Figure 31: Temperature elevation of EMT6 cells after NIR laser treatment at room temperature.	101
Figure 32: Viability of EMT6 cells after NIR laser treatment at 37°C in an incubator.	103
Figure 33: Viability of HUVEC cells after NIR laser treatment at 37°C in an incubator.	105
Figure 34: Cytokine concentrations in serum 7 days after PTT in mice treated with combination therapy of SWCNT-ANXA5 mediated PTT and anti-CTLA-4.....	109
Figure 35: TNF- α concentrations in serum 24 hours after PTT in mice treated with IV injection or IT injection of SWCNT-ANXA5.	110
Figure 36: Cytokine concentrations in serum 1 day (24 h) and 7 days (168 h) after PTT with different final temperatures.	113
Figure 37: Results of combinatorial photothermal therapy (PTT) and checkpoint inhibition (anti-PD-1) in EMT6 tumors.	116

Figure 38: Tumor Volumes on days 9, 14, and 21 after tumor inoculation of combinatorial photothermal therapy (PTT) and checkpoint inhibition (anti-PD-1) in EMT6 tumors.	116
Figure 39: Splenic cell analysis of combinatorial photothermal therapy (PTT) and checkpoint inhibition (anti-PD-1) in EMT6 tumors.	118
Figure 40: Tumor control from SWCNT-ANXA5 mediated PTT at 45°C for longer irradiation times in EMT6 tumor model	120
Figure 41: Results of combinatorial therapy of checkpoint inhibition (anti-PD-1) and photothermal therapy (PTT) at 45°C (immediately stopped or kept for 5 min) and in EMT6 tumors.....	122
Figure 42: Results of combinatorial therapy of checkpoint inhibition (anti-PD-1) and photothermal therapy (PTT) at 45°C (immediately stopped or kept for 5 min) in 4T1 tumors.	126
Figure 43: The anti-cancer innate immunity cycle.....	129
Figure 44: chemical structure of imiquimod (IMQ).	131
Figure 45: Long term survival study of combinatorial therapy of anti-PD-1, imiquimod-loaded hydrogel and photothermal therapy (PTT) at 55°C in 4T1 tumors.	133
Figure 46: Serum cytokine concentration of combinatorial therapy of anti-PD-1, imiquimod-loaded hydrogel and photothermal therapy (PTT) at 55°C in 4T1 tumors..	136
Figure 47: Analysis of splenic cells after combinatorial therapy of anti-PD-1, imiquimod-loaded hydrogel and photothermal therapy (PTT) at 55°C in 4T1 tumors.	138
Figure 48: Heating rate of (6,5) SWCNT and few walled CNT suspended in sodium dodecyl sulfate (SDS) in RF field..	143
Figure 49: Heating rate of (6,5) SWCNT and few walled CNT suspended in sodium deoxycholate (SDC) in 13,56 MHz RF field.	144
Figure 50: Assessment of radiofrequency responsivity of (6,5) SWCNT suspended in different surfactants.....	145
Figure 51: Analysis of the effect of the suspension of (6,5) SWCNT in solvent ethanol.	147
Figure 52: Heating rate of SWCNT-ANXA5 conjugate in 13.56 MHz RF field.	148

Figure 53: Heating rate of different chiral CNT suspended in sodium dodecyl sulfate (SDS) in 13.56 MHz RF field.....	150
Figure 54: Effect of the geometry of liquid phase on the heating rate of different samples in 13.56 MHz RF field.....	152
Figure 55: Images of the 13.56 MHz RF field irradiation of (6,5) SWCNT and sample PXD2-2069 in a completely filled cuvette.....	154
Figure 56:	155
Figure 57: Assessment of the effect of frequency in the responsivity of SWCNT to the RF irradiation at 15 W power output.	156
Figure 58: Analysis of statistical significance between samples irradiated with 100 W output power.	158
Figure 59: EMT6 cells in Petri dishes treated with 13.56 MHz RF field at 600 W.....	159
Figure 60: RF irradiation of euthanized mice at 400 W.....	161
Figure 61: Irradiation of tumor-bearing mice with 13.56 MHz RF field in small plates.	163
Figure 62: DM1 standard curve.....	164
Figure 63: Annexin A5 contribution to 288 nm signal.....	165
Figure 64: SDS-PAGE gel of ANXA5 and ANXA5-DM1.	166
Figure 65: Contribution of AuNP to Bradford assay.	167
Figure 66: Agarose gel electrophoresis of AuNP and AuNP-ANXA5-DM1 conjugate.	168
Figure 67: Cell viability of EMT6 cells treated with free DM1 and DM1 conjugates.....	170
Figure 68: Standard curve for low concentration SWCNT suspension using 250 μ L samples in 96-well plates.	206
Figure 69: Standard curve for high concentration SWCNT suspension using 100 μ L samples in 96-well plates.	207
Figure 70: Protein standard for Bradford assay.	208
Figure 71: IL-12 p70 concentration in serum 7 days after PTT in mice treated with combination therapy of SWCNT-ANXA5 mediated PTT and anti-CTLA-4.....	209
Figure 72: Extra data from cytokine concentrations in serum 1 day (24 h) and 7 days (168 h) after PTT with different final temperatures in EMT6 tumors.	210
Figure 73: Tumor volumes from combinatorial photothermal therapy (PTT) and checkpoint inhibition (anti-PD-1) in EMT6 tumors from days 5 to 25.	211

Figure 74: Tumor volumes from combinatorial photothermal therapy (PTT) and checkpoint inhibition (anti-PD-1) in EMT6 tumors from days 30 to 45.	213
Figure 75: Tumor volumes at various days for combinatorial therapy of checkpoint inhibition (anti-PD-1) and photothermal therapy (PTT) at 45°C (immediately stopped or kept for 5 min) and in EMT6 tumors.	214
Figure 76: Standard curve of imiquimod (IMQ) in methanol.	216
Figure 77: Long-term survival study of combinatorial therapy of anti-PD-1, imiquimod-loaded hydrogel and photothermal therapy (PTT) at 55°C in 4T1 tumors.	217
Figure 78: Survival curves of individual groups compared to control in long-term survival study of combinatorial therapy of anti-PD-1, imiquimod-loaded hydrogel and photothermal therapy (PTT) at 55°C in 4T1 tumors.	219
Figure 79: Tumor volumes from days 6 to 27 in long-term survival study of combinatorial therapy of anti-PD-1, imiquimod-loaded hydrogel and photothermal therapy (PTT) at 55°C in 4T1 tumors.	220
Figure 80: Tumor volumes from days 31 to 50 in long-term survival study of combinatorial therapy of anti-PD-1, imiquimod-loaded hydrogel and photothermal therapy (PTT) at 55°C in 4T1 tumors.	222
Figure 81: Thermal image analysis with ThermoCAM Researcher Pro 2.7 Software for experiment shown in Figure 58.	223
Figure 82: Details of the setup to concentrate the RF field to abdominal area of the mouse with smaller.	223
Figure 83: Details of the setup to ground excess charges built up from RF irradiation on mouse extremities.	224
Figure 84: Standard curve of AuNP.	225
Figure 85: Horizontal electrophoresis gel casting.	274

List of Tables

Table 1: Cell staining antibody cocktail for flow cytometric analysis of splenic cells	78
Table 2: Chemical structure of the surfactants used for suspending (6,5) SWCNT	87
Table 3: Percentage of each chirality type and length of CNT samples produced by CHASM™. Comparatively, the (6,5) SWCNT used in the PTT project has a length of ~1.5 μm.	89

List of Equations

Equation 1: Assessment of SWCNT-ANXA5 conjugation	69
Equation 2: Cell viability quantification from absorbance units in Alamar Blue Assay ...	72
Equation 3: Tumor volume from size measurement	73

Abstract

Cancer is considered the single most critical barrier to improving life expectancy in every country. More specifically, the high prevalence of breast cancer is a global health concern, but there are no safe or effective treatments for it at its advanced stages. Those facts urge the development of novel treatment strategies.

Annexin A5 (ANXA5) is a natural human protein that binds with high specificity to phosphatidylserine, a phospholipid tightly maintained in the inner leaflet of the cell membrane on most healthy cells but externalized in tumor cells, tumor vasculature, and metastatic cells. We have linked annexin A5 to single-walled carbon nanotubes (SWCNT) and gold nanoparticles (AuNP) in this work.

First, we have developed a targeted photosensitizer for photothermal therapy (PTT) of solid tumors through the functionalization of SWCNT to ANXA5: the SWCNT-ANXA5 conjugate. The ablation of tumors through the SWCNT-ANXA5-mediated PTT synergizes with checkpoint inhibition creating a systemic anti-cancer immune response. This treatment strategy was tested in two murine breast cancer tumor models, EMT6 and 4T1. Although EMT6 tumors are aggressive and metastatic, 4T1 tumors are considered even more threatening and less immunogenic than EMT6. For both tumors, enhanced therapeutic effects were achieved. While EMT6 tumors were treated with lower temperatures in the PTT, 4T1 required higher temperatures and the addition of an immune adjuvant to induce curative effects. For both studies, evidence of immune system activation strengthens the hypothesis of an abscopal effect. SWCNT-ANXA5 was also studied as a responsive material for radiofrequency ablation (RFA), showing an impressive heating rate and potential for carbon nanotube-mediated RFA of tumors.

Lastly, a multi-modal conjugate for the detection and therapy of cancer was developed linking ANXA5 to a chemotherapeutic drug, mertansine (DM1), and gold nanoparticles (AuNP) for drug delivery and contrasting agent in microCT scans in the diagnosis of breast cancer. Those linkages created the conjugate AuNP-ANXA5-DM1. This novel agent was able to induce cytotoxic effects and has the potential to increase the effectiveness of chemotherapeutic delivery to solid tumors.

CHAPTER 1 - INTRODUCTION

1.1 The cell and its plasma membrane

Cells are considered the elementary part of living organisms. The “cell theory” was first developed in 1839 by Schwann and Schleiden and proposed that all living things are composed of small fundamental structural and functional units: cells¹. Consequently, all organisms’ life activities take place within their cells. All cells are derived from pre-existing cells because they contain genetic information (DNA) passed down during replication¹.

The entity that distinguishes the intracellular content from its surroundings is the plasma membrane. It is composed fundamentally of the phospholipid bilayer. Phospholipids are molecules that have a hydrophilic head, usually consisting of phosphate groups, and fatty acid tails, which are hydrophobic. The intrinsic tendency of hydrophobic regions to assemble in close proximity to exclude water molecules drives the spontaneous formation of the bilayer. Additionally, the interaction of phosphate heads with the excluded aqueous environment promotes the stability of the structure. Therefore, the membrane lipid bilayer has the hydrophobic tails concealed in the hydrophobic core, but the polar heads are revealed to both opposing sides of the aqueous solution of the extracellular and intracellular environment² (see **Figure 1A**).

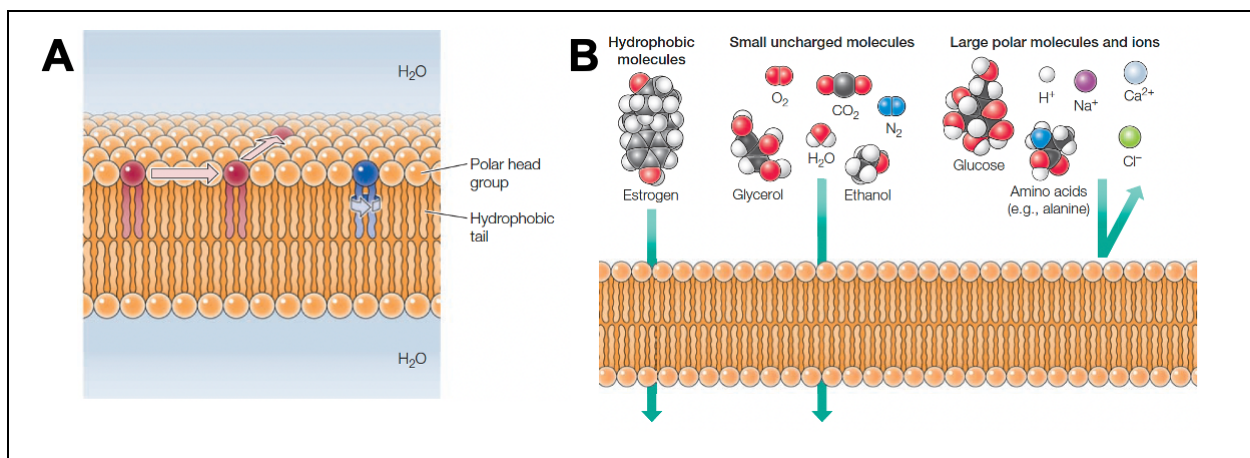


Figure 1: The phospholipid bilayer. A) phospholipid bilayer: Phospholipids form stable bilayers spontaneously, with their polar head groups exposed to water and their hydrophobic tails buried within the membrane's interior. Within the bilayer, individual phospholipids can rotate and move laterally. B) Permeability of phospholipid bilayers:

The phospholipid bilayer allows gases, hydrophobic compounds, and small uncharged molecules to diffuse readily. Conversely, the bilayer is impermeable to larger polar molecules like glucose, amino acids, and ions. (Figures from Cooper, G. M. *The cell: a molecular approach*. Sinauer Associates, an imprint of Oxford University Press, 2019²)

The formation of a centered oily phase restricts the movement of most molecules between the two sides of the bilayer structure. That limitation is called selective permeability. Small non-polar molecules can easily cross the membrane due to their ability to solubilize into the lipidic phase. Small uncharged ones, such as water, can diffuse through the membrane at a lower rate. Charged species like ions are impeded from crossing the membrane (see **Figure 1B**). Selective permeability grants the cells the ability to manage and sustain a particular internal composition different from its surroundings^{3,4}

A set of specialized proteins buried in the phospholipid bilayer perform the transportation of the molecules that do not spontaneously pass through the membrane. In fact, the proposition that the cell membrane is constituted by integral proteins randomly embedded in the essential structure of the phospholipid bilayer was first made in 1972 by Singer and Nicolson⁵, and was called the fluid-mosaic membrane model (FMMM). FMMM proposed that, along with the spontaneous formation of the phospholipid bilayer due to hydrophobic and hydrophilic interactions, transmembrane proteins would coexist inside of the membrane by exposing their non-polar amino acid residues to the lipidic phase and their polar groups to the aqueous environment. Therefore, integral proteins are the other principal constituent of the cell membrane, making from 25 to 75% of the mass of the various membrane types⁶. Other functions of the membrane proteins include, but are not limited to: interactions with the extracellular matrix, receptors that collect external signals, and promote intracellular cascades (cell signaling)⁷.

The different interactions between the various components of the cell membrane establish lipid rafts and specialized cell domains, ideas that are in accordance with the “mosaic” part of the theory. The introduction of more complex interactions, such as membrane-associated cytoskeletal and extracellular structures, changed the model

proposed by Nicholson and Singer in 1972. As new interactions and complexity are found, more components are included in the model⁶, as shown in **Figure 2**.

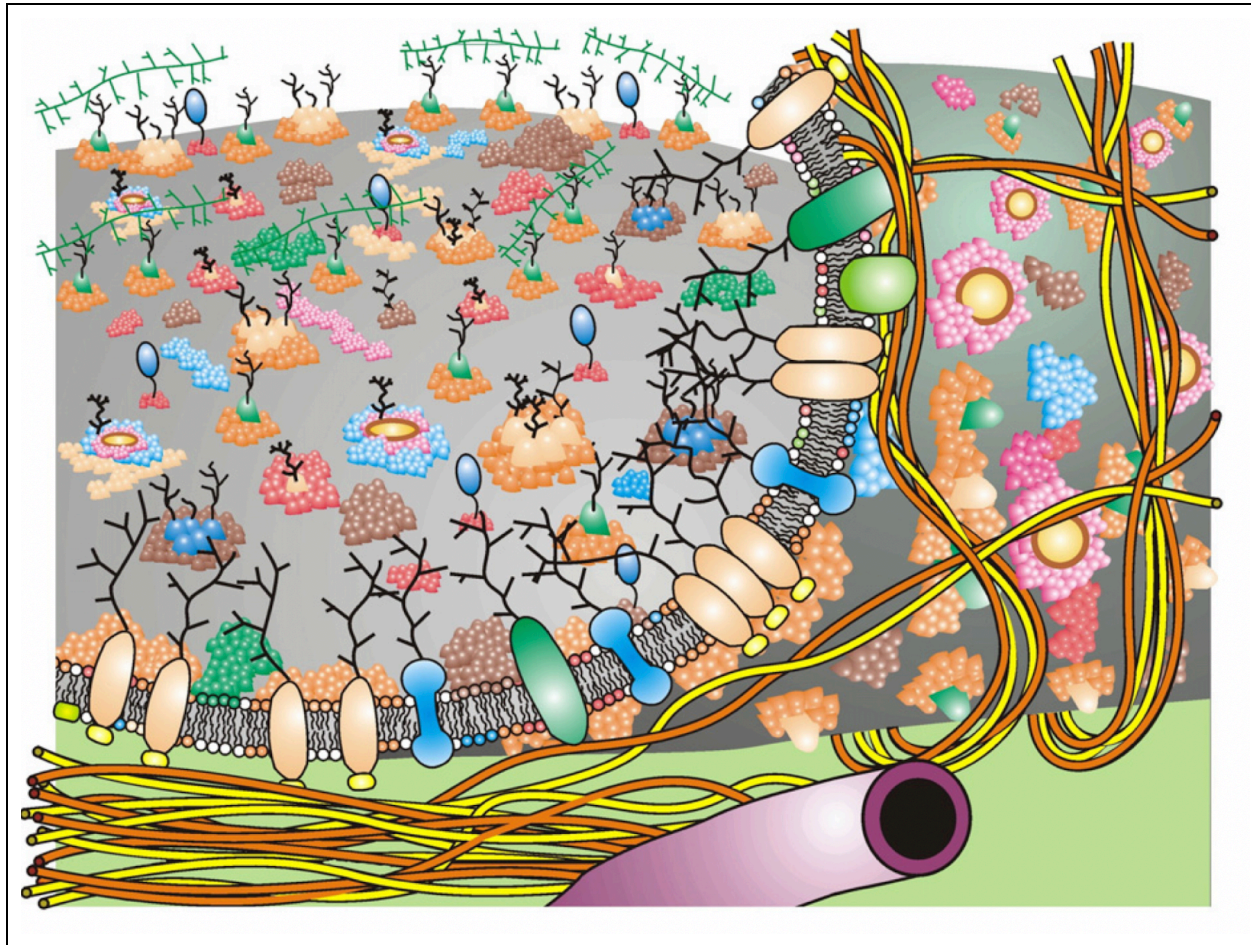


Figure 2: Updated fluid—mosaic membrane model (2014). The membrane has domain structures, membrane-associated cytoskeletal, extracellular structures, different integral proteins, glycoproteins, lipids, and oligosaccharides. Inner surface show cytoskeletal fencing. Image from Nicolson, 2014⁶.

1.1.1 Plasma membrane asymmetry: the default state of cells

The plasma membrane is composed of five major classes of phospholipids: phosphatidylcholine (PC), phosphatidylethanolamine (PE), phosphatidylinositol (PI), sphingomyelin (SM), and phosphatidylserine (PS)⁸, as shown in **Figure 3**. Although PS

is not the most abundant phospholipid in the plasma membrane, it has a vital role in the research presented in this work, which will be introduced later.

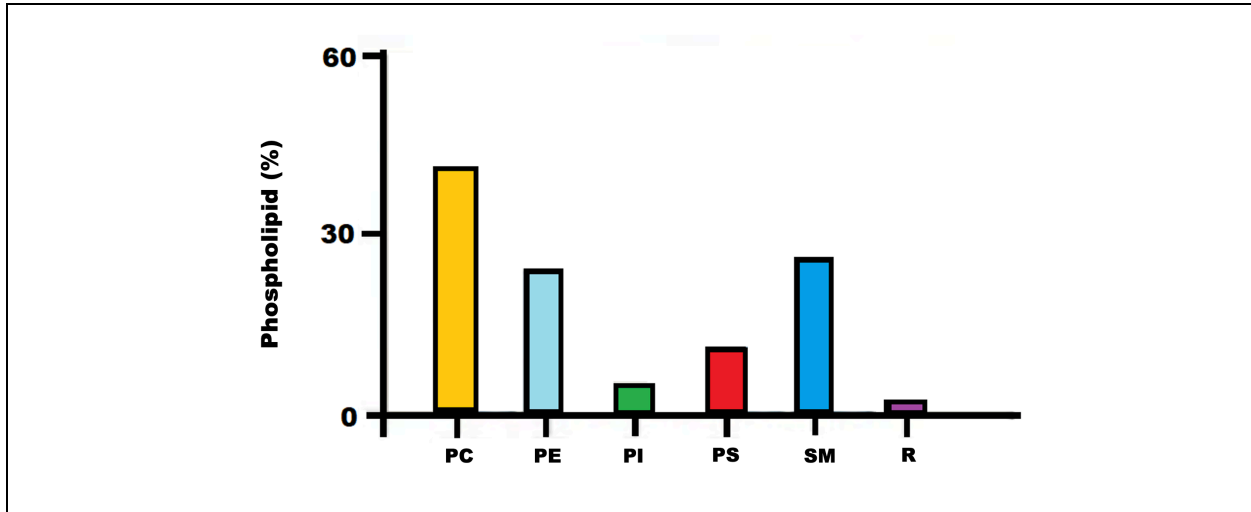


Figure 3: Lipid steady-state composition of the plasma membrane. Data expressed as a percentage the total phospholipid composition of mammalian cells. Image adapted from van Meer et al., 2008⁹.

Another important plasma membrane concept from 1972 was introduced by Bretcher: **lipid asymmetry**. Bretcher¹⁰ used chemical reagents that specifically label PS and PE on red blood cells (RBC) and found that traces of those phospholipids were labeled on the surface of intact RBC. Still, the labeling was very efficient on damaged RBC. With that experiment, it was concluded that PS and PE are preferentially localized on the cytoplasmic leaflet of the plasma membrane of undamaged cells. Since then, various other groups have studied the localization of the different phospholipids across the plasma membrane using other techniques¹¹⁻¹⁶. It has been established that the totality of eukaryotic cells confines almost all charged lipids to the cytosolic leaflet of the plasma membrane. Therefore, the outer layer is composed primarily of PC and SM, while PS and PE are located in the inner leaflet¹⁶, as shown in **Figure 4**.

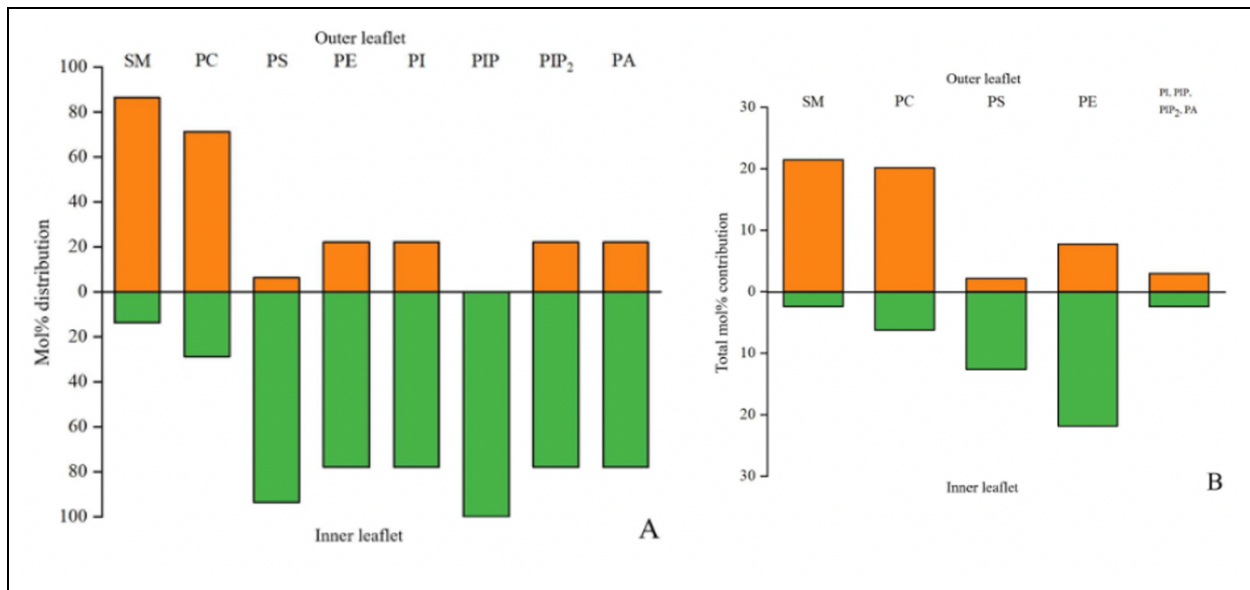


Figure 4: Distribution of phospholipids on each leaflet of the red blood cell plasma membrane. A) molar percentages of each lipid in each membrane leaflet: SM and PC are concentrated in the outer leaflet, while all other lipids, especially PS and PE, are concentrated in the inner leaflet. B) mole percentage of the total amount of phospholipid in the membrane. PS is the major anionic phospholipid present in the inner leaflet. Abbreviations: SM, sphingomyelin; PC, phosphatidylcholine; PS, phosphatidylserine; PE, phosphatidylethanolamine; PI, phosphatidylinositol; PIP, phosphatidylinositol-4-phosphate; PIP₂, phosphatidylinositol-4,5-bisphosphate; PA, phosphatidic acid. Figure from Clarke *et al.*, 2020¹⁷.

Eukaryotic cells ubiquitously maintain lipid asymmetry across the two leaflets of the plasma membrane bilayer¹⁸. Lipid asymmetry conservation requires cell energy expenditure. Initially, it was thought that, once established, the lipid asymmetry would last for the remaining time of cell life due to very slow spontaneous translocation of the phospholipids between the leaflets in synthetic lipid vesicles¹⁹. Nonetheless, measurements on the flip-flop of phospholipids in lipidic vesicles encrusted with proteins had a much smaller half-life of minutes^{20–22}. It is hypothesized that the presence of transmembrane proteins creates defects in the vesicle structure that reduce the energy barrier for the translocation of the phospholipids between the leaflets²³. Therefore, if the

lipid translocation in natural cellular membrane conditions is spontaneous and rapid, then the cell must spend energy on maintaining the lipid asymmetry.

Cell membrane-associated and energy-consuming enzymes have been identified as being responsible for maintaining lipid asymmetry: flippases are the ones that translocate phospholipids from the extracellular side to cytoplasmic leaflet; floppases push them from the intracellular to the extracellular side of the plasma membrane. Another group of transmembrane proteins that transport lipids across the membrane is scramblases, although they do not require energy to facilitate bidirectional lipid translocation^{17,24-26} (see **Figure 5**). It is worthwhile to point out that even though scramblases' presence in the plasma membrane is inherent, their natural state is inactive, requiring activation by either signaling or cleavage.

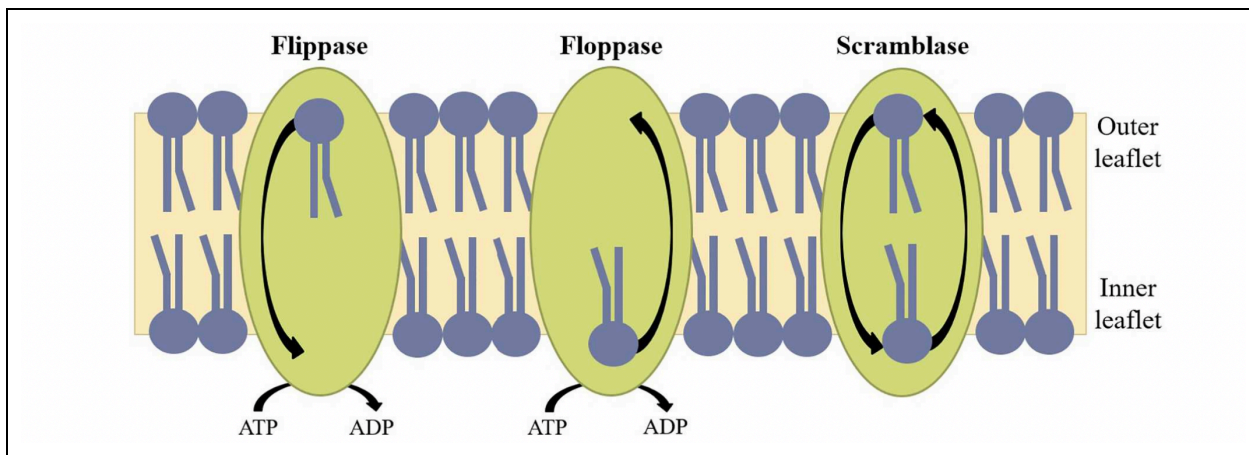


Figure 5: The three classes of phospholipid translocases: flippases, floppases, and scramblases. Flippases actively move PS and PE from the outer to the inner leaflet of the plasma membrane against a concentration gradient using ATP. Floppases use ATP to transport PC, SM, and cholesterol against concentration gradients in the opposite direction (inner to outer leaflet). Both flippases and floppases contribute to maintaining lipid asymmetry across the membrane, which requires energy from ATP hydrolysis to drive the process because it is a nonequilibrium phenomenon. Scramblases facilitate the movement of lipids along concentration gradients. Scramblases are ATP-independent because they lead the membrane to approach an

equilibrium distribution of phospholipids across the membrane, therefore abolishing lipid asymmetry²⁷. Figure from Clarke *et al.*, 2020¹⁷.

Flippases were firstly identified as ATP-dependent translocases. Initial evidence showed that the depletion of ATP inhibits the flipping of the PS and PE to the inner leaflet of the plasma membrane²⁸. Additionally, the same enzymes had their activity inhibited by treating cells with phosphate analog orthovanadate, a common characteristic of the family of sodium/phosphate pumps called P-type ATPases. The amino acid sequencing of those flippases confirmed that they were part of the P-type ATPases family^{29,30}. Currently, the flippases are classified as a subfamily known as P4-ATPases^{15,17}.

Conversely, floppases were recognized as part of a family of enzymes that are ATP-binding cassette transporters (or ABC transporters). This family can translocate many types of molecules through the plasma membrane. Although the family has many physiological roles, the transport of PC and SM from the cytoplasmic leaflet to the extracellular side is an essential function. ABCA1, ABCA3, ABCA4, ABCA7, ABCB1, ABCB4, and ABCC1 are all ABC transporters that export lipids to the outer layer of the cell membrane^{31,32}.

Both flippases and floppases are crucial in maintaining lipid asymmetry, primarily because they transport lipids against the concentration gradient. The prevention of the downhill movement of the lipids during transport requires complex conformational changes, which lead to a relatively low turnover (less than 100 s^{-1})³³. Conversely, scramblases have much higher turnover rates (greater than 1000 s^{-1})³⁴. Thus, floppases and flippases are constantly pumping lipids to maintain the lipid asymmetry and their expression in the plasma membrane is much higher than scramblases¹⁷. The lipid asymmetry elimination due to the scramblases' activation is very rapid.

1.1.2 Scramblase Activation and Phosphatidylserine Exposure

As previously mentioned, phosphatidylserine (PS) is steadily maintained in the inner leaflet of the cell membrane by the action of flippases. This physiological

mechanism that occurs continually during mammalian cells' lifespan requires energy expenditure. Reasonably, the cells must benefit from allocating considerable effort to the specialized localization of those phospholipids. Interestingly, the exposure of PS on the surface of the cells has physiological significance, for example, in blood coagulation and apoptosis.

The plasma membrane scramblases are responsible for the disruption of the lipid asymmetry and, consequently, exposure of PS on the outer leaflet. Those transmembrane proteins translocate lipids between the leaflets bidirectionally and non-selectively, following the energetically favorable direction established by each phospholipid's concentration gradient. Contrary to the floppases and flippases that need conformational changes to function appropriately, analogous to ion pumps, scramblases perform the translocation similarly to ion channels, which spontaneously allow the passage of lipids and promote an efficient kinetic process^{33,35}. Consequently, the exposure of PS on the cell membrane due to the activation of scramblases is a rapid process.

The two classical causes of PS exposure are blood coagulation and apoptosis. Respectively, two major classes of scramblases have been identified in correlation to those processes: transmembrane protein 16 (TMEM16) and XKR.

TMEM16 is a family of plasma membrane proteins identified as Ca^{2+} -dependent scramblases. The most expressed member of this family is TMEM16F. After its 3D structure determination, the conformational changes during lipid translocation suggested the Ca^{2+} binding to TMEM16F induces the opening of a cavity for the passage of phospholipids^{36,37}. The visual depiction of the TMEM16F translocation of phospholipids is shown in **Figure 6**, also known as “the credit card model”.

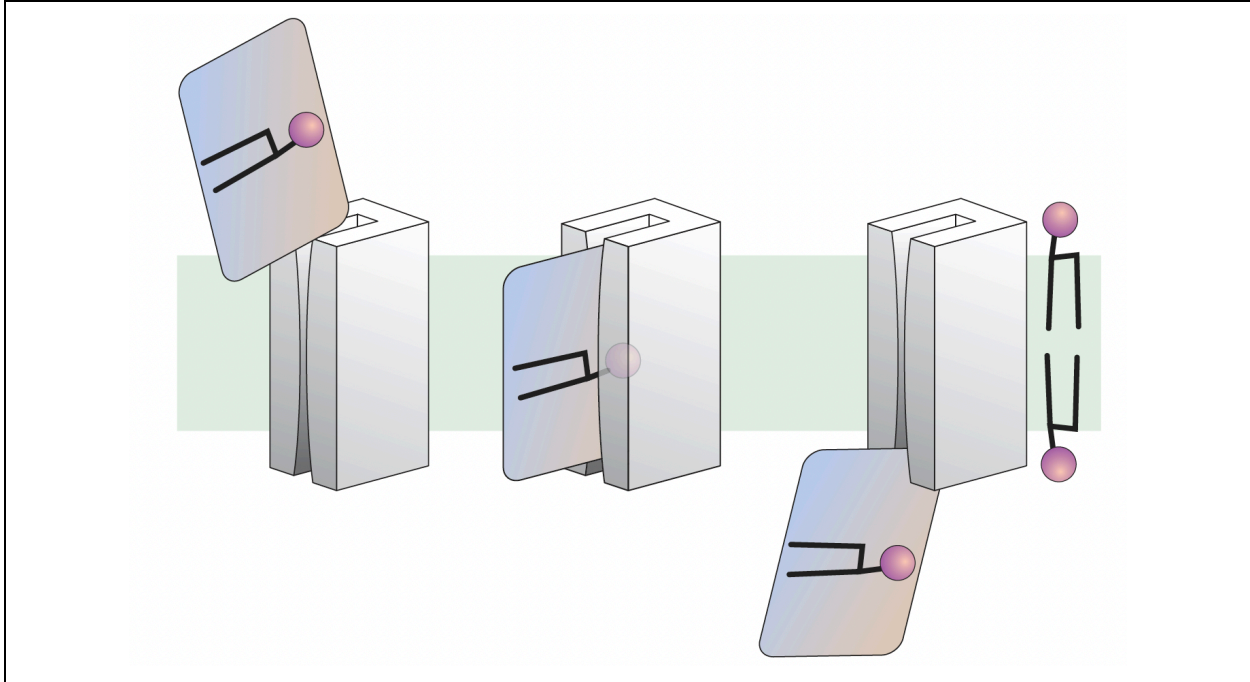


Figure 6: The credit card model for the mechanism of protein-mediated lipid transport. Flippase/scramblase-mediated phospholipids transfer between the bilayer leaflets (light green) is depicted as a credit card swiping through a card reader. The polar head group of the lipid is the magnetic stripe on the credit card, and lipid's acyl chains correspond to the rest of the card. The card reader representing the hydrophilic groove shields the polar headgroup from the membrane's hydrophobic interior during transit. Figure from Kobayashi & Menon, 2018 ²⁶.

The activation of TMEM16F occurs in platelets during blood coagulation, which is critical in preventing blood loss. The process starts with the initial activation of platelets by subendothelial factors, mainly collagen, after endothelial damage, which promotes the release of coagulant mediators from platelets. This activation also triggers cell signaling that stimulates the release of Ca^{2+} from the cytoplasmic stores and the opening of Ca^{2+} channels on the plasma membrane. Consequently, the cytoplasmic Ca^{2+} concentration in the platelet increases, which is the signal for activation of TMEM16F. As mentioned previously, the functioning TMEM16F scramblase quickly promotes the loss of lipid asymmetry and the exposure of PS on the cell membrane.³⁸

In this context, PS on the surface is essential for the attraction of clotting factors and consequent increase of their concentration locally on the surface of the platelets. Additionally, PS acts as a catalytic surface for the coagulation cascade^{38–40}. This mechanism is summarized in **Figure 7 (left panel)**.

While the PS exposure is mediated by TMEM16F scramblase during platelet activation, another scramblase is responsible for that process on apoptotic cells: Xkr8⁴¹. This scramblase is activated through cleavage that is performed by caspases, peptidases related to the machinery of apoptotic cell death.

Apoptosis is a critical genetically controlled physiologic process for tissue homeostasis. It is also called programmed cell death since it disposes of damaged and old cells using controlled means that prevent the release of toxic cytoplasmic contents. Although two different pathways have been identified as apoptosis triggers, both lead to the activation of caspases^{42,43}. Therefore, the activation of caspases – intrinsic to the apoptosis cascade - promotes activation of XKR8 scramblases and consequent PS externalization.

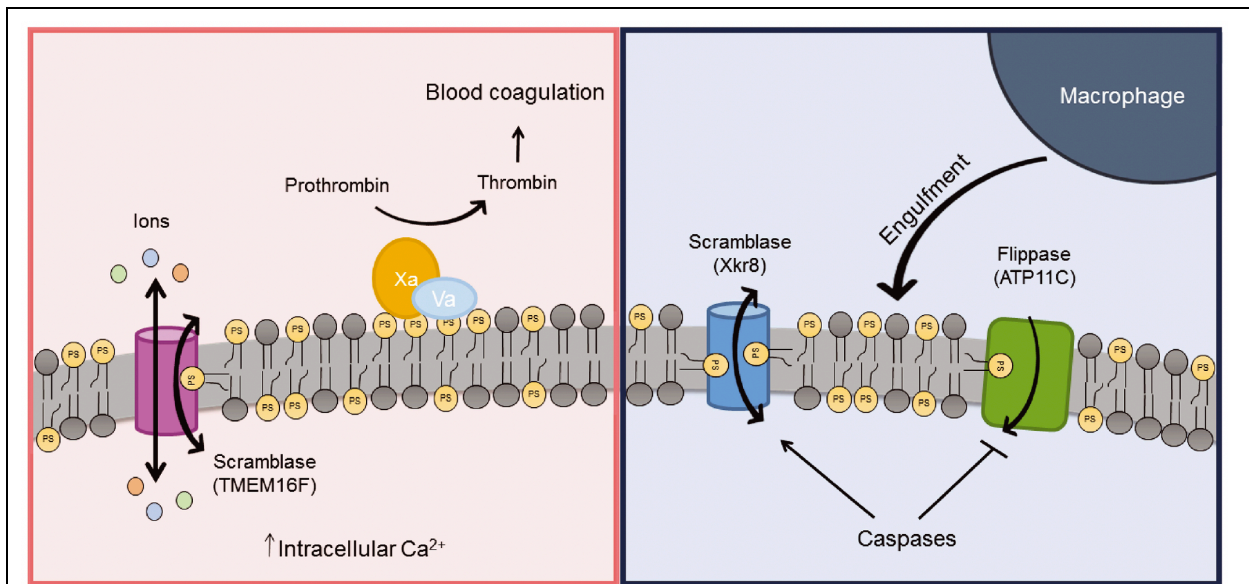


Figure 7: Pathways phospholipid scrambling during blood coagulation and apoptosis. Left panel: The blood coagulation process leads to an elevation in intracellular Ca^{2+} level, which stimulates TMEM16F scramblase activity on platelets. The scrambling of those membrane components causes exposure of PS on the

surface, where it acts as a platform on which coagulation protein complexes assemble. Right panel: Apoptosis caspases activate scramblase activity. Caspase might also inactivate flippase activity (ATP11C) by cleaving at their caspase-recognition sites, which prevents the reestablishment of lipid asymmetry. Phospholipid scrambling causes PS to be exposed on the surface of the apoptotic cell, where it acts as an 'eat me' signal for macrophages. Image from Hankins *et al.*, 2015⁴⁴.

The duration of PS activation on cells by both scramblases is distinct. While the activation of TMEM16F by Ca^{2+} cytoplasmic concentrations is a reversible process, Xkr8 activation from caspase cleavage is permanent. Therefore, the PS expression related to the blood coagulation cascade is temporary, yet the apoptotic PS externalization is changeless, exacerbated by caspase cleavage's everlasting deactivation of ATP11C.

The purpose of externalized PS on apoptotic cells is to be a signal for macrophage engulfment, which has been called the "eat-me signal" (see **Figure 7, right panel**). Because the primary purpose of this process is to eliminate cells without damaging the surrounding tissue, this mechanism is also known to promote the suppression of inflammatory responses. Antigen-presenting cells (APCs) have phosphatidylserine receptors (PSR) that recognize the overexpression of PS on apoptotic cells. The binding of PS to PSR triggers the phagocytosis of the apoptotic cells. This binding also induces the release of anti-inflammatory species in that region by the APCs, which dampens the inflammatory response. Therefore, PS externalization is also correlated to the generation of dampening inflammatory signals^{45,46}. Ironically, this same fundamental process for tissue homeostasis is used by cancer cells to reduce inflammatory immune response and promote cell proliferation⁴⁷.

1.1.3 PS externalization on cancer cells and tumor vasculature

While the default state of healthy cells is the maintenance of PS in the inner leaflet of the plasma membrane, externalization of PS on the surface of cancer cells

appears to be prevailing in many cancer types⁴⁸. Many studies have identified high PS content on the outer leaflet of the plasma membrane of a multitude of cancer cell lines^{48–50}. Even though cancer cells are non-apoptotic, they have increased amounts of PS on the outer leaflet of the plasma membrane. Additionally, PS externalization has been recognized in the tumor vasculature^{51,52}, metastatic tumor cells⁴⁸, and tumor-derived microvesicles⁵³.

This phenomenon has been associated with three molecular mechanisms: 1) lower activity of flippases, the enzyme that transports PS from outer to inner leaflet; 2) higher intracellular concentration of Ca^{2+} , which is known to activate scramblases; 3) higher overall concentration/production of PS on the tumor cells characterized by increased activity of PS synthesizing enzymes⁵⁰. Additionally, the overexpression of scramblases, such as TMEM16F⁵⁴, and the lower expression of floppases (ATP11b)⁵⁵ are potential mechanisms for the PS externalization on non-apoptotic cancer cells.

Tumor cells have developed mechanisms to circumvent immune destruction. PS exposure is a hallmark of apoptosis as an “eat-me signal” for antigen-presenting cells (APCs), such as macrophages and dendritic cells, as part of the apoptotic machinery for non-immunogenic clearance^{56,57}. As previously mentioned, the phosphatidylserine receptors (PSR) on APCs recognize PS externalization on apoptotic cells, triggering phagocytosis by immune cells. Even though cancer cells overexpress PS on their surface, they are not engulfed by APCs. This paradox has been correlated to the hyperexpression of CD47, a cell surface ligand that sends a potent “don’t eat me” signal to macrophages⁵⁸. Thus, immune cells fail to act on the destruction of tumor cells in the presence of PS on the surface of cancer cells.

Furthermore, cancer cells use the anti-inflammatory effects of PS on APCs to induce a tumor-favoring environment. Cancer cells’ PS overexpression causes the shed of soluble phosphatidylserine (sPS). sPS binds to PS receptors (PSR) on APCs (dendritic cells, macrophages, and T-cells), which activates their production of anti-inflammatory species, such as IL-10, TGF- β , and prostaglandin E2 (PGE2). Furthermore, cancer cells overexpress themselves PSR, which their own shed sPS can trigger. This binding also induces cancer cells to produce the same anti-inflammatory species (IL-10, TGF- β , PGE2). Those species act on macrophages, dampening their anti-tumoral

response, thus generating tumor-associated macrophages⁵⁹. The same species also inhibit dendritic cell antigen presentation to T-cells, which promote regulatory T-cells⁶⁰. Additionally, the PSR firing on macrophages caused by cancer surface PS and sPS induces a change in macrophage polarization from pro-inflammatory (M1-like) phenotype to a protumor (M2-like) phenotype⁶¹.

Likewise, tumor-derived microvesicles also promote an anti-inflammatory tumor microenvironment. Those vesicles have enhanced PS exposure, which enhances apoptotic cell removal by phagocytes. This immunological silent removal inhibits inflammatory response, promoting an immunosuppressive tumor microenvironment⁶¹. Those microvesicles are also correlated to the T-cell response suppression by arresting the T-cell signaling cascade⁶².

1.2 Annexin A5 binds to externalized phosphatidylserine

The contrasting PS expression between cancer and healthy cells compels the use of PS as a target for cancer treatment. Whereas the absence of externalized PS is the default state of far most healthy cells, PS is externalized in cancer cells, tumor vasculature, and metastatic cancer cells. The lack of PS on healthy cells might reduce the effect of PS-targeted therapies on those cells, reducing the overall side effects. Due to the relevance of targeting treatment regimens in the prognosis of cancer treatment, it is of utmost importance to develop new targeting strategies.

In this work, annexin A5 has been used as a targeting strategy for externalized PS because this relatively small soluble protein (~36 kDa) binds specifically to PS clusters on the surface of the plasma membrane. Annexin A5 (ANXA5) was first identified in 1985 due to its anticoagulant effect⁶³. It has been proved that ANXA5 has a high binding affinity to negatively charged phospholipids such as PS. The binding occurs through a calcium-mediated mechanism⁶³⁻⁶⁵. Therefore, the natural concentration of Ca²⁺ in the bloodstream facilitated the efficient binding of ANXA5 to PS on the surface of cells⁶⁶.

The structure of ANXA5 was elucidated by X-ray crystallography⁶⁷. The tertiary arrangement is shaped as a slightly curved structure formed by four domains aligned cyclically⁶⁸, as shown in **Figure 8**. Both the calcium and the PS binding sites are located on the curved structure's convex side, consequently consisting of the side facing the membrane. Non-covalent interactions between the distinct domains maintain this architecture (see **Figure 9**).

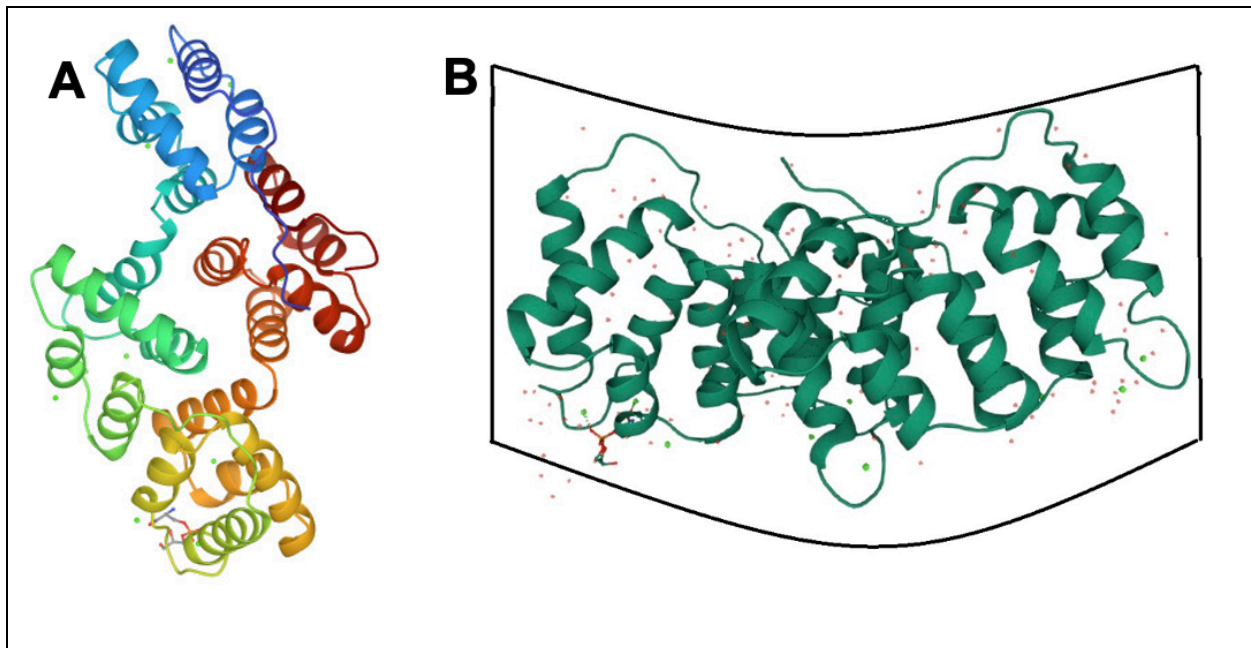


Figure 8: Three-dimensional model of human annexin A5. A) Visualization of the 3D structure from the top, considering the binding sites at the bottom of the protein (regions that interact with the PS-bearing plasma membrane). B) Side view of the 3D structure depicting the convex attachment region to the membrane and the concave area. Images from the RCSB PDB (rcsb.org) of PDB ID 1A8A ([Swairjo, M.A., Concha, N.O., Kaetzel, M.A., Dedman, J.R., Seaton, B.A.](#) Ca(2+)-bridging mechanism and phospholipid head group recognition in the membrane-binding protein annexin V. (1995) *Nat Struct Biol* **2**: 968-974.⁶⁹) DOI: [10.2210/pdb1A8A/pdb](https://doi.org/10.2210/pdb1A8A/pdb)

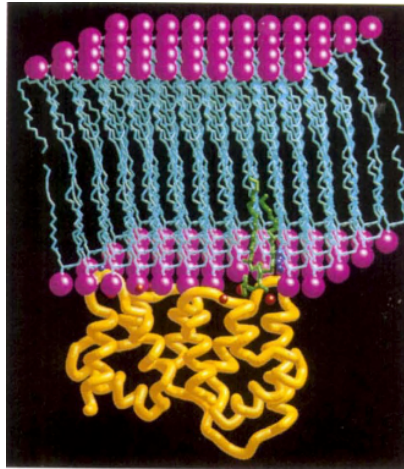


Figure 9: Three-dimensional model of Ca^{2+} -dependent binding of Annexin A5 to membrane model showing. The positions of protein, PS and Ca^{2+} atoms were derived from crystallographic data, whereas acyl chain of the bound lipid was modelled graphically. Yellow: protein backbone; light blue: membrane lipid acyl chains; red: Ca^{2+} ions; green: bound phosphatidylserine; magenta: membrane lipid polar heads. Image from Swairjo *et al.*, 1995⁶⁹.

It is believed that the convexity of the protein promotes shape changes in membrane regions where it binds, inducing a complementary curvature of the membrane to the protein assembly. The reasoning is that all four ANXA5 domains have PS-binding sides, even the ones that would be more distant from the membrane if the membrane had a straight or outward bent conformation⁷⁰.

Furthermore, whereas soluble ANXA5 flows in the bloodstream as monomers, the bonding to the membrane induces the polymerization of ANXA5 molecules into trimers. Studies on membrane-bound ANXA5 using electron crystallography indicate that ANXA5 molecules associate due to protein-protein interactions and form a two-dimensional crystal lattice - the symmetrical arrangement of atoms inside a crystalline structure. The eventual conformation of the trimer after association also results in a convex geometry that reshapes the membrane⁷¹. The membrane-bound ANXA5 trimer can further associate with other trimers through the interaction of amino acid residues on domain III. Different organizations of crystal lattice can be formed and are influenced by the concentration of Ca^{2+} in the proximity and the

level of PS externalization. Therefore, the crystal lattice can be created by trimers, dimers of the trimers, and trimers of the trimers⁷², as shown in **Figure 10**.

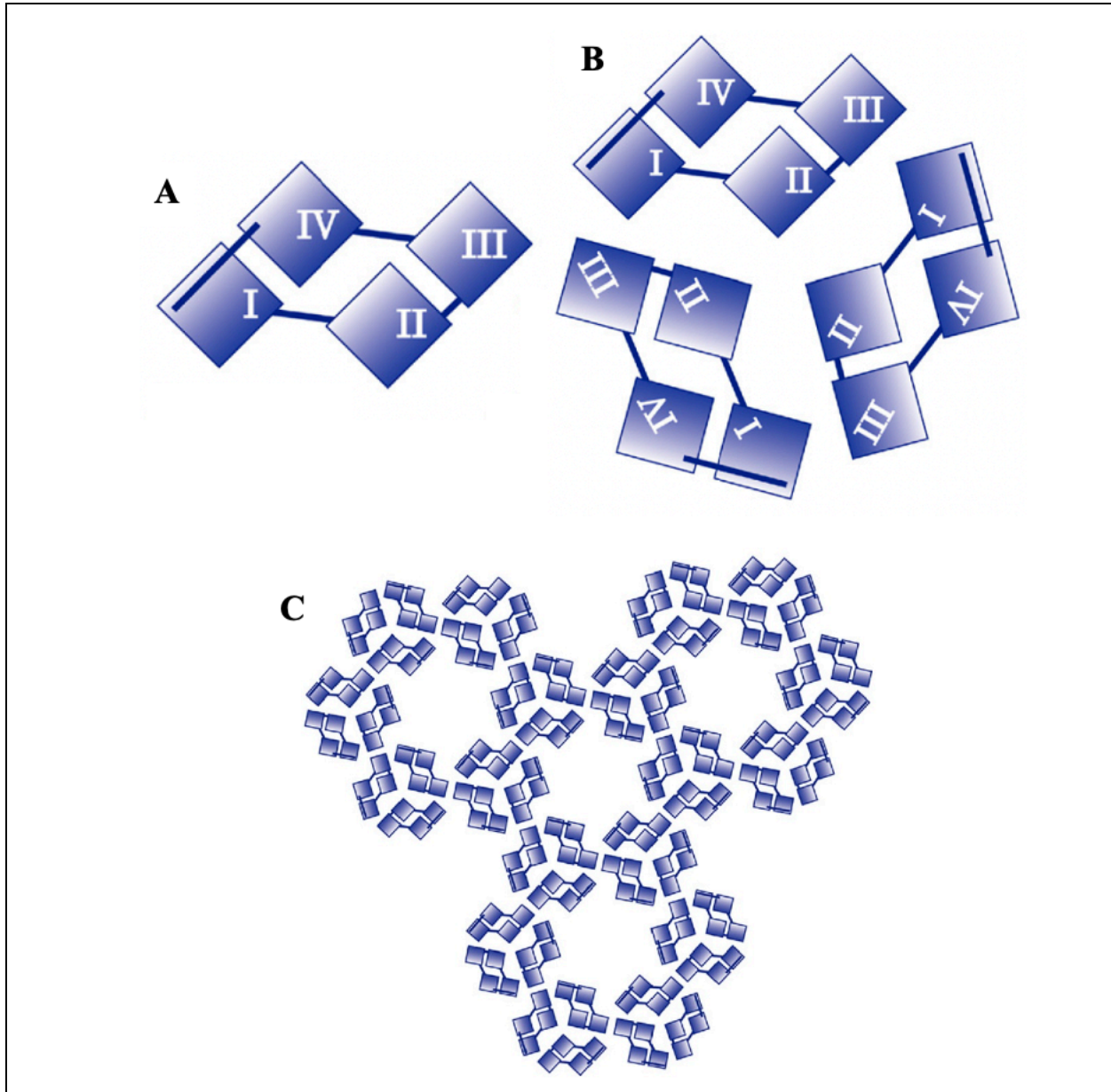


Figure 10: Annexin A5 domains and trimerization: A) Representation of monomeric annexin A5 and its four domains. B) Membrane-bound annexin A5 assembly into a trimer: this organization leads to the location of every domain II from each monomeric protein in the center of the trimer. Trimerization induces the formation of a two-dimensional crystal lattice characterized by P6 symmetry. C) Representation of the

trimer of trimers of the membrane-bound annexin A5. Image from van Genderen *et al.*, 2008⁷³.

One of the main functions of ANXA5 is anticoagulation. Two mechanisms have been proposed for the anticoagulation properties of ANXA5. First, the binding of ANXA5 to the externalized PS on the surface of activated platelets, a catalytic surface for the coagulation cascade, competes with the binding of coagulation factors to the catalytic surface⁷⁴. Additionally, the formation of the 2D crystal lattice on the surface of the platelets due to ANXA5 binding inhibits the formation of prothrombinase due to the limitation of lateral movements of its precursors⁶⁵. Second, the PS-bearing blebs generated by activated platelets, also called microparticles (MP), have a coagulant effect and promote the further activation of the coagulation cascade because of the presence of the PS-rich catalytic surface. Therefore, the ANXA5 binding to platelet MP inhibits the procoagulant activity of those blebs identically to ANXA5 on the surface of platelets⁷⁵. ANXA5 might also inhibit the formation of blebs by restricting the outward membrane conformation necessary for the shedding of MP, which is correlated to the induction of a concave shape of the membrane on the ANXA5 binding region⁷⁶.

It is hypothesized that the binding of ANXA5 to the cell membrane promotes internalization. The formation of convex ANXA5 trimers on the surface of cells causes invagination of the plasma membrane and consequent endocytosis. The complementary membrane shape to the trimer convexity, followed by the formation of the crystal lattice, induces membrane arching, which consequently results in the vesicle generation⁷⁰, as shown in **Figure 11**. This hypothesis is supported by evidence of ANXA5 internalization into the cytosol by stressed cardiomyocytes, myoblasts, and apoptotic neurons⁷⁷. Additionally, studies in Jukart cells and HeLa tumor cells have shown that ANXA5 internalization is independent of the classical endocytic pathways commonly responsible for internalizing extracellular proteins: macropinocytosis or receptor-mediated internalization⁷⁰.

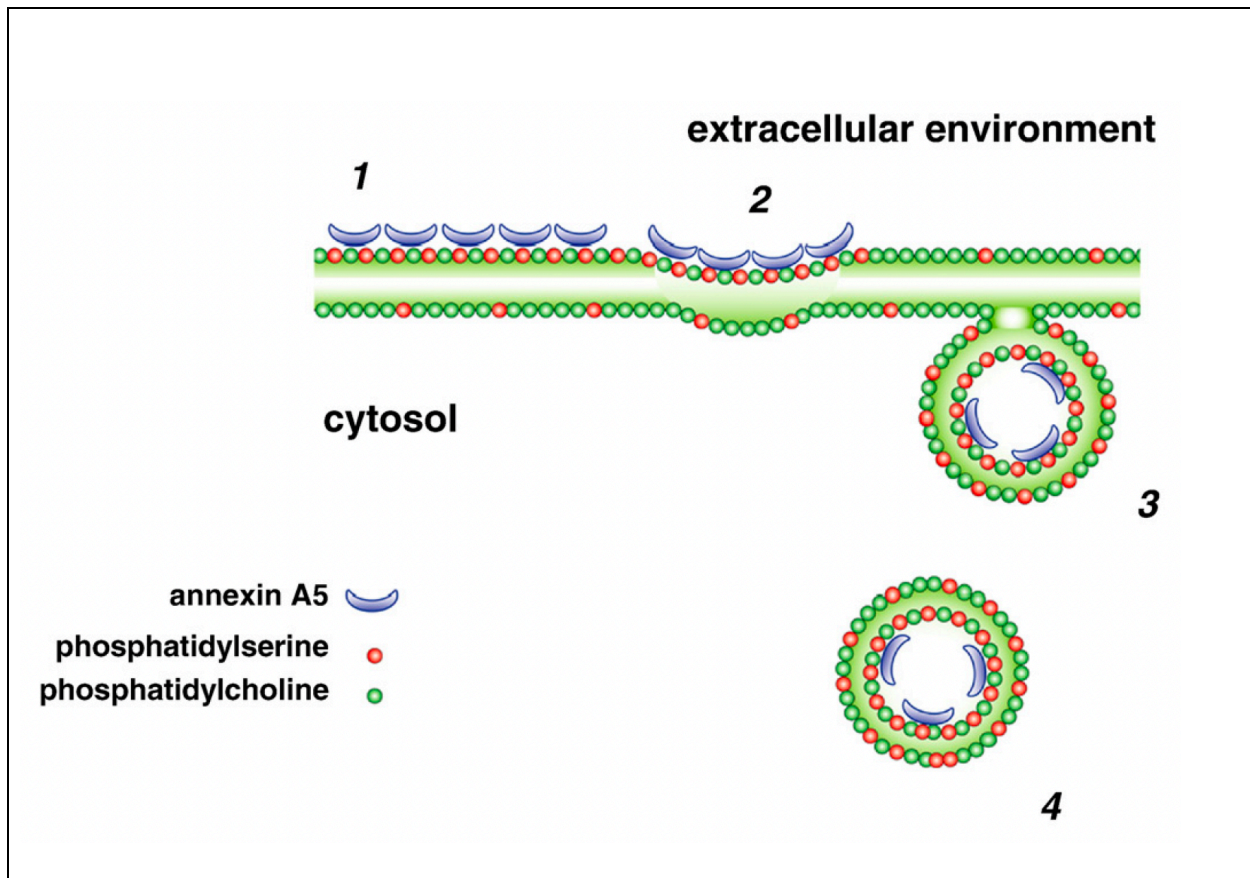


Figure 11: Annexin A5 binding to phosphatidylserine induces endocytosis. (1) ANXA5 binds to PS; (2) two-dimensional crystallization of ANXA5 causes a bend on the plasma membrane; (3) formation of an endocytic vesicle; (4) vesicles separate from the plasma membrane. Image from van Genderen *et al.*, 2008 ⁷⁸.

The fact that annexin A5 binds strongly and specifically to externalized phosphatidylserine of a minority of cells that had left the membrane asymmetry default state establishes the protein suitability for targeting agent. Additionally, the evidence that ANXA5 promotes internalization can make this strategy even more efficient for delivering therapeutic agents to tumors.

In this work, the strategy of using ANXA5 as a targeting agent for cancer treatment, specifically triple-negative breast cancer, a subtype of cancer lacking current targeted therapies, will be presented.

1.3. Perspectives on Cancer

1.3.1 Cancer and its relevance worldwide

Cancer is ranked as the primary or secondary major death cause before the age of 70 in 91 countries in the world, according to WHO estimates from 2015⁷⁹ (see **Figure 12**). Although cancer is currently the second most important cause of premature deaths worldwide, it might outweigh cardiovascular diseases (CVD) in this century. This prediction is based on two factors: (1) in countries where cancer is the primary cause of death, the rate at which cancer incidence decreases is similar to CVD's rate of decrease, which would lead to the maintenance of cancer ranking above CVD; (2) in countries where CVD is the primary cause of death and cancer is the second, the rate at which CVD declines is more significant than the decline of cancer incidence, which would result in a switch in positions in the rank⁸⁰.

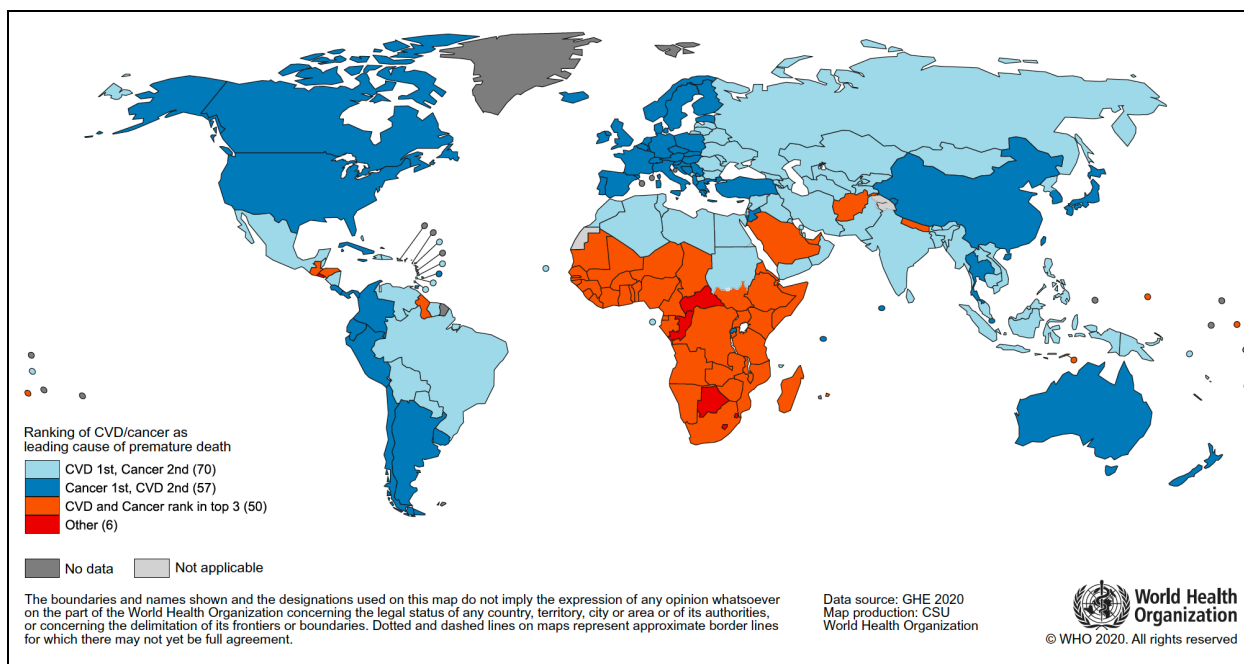


Figure 12: Global map ranking cancer as a leading cause of death at ages below 70 years in 2019 for each country. The legend includes the number of countries in each ranking group. Source: World Health Organization. Image from Bray *et al.*, 2021⁸⁰.

The incidence of cancer has been growing worldwide and also has its mortality. Although population aging is one of the causes of this increase in cancer rates, the prevalence of the principal risk factors associated with cancer development is likewise critical to that upsurge. Cancer risk factors include but are not limited to tobacco use, physical inactivity, excess body weight, and reproductive patterns⁸¹. In developed countries, the higher decrease in the mortality rate from coronary heart diseases and stroke results in a rising in the prominence of cancer as a leading cause of death. In underdeveloped countries, improving living conditions has increased life expectancy, primarily due to the decline in deaths related to infectious diseases. Those factors, allied to the advancement of cancer reporting, also lead to increased cancer incidence in developing areas. Further, cancer rates tend to shift from infection-related and poverty-related cancers (cervix, stomach, and liver) to cancers common in developed countries (lung, breast, colorectum, and prostate). Those changes are related to the economic transition that occurs with mechanization, leading to changes in eating patterns and cultural shifts in women's roles in society⁸². Even when isolating higher life expectancy, better cancer rate reports, and regional patterns, lifestyle and environmental degradation are still important factors responsible for the escalation in cancer rates worldwide⁸².

Accordingly, cancer is predicted to be the primary cause of mortality and thus the single most critical barrier to improving life expectancy in every country on the planet, according to the World Health Organization (WHO) in the twenty-first century⁸³. Although extensive research has improved cancer detection and treatment over the years, there is still a need to enhance current therapies and develop novel therapeutic strategies.

1.3.2 What's cancer? The hallmarks

Cancer emerges from normal cells that progressively acquire capabilities that give them tumorigenic and eventually malignant phenotypes. Cancer is a genomic disease in which point mutations gradually accumulate, inducing structural and functional changes to cells⁸⁴. Although a wide variety of cancer types has been classified, which is

ultimately the result of the diversity of this cohort of diseases, hallmarks have been proposed to explain the shared traits between distinct tumor tissues⁸⁵.

The hallmarks of cancer are a set of cellular phenotypes progressively acquired during a cell progression from healthy to neoplastic, which are essential to generate malignant tumors. Enabling characteristics are traits that allow tumorigenic cells to obtain the hallmark capabilities. **Figure 13** shows the most recent list of hallmarks (and two enabling characteristics). As the cellular and molecular mechanisms involved in tumorigenesis are unraveled, the proposed list of hallmarks changes over time.

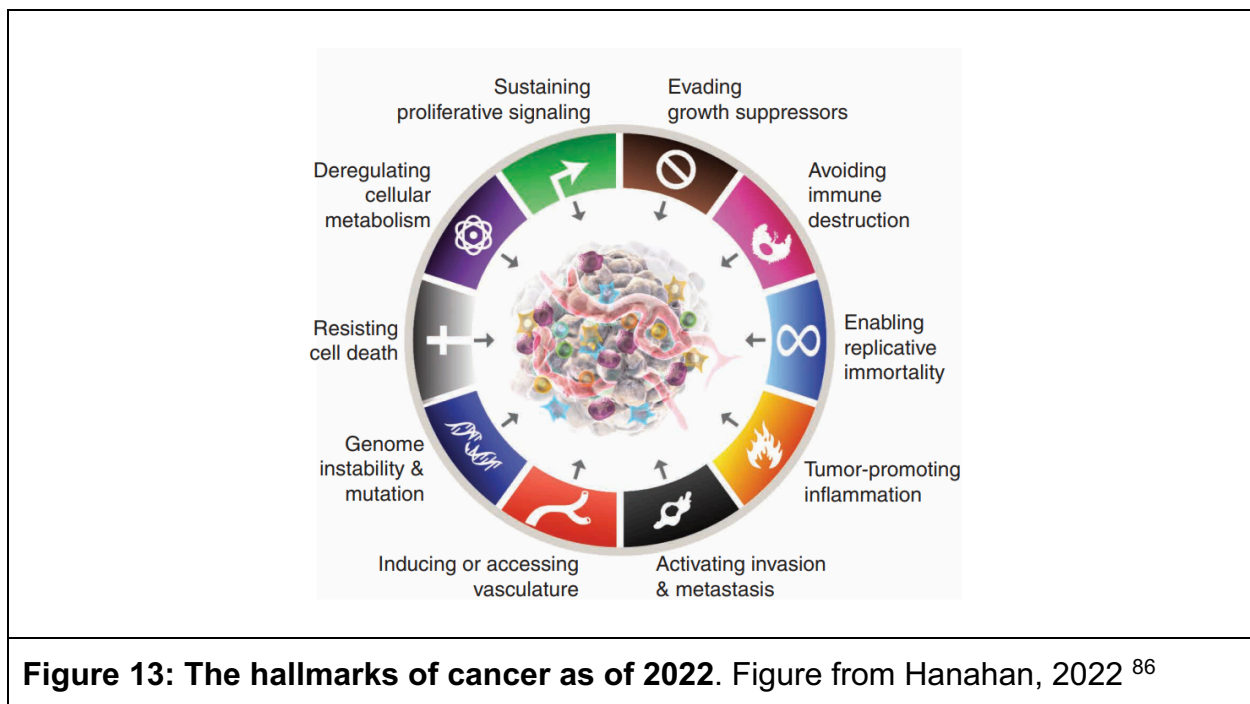


Figure 13: The hallmarks of cancer as of 2022. Figure from Hanahan, 2022 ⁸⁶

The hallmarks establish a framework of rationalization for the complexity of these group of diseases and help direct the development of strategies to treat cancer by targeting each trait. Therefore, in this work, it will be presented the hallmarks of cancer.

Sustaining proliferative signaling: Normal tissues perform specific management of the levels of production and liberation of growth-promoting signals. Those signals guide cells to growth (increasing cell size) and divide (mitosis). The control of the number of cells in a tissue guarantees the maintenance of ordinary structure and function.

It is also essential for homeostasis – a state of active preservation of reasonably stable conditions necessary for survival. The most common molecules that induce proliferative signals are growth factors. In normal cells, they are believed to be released in a spatially and timely specific manner⁸⁵. Cancer cells deregulate those signals by different means: 1) production of growth factor ligands (autocrine stimulation); 2) stimulating the stromal cells to produce growth factors; 3) increase the number of receptor proteins on the surface of the cell, which leads to hyperresponsive to average amounts of growth factors; 4) structural alteration in the receptors allowing ligand-independent firing; 5) constitutive activation of molecules downstream the of the pathways, which leads to growth factor response independent of growth factor ligand firing^{87,88}.

Evading growth suppressors: Until now, dozens of genes responsible for limiting proliferation in normal cells have been discovered. The most canonical are the ones that encode RB (retinoblastoma-associated) and TP53 proteins, which are part of an extensive and redundant control network that suppresses proliferation. The RB protein is responsible for integrating signals from both the extra and the intracellular milieu and determining whether to enter or not into the cell division cycle, as a sentinel of the cell cycle⁸⁹. TP53 is responsible for interpreting the intracellular stress signals, especially the degree of genome damage, ultimately triggering apoptosis⁹⁰. In cancer cells, malfunction of the RB pathway leads to persistent cell proliferation. TP53 malfunction leads to replication of cells that have genome damage⁹¹.

Another way that cancer cells overcome proliferation suppressive signals is through disregarding “contact inhibition.” Even when cultured in 2D (tissue flasks), healthy cells only grow to confluent monolayers. That exact inhibition mechanism was proved to happen in the 3D geometry *in vivo*. Two mechanisms have been identified for contact inhibition: the Merlin protein and LKB1 epithelial polarity protein.

The Merlin protein is a product of the well-recognized tumor suppressor gene NF2. Merlin couples surface adhesion molecules to transmembrane receptor tyrosine kinases receptors—cell surface receptors that are responsible for transducing extracellular signals into the cells and are critical regulators of normal cellular processes. (eg. E-cadherin to the endothelial growth factor receptor, EGFR). Thus, Merlin is

responsible for coordinating contact inhibition by strengthening this attachment that increases cell-to-cell adhesivity and by sequestering growth factor receptors from the surface of the cells⁹². LKB1 organizes epithelial structure and helps maintain tissue integrity⁹³. The suppression of LKB1 turns epithelial cells susceptible to oncogenes, characterizing it as a tumor suppressor gene, and its loss is found in human cancers⁹⁴. Therefore, the loss of those genes is correlated to the inability of cells to control the construction and maintenance of complex tissues.

Resisting cell death: Apoptosis is complex machinery that, once triggered, gradually disassembles the cells and signals neighboring ones for consumption. During this process, the plasma membrane is preserved, so intracellular contents are not spilled into the extracellular environment, avoiding the development of inflammatory reactions. Hence, apoptosis is responsible for maintaining a controlled number of cells in the tissue, keeping the balance between cell reproduction and cell death⁴³. Moreover, the apoptotic machinery is triggered as a response to stresses that might happen during the tumorigenic process, preventing the onset of cancers. This mechanism is considered one of the main barriers to cancer development⁹⁵⁻⁹⁷.

Nonetheless, tumor cells have developed many strategies to evade apoptosis. The most canonic way is due to the loss of TP53 tumor suppression function (as mentioned before, that is one of the major components in sensing genome damage and the consequent triggering of apoptosis)⁹⁸. Other ways of circumventing this machinery include increasing the expression of antiapoptotic regulators or survival signals and downregulating proapoptotic factors⁶⁹.

Unlike apoptosis, necrosis is a type of cell death where cells increase in size and explode, releasing the intracellular contents⁹⁹. This release is believed to be proinflammatory, and its effects are advantageous for tumors¹⁰⁰. The proinflammatory signals can recruit inflammatory immune cells with tumor-promoting roles, such as stimulating angiogenesis, cancer cell proliferation, and invasiveness. Therefore, even though necrosis seems suitable for tissue homeostasis because it is a form of cell death that can contribute to the diminishing of hyperproliferation, most tumors tolerate a certain

amount of necrotic cell death as a mechanism to maintain inflammatory tumor-promoting cells in the tumor environment¹⁰¹.

Enabling replicative immortality: Normal cells can only go through a limited number of cell division cycles. Once they reach that threshold, they enter either stage of *senescence*—an irreversible stage of non-proliferative but viable cells, which is considered another barrier to proliferation—or the *crisis phase*, where the cell dies by apoptotic means^{102,103}. In rare cases, cells cultured *in vitro* develop unlimited replication characteristics, called immortalization. For those cells, senescence or crisis does not happen after some cell cycles. This anomaly is associated with telomeres: the multiple tandem hexanucleotide repeats that protect the ends of chromosomes from end-to-end fusions. It is believed that the length of the telomeres predicts how many division cycles a cell can pass through before entering a crisis state, thus considered a cellular clocking device. In that way, it is also believed that the telomere is a defense against the development of neoplasia^{104,105}.

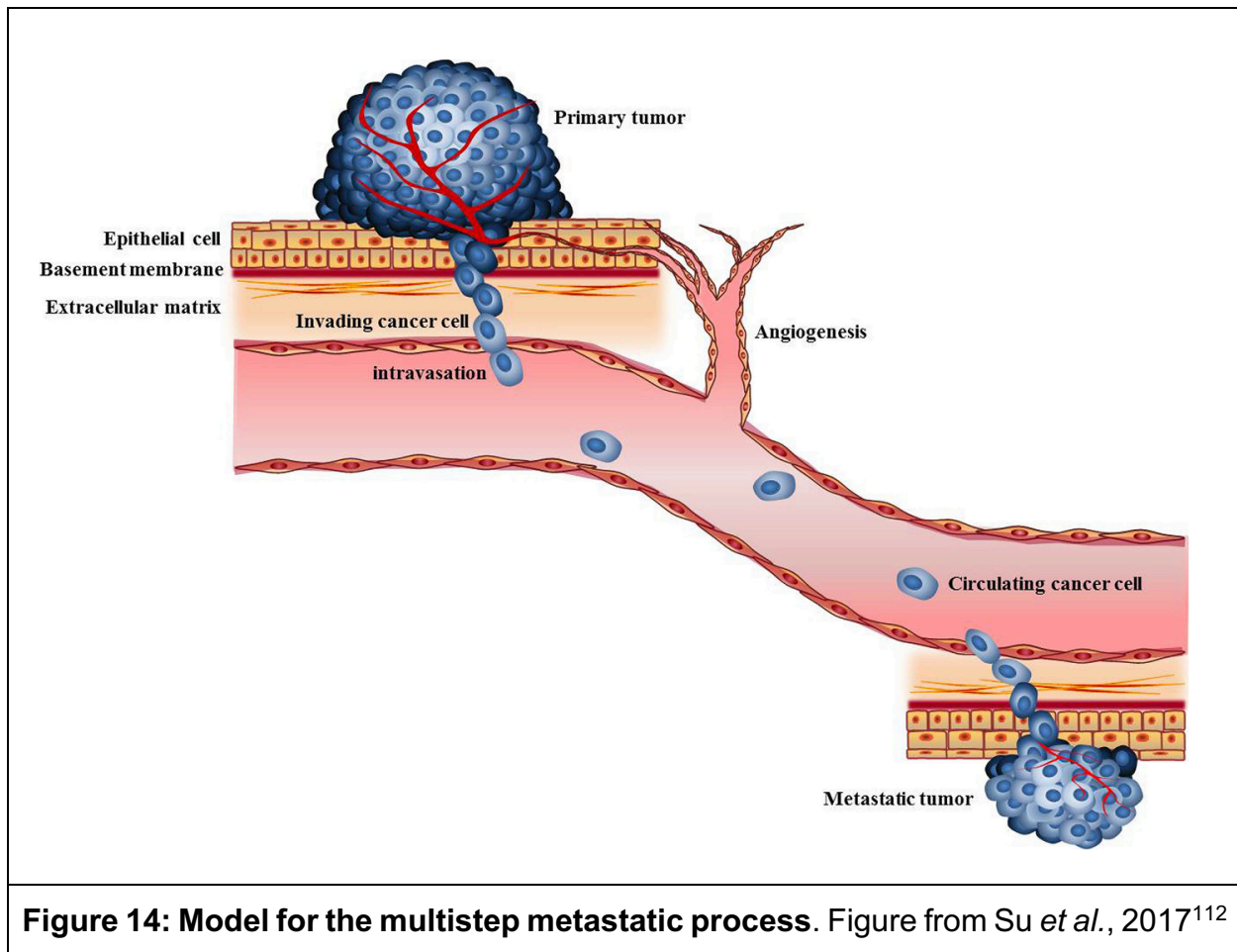
Nonetheless, it is seen that telomerase, an enzyme specialized in elongating the telomere, is highly expressed in most cancers, counteracting the natural telomere erosion. This effect maintains the telomeric DNA at a length that avoids entering into senescence and apoptosis, causing immortalization¹⁰⁶. Because telomeres protect the genome from chromosomal breakage and fusion, it is believed that early stages of neoplasia benefit from the telomere erosion and absence of telomerase activity, speeding genomic alterations that lead to gaining of oncogenes and loss of tumor suppressor genes¹⁰⁷. Therefore, the delay in acquiring telomerase activity generates tumor-promoting mutations, especially in the absence of TP53 surveillance of genomic integrity. Eventually, telomerase activation stabilizes the mutant genome and conferred unlimited replication capacity^{108,109}.

Inducing angiogenesis: Angiogenesis is the formation of the vasculature, which includes the sprouting of new vessels and their assembly. It occurs only during embryogenesis in fetuses, during wound healing, and in the female reproductive cycle in adults. Contrastingly, tumor progression is customarily accompanied by an “angiogenic switch,” where normal vasculature is incentivized to sprout new vessels to maintain

nutrient supply and evacuation of metabolic wastes of growing tumors. Due to rapid sprouting, tumor vasculature is convoluted, leaky, excessively branched, and presents enlarged and distorted vessels with excessive endothelial cell proliferation and apoptosis¹¹⁰. As previously mentioned, this leaky vasculature is also accompanied by the externalization of phosphatidylserine (PS) on the tumor vasculature, which is used in this work as a targeting biomarker for cancer therapies.

Activating invasion and metastasis: Normal solid tissue cells are trapped within the tissue structure due to the expression of E-cadherin, a cell-to-cell adhesion molecule. This molecule assembles the extracellular matrix, forming an adherent junction between neighboring epithelial cells. Hence, the expression of E-cadherin is believed to suppress invasiveness and metastatic phenotypes in carcinomas. Alternatively, carcinomas frequently undergo diminished expression or inactivation of E-cadherin caused by mutations. Further, the expression of adhesion molecules involved in cell migration is usually increased in tumor cells. For example, N-cadherin, which is characteristically expressed in migrating mesenchymal cells and neurons during the formation of organs in fetuses, is usually upregulated in carcinomas¹¹¹.

In tumor cells, the acquired capability of migration is one of the first steps in the process of metastasis. One can schematize this process as discrete steps, as follows: 1) local invasion; 2) intravasation: tumor cells move from the primary tumor into the blood and lymphatic vessels in the surroundings; 3) transit: tumor cells move through the blood and lymphatic vessels to other parts of the system; 4) extravasation: tumor cells escape from the lumina of those vessels into the parenchyma of tissues; 5) micrometastasis: formation of small tumors in the new location; 6) colonization: growth of the micrometastasis into macroscopic tumors¹¹². **Figure 14** summarizes those steps.



Metastasis is estimated to cause the death of 90% of cancer patients¹¹³. This work will present the strategy of combining photothermal therapy with checkpoint inhibition to treat metastatic cancers.

Reprogramming cell metabolism: Under aerobic conditions, healthy cells process glucose through glycolysis and oxidative phosphorylation. The latter result in a complete breakdown of glucose into CO₂, resulting in higher ATP production. In anaerobic conditions, the absence of O₂ necessary for oxidative phosphorylation limits the glucose metabolism to glycolysis, yielding much lower ATP production. Despite the decreased ATP output, cancer cells usually switch their metabolism to “aerobic glycolysis”¹¹⁴. One of the reasons for this phenomenon is that the metabolites from glycolysis can be used in the biosynthesis of other macromolecules crucial for cell proliferation¹¹⁵. The proteins involved in the other hallmarks of cancer are responsible for this switch in the tumor cell

metabolism. Therefore, the widespread of this phenotype in cancer cells is considered a hallmark of cancer⁸⁵.

Avoiding immune destruction: Immune surveillance is a theory that explains healthy tissue's prevention of cancer emergence. In that theory, immune system cells constantly monitor tissue-building cells for signs of tumorigenesis. Therefore, for the development of solid tumors, cells with tumorigenic tendencies had to undergo adaptations to evade immunological killing. The evidence of increased cancer incidence in immunocompromised populations supports this theory¹¹⁶. Additionally, the use of carcinogens in genetically engineered immune-compromised mice has shown higher incidence and more rapid tumor growth than in mice that are immunocompetent¹¹⁷. Both innate and adaptive immune systems might be critical in tumor prevention and, therefore, tumor eradication. In this work, one of the strategies for cancer treatment is the modulation of the immune system for developing anti-tumoral activity, thus counterbalancing cancer immune evasion.

Knowing all those attributes shared by cancer of all types is essential for developing strategies to counteract the tumor-enabling characteristics. Although those aspects are common to most tumor types, cancer is still a variety of diseases. Therefore, a cancer treatment study needs to focus on a specific type of tumor, which correlates to the choice of a reliable tumor model.

The focus of this work is to study breast cancer treatment, even though some of the strategies might be translatable to other types of tumors. The following section will introduce the characteristics of breast cancer and, more importantly, a very deadly subtype of breast cancer: triple-negative breast cancer.

1.3.3 Breast cancer

Breast cancer (BC) is the most common cancer in women worldwide (see **Figure 15**) and the most frequently diagnosed cancer in 154 of 185 countries in the world⁸³. BC is also the most prevailing cancer-related death in women, being the leading cause of death in 100 of all countries⁸³. Despite the decrease in mortality in high-income countries, BC incidence has increased worldwide¹¹⁸. One in every 20 women is affected by BC globally, while this statistic rises to one in every 8 women by age 85 who live in developed countries ¹¹⁹.

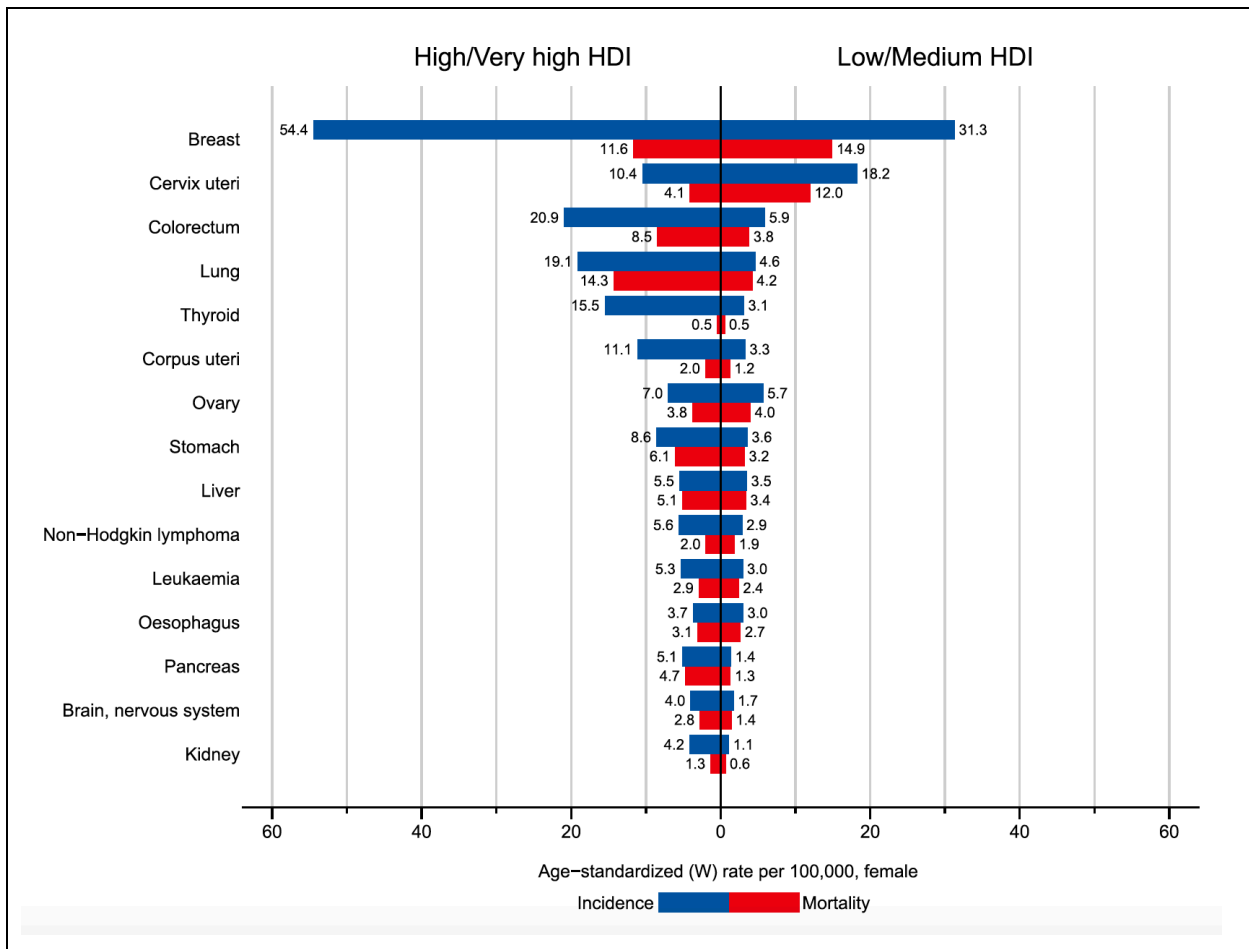


Figure 15: Incidence and mortality age-standardized rates in high/very-high human development index (HDI) regions versus low/medium HDI regions among women in 2018. The 15 most common cancers in 2018 are shown in descending order

of the overall age-standardized rate for both sexes combined. Source: GLOBOCAN 2018. Figure from Bray *et al.*, 2018⁸³

Even though genetic components are responsible for 5-10%, non-hereditary elements are the most relevant causes of BC cases. The risk factors include, but not limited to: long menstrual history, aggravated by historical decrease of menorrheal from 17 to 12 years since 1950¹²⁰, and increase in menopausal age from 49 in the beginning of the last century to 51 years¹²¹; reproduction patterns: childbearing grants long-term protection against BC, granted that the earliest the first pregnancy happens, the longer the protection last, while the having the first pregnancy after 35 years of age increase the risk of BC compared to nulliparity (no pregnancy); absence of breastfeeding: the longer one breastfeeds, the steeper is the decrease of BC risk; use of exogenous estrogen as oral contraceptive or hormone replacement therapy induce the formation of BC; weight gain after age 18 years, excess body weight at menopausal ages increase chances of BC; physical inactivity: moderate to vigorous physical activities decrease BC risk by 20%; alcohol consumption: while a consumption of 3-6 glasses of wine per week increase the chances of BC by 15%, the daily consumption of alcohol (two glasses of wine) increases the chances by 50%. Alcohol consumption is the most significant modifiable BC burden in pre-menopausal woman⁸¹. Unfortunately, endogenous hormonal exposure, the primary risk factor for breast cancer, is difficult to be changed. It is worth mentioning the BC susceptibility genes, BRCA1 and BRCA2, that cause BC in 70% of women carrying them by age 80.

Mortality of BC has reduced significantly due to the development of novel chemotherapeutic drugs and adjuvant therapy¹²². Still, there is a lack of targeted therapies, especially for a subtype named triple-negative breast cancer, as will be discussed in the next section.

1.3.4 Breast cancer classifications and available therapies

Even though distinguishing the primary cancer location is a way to classify cancers (as shown in **Figure 15**), each cancer type is still a large group of diseases. Accordingly, breast cancer (BC) is a heterogeneous disease that develops in breast tissue, presenting different biological characteristics and, consequently, distinctive outcomes and responses to treatment. Clinicians have created classifications for breast cancer, attempting to predict tumor behavior and guide the selection of treatment strategies.

To exemplify the variety of breast cancer subtypes, one can classify BC histologically. Broadly, histology analysis generates two main subtypes based on the invasiveness of the tumor: *in situ* carcinoma or invasive (infiltrating) carcinoma. Those subtypes can be further separated into subgroups, as shown in **Figure 16**¹²³.

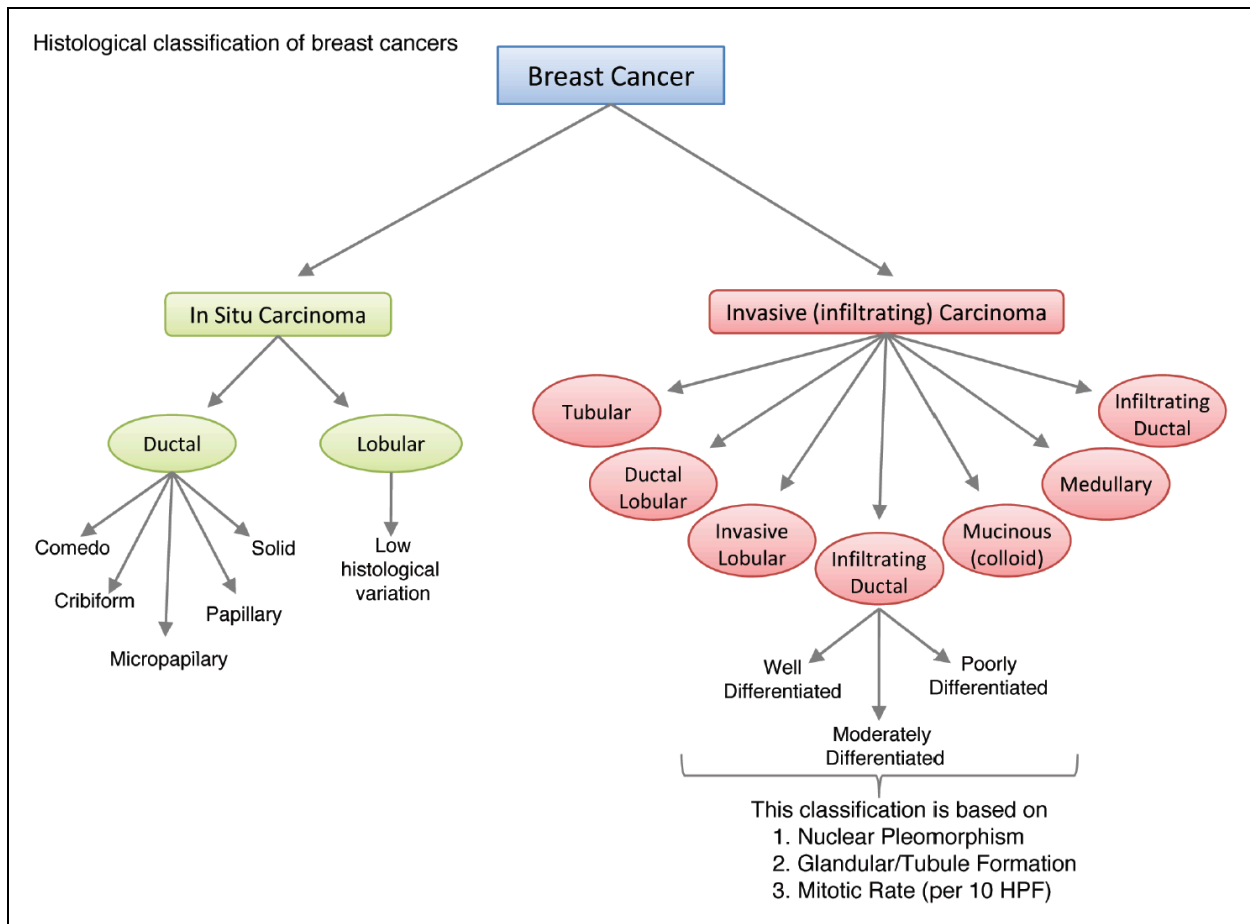


Figure 16: Histological classification of breast cancer subtypes shows the heterogeneity in breast cancer due to growth patterns and architectural features.

HPF: high power field. Figure from Malhotra, *et al.* 2010 ¹²³.

Currently, the treatment strategies for BC involve surgery, radiation therapy, targeted therapy, and chemotherapy¹²⁴. The rationalization of the treatment course needs to be individualized due to the heterogeneity of the disease between patients. Surgery strategies have shifted from radical mastectomy to breast-conserving surgery allied to breast radiation¹²⁵. Additionally, correlations between pre-operative chemotherapy and an increase in locoregional management, disease-free survival, and overall survival have also established that treatment option as a typical treatment course¹²⁶.

Even though chemotherapeutic agents have debilitating side effects related to their use, their use is still crucial for preventing recurrence in many BC patients. The

commonly used chemotherapeutic agents are: docetaxel, which inhibits microtubule formation, thus disrupting mitosis; cyclophosphamide, an alkylating agent that disrupts DNA replication; paclitaxel, which also inhibits microtubule formation; adriamycin, a disruptor of DNA replication; docetaxel, a microtubule formation inhibitor; carboplatin, which disrupts DNA replication by crosslinking to DNA¹²⁴. The most common side effects include, but are not limited to, asthenia, edema, myalgias, myelosuppression, and sensory neuropathy. The less common side effects can involve uterine cancer, thromboembolic disease, osteoporosis, febrile neutropenia, and congestive heart failure¹²⁴.

From listing toxicities associated with chemotherapeutic agents, it is intuitive to conclude that there is a need to develop novel therapies that are more effective at treating BC patients and have significantly reduced side effects. The most effective recognized strategy to achieve that goal is targeted therapies.

One of the most routine analyses for breast cancer classification is immunophenotyping: the assessment of tumor molecular markers. This classification is based on molecular and histological evidence and assesses whether the primary tumor expresses surface receptors, which characterize the tumor's responsivity to currently available targeted treatments. Biopsied tissue is prepared and stained for the presence of estrogen receptor (ER), progesterone receptor (PR), and human epithelial growth factor receptor 2 (HER2, most recently named ErbB2) expression¹²⁷. After immunohistochemical techniques are applied to biopsied tissue, they are classified as luminal A (ER/PR+, and HER2-), luminal B (ER/PR+, and HER2+), HER2 enriched (PR/ER-, but HER2+), and Basal Like, also known as triple negative breast cancer¹²⁸. Although many other classifications of BC were developed, receptor status is considered the most effective in the prediction of response and prognosis of available treatment options^{129–131}.

Targeting estrogen and progesterone receptors by endocrine therapy has transformed breast cancer's global impact. Those strategies decrease breast cancer recurrence and overall survival when applied to women diagnosed with early stages BC and are positive for ER. This receptor is responsible for activating oncogenic growth pathways in cancer cells, enabling proliferative characteristics. The progesterone

receptor is considered a marker for ER signaling, making PR+ tumor cells responsive to ER-targeted treatments¹³². Biopsied cancerous tissue that expresses at least 1% of either ER or PR positive staining is considered hormonal positive (HR+). The percentage of cases diagnosed with HR+ is around 70%, including ErbB2+ or ErbB2-¹³³.

Tamoxifen is the most prevalent drug used for the treatment of ER-positive BC, and it was the first targeted treatment for BC ever discovered¹³⁴. Because of its targeting capabilities, it has improved therapy outcomes, saving many lives for the last 40 years while lacking the debilitating side effects that were commonly associated with BC treatment in most patients. Tamoxifen acts as a selective estrogen receptor modulator, antagonizing the ER in breast tissue and thus inhibiting those ER proliferative capabilities in the tumor cells. The historical importance of tamoxifen is also related to the establishment of the effectiveness of targeted treatments in cancer research¹³⁵. Tamoxifen has reduced the recurrence of ER+ BC by 50% and the morbidity rates by 28%.¹³⁴

Another type of adjuvant endocrine therapy that targets ER+BC is aromatase inhibitors. Those drugs deplete estrogen in breast tissue in post-menopausal women by inhibiting aromatase, an enzyme that converts precursors of estrogen into this hormone that fires the ER, consequently also inhibiting its proliferative activities. Third-generation aromatase inhibitors currently available are letrozole, anastrozole, and exemestane.¹³⁶

Patients diagnosed with non-metastatic HR+BC are usually subjected to 5 years of tamoxifen to reduce chances of recurrence or can choose the switch strategy, consisting of the use of initial 2-3 years of tamoxifen and followed by the use of aromatase inhibitor until completion of 5 years¹³⁷. Because estrogen fires the ER and subsequently generates proliferative signals, pre-menopausal women are usually subjected to menopause-inducing therapies¹³⁸. The addition of chemotherapeutics agents to endocrine therapies occurs depending on late staging or higher grades of cancer¹³⁹. Even though endocrine therapies have saved many lives, resistance to treatment, especially when therapy takes longer than 5 years, is a clinical challenge¹⁴⁰.

Another critical receptor for which targeted therapies were developed is the epidermal growth factor 2 (ErbB2, formerly known as HER2). A patient is considered ErbB2 positive when the cancerous cells stain strongly ErbB2 protein or when the ErbB2 gene is overexpressed¹⁴¹. This receptor is positive in approximately 20% of breast cancer cases. About 50% of those are also HR+¹⁴². Before targeted therapies were developed, the overexpression of this receptor was correlated with a more aggressive and poorer prognosis¹⁴³. ErbB2 is a growth factor receptor that induces potent proliferative and anti-apoptosis signals, thus enabling oncogenic phenotype¹⁴⁴.

The most common treatment options for ErbB2+ BC are anti-ErbB2 antibodies and small-molecule tyrosine kinase inhibitors. For instance, trastuzumab and pertuzumab are recombinant humanized monoclonal antibodies that bind to the extracellular domain of the ErbB2 receptor and inhibit homodimerization, resulting in the prevention of receptor firing¹⁴⁵.

The standard of care for non-metastatic ErbB2+ patients is trastuzumab in combination with paclitaxel¹⁴⁶. Pertuzumab is incorporated into the regimen when the patient is at higher risk, which is correlated to tumor size and affected lymph nodes¹⁴⁷. When ErbB2+ cancer is metastatic, a combination of taxane, trastuzumab, and pertuzumab is used as the first line of therapy, and the antibody-drug conjugate tDM1 is added later (trastuzumab linked to mertansine, a drug studied in this work for the conjugation with ANXA5 and gold nanoparticles)¹⁴⁸.

Another way to classify BC is staging, which measures the disease's spread level by the time of diagnosis. Stage I is characterized as a small primary tumor (less than 2 cm in size) without lymph node involvement. Stage II comprises primary tumors between 2-5 cm, with only local lymph nodes affected. Stage III are primary tumors that are bigger than 5 cm, and cancer has usually affected muscles and skin while also affecting lymph nodes in the area, but it has not spread to other parts of the body¹⁴⁹. Stage IV is when cancer has spread to any body part, also known as metastatic breast cancer. Due to the widespread mammography, 62% of BC diagnosed in the United States have not yet spread from the primary tumor (Stage I). Thirty-one percent of the diagnosed cancer involved the lymph nodes. Merely 6% of patients are diagnosed with Stage IV

breast cancer¹²⁴. It has been proven that the diagnosis of nonpalpable tumors (smaller than 1.5 cm) by mammography leads to a better prognosis¹⁵⁰.

Even though the percentage of women diagnosed with Stage IV BC is small, metastatic breast cancer is a substantial challenge because it is incurable for practically all the patients diagnosed at this stage. The purpose of the treatment is symptom palliation and to prolong life. The course of treatment is systemic therapies, either pre-operative or post-operative chemotherapy, and local therapies, such as surgery and radiation, are used for palliation¹²⁴.

When the cancer cells lack the expression of either hormonal receptor or ErbB2 receptor, the cancer is classified as triple-negative breast cancer (TNBC)¹²⁹. Due to the absence of targeted treatments available for this subtype of cancer, the outcomes for patients are poorer compared to the other subtypes: the 5-year specific survival for HR+ErbB2- and HR-ErbB2+ are respectively greater than 99 and 95% for stage I, while for TNBC is 85%; for metastatic BC, median survival ranges from 4 to 5 years for receptor-positive cancer, while it drastically decreases to 10-13 months for TNBC¹⁵¹. In this work, we study a strategy for targeting and treating triple-negative breast cancer; thus, more attention will be given to it.

1.3.5 Triple negative breast cancer

The absence of targeting receptors expression characterizes triple-negative breast cancer (TNBC). It affects approximately 10 - 20% of the women diagnosed with breast cancer^{152,153}. Early-stage TNBC presents about 37% death in the first 5 years after surgery, and metastatic TNBC has short progression-free survival has a median of 3 to 4 months^{154–157}. Poor prognosis is strongly associated with the lack of targeted therapies. The limited options also increase the incidence of cancer recurrence in TNBC patients¹⁵¹.

More specifically, the lack of molecular targets makes the endocrine and HER2 targeted therapies inefficacious against TNBC; thus, chemotherapy is the standard approach for its treatment. Using neoadjuvant (pre-operative) therapies generates a

higher remission rate than ErbB2+ BC and significantly improves the prognosis. The recommended treatment regimen is taxanes, anthracycline, cyclophosphamide, cisplatin, and fluorouracil. Many combinations are possible, and optimization of regimens is necessary for improved outcomes^{124,151}. Taxanes and anthracyclines are very important for the treatment of TNBC. The addition of platinum agents increases complete pathological response (pCR) but causes higher rates of hematological side effects and treatment discontinuation¹⁵⁸. Patients with germline BRCA1/2 mutation (accounting for 10% of TNBC) are usually more sensitive to platinum-based agents¹⁵⁹. Ironically, TNBC has a higher response to chemotherapy than the other BC types, but it has not resulted in a better prognosis¹⁶⁰.

Clinical trials have been designed to improve TNBC patients' outcomes using combination chemotherapy. The improved response rates correlated to increased toxicity and did not increase patient survival. Sequential single-agent chemotherapy is recommended for metastatic TNBC (mTNBC) due to the increased toxicity of combined chemotherapy¹⁶¹. Conversely, in this work, it will be shown that a combination of different treatment strategies induced better outcomes in mTNBC murine tumor model without signs of increased toxicity.

Even though TNBC is commonly contemplated as a single disease, molecular profiling of patient samples shows that this cancer subtype is highly heterogeneous. TNBC is usually treated uniformly across different sets of patients. One of the attempts to subdivide TNBC and encourage the development of more precise therapies was made by Lehmann *et al.*¹⁶², based on gene expression profiling subtyping. It identified six subtypes based on the analysis of 587 TNBC patients: basal-like 1, basal-like 2, mesenchymal (M), mesenchymal stem-like (MSL), immunomodulatory (IM), and luminal androgen receptor (LAR). This subdivision helps guide the clinical treatment of TNBC by correlating targeted therapies to responsiveness.

According to this subclassification, the high expression of some genes guided a more personalized approach in the adoption of targeted treatment: BL1 subtype is correlated to DNA repair and cell-cycle-related genes. BRCA 2 mutation is part of this subset. Possible treatment options are poly (ADP-ribose) polymerase (PARP) inhibitors. Both BL1 and BL2 may be targeted by mTOR inhibitors and growth factor inhibitors, such

as lapatinib, gefitinib, and cetuximab. BL1 patients are usually very responsive to cisplatin treatment as well. M subtype is related to high activation of cell-migration-related signaling pathways and differentiation pathways. They are prone to chemotherapy resistance and are treated with mTOR inhibitors and drugs targeting epithelial-mesenchymal transition. MSL subtype is correlated to high levels of stemness-related genes, HOX genes, and mesenchymal stem cell-specific markers. PI3K inhibitors, Src antagonists, and antiangiogenic drugs are potential treatment options for both M and MSL subtypes. IM subtype highly expresses immune-cell-associated genes. Immune checkpoint inhibitors are recommended for this subtype. Although the LAR subtype does not express ER/PR receptors (as for being TNBC), it has hormonal-related signaling pathways highly expressed. Anti-androgen receptor drugs are recommended for this subtype¹⁵¹.

The gene-expression subtyping was identified as an independent predictor of pCR status in patients who underwent standard chemotherapy regimens¹⁶³. Nonetheless, the clinical relevance of this subtyping is still in debate since additional studies are required to validate if this subclassification can predict the risk of relapse and chemotherapy responsiveness¹⁶⁰.

The last few years have been fruitful in developing novel targeted strategies for cancer treatment. Various pathways have been associated with TNBC oncogenicity and thus are potential or approved targets to treat TNBC, as shown in **Figure 17**.

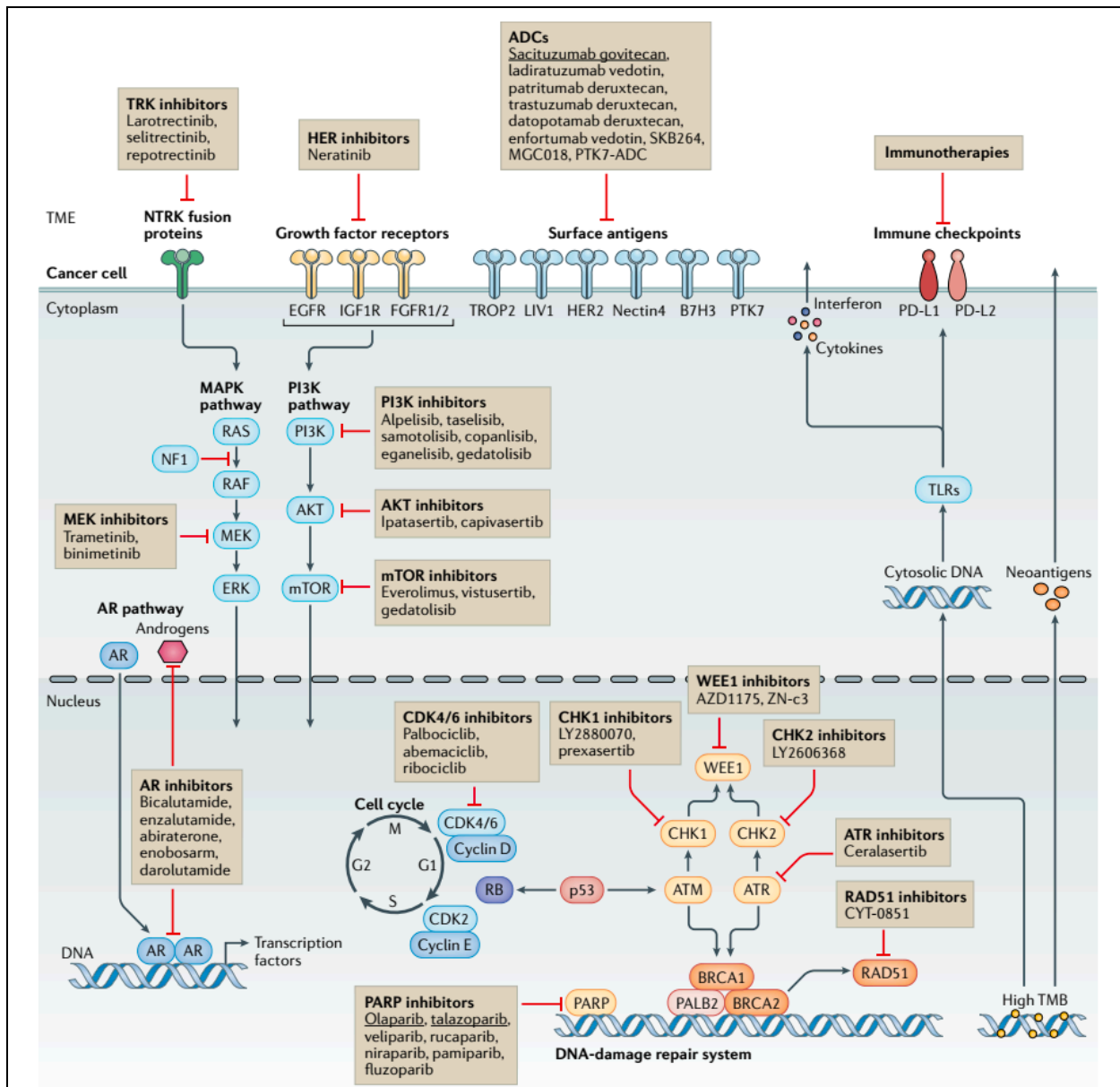


Figure 17: Targetable pathways of oncogenic signaling pathways in TNBC. Boxes present the drugs that target those pathways, and the underline ones are approved. ADCs: antibody-drug conjugates; AR: androgen receptor; PARP: poly(ADP-ribose) polymerase; TLR: Toll-like receptor; TMB: tumor mutational burden; TME: tumor microenvironment; TROP2: trophoblast cell-surface antigen 2. Figure from Bianchini, *et al.* 2022.¹⁶⁴

Poly-(ADP-ribose) polymerase is a family of enzymes that aid DNA single-strand break recognition and DNA repair, which correlates to genomic stability. Some TNBC, including BRCA1 and 2, rely on PARP to survive. Therefore, the inhibition of this enzyme promotes cell death¹⁶⁵. Olaparib and talazoparib are PARP inhibitor (PARPi) antibodies approved for BRCA1 and 2, HER2-metastatic BC^{166,167}. There is evidence that the combination of PARP inhibitors and DNA-damaging chemotherapy produces synergistic effects against cancer but promotes toxicity¹⁶⁸. PARP inhibitors have been proven effective in clinics, encouraging the testing for BRCA in all TNBC patients. Tumors that undergo somatic and epigenetic mutation of those genes might also be sensitive to PARPi¹⁶⁹.

Antibody-drug conjugates (ADCs) are recombinant monoclonal antibodies (Ab), covalently bound to cytotoxic agents, thus selectively delivering drugs to cells expressing the epitopes that the antibody recognizes. Sacituzumab govitecan is an ADC consisting of an Ab that targets TROP2 – trophoblast cell-surface antigen, associated with pro-oncogenic signaling pathways¹⁷⁰ – linked to the drug SN-38, a DNA topoisomerase. It was approved as the third of the later line of treatment for patients with mTNBC¹⁷¹.

Ladiratumumab vedotin consists of an Ab that targets zinc transporter ZIP6, also known as LIV1, to a microtubule-disrupting agent called monomethyl auristatin E. LIV1, which is a transmembrane protein that is limitedly expressed in non-cancerous cells but is highly expressed in solid tumors, including in 70% of TNBC¹⁷². Although it has not yet been approved, it has shown remarkable results in the phase I trial for mTNBC¹⁷³.

As shown in **Figure 17**, many other possible targeted treatments are currently being assessed in clinical trials for their efficacy against TNBC. PI3K-AKT pathways are related to many hallmarks of cancer. Its deregulation occurs in approximately 50% of TNBC, correlated to sensitivity to PI3K inhibition¹⁷⁴. Currently targeting this pathway in clinical trials are alpelisib, ipatasertib, and capivasertib. Nonetheless, the strong pre-clinical rationale related to targeting these pathways has not resulted in encouraging results¹⁶⁴.

The MAPK pathway is another oncogenic cascade possible to target for cancer¹⁷⁵, although it is only seen in approximately 3% of TNBC¹⁷⁶. Compensatory

activation of alternative signaling pathways might hinder the effectiveness of this strategy. Therefore a dual inhibition might increase effectiveness¹⁷⁷. Additionally, clinical trials combining MEK inhibitors and chemotherapeutic agents will happen soon¹⁶⁴.

The LAR molecular subtype is characterized by elevated expression of the androgen receptor (AR). Bicalutamide¹⁷⁸ and enzalutamide¹⁷⁹ are AR inhibitors that have shown relevant anticancer activity. The addition of PI3K inhibition might also be advantageous for LAR TNBC since LAR is also enriched with PIK3CA mutations¹⁸⁰.

Immunotherapy is another strategy to target TNBC. Due to the importance of immune checkpoint inhibition in this work, immunotherapy in TNBC will be discussed later in this text (see section 1.4.2 – Immunotherapy).

Even though tremendous improvements have been achieved in the last few years due to the development of new targeted strategies, a targeting strategy that would be effective for most TNBCs has not been developed. PS targeting is a promising approach since most of the cancer cells, tumor vasculature, and metastatic cancer cells in TNBC express PS on the outer leaflet of the plasma membrane.

Accordingly, the alarming statistics related to triple-negative breast cancer give a tangible perspective on how the lack of targeted therapies forsakes the hope of patients diagnosed with this disease. It also strongly compels the urge for the development of targeted therapies. When triple-negative breast cancer has metastasized, the chances of survival are even smaller. In this work, we studied a TNBC-targeted treatment that not only may be able to treat primary tumors but also generate a systemic immune response against metastatic breast cancer. The use of annexin A5 (ANXA5) as a targeting protein for TNBC is promising, and the use of ablation techniques in combination with immune system modulation molecules is favorable for a systemic anti-cancer response.

1.4 Novel strategies for cancer treatment

1.4.1 Photothermal therapy

The use of heat in cancer treatment, also called thermoablation, has been explored extensively and aims at destroying the tumor without damage to the surrounding tissue^{181–183}. Photothermal therapy (PTT) is an irradiation-based thermoablation, using photons from the near-infrared range (750 – 1350 nm) to illuminate a pertinent area. The PTT-mediated hyperthermia induces tissue damage in temperatures greater than to 41°C¹⁸⁴. Due to limitations of laser penetration and heat transfer, temperatures of 45–55°C are necessary to ablate most of the tumor volume efficiently^{181,185}. Temperatures around 41°C cause the production of heat-shock proteins, which have protective effects that alleviate the damage after thermal stress¹⁸⁶. The rising of tissue temperature above 42°C induces irreversible tissue damage. Cell necrosis happens when tissue is heated up in the range of 42-46° for 10 min. Microvascular thrombosis and ischemia have resulted from temperatures between 46-52°C. Temperatures above 60°C induce protein denaturation and plasma membrane destruction, resulting in instantaneous cell death¹⁸⁷.

The adoption of laser therapy for the treatment of tumors has been reported since the decade of 1960¹⁸⁸, but the first attempts to use this therapy strategy suffered from non-selectivity and the requirement of exceedingly high power densities to promote therapeutic results¹⁸⁹. Subsequently, adding artificial photosensitizers to improve the efficiency of photothermal therapy decreased the energy levels required for ablation and improved the targeting of diseased areas.

Tumor ablation through laser irradiation has constraints that include low cancer selectivity due to natural chromophores in healthy tissue and the need for high power density. The selectivity is only achieved with precise control of the irradiation area, which might be hindered in deep tissue tumors, where imaging techniques are required for irradiation.

Photosensitizers, also called photothermal agents, intake electromagnetic radiation in the range between visible and infrared light and convert it to heat, promoting tissue damage^{190–192}. Many materials have been studied for their use as photothermal

agents. Organic compounds, such as organic dyes, porphyrins, and polymeric materials, have excellent biocompatibility and quick clearance^{193–196}. Nonetheless, those compounds suffer from low efficiency in transforming light into heat and photobleaching before applying the NIR irradiation on the tumor. Inorganic photosensitizers, such as carbon, gold, phosphorus, and copper-based nanoparticles, have also been used as mediators of PTT^{197–200}. Although they encounter poor biocompatibility compared to the organic ones, they have greater NIR absorption and high NIR-heat conversion efficiency. To overcome the biocompatibility issues, various research groups have performed modifications of the surface, size, and composition of those nanomaterials to promote faster clearance. Additionally, the attachment of targeting agents to nanoparticles has increased their intratumoral bioavailability^{201,202}.

The heating mechanism of photothermal therapy mediated by photosensitizers has been elucidated. The NIR-irradiation emits photons that, when absorbed by photosensitizers, excite their electrons from their ground state to an excited state. The electrons then decay non-radiatively by vibrational relaxation. Those vibrations promote collisions with the surrounding molecules, thus increasing the kinetic energy of the microenvironment²⁰³ (see **Figure 18**).

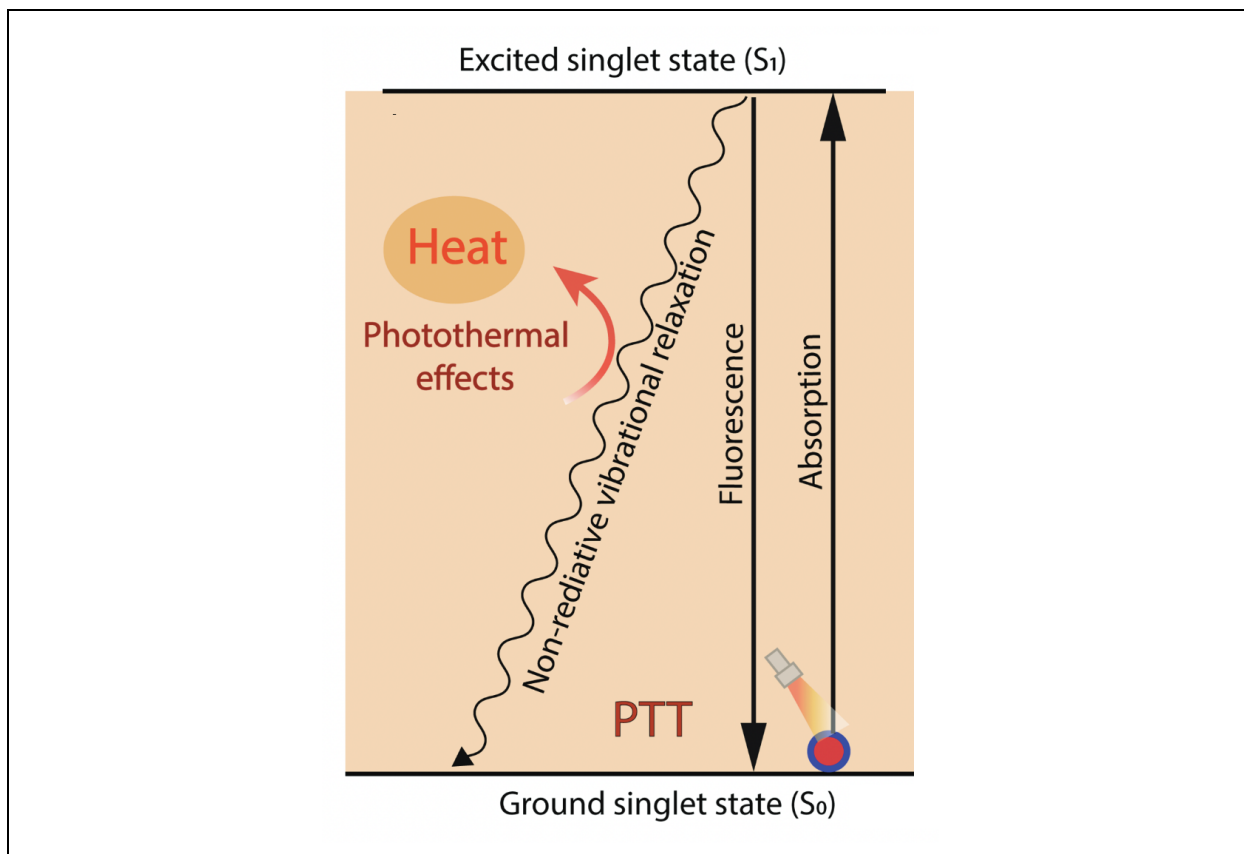


Figure 18: Mechanisms of photothermal effect during PTT. Photosensitizers absorb photon energy from NIR, migrating from the ground singlet state (S₀) to an excited singlet state (S₁). When returning to the ground singlet state, they undergo nonradiative vibrational relaxation, increasing the surrounding microenvironment temperature and causing cell death. Image modified from Zhao *et al.*, 2022²⁰⁴

Photothermal therapy mediated by photosensitizers is a highly targeted treatment option due to the dual selectivity strategies. First, the control of the region of irradiation aiming the laser in the desirable area (tumor) prevents damage to unwanted parts of the body. Second, the localization of photosensitizers in the affected regions provides another level of selectivity. Their linkage to targeting agents (such as annexin A5 in this work) can further increase the accumulation of photosensitizers in tumors. Invasive techniques, such as laparotomies and thoracotomies, can be avoided when treating deep-seated tumors using endoscopy and interventional procedures with optical fibers.

One of the most relevant challenges in tumor treatment is hypoxic regions in the primary tumor because of the lack or minimal blood flow that prevents the delivery of therapeutic agents. Hypoxia is characterized by oxygen levels below physiological requirements correlated to malignant proliferation and dysfunctional vascularization. Hypoxia induces activation of complex cell signaling pathways that lead to metabolism changes related to cell quiescence, ultimately leading to treatment resistance and selection of aggressive cancer cells²⁰⁵. Tumor ablation is a very effective strategy for the treatment of hypoxic and drug-resistant cancers because the heat transfer in tissue, although ameliorated by vascularization, does not require blood flow to reach hypoxic areas of the tumor. Therefore, PTT can be an effective strategy to induce cell death in regions of tumors that were previously unreachable by common therapeutic approaches and prevent recurrence and metastasis related to untreated hypoxic areas of tumors²⁰⁶. This effect is further advanced by photosensitizers because of the more efficient heating patterns seen in the tumor with the addition of those agents during photothermal therapy.

Despite the improved aspects of photosensitizer-mediated PTT, the clinical development of photothermal therapy has been restricted to the approval of laser devices. Thriving pre-clinical research has shown encouraging results with the combination of laser and photosensitizer. Unfortunately, the aspects related to the approval of therapies in humans favor single-agent strategies, thus hindering the advance of photosensitizer-mediated PTT. Indeed, to date, only one pilot clinical trial has been done in the US that involves the laser and photosensitizer approach for the treatment of prostate cancer. In that trial, gold silica nanoshells (AuroShells – 120 nm) were delivered intravenously and localized in the tumor due to leaky tumor vasculature and defective lymphatic drainage, also known as enhanced permeability and retention (EPR) effect²⁰⁷. The laser system was already preapproved by the time of clinical evaluation of the nanoparticle. It consists of an 810 nm laser (+/- 10 nm) coupled with a cooled laser applicator system (Visualase, Inc, Houston, Texas). The optical fiber is localized inside a cooled catheter (16G Cooled Catheter System - CCS) that is cooled by circulating room temperature saline in the lumen of the catheter, and a peristaltic pump promotes the saline circulation. The peristaltic pump was also previously approved by the FDA²⁰⁸. Ninety-four percent of patients had

their tumors successfully removed, with no severe side effects or significant changes to their symptoms or sexual health scores²⁰⁷.

Other two clinical trials assessed the effect of this nano-shells mediated photothermal therapy on metastatic lung cancer and head and neck cancer (NCT01679470, NCT00848042). Still, the results were not conclusive in terms of the anticancer activity²⁰⁹.

Other laser devices have been approved for the treatment of various cancer types. A Nd:YAG laser was approved for the irradiation of obstructing bronchial cancer via endoscopy²¹⁰. Laser interstitial therapy is approved for prostate cancer²¹¹, hepatocellular carcinomas^{212,213}, liver metastasis of colorectal carcinoma via MRI guidance²¹⁴, and MRI-guided laser interstitial irradiation therapy for brain tumors²¹⁵ and benign mammary tumors²¹⁶.

A clinical trial is in progress to assess the use of an 805-nm laser diode system (Novilase) guided by ultrasound or stereotactic image for the percutaneous laser photothermal therapy of early-stage BC. In this study, the laser fiber inside was coupled with thermal sensors. Photothermal therapy ended immediately when temperature readings reached 60°C or when it reached 51°C for longer than 2 min. A high percentage (84%) of the patients had complete tumor ablation assessed by pathology analysis²¹⁷.

Another clinical trial in Peru was performed with the injection of indocyanine green and the immunoadjuvant glycated chitosan. The superficial breast cancer tumors were irradiated with an 805-nm laser at a power of 1 W/cm² for 10 min. Clinical beneficial response rate from the treatment was 75%²¹⁸.

The addition of a photosensitizer to photothermal therapy can increase the selectivity of the target tissue and lower the power necessary for ablation, which might simplify the devices that usually require cooling systems. One type of material that can be used as a photosensitizer is carbon nanotubes. In cancer therapeutics, their ability to strongly absorb near-infrared light in the range at which water and hemoglobin have minimum absorption makes them suitable for the application in photothermal therapy^{219–221} (see **Figure 19**). Moreover, CNT has high photon-to-heat energy conversion efficiency and high cross-sectional energy absorption²²².

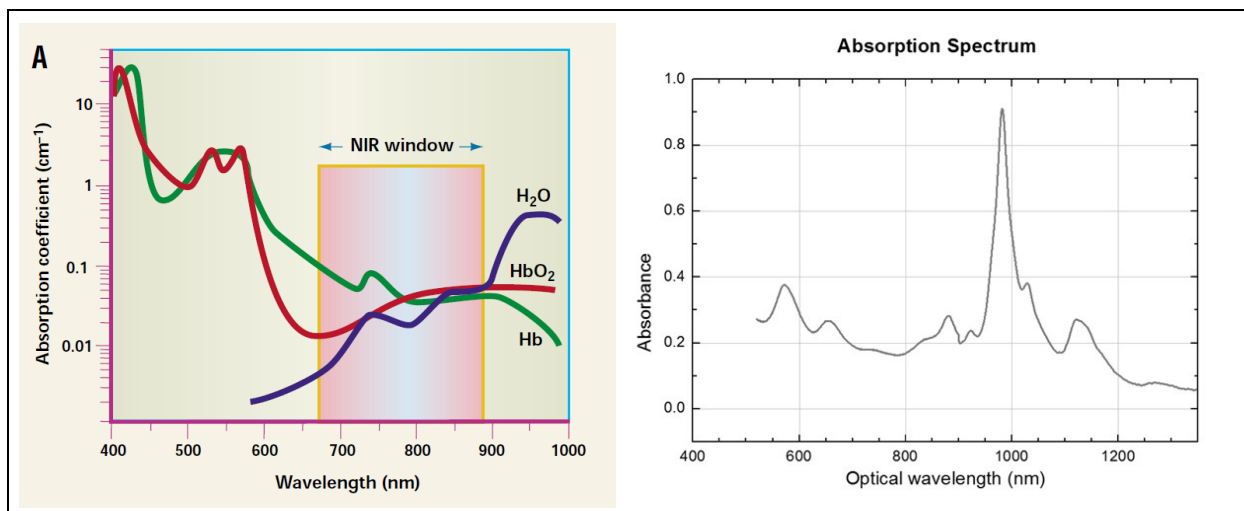


Figure 19: Comparison of water and hemoglobin absorbance to carbon nanotubes: A) water and oxy and deoxyhemoglobin have similar absorbance in NIR range²²⁰. B) absorption spectrum of (6,5) SWCNT in the near-infrared range.

The stress during photothermal therapy promotes an immune response, which is associated with a cellular mechanism known as immunogenic cell death (ICD). As mentioned in section 1.1.2 (Scramblase activation and phosphatidylserine exposure), apoptosis is deliberately immunogenic silent to prevent inflammatory response in tissue turnover and homeostasis. This type of cell death is classified as programmed cell death (PCD), where the molecular machinery is encoded and governed genetically^{223,224}. Nonetheless, when stress is applied to cells, PCD might generate inflammatory responses that can lead to the activation of cytotoxic T cells and, subsequently establishment of immunological memory. This process is referred to as ICD²²⁵.

While cancers have as one of the hallmarks the ability to avoid immune destruction (see **Figure 13**: The hallmarks of cancer), ICD can establish an anticancer adaptive immune response that might counterbalance the equilibrium between cancer cells and immune cells towards the induction of antitumoral immunity²²⁶. Indeed, during the oncogenic process, cancer develops mechanisms to avoid ICD to guarantee immune evasion²²⁵.

As part of the definition of ICD, two mechanisms have been distinguished as ways to prove the induction of ICD: antigenicity and adjuvanticity. Antigenicity is the expression and presentation of highly immunogenic antigens that can be recognized by naïve T cells (they are not shielded by central tolerance in the formation of T cells thymic selection that removes self-recognizing T cells)²²⁷. Two types of antigens are related to this mechanism: tumor neoantigens (TNAs), the ones that are not covered by central tolerance, and tumor-associated antigens (TAAs), the ones for which the central tolerance is faulty. Malignant cells' exposed TNAs may have low structural homology to self-epitopes; as a result, they may mimic microbial epitopes in part and effectively trigger *de novo* immune responses. Conversely, TAAs are self-antigens that are not uniquely expressed in cancer tissue but are also found in healthy tissue. Nonetheless, TAAs are relevant in the activation of an antitumoral immune response, especially in the presence of high adjuvanticity²²⁸. Adjuvanticity is the release of danger signals (damage-associated molecular patterns - DAMPs) that are responsible for the recruitment and maturation of antigen-presenting cells (APCs). The application of stressors on cells can induce an intense and kinetically suitable release of DAMPs that promote APCs recruitment and maturation^{229,230}. In short, immunogenic cell death occurs when the cell stress releases both tumor antigens and DAMPs that prompt the activation of T cell-mediated immunogenicity. The mechanism is summarized in **Figure 20**.

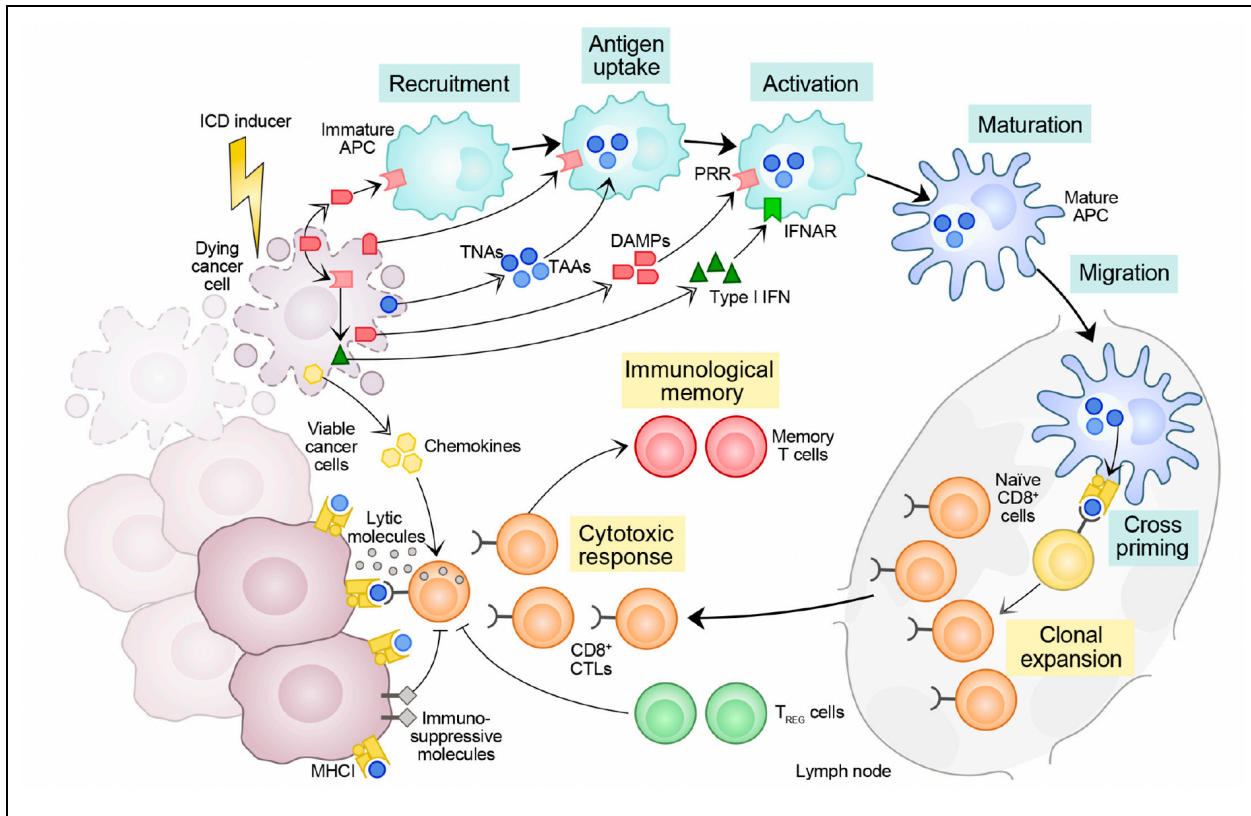


Figure 20: Immunogenicity of cell death. Adaptive immune response against antigens from dead cells can be upregulated cell death caused by stress when two additional factors occur: 1) generated antigens are not recognized as central tolerance. 2) dying cells release DAMPs and cytokines in a favorable spatiotemporal pattern that promotes APCs' recruitment, maturation, and phagocytic activity. After collecting and presenting the anti-tumoral antigens, those APCs migrate to lymph nodes and induce the activation of cytotoxic T cells. Then, cancer cells expressing either tumor neoantigens or tumor-associated antigens are subjected to ICD when cytotoxic T-cells migrate back into the tumor site. The effectiveness of the cytotoxic T lymphocyte (CTL)-dependent immune response depends not only on the initial stress stimulus but also on the absence of a strong immunosuppressive tumor microenvironment that might prevent the initiation or execution of the whole process of immune activation. Image from Galluzzi *et al.*, 2020²²⁸

The most common measurements to demonstrate the stimulation of ICG are the translocation of calreticulin to the surface of the cells and the release of adenosine

triphosphate (ATP) and high-mobility group box-1 protein (HMGB1) to the extracellular environment since both result in the uptake by APCs that ultimately stimulate the antigen-specific antitumoral immune response²³¹. Other immunostimulatory signals are, but are not limited to: cellular nucleic acids; annexin A1; cytokines like IFN, CCL2, CXCL1 CXCL10; heat shock proteins like HSP70 and HSP90; cytosolic components like F-actin; mitochondrial products such as DNA, reactive oxygen species (ROS), cardiolipin, TFAM²²⁸. There is strong evidence that PTT cause immunogenic cell death^{209,232,233}.

Moreover, growing clinical evidence shows that various ICD inducers frequently used to treat cancer patients work in conjunction with immune checkpoint blockade (ICB) therapy, also known as immunotherapy, as long as they do not interfere with immunostimulatory signals or the activity of lymphocytes infiltrating the tumor²³⁰. Therefore, in the subsequent sections, immunotherapy will be presented, and its combination with PTT for the generation of a systemic immune response is one of the main pillars of this work.

1.4.2 Immunotherapy

The immune system is responsible for recognizing and eliminating threats. It is composed of white blood cells and tissue of the lymph system, which includes bone marrow, thymus, spleen, tonsils, lymph nodes, and lymph vessels. As part of this recognition mechanism, the immune system is trained to differentiate between self and non-self. The immune system is theoretically divided into innate immunity and adaptive immunity. Innate immunity is active since birth and is comprised of not only the physical barriers that separate us from the environment, such as skin and mucous membranes, but also an advanced system of cells: natural killer (NK) cells, eosinophils, basophils, and phagocytic cells, including mast cells, neutrophils, monocytes, macrophages, and dendritic cells (DCs). The innate immunity is non-specific but efficient at eliminating threats. When the innate immune response is insufficient to eliminate them, the adaptive immune response is mounted, which is antigen-specific but time-dependent. The adaptive immune response consists of lymphocytes, including B and T cells. It involves B-cell

antibody production and activation of APCs to activate helper T-cells, which then stimulates the activation of cytotoxic T-cells. Eventually, immunological memory is achieved, which prevents the recurrence of the threat by rapid response triggered by an antigen that was previously recognized. Cytokines are generated by immune and nonimmune cells in response to cellular stressors such as infection, inflammation, and cancer, acting as messengers to coordinate cellular connections and communications of the immune system. This powerful machinery can attack and destroy non-self substances, such as bacterial and viral infections. Another crucial role of the immune system is immunosurveillance, in which the cells from the immune system identify abnormal cells and clear them (a mechanism related to apoptosis). As previously mentioned, one of the cancer hallmarks is the avoidance of immune destruction, which develops during tumor progression²³⁴. Cancer immunotherapy is the strategy of modulating the immune system to kill tumor cells.

There are several different types of immunotherapy. Oncolytic virus therapy, which uses genetically modified viruses to infect cancer cells and trigger a proinflammatory setting that culminates in a systemic antitumoral immune response²³⁵. Cancer vaccines use tumor-specific antigens to activate an antitumoral cytotoxic T-cell response or isolated DCs. Those cells are pulsed with tumor cell lysates and antigens *ex vivo* and then reinfused into the body²³⁶. Other strategies include genetic modification of tumor cells to immune cells stimulating factors²³⁷. Cytokine therapies, such as IL-2 and IFN- α , consist of the injection of large doses of those molecules as immunostimulatory signals to promote tumor regression. The therapeutic benefits of those molecules were accompanied by poor tolerability and severe toxicity, so there are studies with them in combination with other immunotherapies²³⁸. Adoptive cell transfer uses isolated and *ex vivo* genetically engineered immune cells that are reinjected into the patient. The most common types are chimeric antigen receptor (CAR)-T cells and T-cell receptor (TCR) engineered T cells²³⁹. Immune checkpoint inhibitors are another type of immunotherapy and will be discussed more thoroughly.

In 2018, the Nobel Prize in Physiology and Medicine was awarded to James P. Allison and Tasuku Honjo “for their discovery of cancer therapy by inhibiting negative immune regulation.” The molecules responsible for these results are immune checkpoint

inhibitors (ICIs). The work from both Nobel Prize winners was crucial in discovering one of the mechanisms of cancer immune evasion: checkpoint inhibition. Cancer cells express immune inhibitory ligands that suppress the activation of T cells when they bind checkpoint proteins. Checkpoint inhibitors bind to either the checkpoint protein (receptor on the surface of the T cells) or the ligand on the surface of the tumor cells, therefore blocking the interaction receptor/ligand that allows the tumor to escape the killing of the cytotoxic T cells²⁴⁰. One example of this interaction is the PD-1 (T cell receptor) and PD-L1 (tumor cell ligand). The binding of checkpoint inhibitor antibodies, either anti-PD-1 or anti-PD-L1, allows T cells to kill tumor cells²⁴¹ (see **Figure 21**). Another well-studied checkpoint antibody used in this work is anti-CTLA-4, which blocks the interaction of the checkpoint protein CTLA-4 on T cells to the B7 protein on tumor cells²⁴².

In short, the upregulation of immune checkpoint molecules on tumor cells obstructs T cells' ability to perform their immune surveillance functions. When another molecule (an ICI) binds to either the receptor on T-cells or the ligand on tumor cells, that obstruction is canceled, which promotes T-cell-mediated antitumor immunity (**Figure 21**).

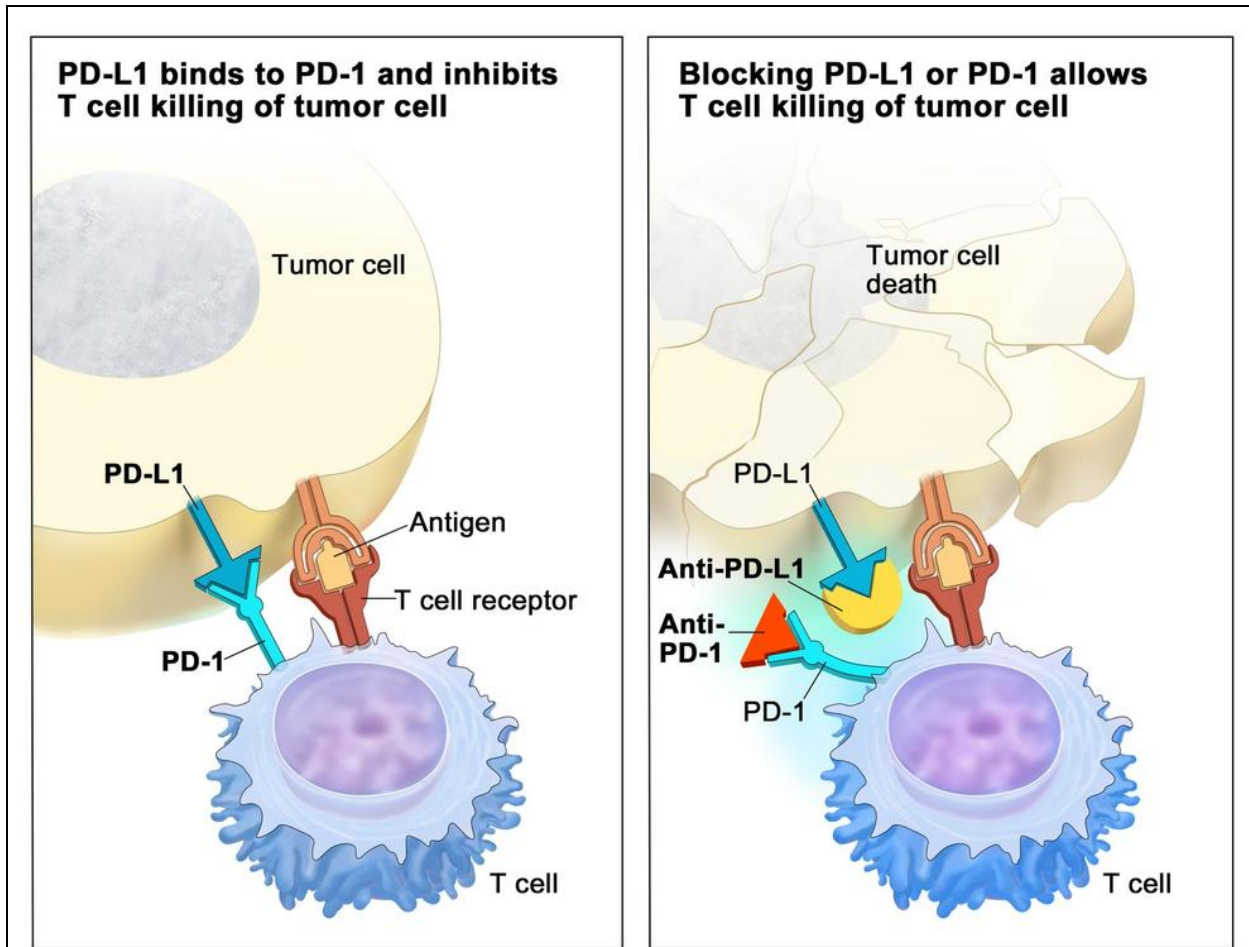


Figure 21: Interactions between PD-1 and PD-L1 on T cells and cancer cells and checkpoint inhibition. Image from: <https://nci-media.cancer.gov/pdq/media/images/774646.jpg>

Immunotherapy through checkpoint inhibition has arisen as the primary treatment of multiple cancers, including metastatic melanoma, non-small cell lung cancer (NSCLC), renal cell carcinoma (RCCs), and bladder or urothelial cancer²⁴³. Nonetheless, some tumor types are not very responsive to immunotherapies, which has been associated with the low density of tumor-infiltrating lymphocytes. More specifically, patients with high densities of CD8+ T cells at the tumor margin present a better response to immunotherapy²⁴⁴.

Breast cancer is one of the types of tumors that has been considered immunologically cold. The first immunotherapy approved for breast cancer was in

combination with the chemotherapy of paclitaxel for triple-negative breast cancer. Other combinations of chemotherapy and checkpoint inhibition have been studied in clinical trials²⁴⁵. Even though immunotherapy is effective in some breast cancer patients, more studies are necessary to improve safety and efficacy.

Due to the very localized destruction of tumor cells induced by photothermal therapy and the induction of immunogenic cell death, it is believed that combining immunotherapy with photothermal therapy creates a synergistic effect efficient in the treatment of cold tumors²⁰⁴. The benefits of exploiting PTT-induced ICD to enhance immunotherapy are remarkable. ICD generated by PTT allows for the successful removal of the treated tumor with the assistance of surrounding immune cells. At the same time, the tumor-specific antigens can function as an *in situ* anti-cancer vaccination²⁴⁶. While the native tumor antigens are weak at activating the immune response, their immunogenicity can be enhanced by the release of DAMPs during PTT²⁴⁷. Tumor ablation is also accompanied by the release of pro-inflammatory cytokines that promote the attraction and activation of immune system cells²⁰³.

Therefore, in this work, we studied the combination of SWCNT-mediated photothermal therapy and checkpoint inhibition to induce a systemic anti-cancerous immune response.

1.4.4 Radiofrequency ablation

Radiofrequency ablation (RFA) is another method for treating malignant diseases that utilizes radiofrequency waves in the range of 10 kHz to 900 MHz to generate heat and consequently induce tissue damage. This therapeutic strategy is currently used in clinical settings to treat deep-rooted cancers such as liver, kidney, adrenal gland, bone, lung, and breast²⁴⁸.

Radiofrequency waves are considered safe compared to other types of radiation used in clinics because they are in the low energy range of the electromagnetic spectrum. Consequently, RF radiation is non-ionizing, meaning it does not have sufficient energy to detach electrons from atoms and molecules, producing free radicals. While ionizing radiation ultimately promotes tissue damage and cancer due to damage to the

genetic material in cells, RF radiation can only cause damage by the induction of heating in the system, which can be controlled in the clinical setting. The sizable length of the RF waves leads to high penetration in live tissue, which is the primary reason for their use in deep-rooted cancers.

The prevailing method of concentration of the radiofrequency (RF) waves is the introduction into the diseased tissue of a needle-like electrode directly connected to the RF generator. The RF radiation prompts the heating of the surrounding volume. The Food and Drug Administration (FDA – the American agency responsible for the regulation of products related to public health) approved a procedure for the treatment of hepatocarcinoma with RFA that requires the use of imaging techniques, such as ultrasound, a computerized tomography (CT) scan, or magnetic resonance imaging (MRI), to guide the position of the electrode into the tumor. In this context, highly efficient treatment, meaning low local tumor recurrence, is achieved when complete ablation occurs during a treatment session, including all tumor margins. The recurrence rate can reach 60% when there is incomplete ablation. The inefficient ablation might happen due to difficulty localizing the tumor with available imaging techniques, heat transfer limitations, and heat dissipation through the bloodstream. Those factors lead to the heterogeneous heat of cancer, impeding the temperature rise to cytotoxic levels in the whole tumor volume. Other drawbacks of the RFA ablation are the invasiveness of probe-needle insertion and the non-selectiveness of the heating, which damages non-cancerous zones and surrounding tissue^{249–251}.

One of the ways to reduce invasiveness and increase tissue selectiveness is the utilization of RF-responsive materials allied to the application of an external RF generator. Various nanomaterials have shown responsiveness to heating *in vitro* in the RF field, such as gold, iron oxide, cobalt, quantum dots, and carbon-based nanomaterials^{252–254}.

Due to the formation of a dipole at the ends of SWCNT from the accumulation of opposing charges, electromagnetic waves cause nanotubes to vibrate. Those vibrations can be dissipated into the surrounding, which promotes the increase in temperature^{255–257}.

In a study by Gannon *et al.*²⁵⁸, CoMoCAT single walled carbon nanotubes functionalized with a polymer based on polyphenylene ethynylene (kentera) were studied *in vitro* in a 13.56 MHz RF field and showed significant heat compared to control at low concentrations of SWCNT in suspension. *In vitro* studies have shown cytotoxic effects with the irradiation at 800 W of cells. *In vivo* studies in hepatic tumors in rabbits have also shown induction of tumor necrosis 48 hours after the irradiation of tumors with 600 W of the non-invasive RF field generated between plates where the rabbits were placed. An area of 2-5 mm healthy tissue around the tumor depicted thermal injury. The control group (no SWCNT) did not have signs of tumor necrosis nor thermal injury²⁵⁸. Although no long-term tumor volume monitoring and survival of the animals were reported in the study, those results are evidence that the use of SWCNT in the radiofrequency field as a non-invasive RFA method (external plate irradiation) might also generate anti-tumoral effects similarly that SWCNT-ANXA5 mediated PTT has induced in our previous studies.

Therefore, efforts to study SWCNT as an RF-responsive material are also part of the scope of this work.

1.4.5 Targeted single-walled carbon nanotubes as photosensitizer and radiofrequency responsive material

Discovered in 1991 by Iijima²⁵⁹, carbon nanotubes (CNT) are nano-scaled cylinders of carbon atoms covalently linked with sp^2 hybridization state. Those particles can be idealized as a single sheet of graphene or multiple coaxial sheets, respectively named single-walled carbon nanotubes (SWCNT) and multi-walled carbon nanotubes (MWCNT). CNT's unique physical properties have attracted their use in numerous applications^{260–263}.

The properties of CNT are related to the manner carbon atoms assemble in the cylindrical structure, also called chirality. The classification of the chirality is based on the direction that a theoretical graphene sheet is rolled up to generate the carbon nanotube. This classification is based on the chiral angle, the direction of the hypothetical graphene sheet rolled to form the carbon nanotube. The 0° is defined as the direction where the vector crosses parallelly to two of the sides of the hexagons, a structure usually

nominated as armchair²⁶⁴, as shown in **Figure 22**. The direction that perpendicularly crosses the two parallel faces of the hexagon is called zig-zag, and all the other CNT formed by intermediate angles are called chiral. The direction of the chiral vector is identified by the pair of indices (n,m) correlated to the chiral angle, and the diameter of the CNT is associated with the integer multiplying those indices²⁶⁵. As seen in **Figure 22**, the chirality of the CNT establishes if the CNT has metallic or semi-conducting properties.

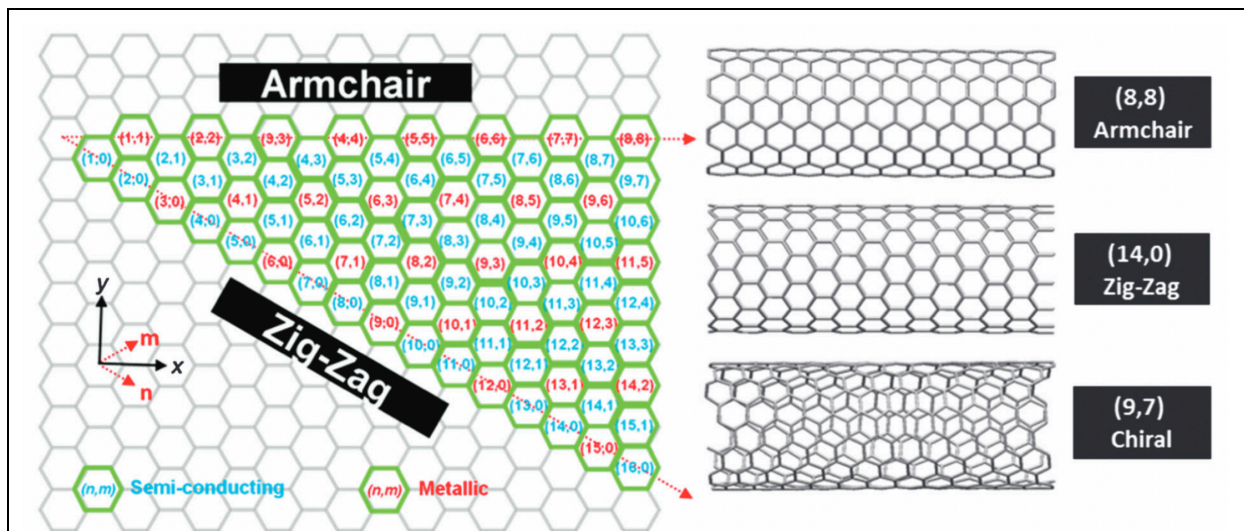
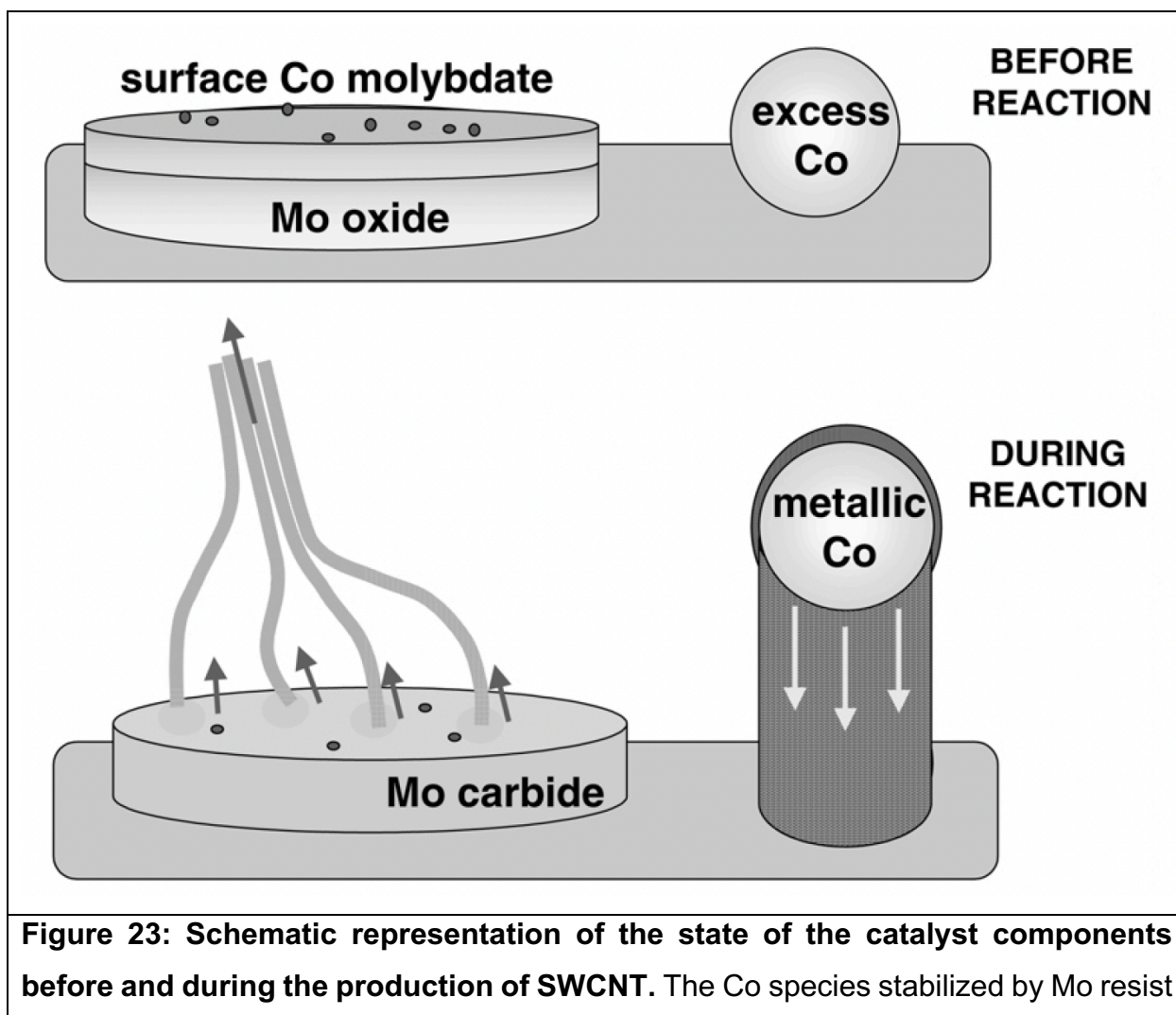


Figure 22: SWCNT helicity map and examples of (n,m) chiral vectors that give rise to the armchair, zig-zag, and chiral nanotube structures with metallic or semi-conducting electronic character. Figure from Hodge *et al.*, 2012²⁶⁴.

The optical properties of CNT are intrinsically related to the chirality of the carbon structure because of the correlation with the optical transitions²⁶¹. The chirality also influences the thermal conductivity of this nanomaterial: for example, armchair and zigzag CNT have higher thermal conductivities compared to chiral CNT²⁶⁶. Enriching CNT with certain chiral angles results in enhanced properties due to the correlation between chirality and properties. Therefore, the interest in obtaining an abundance of CNT that have virtually a unique chirality has grown. The most promising way to produce CNT with high purity of certain chiral angles is preferential synthesis, where the parameters utilized in the production process, such as catalyst and precursor, are meticulously designed to generate CNT with specific chiral angles²⁶⁴.

Although many challenges exist in the production of CNT with high selectivity, high quality, high yield, and low cost, a scalable process to produce CNT was developed at the chemical engineering department of the University of Oklahoma²⁶⁷. The method uses a cobalt-molybdenum catalyst on silica support and CO precursor in fluidized bed reactors (see **Figure 23**). The CO disproportionation on the surface of the specifically designed catalyst at high temperatures (700-950°C) produced considerable amounts of SWCNT with high selectivity above 80% towards the (6,5) and (7,5) chirality^{268,269}. The process – trademarked as CoMoCAT[®] – is nowadays considered a milestone in the production of carbon nanotubes, enabling the usage of these nanomaterials in many applications^{270–273}.



reduction and sintering before the reaction. Under CO, Mo becomes carbide while Co becomes metallic and generates the SWCNT. The excess Co, not stabilized by Mo, produces MWNT and fibers. Figure from Resasco *et al.*, 2002²⁷⁴

In this work, the CoMoCAT[®] (6,5) SWCNT was used for photothermal therapy due to high absorbance in the near-infrared range and peak absorbance at 980 nm. A veterinarian laser that irradiates at 980 nm has been selected to match the SWCNT's peak absorbance. Other chiralities were studied for carbon-nanotube-mediated radiofrequency ablation.

1.4.6 Theranostic platform composed of protein-drug conjugate linked to gold nanoparticles

As previously mentioned, traditional chemotherapies cause a wide-ranging adverse effects on undesired targets such the brain system, immunological system, and gastrointestinal tract. Less than 1% of a given medicine, when given freely, is known to reach the tumor site and exert an anticancer effect; the remaining portion is distributed throughout the tissues of the organism²⁷⁵. A chemotherapeutic drug's distribution to the tumor site can be improved by combining it with a targeted carrier agent. With targeted therapy, the chemotherapeutic agent is delivered specifically to the tumor location, sparing healthy cells from unintended side effects and enabling the use of a lower effective dose of the medicine. Therefore, drugs would be optimally and precisely delivered to cancer cells by being conjugated to a carrier agent unique to tumor cells²⁷⁶. Protein-drug conjugates offers a plasma-circulating vehicle that will only release the active drug molecules once they are attached to tumor-specific antigens.

Here, we present the strategy of conjugating a drug, mertansine, to ANXA5 to create a targeted chemotherapeutic agent for cancer. As mentioned before, ANXA5 is a protein that specifically binds to cancer cells, tumor vasculature, and metastatic cancer cells. Therefore, ANXA5 is a suitable candidate for the carrier of drugs to cancer.

Mertansine (drug maytansinoid 1, DM1, 738.3 Da) is a microtubule inhibiting agent that causes M phase mitotic arrest, by supposedly binding to tubulin on the beta-tubulin domain preventing longitudinal microtubule assembly^{277,278}. Maytansinoids were discovered in the 70s, and evoked strong interest for their potential for anticancer treatment. In a phase 1 clinical trial that occurred in 1978, maytansine induced remission in many leukemia patients, and vincristine-resistant patients showed significant improvement. However, maytansine exhibited substantial central nervous system and gastrointestinal toxicity. Lethargy, weakness, and insomnia were also often reported side effects of the medication, along with ubiquitous severe vomiting and diarrhea²⁷⁹. By the early 1980s, the excitement around maytansinoids had mostly subsided as a result of the therapeutic outcomes being underwhelming at the maximal tolerated doses (MTDs), which were only about 1 mg/m² ²⁸⁰. Later in the 80s, a modification to the chemical structure of original mantensine introduced a sulfhydryl group to allow a disulfide bridge between drug and proteins. The modified drug was named the “drug-maytansinoid-1” or DM1 (**Figure 24**). Clinical trials in the 2000s with antibody-DM1 conjugates and pre-clinical research revealed maximal tolerable weekly doses of 115 mg/m², more than 100 times the amount permissible with the free drug, and 1000 times lower toxicity to untargeted cells.

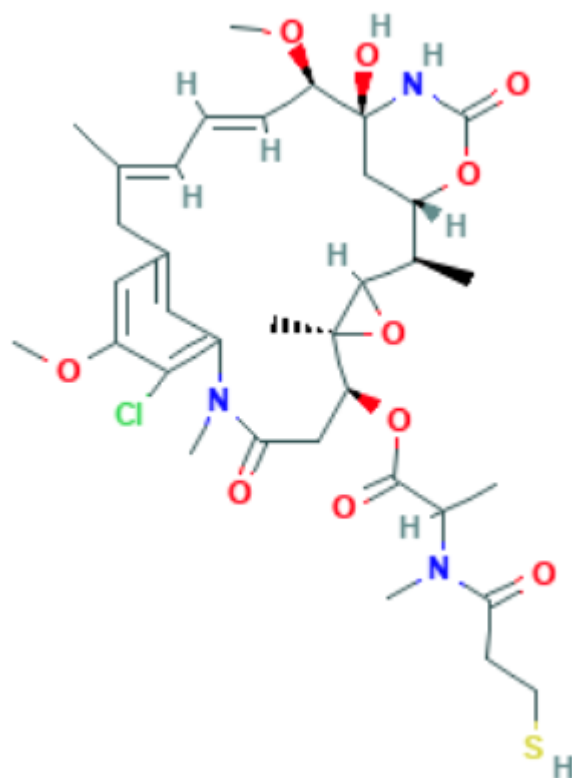


Figure 24: Mertansine Chemical Structure, Formula: $C_{35}H_{48}ClN_3O_{10}S$

Even though the antibody-DM1 conjugates have enabled the clinical use of DM1 as a therapeutic agent, antibody-drug conjugates can have limited action due to poor antigen expression in most tumor strains and quickly varying tumor phenotypes. Therefore, ANXA5 is a promising carrier of DM1 that might increase the possible targets for the drug, due to the ubiquitous expression of PS on the surface of cancer cells, vasculature, and metastasis. Therefore, in this lab, ANXA5-DM1 has been developed.

Another way that ANXA5 can be used in cancer related settings is as a targeting agent in enhanced MicroCT imaging via gold nanoparticles (AuNP). Even though mammograms are the standard diagnostic tool for BC, they do not detect variations in breast density, which leads to the need of biopsies and MRIs. In this lab, a novel and highly specific cancer targeting gold nanoparticle was developed to improve the accuracy of detection of breast cancer, by linking AuNP to ANXA5²⁸¹. AuNP-ANXA5

conjugate are used as enhanced contrasting agents for CT scans. The higher density of targeted AuNP, when bound to tumor vasculature and cancer cells, attenuate the X-rays generated by CT device more efficiently than the soft tissue surrounding it, generating contrasting signals. The AuNP-ANXA5 mediated CT scan can improve sensitivity and specificity of breast cancer detection, distinguishing a thick breast or a breast with microcalcifications from a breast tumor. The results of AuNP-ANXA5 enhanced microCT was published in Virani *et al.*²⁸¹.

In this work, a novel multi-model nanoparticle for detection and therapy of cancer has been developed by linking the ANXA5-DM1 chemotherapeutic conjugate to AuNP.

CHAPTER 2 - MATERIALS AND METHODS

2.1 Materials

2.1.1 Protein production and purification

The plasmid encoding annexin A5, pET-30 Ek/LIC/ANX, was previously constructed in this lab by Ph. D. student Naveen Palwai. The plasmid is designed to express annexin A5 having an N-terminal (His)₆ tag and an HRV 3C protease site next to the N-terminus of annexin A5. Sodium hydroxide (NaOH), sodium chloride (NaCl), tryptone, kanamycin, yeast extract, isopropyl-beta-D-thiogalactopyranoside (IPTG), N-*p*-tosyl-L-phenylalanine chloromethyl ketone (TPCK), phenylmethylsulfonyl fluoride (PMSF), β-mercaptoethanol, and sodium phosphate dibasic (Na₂HPO₄) were purchased from Sigma Aldrich (St. Louis, MO). HRV 3C protease was purchased from Acro Biosystems (Newark, DE). The HisTrap chromatography column (5 ml) was purchased from Cytiva (Marlborough, MA). Flow adapters were purchased from Bio-Rad (Hercules, CA). The 12-14 kDa regenerated cellulose dialysis membrane was from Fisher Scientific (Pittsburgh, PA). Laemmli sample buffer, ladder (marker), 4-20% mini-protean TGX stain-free pre-casted polyacrylate gels, Bio-Rad 10x Tris-glycine-SDS buffer, and Bradford dye reagent were purchased from Bio-Rad Laboratories (Hercules, CA). Imperial™ protein stain was purchased from Thermo Scientific (Waltham, MA).

2.1.2 SWCNT-ANXA5 conjugation

Purified and freeze dried (6,5) CoMoCAT SWCNTs (average diameter 0.8 ± 0.1 nm) were provided by CHASM (Norman, OK). DSPE-PEG-mal (3.4 kDa) was purchased from Creative PEGWorks (Winston Salem, NC). Spectra-Por® dialysis membranes (2 and 100 kDa) from Spectrum Laboratories, Inc. (Rancho Dominguez, CA). Bradford protein reagent was from Bio-Rad (Hercules, CA). L-cysteine amino acid was acquired from Sigma Aldrich.

2.1.3 Cell culture

All cell lines and cell media were purchased from American Type Culture Collection (ATCC, Manassas, VA, USA), except for HAAE-1, which was purchased from Coriell Institute (Camden, New Jersey, USA). Waymouth's MB 752/1 medium, Roswell Park Memorial Institute 1640 medium (RPMI-1640), and Hams F-12 medium were purchased from Gibco (Thermo Fisher, Waltham, MA). Antibiotic-antimitotic (10,000 IU Penicillin, 10,000 $\mu\text{g/ml}$ Streptomycin, and 25 $\mu\text{g/ml}$ Amphotericin B) was purchased from Corning (Kennebunk, MA, USA). Endothelial cell growth kit BBE (0.2% bovine brain extract, 5 ng/ml EGF, 10 mM L-glutamine, 0.75 Units/ml heparin sulfate, 1 $\mu\text{g/ml}$ hydrocortisone, 50 $\mu\text{g/ml}$ ascorbic acid, 2% FBS) was purchased from ATCC. Trypsin/EDTA was purchased from Thermo Fisher Scientific.

2.1.4 *In vivo* studies

BALB/cJ mice were purchased from Jackson Laboratory (Bar Harbor, ME). Anti-CTLA-4, ELISA kits, and flow cytometry staining antibodies were purchased from Biolegend (San Diego, CA). Anti-PD-1 was purchased from Bio X Cell (Lebanon, NH). PEGSH was purchased from JenKem Technology USA (Plano, TX). PEGDA was purchased from Sigma Aldrich (St. Louis, MO). Imiquimod was purchased from Thermo Fisher Scientific.

2.1.5 Gold nanoparticle conjugation

Gold nanoparticles (15 nm) were purchased from Nanoprobes (Yaphank, NY). NH_2 -PEG-SH (PEG molecular weight of 3.4 kDa) linker was from Creative PEGWorks. Sulfo-SMCC was purchased from TCI America (Portland, OR) and mertansine (DM1) was purchased from MedChemExpress (Princeton, NJ).

2.2 Protein production and purification

Recombinant ANXA5 was produced as previously described²⁸². In brief, BL21(DE3) *Escherichia coli* (*E. coli*) harboring the plasmid containing pET-30 Ek/LIC/ANXA5 were initially incubated at 37°C with agitation (200 rpm) overnight in 10 mL of TB medium with kanamycin (35 µg/ml). The initial culture was added to 1 L of fresh kanamycin enriched-TB medium and incubated until the OD_{600 nm} of the solution was at 1.2 (absorbance reading at 600 nm). Protein expression was then induced by adding isopropyl-D-thiogalactopyranoside (IPTG of 0.4 mM) to the medium, and the culture was left to incubate for a further 19 h at 25°C. The ANXA5-expressing bacteria were collected by centrifugation (1100 g for 10 min) and resuspended in a sonication buffer. Bacteria cells were lysed by sonication using on/off cycles (30 s on and 30 s off, five times total). The lysate containing all the cellular proteins, including the ANXA5 protein with an N-terminal six histidine tail (His-Tag), was centrifuged to remove cell debris (3500 g for 2 h). The debris-free supernatant was collected and loaded into a nickel HisTrap column. After various washing steps, including endotoxin washing with 1% TRITON X-114, ANXA5 protein (with an N-terminal six histidine tail) was eluted with a 500 mM imidazole buffer, displacing His-Tag from the column. After dialysis against 20 mM sodium phosphate buffer (adjusted pH 7.4), the His-Tagged protein was cleaved with the HRV 3C protease. Final column purification was performed by loading cleaved protein into the affinity column and collecting the first flow-through with ANXA5 without His-Tag. The protein solution was dialyzed against a 20 mM-sodium phosphate buffer containing 100 mM NaCl (pH 7.4) a final time before being aliquoted in cryogenic vials and flash-frozen in liquid nitrogen. Aliquots were placed in a -80°C freezer for long-term storage. The purified protein was quantified using the Bradford assay and analyzed with SDS-PAGE electrophoresis for purity. Detailed protein production protocol is available in Appendix B1 and B2. Bradford assay and SDS-page electrophoresis protocols are accessible in Appendix B3 and B4, respectively.

2.2 SWCNT-ANXA5 conjugate

2.2.1 ANXA5 conjugation to SWCNT

The conjugation was performed using a DSPE-PEG-maleimide linker (3.4 kD) using a protocol that was modified from one previously used²⁸². SDC solution (2%) replaced 1% sodium dodecyl sulfate (SDS) solution in the original protocol to increase the availability of (6,5) SWCNT in suspension. SWCNT (6 mg) were added to 5 ml of a 2% sodium deoxycholate (SDC) solution and sonicated for 1 h at 19.8 W of power ($E = 35,640 \text{ J}$) (VirSonic 100 ultrasonic cell disruptor, VirTis). Sonicated SWCNT was centrifuged in an ultracentrifuge (16,000 g) for 1 h to discard non-suspended SWCNT aggregates. Suspended SWCNT, characterized by a dark-colored aqueous suspension, was then stored in small glass vials at room temperature. The DSPE-PEG-MAL linker was then dissolved in 2% SDC solution at a concentration of 1.5 mg/ml. The linker solution (1 ml) was added to 5 ml of the SWCNT suspension and mixed at room temperature for 30 min with gentle shaking. After that, the suspension was transferred into a 2-kDa dialysis membrane and dialyzed for 8 h against 3 liters of deionized water. The dialysate was changed after the first 4 h. ANXA5 was then reconstituted from frozen vials, and its concentration was accessed by Bradford assay. Protein concentrators (10 kDa) were used to increase concentration to approximately 5 mg/ml concentration. SWCNT-linker suspension (2 ml) was mixed with the concentrated ANXA5 (1 ml of 5 mg/ml totaling 5 mg of ANXA5) at room temperature for two hours with gentle shaking. Any unreacted linker sites were blocked with L-cysteine (0.048 mg to give a molar ratio of L-Cys/Linker was equal to 3:1), which was added to the suspension and allowed to react for 1 h at room temperature with gentle shaking. The suspension was then dialyzed using a 100 kDa dialysis membrane to remove any unbound ANXA5 or L-cysteine for 8 h against 3 L of 20 mM sodium phosphate buffer (pH 7.4) with a dialysate change after 4 h. The final suspension was centrifuged at 16,000 g for 1 h to remove any aggregates. The

conjugate was stored in a glass vial at 4°C until use. Conjugate was used within 1 week of the end of conjugation (see protocol in Appendix B5).

2.2.2 SWCNT standard curve

A standard suspension of SWCNT (1200 mg/L) was obtained similarly to the conjugation protocol. More specifically, a precise mass of 6.0 mg of SWCNT was measured and analytically transferred into a glass vial. A volume of 5.0 ml of 1% sodium dodecyl sulfate (SDS) solution, measured with a volumetric pipette, was used to transfer SWCNT into the glass vial. The glass vial was meticulously checked for the presence of SWCNT outside of the liquid phase. Any remaining SWCNT bundles were washed off from the wall into solution with the SDS solution from inside the vial. Sonication was performed for 1 h, and the suspension was not centrifuged to avoid mass loss. Serial dilutions were performed using the SDS solution. Triplicates of each concentration were added to different wells in a 96-well plate. Endpoint absorption at 800 nm was measured with a plate reader using the SDS solution as blank (see protocol in Appendix B6).

2.2.3 SWCNT-ANXA5 characterization

Both SWCNT and ANXA5 concentrations were assessed at the end of the conjugation. SWCNT concentration in the conjugate was measured with endpoint absorption at 800 nm and compared to the standard curve previously obtained. ANXA5 concentration was obtained by standard Bradford Assay. Protein to carbon nanotube mass ratio was determined, and the conjugation was considered successful when the ratio was greater than 5, as shown in the **equation 1**:

Equation 1: Assessment of SWCNT-ANXA5 conjugation

$$\frac{ANXA5}{SWCNT} = \frac{\text{Concentration of ANXA5} \left[\frac{mg}{ml} \right]}{\text{Concentration of SWCNT} \left[\frac{mg}{ml} \right]} > 5$$

2.2.4 SWCNT-ANXA5 sterilization

SWCNT-ANXA5 sterilization is necessary for *in vitro* assays and *in vivo* studies. For that, no more than 1 ml of the suspension was placed in a 30-mm Petri dish, allowing the suspension to form a thin layer uniformly distributed on the surface. The suspension was then subjected to a direct UV (UV-C, shortwave UV at 254 nm) irradiation for 30 min in a laminar flow hood equipped with a Philips UV-C lamp (30 W). Before irradiation, the lamp bulb was cleaned by swabbing with 70% ethanol in a paper towel. After UV irradiation, samples were then stored in an aseptic vial. Further sterility evaluation was demonstrated by the absence of microorganisms in the samples. That assay was done by plating tap water, non-sterile, and sterile SWCNT-ANXA5 suspensions in an agar plate enriched with Luria-Bertani (LB) medium.

2.3 Cell culture

EMT6 murine breast carcinoma cells were cultivated with Waymouth's MB 752/1 medium supplemented with 2 mM glutamine, 15% FBS, and 1% of antibiotic-antimitotic (10,000 IU penicillin, 10,000 µg/ml streptomycin, and 25 µg/ml amphotericin B). 4T1 murine breast cancer cells were cultivated with Roswell Park Memorial Institute 1640 medium (RPMI-1640) supplemented with 10% FBS and 1% antibiotic-antimitotic.

Human umbilical vein endothelial cells (HUVEC) were cultured in vascular cell basal medium supplemented with endothelial cell growth kit BBE (0.2% bovine brain extract, 5 ng/ml EGF, 10 mM L-glutamine, 0.75 Units/ml heparin sulfate, 1 µg/ml hydrocortisone, 50 µg/ml ascorbic acid, and 2% FBS) and 1% antibiotic-antimycotic. Human abdominal aorta endothelial (HAAE-1) cells were cultured in Hams F-12 medium supplemented with 30 µg/ml endothelial cell growth supplement (15 mg/500 ml media), 17.5 U/ml Heparin (8750 U/500mL or 17.5 mg heparin/500 ml), 10% FBS, and 1% antibiotic-antimycotic. Additionally, before culturing HAAE-1 cells, plates and wells were incubated with 0.1% porcine gelatin for 30 min in the incubator at 37°C to promote cell attachment. Gelatin was aspirated before cell seeding.

All adherent cells were passaged using 0.25 % (w/v) trypsin in 0.53 mM EDTA before reaching 85% confluency. All cell lines were cultured under a 5% CO₂-supplemented atmosphere at 37°C. The medium was refreshed every 48 h. During assays, adherent cancer cell cultures were grown to less than 75% confluence, and healthy cell lines cells were grown to confluency for inhibition of PS expression upon confluency.

Mammalian cell culture was performed in a strictly sterile environment in Biological Safety Cabinet Class II equipped with high-efficiency particulate air (HEPA) filters. Materials and utensils were either sterilized either by the supplier or by autoclave. The sterility of mammalian cell culture was maintained by following aseptic technique protocols, which are available in Appendix C.

2.4 *In vitro* studies with SWCNT-ANXA5-mediated PTT

The cells that were previously grown in T-75 flasks were seeded at 2×10^5 into sterile surface-treated 24-well plates. At 24 h after seeding, cell media was aspirated, and fresh media enriched with 6 mg/L SWCNT-ANXA5 suspension and 2 mM of Ca²⁺

(CaCl₂) was added to the wells. Incubation was performed for 2 h at 37 °C. The wells were washed three times with sterile phosphate buffer saline (PBS) to remove unbound SWCNT-ANXA5. Each group was evaluated at least in triplicate. Different controls were studied to guarantee the specificity of the assay.

Each well subjected to the laser treatment was irradiated for different time periods at an energy density of 1 J/cm² using a Diodevet-50 NIR laser at 980 nm (B&W Tek Inc., Newark, DE). The irradiation was always performed by having the plate sitting on top of a platform and aiming the optical fiber at the bottom of the plate, positioned a few centimeters away from the bottom to obtain the desired size beam. Each well was carefully adjusted to be centered with the laser beam. The size of the beam was adjusted using a laser sensitive paper (Zap-it[®] paper) which burns when exposed to a laser beam. The entire irradiation session was conducted by having the cells in a sterile environment by not removing the plate's lid. Depending on the experiment, the irradiation was performed at room temperature or inside an incubator at 37°C to mimic physiological temperatures.

The attenuation of power from the fiber was determined by a power meter (Ophir Optronics Ltd., Israel). After having the fiber accurately aligned with the well, the power attenuation inherent to the optical fiber and the plate was determined by using the power meter. The power meter probe was placed on top of a microtiter plate (without the lid on), and the power was determined to reach a power level of 1 W/m². The entire irradiation session was done either at room temperature or inside an incubator that maintained the temperature constant at 37°C. More details about this procedure is available in Appendix C8.

The cell viability was determined by using the Alamar Blue assay, which evaluates the metabolic activity of the cells. It consists of a non-toxic and non-fluorescent dye (resazurin), which is reduced to a fluorescent pink species (resorufin) inside a metabolically active cell. The Alamar Blue assay was performed under sterile conditions by aspirating old media and adding fresh media enriched with 10% Alamar Blue reagent. The cells were incubated for 2-4 h at 37 °C until the control wells were bright-pink fluorescent. The colorimetric changes are then evaluated by measuring with 530 nm excitation and 590 nm emission (50 sensitivity). The viability was determined by

normalizing the results to the average absorbance of the untreated control wells, which is set to 100%, giving each well the relative viability. The average background fluorescence (no cell wells) was also subtracted from sample fluorescence. Equation 2 shows the percentage viability of a sample.

Equation 2: Cell viability quantification from absorbance units in Alamar Blue Assay

$$\text{Viability}\% = \frac{\text{Treated Fluorescence} - \text{No Cell Blank Fluorescence}}{\text{Untreated Control Fluorescence} - \text{No Cell Blank Fluorescence}} \times 100\%$$

Details about Alamar Blue Assay are available in Appendix C7.

2.5 In vivo studies with SWCNT-ANXA5-mediated PTT

All animal studies were performed following the protocols approved by the Institutional Animal Care and Use Committee (IACUC) of the University of Oklahoma and by staff with proper training. Animals were housed in a pathogen-free facility at the University of Oklahoma and monitored daily.

2.5.1 Tumor implantation in BALB/cJ mice

On the day before tumor implantation, the area around the fourth mammary fat pad in each six-week-old BALB/cJ mouse (Jackson Laboratory; 000651) was shaved using a hair removal cream. The cream was placed on the fur, left for no longer than 2 min, and removed with a humid paper towel. The mice were injected with either 1×10^5 4T1 cells or 1×10^6 EMT6 cells suspended in 100 μ l of PBS using a 30-gauge needle. The injection was performed subcutaneously in the fourth mammary fat pad, close to the nipple, which characterizes an orthotopic tumor (see Appendix D1).

2.5.2 Mice health and tumor volume assessment

Mice weight and tumor volumes were measured every 3 - 5 days during each study. Tumor volumes were measured using a caliper, and volume (V) was determined through the modified ellipsoid formula, where length (L) is the longest diameter of the tumor and the perpendicular diameter is the width (W), as shown in **Equation 3**.

Equation 3: Tumor volume from size measurement

$$V = \frac{L * W^2}{2}$$

For all the studies, mouse health was assessed every 3-5 days for signs of distress. Mice were euthanized when the tumor size was greater than 15 mm in any of the directions of measurement or when the mice were sick, characterized by dehydration, weight loss greater than 20%, recumbent posture, breathing difficulty, or loss of leg function due to tumor proximity.

2.5.3 Cytokine release in EMT6 tumors treated with combination therapy of PTT and anti-CTLA-4

In previous work in our laboratory, Patrick McKernan *et al.*²⁸³ treated BALB/cJ mice bearing EMT6 tumors with SWCNT-ANXA5 mediated photothermal therapy in combination with checkpoint inhibition of anti-CTLA-4. EMT6 tumors were induced orthotopically, as previously described. Tumors were allowed to grow for 12 days, and when they reached a volume of 60 mm³ (~ 5 mm in diameter), mice received a systemic i.v. injection of 1.2 mg/kg of SWCNT-ANXA5 (mg SWCNT per kg body weight) bioconjugate via the lateral tail vein. After 3 h, a region 5 mm around the tumor boundary was irradiated with NIR light (980 nm) at an energy and power level of 175 J/cm² and 1 W/cm², respectively (time of 175 s; Diodevet-50 NIR laser, B&W Tek Inc., Newark, DE).

Checkpoint inhibition was accomplished by serial i.p. administration of 200 µg anti-CTLA-4 antibody in 100 µl of PBS on days 8, 11, and 16 following tumor inoculation. Mice were separated into five groups (n = 5):

- 1 - **Control**: untreated group.
- 2 - **SWCNT**: mice injected with SWCNT-ANXA5.
- 3 - **α-CTLA-4**: mice injected with anti-CTLA-4
- 4 - **PTT**: mice injected with SWCNT-ANXA5 and treated with photothermal therapy.
- 5 - **α-CTLA-4 & PTT**: mice injected with SWCNT-ANXA5 and anti-CTLA-4 and treated with PTT.

Seven days after photothermal therapy, mice were euthanized for blood collection. Taken samples were centrifugated to collect the serum, and enzyme-linked immunosorbent assays (ELISA) were performed to quantify serum levels of proinflammatory cytokines (TNF- α , IL-6, IFN- γ and IL-12 [p70]). Standard curves were obtained for each cytokine to quantify the concentration in serum samples.

2.5.4 Cytokine release related to intravenous versus intratumoral injection in EMT6 tumor bearing mice

Six-week-old female BALB/cJ mice bearing EMT6 tumors were injected with either intravenous or intratumoral injections of SWCNT-ANXA5 (1.2 mg/kg of SWCNT) when the tumors were around 5 mm in diameter (~60 mm³). Three hours after injections, the tumors were treated by a 980-nm NIR laser for 175 s at 1 W/cm². One day after irradiation, blood samples were collected during euthanasia. The concentration of TNF- α in the serum was quantified by ELISA following procedures from the supplier. Results

from intravenous and intratumoral injections were compared to the untreated group (no injection), as shown in the groups below:

- 1- **Control:** untreated mice; Mice were not injected with SWCNT-ANXA5 injection and were not treated with PTT.
- 2- **Intravenous injection:** Mice were intravenously injected with SWCNT-ANXA5 in lateral tail vein and subjected to PTT treatment.
- 3- **Intratumoral injection:** Mice were intratumorally injected with SWCNT-ANXA5 and subjected to PTT treatment.

2.5.5 Cytokine release related to tumor surface temperature in EMT6 tumor bearing mice

Six-week-old female BALB/cJ mice bearing EMT6 tumors were injected intratumorally with SWCNT-ANXA5 (1.2 mg/kg of SWCNT) when the tumors were around 5 mm in diameter ($\sim 60 \text{ mm}^3$). The tumors were treated by a 980-nm NIR laser at 1 W/cm^2 . The tumor surface temperature was monitored during the irradiation by a thermal camera (FLIR E5-XT), adjusting emissivity to 0.93. Irradiation ceased immediately after the tumor surface reached the temperature assigned to the groups of 45, 50, 55, or 60°C. Mice were euthanized either 1 or 7 days after PTT for blood collection (respectively 24 h and 168 h). The concentration of four cytokines was measured in the serum by ELISA. The control group was intratumorally injected with SWCNT-ANXA5 but not treated with PTT. The groups in this experiment were ($n = 5$):

- 1- **Control:** untreated; Mice were intratumorally injected with SWCNT-ANXA5, but were not treated with PTT
- 2- **45°C:** Mice were intratumorally injected with SWCNT-ANXA5 and treated with PTT (1 W/cm^2) until tumor surface temperature reached 45°C.

- 3- **50°C**: Mice were intratumorally injected with SWCNT-ANXA5 and treated with PTT (1 W/cm²) until tumor surface temperature reached 50°C.
- 4- **55°C**: Mice were intratumorally injected with SWCNT-ANXA5 and treated with PTT (1 W/cm²) until tumor surface temperature reached 55°C.
- 5- **60°C**: Mice were intratumorally injected with SWCNT-ANXA5 and treated with PTT (1 W/cm²) until tumor surface temperature reached 60°C.

2.5.6 Survival of EMT6 tumor bearing mice in combination therapy of PTT at 45°C and anti-PD-1

Six-week-old female BALB/cJ mice were inoculated with EMT6 tumors on day 0. On day 7, when tumors were around 3 mm in diameter, treatment started for the assigned groups with an intraperitoneal injection of anti-PD-1 checkpoint inhibitor at 10 mg/kg. The same injection was performed two more times on days 10 and 15. On day 11, mice were injected intratumorally with SWCNT-ANXA5 (1.2 mg/kg of SWCNT) when the tumors were around 5 mm in diameter (~60 mm³) treated with PTT. The treatment schedule is shown in **Figure 25**:

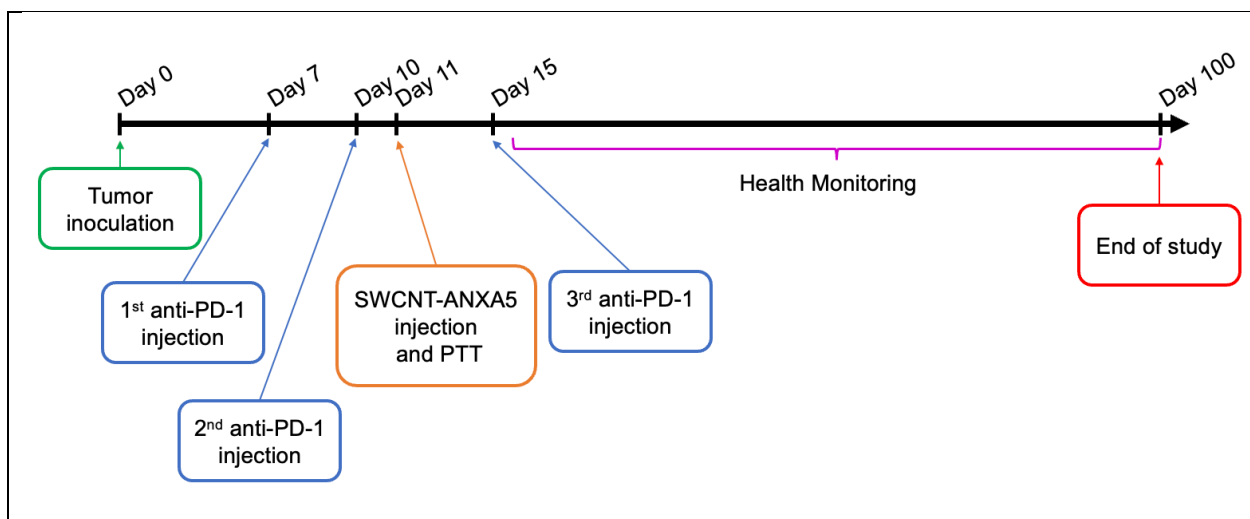


Figure 25: treatment schedule for the combination therapy of EMT6 tumor models with SWCNT-ANXA5 mediated photothermal therapy until 45°C and anti-PD-1.

The tumors were treated by 980 nm NIR laser for at 1 W/cm². The tumor surface temperature was monitored during the irradiation by thermal camera (FLIR e-5), adjusting emissivity to 0.93 and central focus. Irradiation was ceased immediately after the tumor surface temperature reached 45 °C. Mice were assigned to four different groups:

- 1- **Control:** untreated.
- 2- **Anti-PD-1:** Mice treated with 3 injections of anti-PD-1.
- 3- **PTT:** Mice intratumorally injected with SWCNT-ANXA5 and treated with PTT until 45 °C.
- 4- **Anti-PD-1 + PTT:** Mice treated with 3 injections of anti-PD-1, intratumorally injected with SWCNT-ANXA5 and treated with PTT until 45 °C.

Tumor volumes and body weights will be monitored daily after PTT. We reduced the monitoring frequency to every 3 days after finding no evidence of pain or distress. Treated or untreated mice that are in pain or distress, as indicated by being recumbent, were euthanized. Animals that exhibited weight loss greater than 20% from the onset of the study were euthanized. Mice-bearing tumors bigger than 15 mm were also euthanized. The study ended 100 days after tumor inoculation when the remaining mice were euthanized by CO₂ asphyxiation.

2.5.7 Immune response of in combination therapy of PTT at 45°C and anti-PD-1 in EMT6 tumor-bearing mice.

Six-week-old female BALB/cJ mice were inoculated with EMT6 tumors on day 0. Combination therapy of PTT at 45 °C and three injections of anti-PD-1 were

performed according to schedule and groups (n = 4) in section 2.5.6. Mice were euthanized by CO₂ asphyxiation 14 days after PTT, and the spleens were harvested. Spleens were kept in DMEM media 4°C until use. Spleens were mechanically dissociated with a plunger in a Petri dish and strained through a 70 µm filter with 3 ml of flow cytometry staining buffer. Strained cells were centrifuged at 1000 g for 5 min, and the supernatant was discarded. Another 3 ml of flow cytometry buffer was added to resuspend and recentrifuged the cells. The total number of cells in each spleen was determined by a hemocytometer. Cells were resuspended in flow-cytometry staining buffer to a final concentration of 1 x 10⁷ cells/ml. Cells (100 µl) were stained and were first blocked with Fc blocker (anti-mouse CD16/32) to prevent non-target staining for 15 min. After the washing step, cells were stained for myeloid-derived spleen cells (MDSCs), macrophages, and T-cells separately with 50 µl antibody mixture for 1 h at 4 °C, protected from light. Antibody cocktails for each cell stain are listed in **Table 1**. Flow-cytometry staining buffer was used to bring the final volume to 50 µl. After staining, cells were washed three times with 1 ml of flow cytometry staining buffer followed by 5 min centrifugation at 1000 g. After the last wash, cells were suspended in 500 µl of flow-cytometry staining buffer and analyzed via a BD Accuri C6 flow cytometer (San Jose, CA). See Appendix D5 for detailed protocol.

Table 1: Cell staining antibody cocktail for flow cytometric analysis of splenic cells

Cells	Antibodies	Concentration (mg/ml)	Volume (uL)
MDSC	APC-CD11b	0.2	1.25
	PerCP-Ly-6G	0.2	1.25
	FITC-Ly-6G	0.2	0.5
Macrophages	APC-CD11b	0.2	1.25
	PE-F4-80	0.2	1.25
T-cells	PE-Cy7-CD3e	0.2	1.25
	APC-CD8	0.2	2.5
	FITC-CD4	0.2	0.625

2.5.8 Tumor control with PTT treatment keeping tumor surface temperature at 45°C for longer period of time

Six-week-old female BALB/cJ bearing EMT6 tumors were intratumorally injected with SWCNT-ANXA5 (1.2 mg/kg of SWCNT) when the tumors were around 5 mm in diameter (~60 mm³). The tumors were treated by a 980-nm NIR laser at 1 W/cm². Tumors were irradiated until the surface temperature reached 45°C and then held the temperature at 45°C by repeatedly turning the laser off and on. The cycles of turning off and on were repeated for the total time of the irradiation session described in the groups (n = 5):

- 1- **Control**: NIR-irradiation of tumor until surface peak temperature reached 45°C and turn laser off.
- 2- **1 min irradiation session**: NIR-irradiation of tumor until surface peak temperature reached 45°C (start timer) + cycles of off/on laser irradiation to maintain the tumor at 45°C; stop session when timer reaches 60 s.
- 3- **2 min irradiation session**: NIR-irradiation of tumor until surface peak temperature reached 45°C (start timer) + cycles of off/on laser irradiation to maintain the tumor at 45°C; stop session when timer reaches 120 s.
- 4- **5 min irradiation session**: NIR-irradiation of tumor until surface peak temperature reached 45°C (start timer) + cycles of off/on laser irradiation to maintain the tumor at 45°C; stop session when timer reaches 300 s.

After irradiation sessions, tumor volumes and body weights were monitored daily. After finding no evidence of pain or distress daily, monitoring frequency was reduced to every 3-5 days. Animals that are in pain or distress, indicated by being recumbent or anorexic, or when tumors were larger than 15 mm were euthanized by CO₂ asphyxiation and bilateral thoracotomy. The experiment was finalized 15 days after PTT when the remaining mice were euthanized.

2.5.9 Long-term survival of combination therapy of anti-PD-1 and PTT at 45°C for 5 min in mice bearing EMT6 and 4T1 tumors

Two similar experiments were performed to analyze the combination therapy of anti-PD-1 and PTT at 45°C for 5 min in mice bearing either EMT6 or 4T1 tumors. Tumor inoculation was performed as before (100 μ L of PBS subcutaneously injected in the fourth mammary fat pad). EMT6 tumor inoculation was achieved with a suspension of 1×10^6 cells, while 4T1 tumors were established with 1×10^5 cells. From experience, the speed of tumor growth is similar for those two tumor models when those numbers are used. Therefore, the same schedule for treatment was used, as seen in **Figure 25**.

In this experiment, tumor-bearing mice were treated with three injections of anti-PD-1 (intraperitoneal injection on days 7, 11, and 15 at 10 mg/kg), and the tumors were treated by 980 nm NIR laser at 1 W/cm² after intratumoral injection of SWCNT-ANXA5 (1.2 mg/kg), following the schedule in **Figure 25**. Mice were assigned to groups (n = 10) as follows:

- 1- Control:** untreated
- 2- Anti-PD-1 + PTT 45°C (0 min):** three injections of anti-PD-1 and NIR-irradiation of tumor until surface peak temperature reached 45°C and stop session immediately.
- 3- Anti-PD-1 + PTT 45°C (5 min):** three injections of anti-PD-1 and NIR-irradiation of tumor until surface peak temperature reached 45°C (start timer) + cycles of off/on laser irradiation to maintain the tumor at 45°C; stop session when timer reaches 300 s.

After irradiation sessions, tumor volumes and body weights were monitored daily. After finding no evidence of pain or distress from day to day, monitoring frequency was reduced to every 3-5 days. Animals that are in pain or distress, indicated by being recumbent or anorexic, or when tumors were larger than 15 mm were euthanized by CO₂ asphyxiation and bilateral thoracotomy. The experiment was finalized 100 days after PTT when the remaining mice were euthanized.

2.5.10 Carbon nanotube biodistribution after intratumoral injection SWCNT-ANXA5

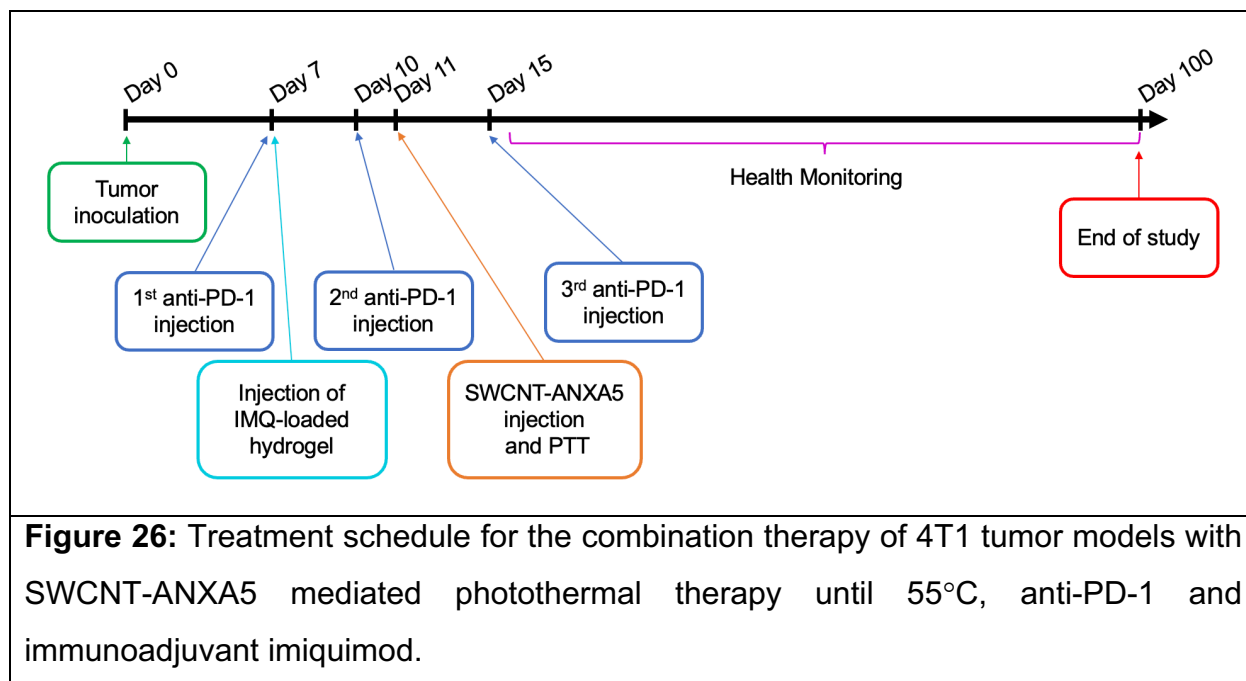
Six-week-old female BALB/cJ (n = 3) were inoculated with EMT6 tumors and were intratumorally injected with SWCNT-ANXA5 (1.2 mg/kg of SWCNT) when the tumors were around 5 mm in diameter (~60 mm³). The tumors were treated by a 980-nm NIR laser at 1 W/cm². Tumors were irradiated until the surface temperature reached 45°C. Mice were euthanized by CO₂ asphyxiation 1, 2, 3, and 4 weeks after PTT. Major organs were harvested and weighed. Organs were frozen and stored in a -80°C freezer.

Tissue lysates for analysis of SWCNT concentration were prepared according to the protocol from Liu *et al.*²⁸⁴. Briefly, after thawing samples, organs were individually ground in a tissue grinder added to lysing buffer composed of 1% SDS, 1% Triton X-100, 10 nM DTT (dithiothreitol), and 40 mM tris-acetate-EDTA buffer to complete volume of 10 ml. Tissue was digested overnight in an incubator at 70°C. Each sample was sonicated for 1 h to resuspend SWCNT from digested tissue. Samples were analyzed using intrinsic SWCNT fluorescence by single excitation fluorescence measurement using an NS MiniTracer (Applied Nanofluorescence, Houston, TX).

2.5.11 Long-term survival of combination therapy of anti-PD-1, immunoadjuvant imiquimod and PTT in 4T1 tumor-bearing mice

Six-week-old female Balb/cJ mice were inoculated with 4T1 mouse mammary tumor cells in the left mammary fat pad. When the tumors reach a size of ~3 mm (day 7), treatment started with intratumoral injection of a hydrogel loaded with IMQ (50 micrograms) and intraperitoneal (i.p.) injection of anti-PD-1 (10 mg/kg). On day 10, the second dose of anti-PD-1 was administered. On day 11, SWCNT-ANXA5-mediated PTT was performed by intratumorally (IT) injecting the conjugate and irradiating the tumor with 980-nm laser with a power density of 1 W/cm² until the tumor surface

temperature reached 55°C. On day 15, mice were again injected intraperitoneally with another dose of anti-PD-1. **Figure 26** shows the treatment schedule.



Mice were assigned to groups (n = 10), as shown:

- 1- **Control** (untreated)
- 2- **Ab**: injections of anti-PD-1 (3x)
- 3- **IMQ**: injection IMQ
- 4- **PTT**: injection of SWCNT-ANXA5 and laser irradiation
- 5- **Ab + IMQ**: injections of anti-PD-1 (3x) + IT injection of IMQ
- 6- **Ab + PTT**: injections of anti-PD-1 (3x) + IT injection of SWCNT-ANXA5 and laser irradiation
- 7- **IMQ + PTT**: injection of IMQ + injection of SWCNT-ANXA5 and laser irradiation
- 8- **Ab + IMQ + PTT**: injections of anti-PD-1 (3x) + injection of IMQ + injection of SWCNT-ANXA5 and laser irradiation

The IMQ-loaded hydrogel was prepared as described by Li *et al.*, 2022²⁸⁵. The hydrogel is composed of the four-arm polyethylene glycol thiol (PEGSH,

95%, MW 5000) and poly (ethylene glycol) diacrylate (PEGDA, MW 700). The gelation occurs due to a Michael addition reaction between PEGSH and PEGDA. For the preparation of 100 μ L hydrogel (12 wt%), 9.375 mg PEGSH and 2.625 mg PEGDA (mass ratio of PEGDA to PEGSH = 0.28 in the hydrogel) were separately dissolved in PBS. IMQ solution in DMSO was added to 50 μ L PEGDA solution (50 mg). Solutions were added to one another, and gelation occurred in 5 min. For mouse injection, solutions were prepared freshly and separately sterilized by filtration with a 0.2 μ m filter. Aliquots of 400 μ L of each solution were mixed in a sterile hood inside the procedure room, where mice were located and injected within 5 min to prevent gelation inside the syringe.

Tumor volumes and survival was monitored for 100 days when the remaining mice were euthanized by CO₂ asphyxiation followed by bilateral thoracotomy. Tumor volumes and body weights were monitored daily after PTT. After finding no evidence of pain or distress daily, monitoring frequency was reduced to every 3 days. Treated or untreated mice in pain or distress, as indicated by being recumbent, were euthanized. Animals that exhibited greater than 20% weight loss from the onset of the study, or for which tumor size surpassed 15 mm in any direction, or that were dehydrated were euthanized.

2.5.12 Immune response mechanistic analysis of combination therapy of anti-PD-1, immunoadjuvant imiquimod and PTT in 4T1 tumor-bearing mice

Six-week-old female Balb/cJ mice were inoculated with 4T1 mouse mammary tumor cells in the left mammary fat pad. Tumors were treated following the same schedule and assigned to the same groups as in the previous section 2.5.11 (see **Figure 26**).

Mice (n = 5) were euthanized 7 days post photothermal therapy to collect blood samples for the analysis of cytokine release. Blood was centrifugated to collect the serum, and enzyme-linked immunosorbent assays (ELISA) were performed to quantify serum levels of proinflammatory cytokines (TNF- α , IL-6, IFN- γ and IL-12 [p70]) following

the protocol from the manufacturer. Standard curves were obtained for each cytokine to quantify the concentration in serum samples.

In another experiment, mice (n = 4) were euthanized by CO₂ asphyxiation 14 days after PTT, and the spleens were harvested for immunophenotypic analysis of splenic cells. Spleens were processed and stained for immunophenotyping by flow cytometry in the same way as described in section 2.5.7.

2.5.13 Statistical Analysis

The statistical significance of *in vitro* studies was assessed using an unpaired t-test with Welch's correction for assumed unequal variances for experiments with only two groups. One-way ANOVA with Dunnett's multiple comparisons was used for tests with more than two groups, comparing treated groups to the control group. The statistical significance of *in vivo* studies was assessed by one-way ANOVA with Dunnett's multiple comparisons comparing treated groups to the control group. In survival experiments with only three groups, one-way ANOVA with Tukey's multiple comparisons comparing every pair of groups was used to assess statistical analysis between tumor volumes. The Mantel-Haenszel log-rank test determined the statistical significance of survival curves by comparing treated groups to the untreated control. All analyses were carried out in GraphPad Prism 8 software.

2.6 Preliminary, *in vitro* and *in vivo* studies with SWCNT-ANXA5 mediated radiofrequency ablation

2.6.1 Analysis of responsiveness to radiofrequency irradiation of (6,5) SWCNT and few walled carbon nanotubes in different surfactants

Suspensions of (6,5) SWCNT and few walled carbon nanotubes (FWCNT, Dr. Resasco's Lab, OU Chemical Engineering) were prepared as before. In brief, 3.0 mg of each CNT was sonicated for 1 h in 6.0 ml of either 1% sodium dodecyl sulfate (SDS) solution or 1% sodium deoxycholate (SDC), yielding a concentration of 500 mg/L. Samples were not centrifuged to avoid mass loss and maintain the suspended concentration. For the radiofrequency irradiation, samples of 1 ml were placed in a 6 ml-cuvette (1 cm × 1 cm × 4.2 cm), creating a 1 cm × 1 cm × 1 cm volume of suspension inside of the vial. Samples were placed in the same room of irradiation 30 min before the experiment to reach thermal equilibrium with the environment. The temperature was measured with a type K thermocouple by inserting the thermocouple junction inside the liquid phase. The temperature was measured immediately before and immediately after irradiation. Samples were placed on top of the lower plate (see **Figure 27**) and were individually irradiated for 60 s with a 13.56 MHz radiofrequency generator and matching network (Comdel System CX-600S ultrastable 13.56 MHz RF generator connected to Comdel MatchPro CPMX-6000 matching network). A radiofrequency field is generated between plates. Different power outputs were tested (100, 200, 300, 400, 500, and 600 W). Samples were tested in triplicate for each testing condition.

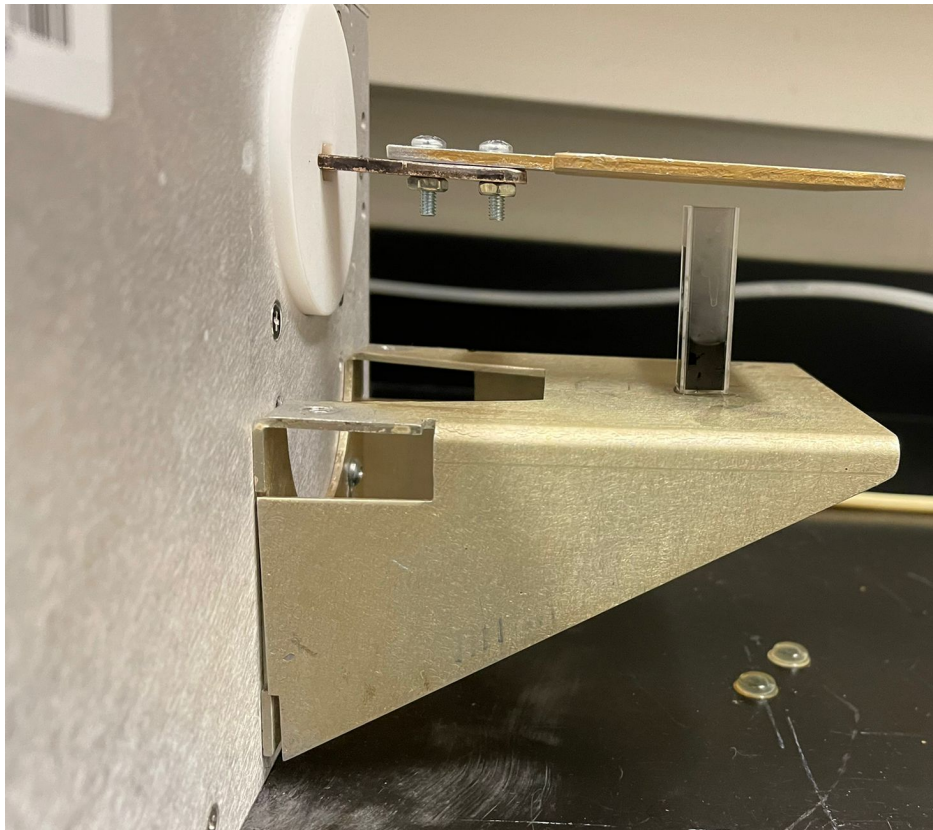
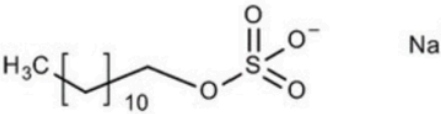
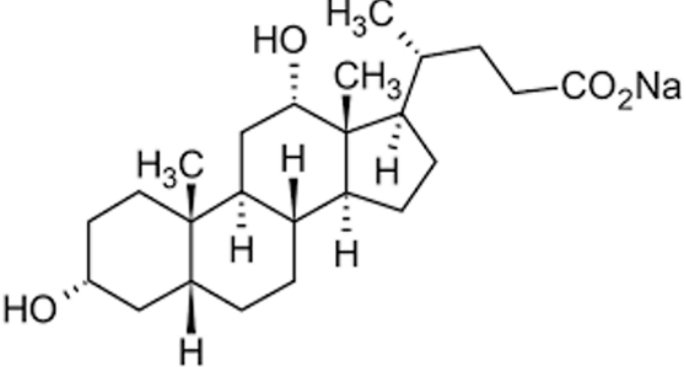
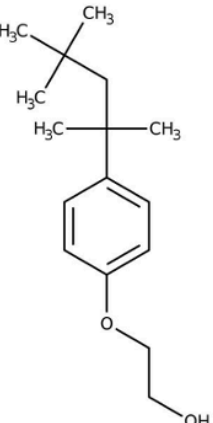
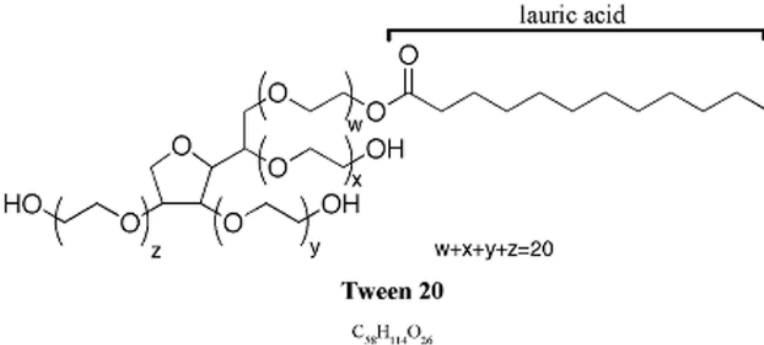


Figure 27: Matching network loading plates.

2.6.2 Assessment of surfactant effect on radiofrequency responsivity of (6,5) SWCNT

The effect of other surfactants was also studied compared to SDS (1%), and SDC (1%). The (6,5) SWCNT was suspended in different surfactants following the previous procedures at a 500 mg/L concentration. TRITON X-100 and TWEEN-20 are both non-anionic surfactants and were used at a concentration of 2%. The structure of the different surfactants is shown in **Table 2**.

Table 2: Chemical structure of the surfactants used for suspending (6,5) SWCNT

SDS	SDC
	
TRITON X-100	TWEEN 20
	 <p style="text-align: center;">Tween 20 $C_{58}H_{114}O_{26}$</p>

2.6.3 Analysis of suspension of SWCNT in solvent ethanol

Instead of using an aqueous environment and surfactants to suspend SWCNT, solvent ethanol was used to analyze if the suspension in solvent improves the responsivity of SWCNT in RF compared to surfactant systems. For that, the responsivity of ethanol was analyzed using 1 ml samples in a cuvette. Then, (6,5) SWCNT were suspended at 500 mg/L in HPLC ethanol by sonication for 1 hour. A 1 ml sample of that suspension was placed in a cuvette and irradiated with a 13.56 MHz RF field.

2.6.4 Analysis of SWCNT-ANXA5 response to radiofrequency irradiation

SWCNT-ANXA5 was produced using protocol from section 2.1.2. The final concentration of SWCNT in the conjugate was 115 mg/L. Samples (1 ml) were placed in 6 ml-cuvette. The temperature was assessed with a type K thermocouple inserted in the liquid phase immediately before and after an irradiation session of 60 s. Samples were placed between loading plates of the Comdel system (13.56 MHz) and irradiated at 300 W power output. Control samples were deionized water (DI water) and phosphate buffered saline (PBS).

2.6.5 Assessment of radiofrequency responsivity of CNT samples with different chiralities

The chirality of CNT determines the properties of carbon nanotubes. For the NIR irradiation, it is known that (6,5) SWCNT is efficient at absorbing that energy and transforming it into heat due to the absorbance spectrum. For RF irradiation, more experiments are necessary to determine which chirality is more responsive for that wavelength. Therefore, an experiment was established to assess chirality's effect on RF responsiveness. CHASM™ provided samples of CNT different chiral enrichments, as shown in **Table 3**.

Table 3: Percentage of each chirality type and length of CNT samples produced by CHASM™. Comparatively, the (6,5) SWCNT used in the PTT project has a length of ~1.5 μm.

Sample Name	% Chiralities				Bundle Length (μm)
	(6,5)	(7,5)	(8,3)	(7,3)	
PXD2-2069	31	15	13	12	0.98
PXD2-2070	25	17	12	11	1.12
PXD2-2071	29	12	13	12	0.96
PXD2-2072	25	23	10	10	0.98

All the sample were suspended at the same concentration of 500 mg/L in SDS 1% by sonication for 1 h. Irradiation was performed in Comdel System following the same procedures in previous section. Maximum power output was used in those experiments (600 W).

2.6.6 Effect of geometry of liquid phase on the responsivity to radiofrequency field

In the previous studies, a 1 ml sample was placed inside a square cuvette. There is evidence in the literature that the geometry of the sample holder affects the heating rate of nanoparticle-mediated radiofrequency ablation²⁸⁶. Therefore, to test that in (6,5) SWCNT suspension, the sample volume was increased to 4.2 ml to fill out the whole cuvette. Therefore, for different samples, deionized water, 1% SDS, (6,5) SWCNT (500 mg/L), and sample PXD2-2069 (500 mg/L) from CHASM™ were tested in RF field at 600 W using both 1 ml and 4.2 ml samples in a cuvette.

2.6.7 Analysis of interface heating and ionization of (6,5) SWCNT in radiofrequency field

Due to the results of high heating of 4.2 ml of (6,5) SWCNT suspensions in a cuvette, allied with the analysis of thermal images of those samples, it was hypothesized that the interphase liquid-air might generate a discontinuity that enhances the effects of the radiofrequency responsivity of the SWCNT suspension, thus having an interfacial response instead of the heating happening in the bulk of suspension. To avoid the impact of the liquid-air interface, commercially available coconut oil was chosen to create another layer of liquid phase on top of the SWCNT aqueous suspension phase. Before that, the heating of the coconut oil was accessed in the 13.56 MHz radiofrequency field to ensure that it would not heat up more efficiently than the SWCNT suspension by placing 1 ml in a cuvette and measuring before and after temperatures with a type K thermocouple.

The explosive response of 4.2 ml samples of SWCNT suspensions in the RF also generated the hypothesis that ionization would happen in the samples. Therefore, a high concentration of sodium chloride (NaCl 6M) was irradiated using the same protocol.

After that, samples of 4 ml of (6,5) SWCNT (500 mg/ml) suspension were placed in a cuvette and covered with 0.2 ml of commercial coconut oil to prevent the effect of the liquid-air interface. Thermal imaging from FLIR E5-XT was used to assess the temperature of samples in different locations of the samples inside the cuvette (liquid-air interface, liquid-liquid interface).

2.6.8 Study of resonant frequency of (6,5) SWCNT in radiofrequency field in 15 W power output regenerator coupled with matching network

In collaboration with Dr. Caleb Fulton (OU Electrical Engineering, Advanced Radar Research Center) and his student Josh Short, an RF device was designed to generate and output an RF field between horizontal plates. This device created RF fields of different frequencies, intending to find the resonance frequency of the (6,5) SWCNT,

which is the frequency in the RF range that the carbon nanotubes would be more responsive to irradiation. Matching conditions in each frequency were measured using a network analyzer. The plate's total power output was estimated to be ~15 W. For the testing in the different frequencies, PEGylated SWCNT was used, which was obtained following the first steps of SWCNT-ANXA5 conjugation. Samples (1 ml) were placed in a cuvette and irradiated for 8 min. The temperature was measured with a type K thermocouple.

2.6.9 Statistical Analysis

Statistical analysis was assessed by unpaired t-test with Welch's correction for assumed different variances in tests with only two groups. One-way ANOVA with Tukey's multiple comparisons test was used in experiments with more than two groups. Analyses were carried out in GraphPad Prism 8 software.

2.7 Gold nanoparticle – annexin A5 – DM1 conjugate

2.7.1 Conjugation

AuNP-ANXA5-DM1 was produced in the lab using modified protocols for conjugation of ANXA5 to DM1, and PEGylation of AuNP followed to linkage to ANXA5-DM1^{287–289}.

First, AuNPs (15 nm) were initially linked to NH₂-PEG-SH at a ratio of 1:4 (w/w) by adding 61.2 mg of HS-PEG-NH₂ in 500 µL of PBS to 1 mg of AuNP in 500 µL of PBS. The reaction was conducted overnight at 4°C with stirring.

Concomitantly, conjugation of ANXA5 to DM1 was performed. Sulfo-SMCC (12 mg) was dissolved in 1000 µL of DI water and added to a high concentration (> 3 mg/ml) of 10 mg of ANXA5 solution. This gives a 100x molar ratio of sulfo-SMCC to ANXA5 and about a 10x molar ratio for the available lysine residues on ANXA5. The

mixture was allowed to react at room temperature for 2 h. After that, DM1 (10.0 mg) was dissolved in 500 μ L of dimethyl sulfoxide (DMSO) and added to ANXA5-SMCC solution; this is a 50x molar ratio to 10 mg of ANXA5. The reaction proceeded overnight at 4°C.

On the next day, cysteine was added to the ANXA5-DM1 conjugate to block unreacted maleimide groups and left for 2 h at 4°C. The conjugate was dialyzed against PBS at pH 7.4 for 4 h at 4 °C with a 12-14 kDa membrane. The Bradford assay was used to determine the final protein concentration. DM1 concentration was determined by reading absorbance at 288 nm of the conjugate and a blank of unconjugated ANXA5 at the same protein concentration and comparing it to a standard curve (see characterization section for more details). After analyzing ANXA5-DM1 conjugation by Bradford for protein concentration and the increased absorbance at 288 nm for DM1 concentration, the DM1/ANXA5 molar ratio was determined. ANXA5-DM1 was also analyzed by SDS-page electrophoresis to confirm conjugation, compared to plain ANXA5.

Parallely, PEGylated AuNPs were washed three times with PBS by centrifugation at 16,000 g for 1 h. Sulfo-SMCC (10 mg) was added to the AuNP-PEG and incubated for 2 h at room temperature with stirring. The AuNP-PEG-SMCC was washed 3 times with PBS by centrifugation at 16,000 g for 1 h. Ten milligrams of ANXA5-DM1 at ~5 mg/ml was added to washed AuNP-PEG-SMCC and incubated overnight at 4°C. The AuNP-ANXA5-DM1 conjugate was purified by three consecutive steps of PBS washing followed by centrifugation (16,00 g for 20 min). The nanoparticle conjugate was quantified via absorbance at 520 nm and a Bradford assay. A scheme of the conjugation is presented in **Figure 28**.

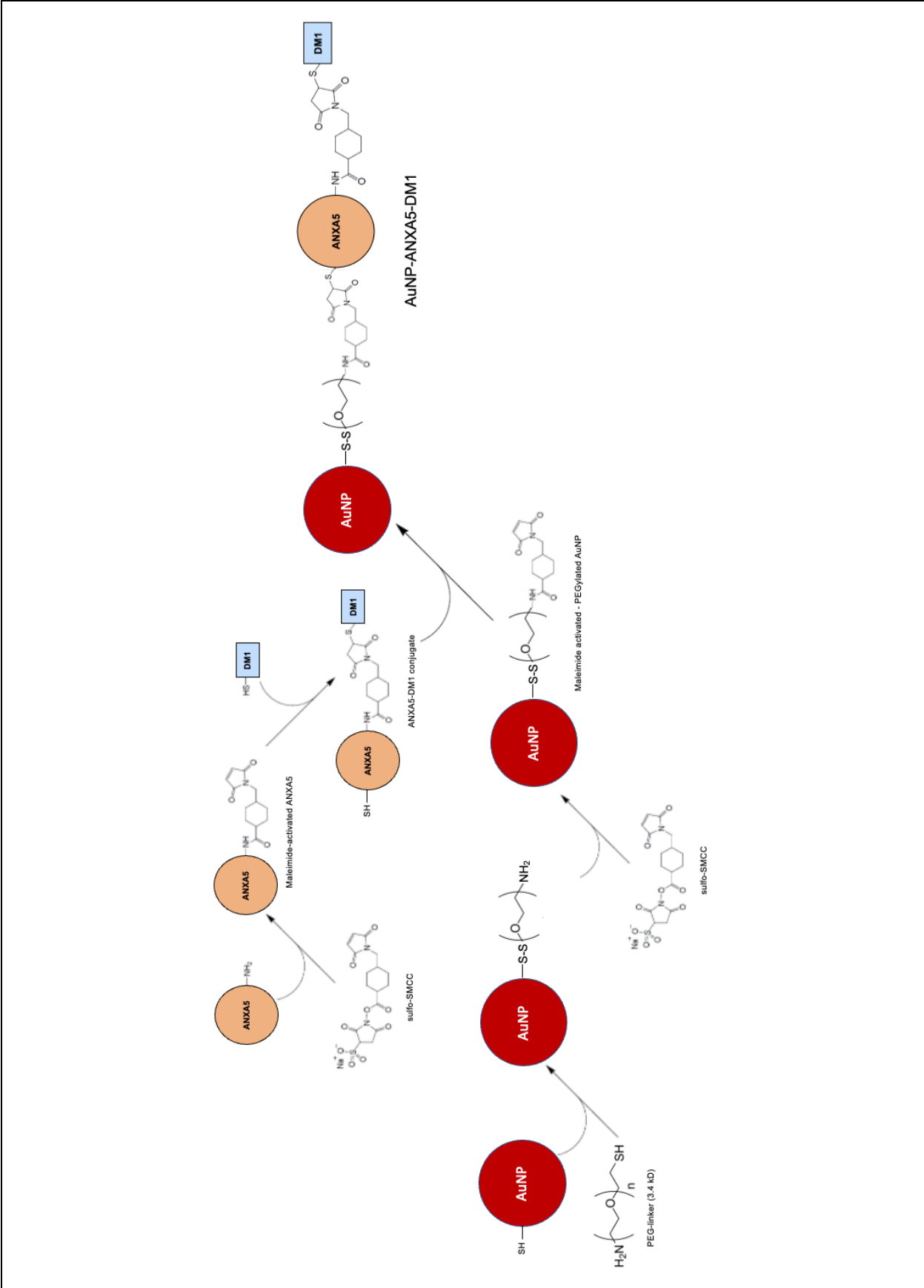


Figure 28: Scheme of AuNP-ANXA5-DM1 conjugation. AuNP were initially PEGylated with linker SH-PEG-NH₂ (3.4 kD) by thiol-thiol addition to form a disulfide bond leaving available amine (NH₂) groups on the nanoparticle. DM1 was conjugated to ANXA5 with linker sulfo-SMCC that activates amines on the protein and links to thiols (SH) on the drug, followed by blocking unreacted maleimide groups with L-cysteine. The available amine groups on AuNP-PEG were then activated with sulfo-SMCC to link to thiol groups in annexin A5 from the ANXA5-DM1 conjugate. For simplification, only one molecule of ANXA5 is shown to be attached to AuNP, and one molecule of DM1 is linked to ANXA5, even though the molar ratios are much greater than that (molar ratios of ~ 1000 for ANXA5/AuNP, and ~9 for DM1/ANXA5).

2.7.2 Characterization

The concentration of DM1 in ANXA5-DM1 conjugate was determined by endpoint absorbance at 288 nm. First, a standard curve of DM1 was obtained by dissolving 3.0 mg of DM1 in 1000 μ L of DMSO. Serial dilutions were performed using DMSO. The standard curve of ANXA5 at 288 nm determined the contribution of ANXA5 to the signal. After the conjugation, ANXA5 concentration was determined by the Bradford assay. Then, that concentration established the contribution of ANXA5 to the 288 nm signal. Then, the conjugate absorbance at 288 nm was read, and the contribution of DM1 to the signal was calculated by subtracting total conjugate absorbance at 288 nm minus the contribution of ANXA5 to the signal and then using the DM1 standard curve to infer the concentration. After obtaining the concentration of both ANXA5 and DM1, the molar ratio of DM1/ANXA5 was determined. This ratio was considered constant after the conjugation to AuNP since measuring the direct concentration of DM1 in the AuNP-ANXA5-DM1 was challenging.

AuNP concentration in AuNP-ANXA5-DM1 was determined by endpoint absorbance at 520 nm and compared to a standard curve. The ANXA5 concentration in the nanoparticle conjugation was determined by a modified Bradford assay, subtracting

the contribution of 5 μ L AuNP at 595 nm in the Bradford reagent. For that, a standard curve of 5 μ L of AuNP in Bradford reagent was also made to determine the contribution of AuNP to the 595 nm signal of the AuNP-ANXA5 in Bradford assay. The concentration of DM1 in AuNP-ANXA5-DM1 was inferred from the ANXA5 concentration in AuNP-ANXA5-DM1 by considering a constant molar ratio between DM1/ANXA5 before and after linkage to AuNP.

Agarose gel electrophoresis was performed to prove conjugation of ANXA5-DM1 to AuNP. Gel was casted in TAE buffer with 1% agarose. Samples were loaded into well using 10 μ L of 2 mg/ml of AuNP. Samples were run in horizontal electrophoresis chamber at 80 V for 10 min.

2.7.3 *In vitro* studies

To analyze the *in vitro* toxicity of AuNP-ANXA5-DM1 compared to ANXA5-DM1 and unconjugated DM1, the EMT6 cell line was used using the same culturing procedures given in session 2.3. After culturing cells in T-75 flasks, EMT6 cells were seeded at a density of 10,000 cells per well and incubated for 24 h to allow the cells to return to a proliferative state. The medium was aspirated and replaced with treated media in quintuplicate groups with eight concentrations of AuNP-ANXA5-DM1, ANXA5-DM1 and unconjugated DM1. Medium was also enriched with 2 mM of Ca²⁺. A control plate with untreated cell controls, and no-cell blanks was also prepared. The control and treated plates were incubated for 72 h at 37°C and 5% CO₂.

After incubation, the treatment media was aspirated, and fresh media enriched with 10% Alamar Blue reagent was added in each well. The plates were incubated with alamar blue for 2 hours at 37°C and 5% CO₂ and analyzed in a plate reader using fluorescence with 530 nm excitation and 590 nm emission. The viability was determined by subtracting the no-cell blank from the untreated cell control and treated experimental plates and then dividing the average fluorescence of the treated experimental groups by the average of the untreated cell control.

CHAPTER 3 – RESULTS AND DISCUSSION

3.1 *In vitro* studies with SWCNT-ANXA5-mediated PTT

Recombinant annexin A5 was successfully produced in *E. coli* and purified by affinity chromatography. Conjugation of SWCNT to ANXA5 was performed using DSPE-PEG-mal (3.4 kDa). After purification, the mass ratio of ANXA5 to SWCNT in conjugate was determined by spectrophotometry. The ANXA5 concentration was determined by Bradford assay and compared to bovine serum albumin (BSA) protein standard curve. As a control, the absorbance of PEGylated SWCNT (addition of the linker to suspended SWCNT and 8 h dialysis against deionized water) at 595 nm was measured and has shown minimal absorption due to the lack of protein. The concentration of SWCNT was determined by measuring the endpoint absorbance at 800 nm and compared to the standard curve. After measurement analyzing 800 nm absorbance of ANXA5, it was seen no significant absorbance at that wavelength. The average annexin V / SWCNT ratio of the different batches of conjugates used for the *in vitro* experiments presented in this dissertation was 28.7 (with a minimum ratio of 22.1 and a maximum ratio of 35.4). It is relevant to highlight that the mass ratio ANXA5/SWCNT is correlated to the concentration of ANXA5 solution added during the conjugation. Therefore, using protein concentrators is crucial to obtain ANXA5 solutions of concentrations around 5 mg/ml.

The photosensitizer abilities of SWCNT-ANXA5 (100 mg/L of SWCNT) were assessed by NIR laser irradiation at 980 nm and 1 W/cm² at different times. PBS and Waymouth's media were also irradiated with the laser during the same durations as the control groups. The final temperature of the tested suspensions and solutions were measured at the end of the NIR irradiation and are shown in **Figure 29**:

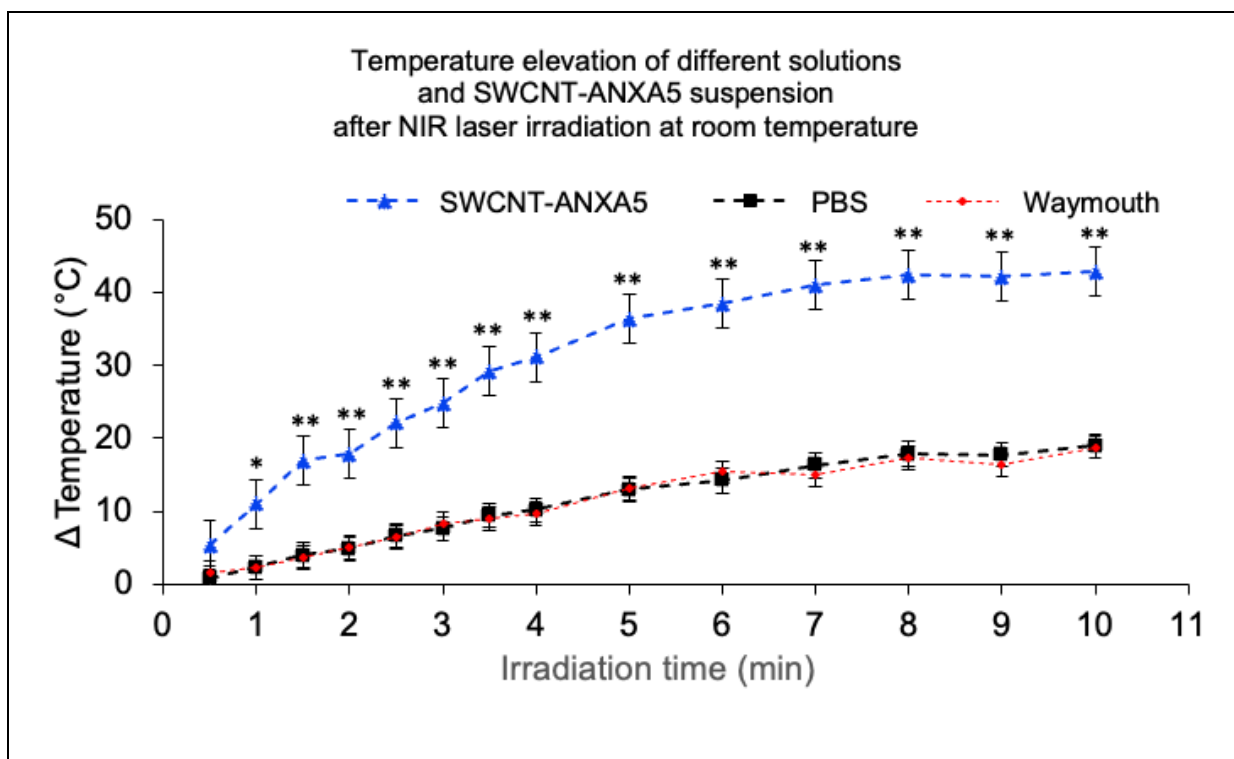


Figure 29: Temperature elevation of different solutions and SWCNT-ANXA5 conjugate suspension after NIR laser irradiation at room temperature. The graph shows the increase in temperature (°C) of 1 mL of conjugate (100 mg/L of SWCNT), PBS, or Waymouth medium as a function of irradiation time (min). The laser wavelength was 980 nm, and the power density was 1.5 W/cm². One-way ANOVA with Dunnett's multiple comparisons was carried out on the GraphPad Prism 8. (n = 2, *p < 0.05 and **p < 0.01).

The SWCNT-ANXA5 had a significantly higher temperature elevation compared to controls PBS and Waymouth medium. After 8 minutes of irradiation, temperature elevation reached a plateau at $\Delta T = 42.5^{\circ}\text{C}$ on average, whereas PBS and Waymouth media reached a plateau at $\Delta T = 17.8^{\circ}\text{C}$. The plateau is accredited to heat transfer from the vial to the surroundings since no insulation was applied to the flasks. Although these data suggest that the laser alone induces a temperature elevation in control samples that resemble body fluids, the temperature elevation is significantly higher when SWCNT-ANXA5 is present. Indeed, previous studies in this lab have shown a temperature increase of tumors when irradiated with the 980 nm laser in the absence

of SWCNT-ANXA5 of around 18°C during laser irradiation of 175 s at 1 W/cm². Nonetheless, the increase was approximately 36°C for the same laser treatment when in the presence of SWCNT-ANXA5 by intravenous injection in mice²⁸³. These results suggest that the conjugate generates a more significant temperature elevation than physiologically resembling liquids.

Furthermore, *in vitro* studies were performed to confirm this concept and its application to PTT. EMT6 cells were grown in 24-well plates and irradiated with a 980-nm laser at 1 W/cm² at different times. Before the NIR irradiation, the cells were incubated with the SWCNT-ANXA5 for 2 h in an incubator at 37°C to allow the conjugate to bind to the cells and washed four times with PBS to remove excess conjugate. As a control, EMT6 cells that were incubated with conjugate were also irradiated. The plates were left at room temperature for around 10 minutes to achieve thermal equilibrium with the environment. Therefore, in this experiment, the cells' initial temperature was room temperature. At the end of the NIR irradiation, an Alamar Blue Assay was performed to determine the viability of the EMT6 cells, and the results are shown in **Figure 30**:

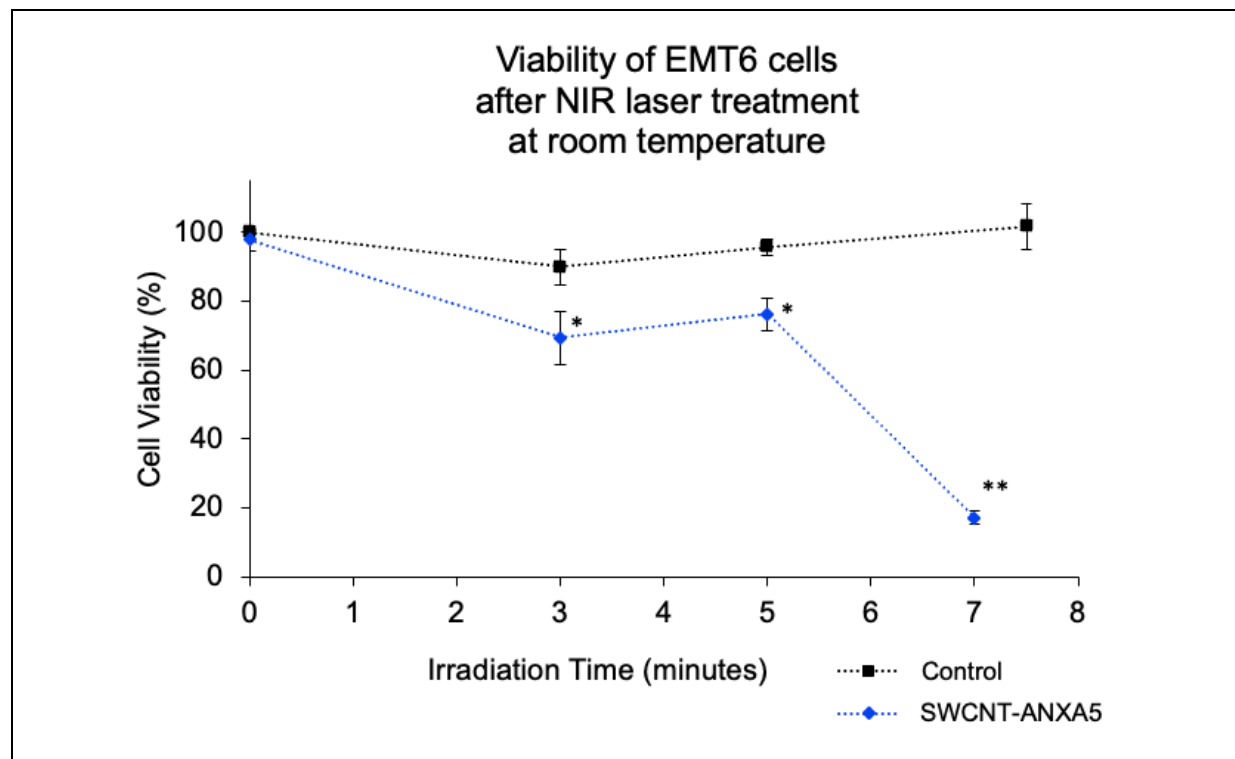


Figure 30: Cell viability of EMT6 cells after NIR laser at treatment room temperature. Relative cell viability of EMT6 cells incubated for 2 hours with the SWCNT-ANXA5 (blue) or not incubated with it as a control (black) prior to laser irradiation. After incubation with the conjugate, the cells were washed four times with PBS. The laser wavelength was 980 nm, and the power density was 1.0 W/cm². Statistical analysis: unpaired t-test with Welch's correction for assumed unequal variances was carried out on the GraphPad Prism 8. (n = 2-3, *p < 0.05 and **p < 0.01).

The NIR-laser treatment at room temperature induced a significant decrease in cell viability after 3 min of irradiation when the cells were previously incubated with SWCNT-ANXA5. The same decline was not observed in the control consisting of EMT6 cells irradiated with the laser in the absence of the conjugate, even in higher irradiation times. After 7 minutes of irradiation, the SWCNT-ANXA5 group had an average viability of 17%. In this experiment, the treatment at room temperature lead to a decrease in the cell viability of the cancer cells exposed to the conjugate. In contrast, the laser alone did not affect cell viability.

Figure 31 shows a similar experiment following the same procedures as the previous one. Nonetheless, the final temperature at the bottom of the well plate was measured using a type J thermocouple instead of measuring cell viability at room temperature. Those experiments were performed separately because the temperature assessment after irradiation by the immersion of a thermocouple disrupts the aseptic conditions of the cell culture, precluding valid cell viability measurements. The temperature rises resulting from the PTT are shown in **Figure 31**:

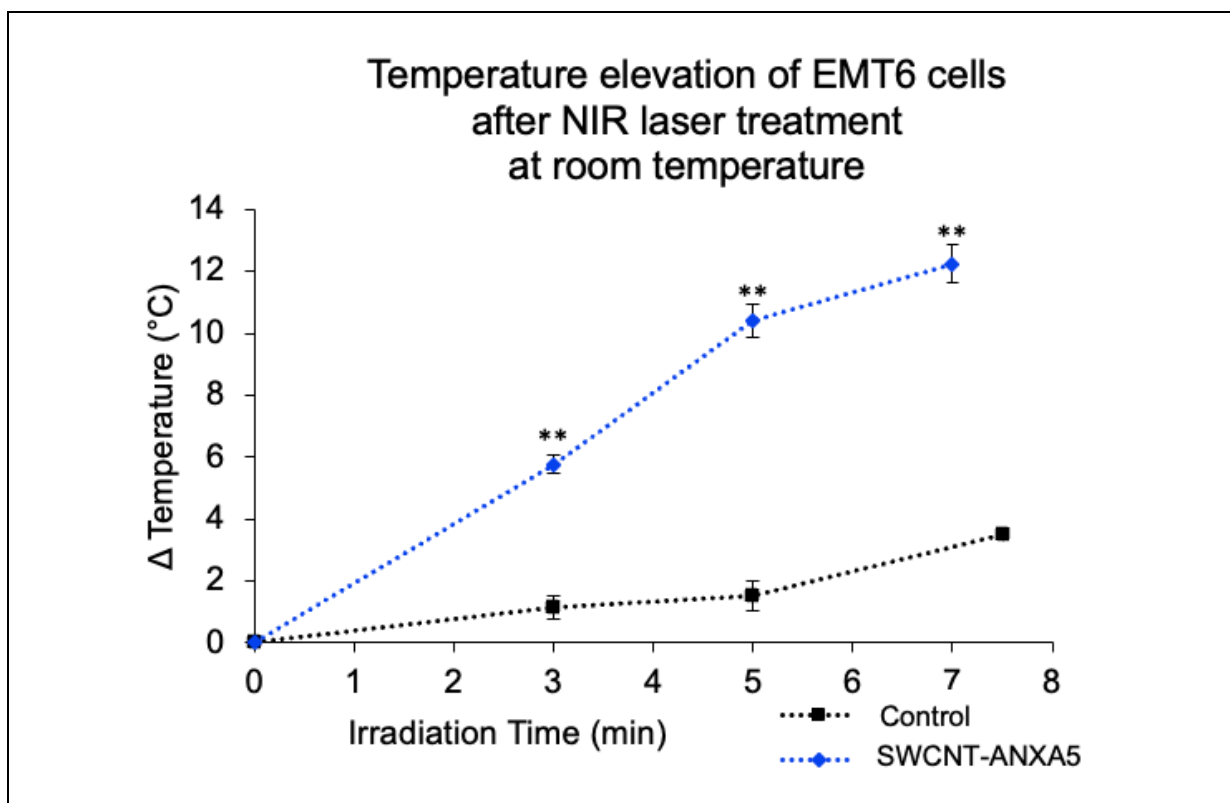


Figure 31: Temperature elevation of EMT6 cells after NIR laser treatment at room temperature. The graph shows the temperature elevation (°C) of EMT6 cells incubated for 2 h with the SWCNT-ANXA5 (blue) or not incubated with it as a control (black) before laser irradiation. After incubation with the conjugate, the cells were washed four times with PBS. The laser wavelength was 980 nm, and the power density was 1.0 W/cm². Statistical analysis: unpaired t-test with Welch’s correction for assumed unequal variances was carried out on the GraphPad Prism 8. (n = 2-3, *p<0.05 and **p<0.01).

EMT6 cells treated with the combination of SWCNT-ANXA5 and PTT showed an increased temperature elevation compared to the control treated with laser irradiation alone. These results suggest that the laser alone does not induce a substantial temperature rise and that combining laser and conjugate is necessary to induce significant heating.

By comparing the results from **Figure 30** and **Figure 31** and assuming a conservative room temperature of 21°C, the higher macroscale temperature reached in

those experiments was around 32°C, which induced cell death in 83% of cells. *In vivo*, tissue damage is believed to occur in temperatures superior to 41°C¹⁸⁴. This discrepancy might be related to the ability of SWCNT to induce a local nanoscale temperature rise, which cannot be assessed by the temperature measurement method used (type J thermocouple). It is hypothesized that the microscale temperature around the cells is much higher than the macroscale temperature assessed by the type J thermocouple in this experiment.

The previous *in vitro* experiments were performed at room temperature. Those results give insights into the effect of an SWCNT-ANXA5-mediated PTT using EMT6 cells, a TNBC model. However, one could argue that EMT6 cells may not react the same at room temperature as at 37°C, especially considering the ablation temperatures in natural physiological conditions of 41°C¹⁸⁴. Therefore, another experiment was performed following the same procedures but carried out at 37°C in an incubator to assess cell viability. Additionally, another control was added to the experiment, consisting of EMT6 cells that were incubated for 2 h with PEGylated SWCNT (following the steps of SWCNT-ANXA5 conjugation but skipping the addition of ANXA5 to it). The results from this experiment are shown in **Figure 32**:

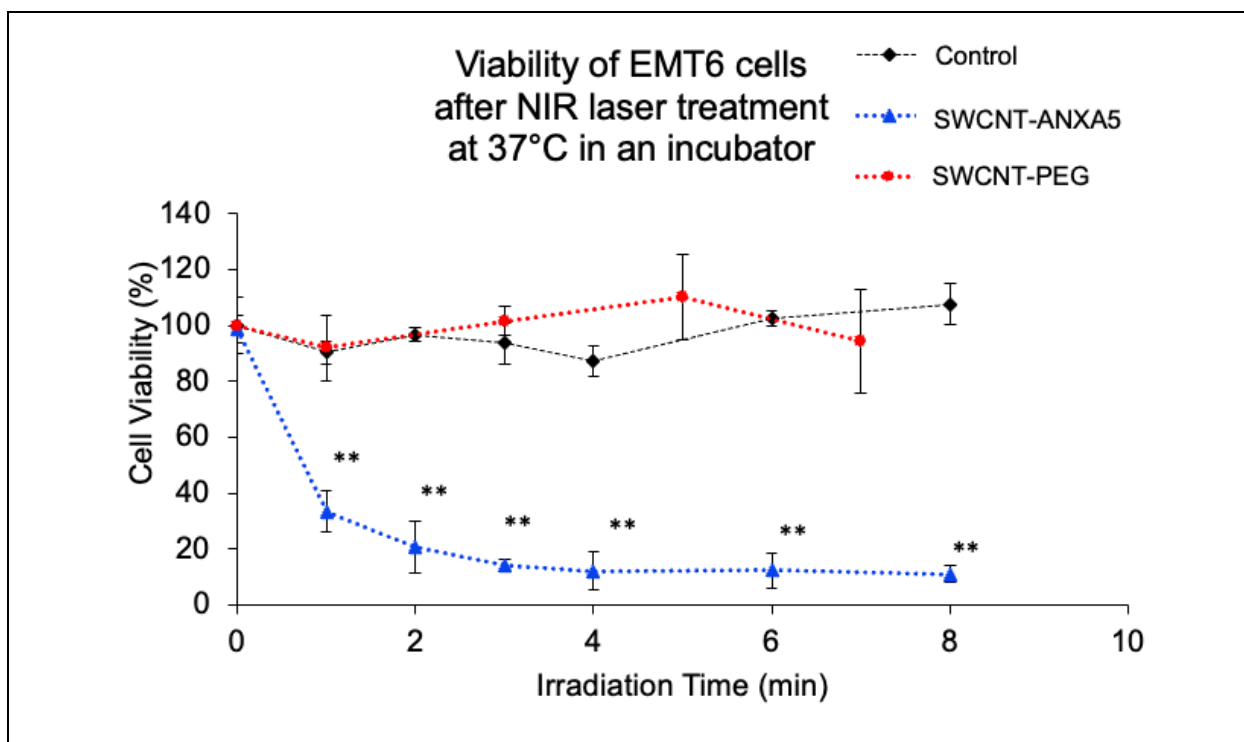


Figure 32: Viability of EMT6 cells after NIR laser treatment at 37°C in an incubator.

The graph shows the relative cell viability of EMT6 cells incubated for 2 h with the SWCNT-ANXA5 (blue), incubated with PEGylated SWCNT (red), or not incubated with conjugate as a control (black), before laser irradiation. After incubation, the cells were washed four times with PBS. The laser wavelength was 980 nm, and the power density was 1.0 W/cm². One-way ANOVA with Dunnett's multiple comparisons comparing treated groups with control group was carried out on the GraphPad Prism 8. (n = 3, *p<0.05 and **p<0.01).

Figure 32 shows that EMT6 cells treated with SWCNT-ANXA5-mediated PTT had a significant cell viability decrease after 1 minute of irradiation. The cell viability drop reached a relative plateau after 3 min of laser irradiation at 14% cell viability on average. This result suggests that the optimal time of irradiation to treat EMT6 cells at 37°C is between 2 and 3 min of laser irradiation.

Comparatively, cells treated with laser alone or SWCNT-PEG-mediate PTT did not result in a significant cell viability drop even after 7 minutes of laser irradiation. These results suggest that ANXA5 is necessary for the SWCNT to bind to the cells since untargeted SWCNT-PEG has been washed away from the wells after four washing steps,

and only the targeted conjugate induces a photothermal effect after laser irradiation *in vitro* at 37°C.

Studies have shown that non-targeted CNT complexes can promote cell uptake and cell death when laser treatment is applied to cell culture in the presence of nanotubes. Nonetheless, the internalization of non-targeted CNT seems to be slower, requiring much more than the two-hour incubation time used in the previous experiment²⁹⁰⁻²⁹². Fisher *et al.*²⁹⁰ showed through two methods the internalization of MWCNT dispersed in Pluronic F-127 (PL-127) after different time-length incubations of 16, 24, and 48 h. RENCA cells were incubated with the CNTs for 24 h, and then DAPI-staining was performed in nuclei. The overlay of the brightfield images displayed CNT as black clusters around the nucleus. Additionally, transmission electron microscopy (TEM) was performed on cells with different CNT incubation times, showing the MWCNT inside cell vacuoles. The irradiation treatment of 15.3 W/cm² for 5 min (1046 nm) significantly reduced the cell viability compared to control groups. Biris *et al.*²⁹² analyzed the internalization of non-targeted MWCNT in HeLa cells DAPI-stained nuclei. Black clusters of MWCNT inside the cells could be visualized through optical microscopy after 48h incubation. Cell death was significantly higher when the cells were treated with MWCNT (48h incubation) and laser irradiation (1064 nm, ~31 W/cm², 4 s) compared with cells with no treatment and cells solely treated with laser. In our studies, the incubation time of both SWCNT-ANXA5 and SWCNT-PEG was only 2 h, which is much shorter than on those other studies. This is evidence that linking ANXA5 to the photosensitizer results in more targeted treatment of the cells.

Different pathways have been analyzed to explain the internalization of CNT without targeting agents, which includes phagocytosis, diffusion, and endocytosis. The degree of dispersion, functionalization, and length of the carbon nanotubes can influence the pathways for cellular uptake²⁹³. Nonetheless, there is evidence in the literature that ANXA5 induces internalization through non-receptor mediated mechanisms²⁹⁴, which might be translated to the SWCNT-ANXA5 and explain the much more effective cytotoxic effect of the PTT *in vitro*. Our lab has gathered evidence of SWCNT-ANXA5 binding to cancer cells, but more experiments need to be performed to prove the internalization of the conjugate.

Another experiment was performed to verify that the conjugate does not affect healthy cells due to the lack of PS externalization. Human umbilical vein endothelial cells (HUVEC) are a healthy cell line that do not express PS in physiological conditions²⁹⁵. When cultured *in vitro*, those cells must grow to complete confluency. Therefore, HUVEC were seeded in 24 wells plates and cultured until 100% confluency. As in previous studies with EMT6 tumor cells, one group was incubated with SWCNT-ANXA5 for 2 h following washing steps, while another group was not incubated with the conjugate. The cells were treated with laser irradiation (980 nm, 1.0 W/cm²) at 37°C inside the incubator. The results are shown in **Figure 33**:

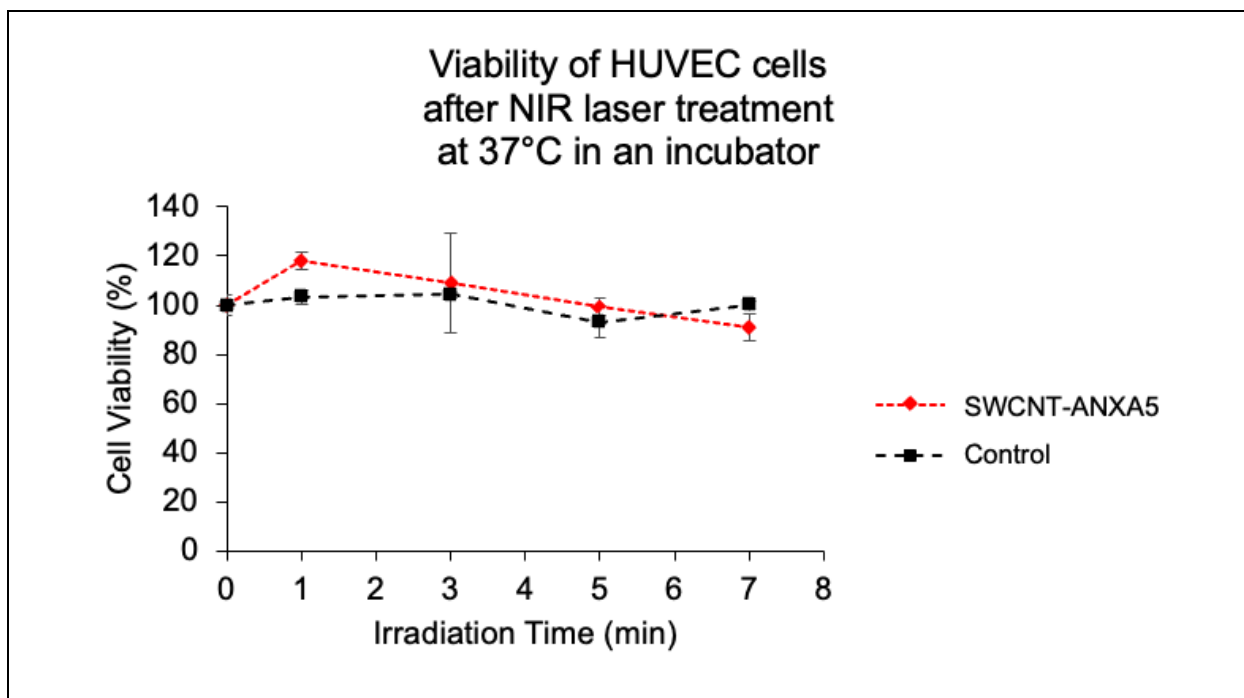


Figure 33: Viability of HUVEC cells after NIR laser treatment at 37°C in an incubator. The graph shows the temperature elevation (in °C) of HUVEC cells incubated for 2 h with the conjugate (in orange) or incubated with VCBM medium as a control (in blue) before laser irradiation. After incubation with the conjugate, the cells were washed four times with PBS. The laser wavelength was 980 nm, and the power density was 1.0 W/cm². Statistical analysis: unpaired t-test with Welch's correction for assumed unequal variances was carried out on the GraphPad Prism 8. (n = 3, *p < 0.05 and **p < 0.01).

Figure 33 shows that even after 7 min of treatment, corresponding to a power density of 420 J/cm^2 , neither SWCNT-ANXA5 nor the control group had a significant cell viability decrease. These results suggest that for the 2 h incubation times the SWCNT-ANXA5 did not bind confluent healthy endothelial cells and, therefore, was washed away during washing steps, resulting in an ineffective PTT. Comparing the results of healthy cells to the ones gathered from PS-expressing EMT6 tumor cells demonstrates the targeting capabilities of ANXA5 to PS-expressing cells.

It has been reported that CNT conjugated to targeting agents can induce cell uptake and enhance the performance of PTT^{296–302}. Shao *et al.*²⁹⁷ studied the internalization and PTT efficiency of MCF7 cells when they were incubated with different SWCNT complexes that had or did not have targeting agents. PEGylated-SWCNT (SWCNT-PEG) were treated with Alexa Fluor 488 (green fluorescence), and after 30 min of incubation on cells, confocal microscopy did not show the internalization of the SWCNT complex. When the SWCNT was conjugated with anti-IGF1R (SWCNT-PEG-anti-IGF1R) and the fluorescent dye, the green fluorescence could be found inside the cell after 30 min of incubation. Furthermore, the PTT efficiency related to the presence or absence of a targeting agent was assessed through optical microscopy. MCF7 cells, previously incubated with SWCNT-PEG and SWCNT-PEG-anti-IGF1R, were subject to NIR laser treatment (808 nm, 800 mW/cm^2 , 3 min). Trypan Blue staining showed that only the cells incubated with targeted SWCNT complex presented blue color, indicating cell death. Despite the lack of quantitative analysis, the experiment's reproducibility was assessed.

Xiao *et al.*²⁹⁶ quantified the efficiency of the PTT allied to targeted and nontargeted SWCNT complexes. SWCNT was conjugated to anti-HER2 IgY. SK-BR-3 cells expressing HER2 receptors were incubated with suspended SWCNT and antibody-functionalized SWCNT for 24 h, followed by NIR irradiation with an 808 nm laser at 5 W/cm^2 for 2 min. Similarly, MCF7 cells, which do not express HER2 receptor, were also incubated with SWCNT-PEG-anti-IGF1R for 24h and subjected to NIR irradiation. Only SK-BR-3 incubated with the targeted SWCNT had statistically significant cell death evaluated by calcein AM/EthD-1 fluorescence staining, evidencing the selectiveness of the targeted CNT complex.

Marches *et al.*²⁹⁹ also studied the improvement in efficiency when targeted CNTs are internalized in cells for PTT. They conjugated SWCNT to two different antibodies: IgG1 anti-Her2 (HER50) as active targeting and anti-human CD22 (RFB4) as the negative control. BT-474 breast cancer cells positive for HER2 receptor were then incubated with both conjugates for a different amount of time and subsequently subject to 808 nm-laser treatment (4 min at 9.5 W/cm²). Quantitative analysis showed that only SWCNT-HER50 conjugate induced statistically significant cell death for incubation times of 30 min, 2 h, 24 h, and 48 h. SWCNT-RFB4 did not promote considerable cell death compared to the negative control.

In conclusion, there is evidence that using targeting agents improves the efficiency of CNT-mediated PTT. In our studies, the use of ANXA5 as a targeting agent is promising due to its potential application in many types of tumors beyond the breast cancer models that are the scope of this dissertation.

In vitro studies provide essential data on individual steps in mechanistic processes in cancer development and therapeutics. Nevertheless, *in vivo* studies are necessary to excel in modeling physiological interactions and tumor microenvironment complexity, including stroma, endothelium, angiogenesis, immunity interactions, and other processes. Another critical factor that can only be analyzed *in vivo* is metastasis, which is the cause of 90% of the deaths related to cancer³⁰³. Therefore, the following section presents the results from *in vivo* studies using SWCNT-ANXA5 mediated PTT to treat triple-negative breast cancer models in mice.

3.2 *In vivo* studies with SWCNT-ANXA5-mediated PTT

3.2.1 EMT6 tumor model treated with SWCNT-ANXA5 mediated PTT

Previous work in our lab was done by treating female BALB/cJ mice bearing EMT6 tumors with combination therapy of SWCNT-ANXA5 mediated photothermal therapy and checkpoint inhibition with anti-CTLA-4. The treatment consisted of three injections of anti-CTLA-4, an intravenous injection of SWCNT-ANXA5, and 980 nm-laser treatment at 1 W/cm² for 175 s. The complete treatment group had a 55% survival at 100 days after tumor inoculation. Nevertheless, anti-CTLA-4 alone and PTT alone increase survival compared to untreated control, but all the mice died before 100 days²⁸³. To study the mechanism of immune system activation for treatment, serum levels of TNF- α , IL-6, IFN- γ and IL-12 (p70) were quantified following procedures described in section 2.5.3. **Figure 34** shows TNF- α , IL-6, and IFN- γ levels for each group (levels of IL-12 (p70) weren't statistically significantly different between samples, so the results are in Appendix A - **Figure 71**).

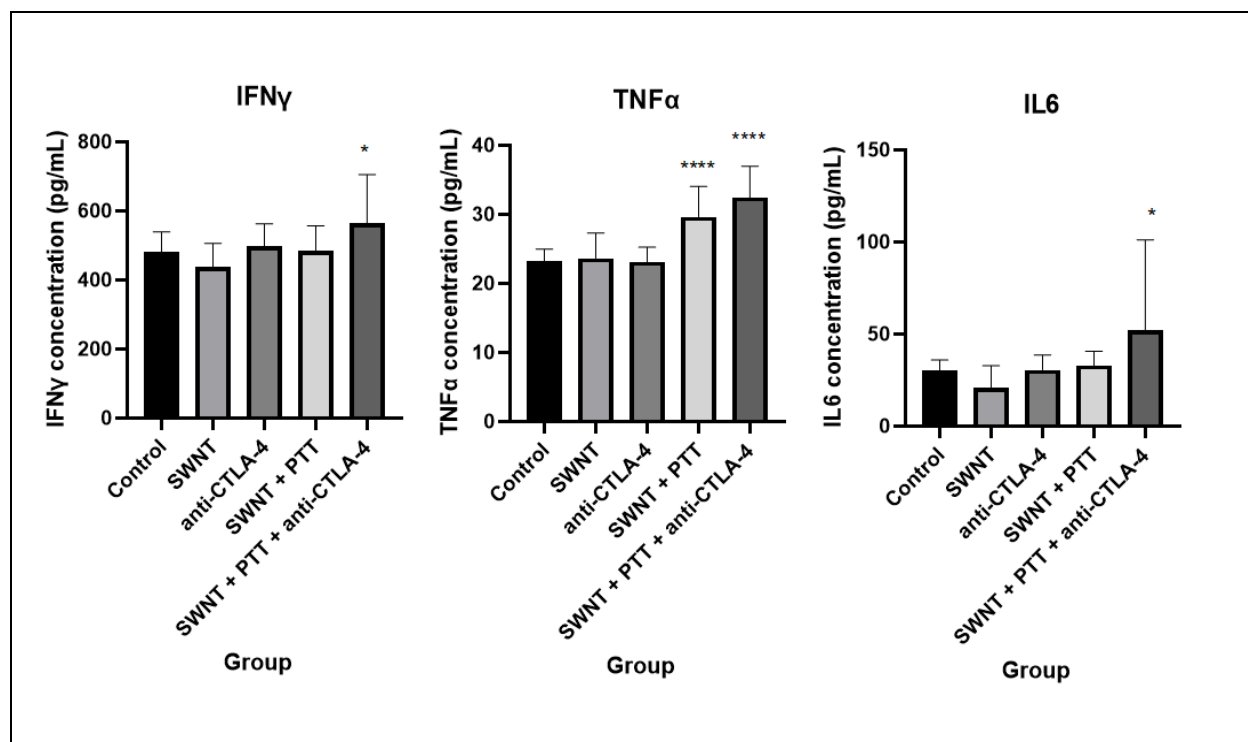


Figure 34: Cytokine concentrations in serum 7 days after PTT in mice treated with combination therapy of SWCNT-ANXA5 mediated PTT and anti-CTLA-4: The diagram shows the level of TNF- α , IL-6, IFN- γ in the serum of mice treated with IV injections of the conjugate, anti-CTLA-4 injection alone, IV injections of conjugate combined with PTT, IV injections of conjugate combined with PTT and anti-CTLA4 injection, or untreated mice as a control. The laser wavelength was 980 nm, and the power density was 1.0 W/cm² for 175 s. Blood samples were collected 7 days after photothermal therapy. Data are presented as mean \pm SE (n = 4–5). For each treatment compared to the control, one-way ANOVA and Dunnett’s multiple comparisons were carried out on the GraphPad Prism 8. (*p < 0.05, and ****p < 0.0001)

Mice treated with anti-CTLA-4 alone or intravenous injection of SWCNT-ANXA5 alone did not significantly increase proinflammatory cytokines in the serum compared to the untreated control. The combination of SWCNT-ANXA5 mediated photothermal therapy and anti-CTLA-4 injections resulted in significantly increased serum levels of TNF- α , IL-6, IFN- γ compared to the untreated control, while mice treated with the combination of SWCNT-ANXA5 + PTT only increased serum levels of TNF- α .

compared to the control group. IFN- γ is known for playing a pivotal role in tumor surveillance, TNF- α is a tumor-associated macrophage activator, and IL-6 enhances lymphocyte and macrophage proliferation. Therefore, the increased levels of those cytokines strengthen the hypothesis that the combination therapy generates a systemic antitumoral immune response.

The published results were encouraging, but we wanted to improve the treatment method and apply the combination therapy to more challenging tumor models. First, we compared the immune system stimulation generated by intratumoral (IT) and intravenous (IV) injection of SWCNT-ANXA5 by measuring the TNF- α levels in serum one day after PTT. After either the IV or IT injection of SWCNT-ANXA5, female BALB/cJ mice bearing EMT6 tumors were treated by a 980-nm NIR laser at 1 W/cm² for 175 s. Blood samples were collected 1 day after irradiation, and levels of TNF- α in the serum were quantified by ELISA. The results are shown in **Figure 35**.

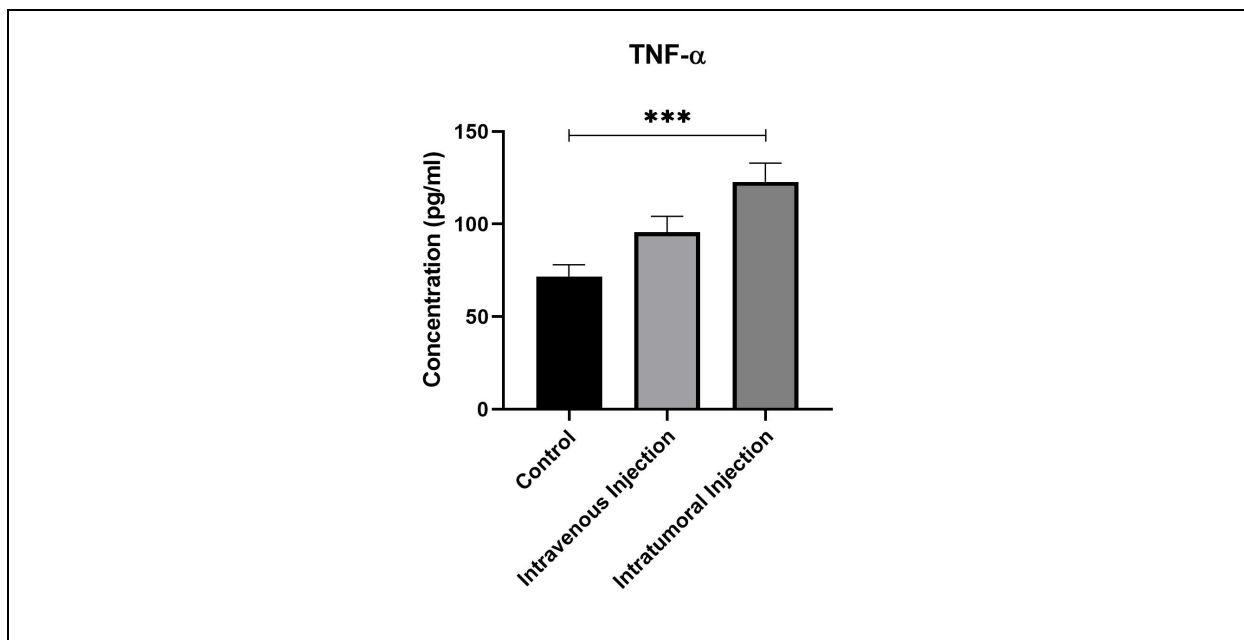


Figure 35: TNF- α concentrations in serum 24 hours after PTT in mice treated with IV injection or IT injection of SWCNT-ANXA5. Mice were treated with a 980 nm laser at a power density of 1.0 W/cm² for 175 s after injection of SWCNT-ANXA5 conjugate intravenously or intratumorally. Blood samples were collected 1 day after PTT, and the levels of TNF- α in the serum were analyzed by ELISA compared to untreated control

(no injection, no PTT). Data are presented as mean \pm SE (n = 4–5). Statistical significance was analyzed for the treated groups compared to the untreated control group by one-way ANOVA with Dunnett's multiple comparisons test. Statistical significance is indicated by ***p < 0.001

In **Figure 35**, mice treated with intratumoral injections of SWCNT-ANXA5 presented significantly increased serum levels of TNF- α (***p < 0.001). In contrast, an intravenous injection was not efficient inducing an increase in the cytokine level compared to the untreated control. This is evidence that the intratumorally injected SWCNT-ANXA5 mediated PTT is more efficient in generating an immune response. Therefore, the subsequent experiments were conducted using intratumoral injection (IT).

One can argue that the clinical relevance of intratumoral injection is questionable. This injection method in clinics would require an imaging-guided technique associated with treating non-superficial tumors. Additionally, some tumor types are inherently non-detectable to most common imaging techniques, which would further limit the applicability of this method. Nonetheless, the current clinical trials involving the ablation of solid tumors already rely on imaged-guided ablation. Therefore, adding one step that uses imaging techniques for the entire PTT procedure would not require a substantial increase in the effort to treat the tumors. Additionally, using the intratumoral injection of SWCNT might prevent the systemic delivery of those particles, ultimately avoiding to accumulation in major organs and lingering clearance. The biodistribution of SWCNT-ANXA5 after intratumoral injection will be discussed later in this work.

Various studies have shown efficient tumor ablation when the conjugates are injected directly inside the tumor and laser irradiation is applied^{207,209,304–312}. Huang *et al.*³⁰⁷ studied the photothermal therapy efficiency on orthotopic squamous cell carcinoma in mice. Tumor-bearing mice were intratumorally injected with different doses of covalently PEGylated SWCNT and subjected to 785 nm laser treatment at different energy density dosages. For each combination of SWCNT and energy dosages, the superficial temperature of the tumors was measured. Additionally, tumor volumes were recorded 11 days after treatment, and survival curves were reported for 45 days. Results showed that the highest dosage of MWCNT and power density (1 mg/ml and 200 W/cm²

for 10 min) caused an increase of 56°C on the surface of the tumor, total tumor regression for 11 days and 62.5% survival for 45 days (n = 8). Zhou *et al.*³⁰⁹ studied the therapeutic effects of PEGylated SWCNTs combined with laser irradiation *in vivo*. Mice that bore non-orthotopic breast cancer models were injected intratumorally with 1 mg/kg and irradiated with a 980 nm laser (1 W/cm², 10 min). The tumor surface temperature reached 76°C after 5 min of irradiation. Tumor volume assessment showed complete tumor regression for the SWCNT+laser treatment group for 30 days and 75% survival for 100 days.

It can be noted that the temperatures obtained in those experiments were extreme, with reports of temperatures of 76°C. Those extreme temperatures are very efficient at ablating solid tumors due to the induction of instantaneous cell death¹⁸⁷. Nonetheless, concerns about the safety of procedures that involve such high temperatures should be addressed. Therefore, in the next experiment, we analyzed the immune activation of PTT by reaching various endpoint tumor surface temperatures. For that, mice were injected intratumorally with SWCNT-ANXA5 and treated with PTT at 1 W/cm². The tumor surface temperature was monitored during the irradiation by a thermal camera. Irradiation ceased immediately after the tumor surface reached the temperature assigned to the groups of 45, 50, 55, or 60°C. The concentration of four cytokines (TNF- α , IL-6, IFN- γ and IL-12 p70) was measured in the serum 1 and 7 days after PTT. The statistically significant results are shown in **Figure 36** (results that were not statistically significant are available in Appendix A – **Figure 72**).

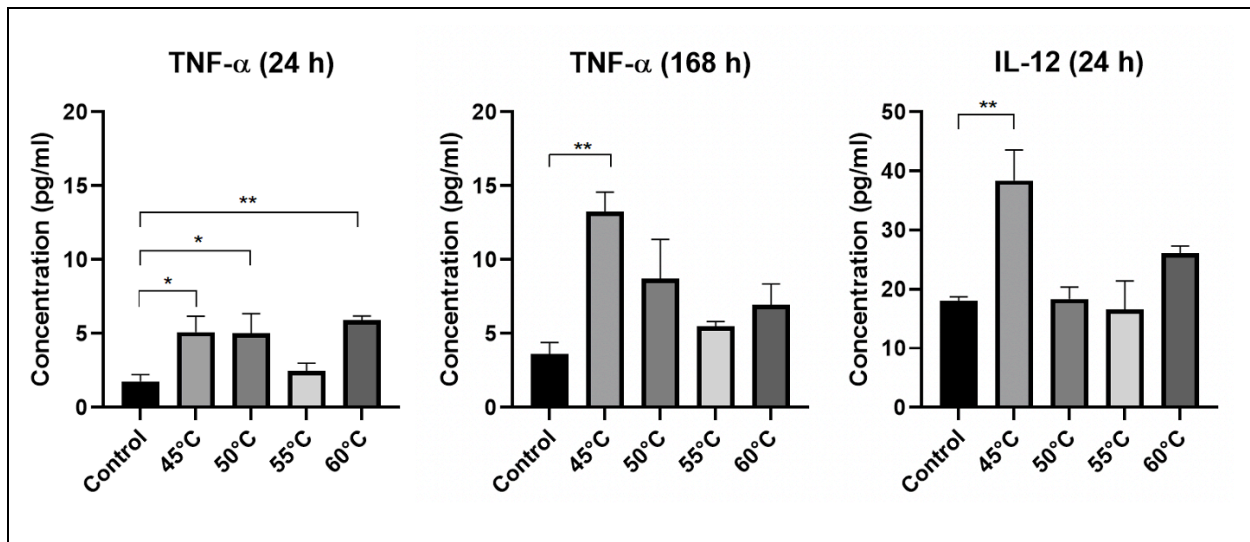


Figure 36: Cytokine concentrations in serum 1 day (24 h) and 7 days (168 h) after PTT with different final temperatures. The levels of TNF- α and IL-12(p70) in the serum of mice treated with 980 nm-laser at power density 1.0 W/cm² after IT injection of SWCNT-ANXA5 conjugate are shown. Blood samples were collected 1 day and 7 days after PTT, and the levels of TNF- α and IL-12 p70 in the serum were analyzed by ELISA compared to untreated control (injected intratumorally with SWCNT-ANXA5 but not treated with PTT). Photothermal therapy was performed until reaching final temperatures of 45, 50, 55, or 60°C were assigned to the groups. Data are presented as mean \pm SE (n = 4–5). Statistical significance was analyzed for the treated groups compared to the untreated control group by one-way ANOVA with Dunnett's multiple comparisons test. Statistical significance is indicated by *p < 0.05 and **p < 0.01.

In **Figure 36**, mice treated with PTT that stopped at 45°C had an elevation of TNF- α (24 and 168 h after PTT) and IL-12 p70 (24 h after PTT). The fact that 45°C PTT increased the level of two pro-inflammatory cytokines at different time-points is evidence that the lower temperature is enough to induce an immune response in an EMT6 tumor model. We hypothesize that higher temperatures induce very rapid cell death and possibly necrotic cell death, impeding the release of danger signals and that cause recruitment of immune cells to the tumor site. Therefore, 45°C is optimal for the induction of immunogenic cell death. More studies are necessary to prove this hypothesis. Nonetheless, the decrease in the final temperature of the PTT is beneficial for the procedure's safety, reducing the chance of damage to surrounding tissue.

Following those results about the injection mode of SWCNT-ANXA5 and tumor surface temperature at the end of irradiation, a long-term survival study was performed with the combination therapy of PTT and checkpoint inhibition with anti-PD-1. EMT6 tumor-bearing mice were injected intratumorally with SWCNT-ANXA5 on day 9 after tumor induction. The tumor size at the time was ~ 5 mm. PTT was performed with 1 W/cm² while monitoring tumor surface temperature with a thermal camera. The NIR irradiation was immediately stopped when the tumor surface temperature reached 45°C. Three doses of anti-PD-1 were injected intraperitoneally in the assigned groups on days 4, 8, and 13 after tumor inoculation. Tumor volumes were monitored every 3 days, and

so were the health conditions of the mice. Mice that seemed sick according to the mouse Grimace scale were euthanized or when the tumor size was greater than 15 mm. Results from this experiment are shown in **Figure 37** and **Figure 38**.

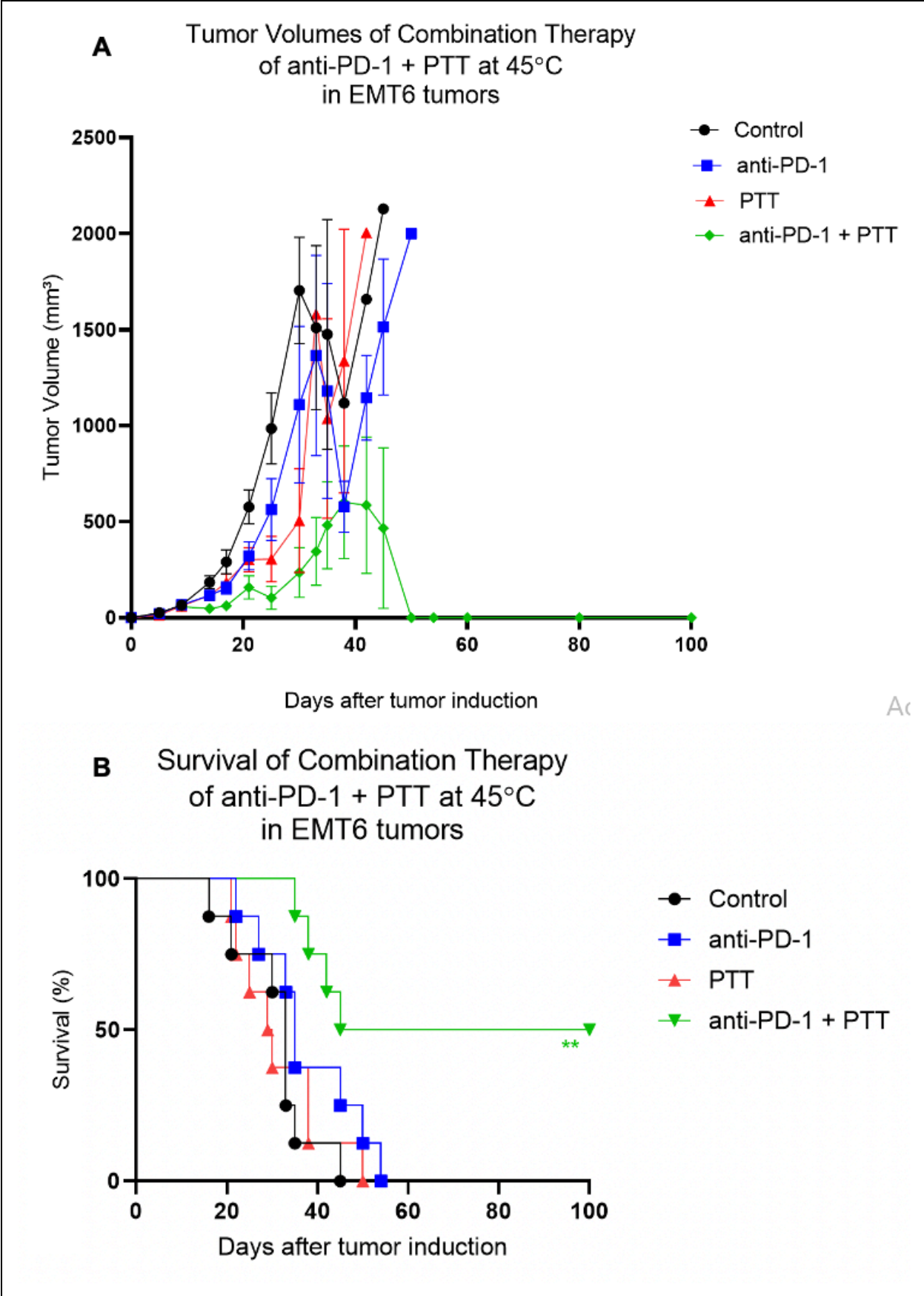


Figure 37: Results of combinatorial photothermal therapy (PTT) and checkpoint inhibition (anti-PD-1) in EMT6 tumors. Mice with well-developed orthotopic syngeneic tumors ($d \geq 5$ mm) were administered an IT dose of 1.2 mg/kg SWCNT-ANXA5. Tumors were irradiated on day 9 after tumor induction with a NIR laser at a power density of 1 W/cm^2 until tumor surface temperature reached 45°C . Select groups received anti-PD-1 (10 mg/kg) on days 8, 11, and 16. A) Tumor volume shown as mean \pm SE ($n = 7$). Statistical analysis is omitted due to overcrowding of data on the graph (available in Appendix A- **Figures 73** and **74**). B) Survival curve of the combination of photothermal therapy and immune checkpoint inhibition. The statistical significance of survival curves was determined by the Mantel–Haenszel log-rank test in GraphPad Prim 8, compared to untreated control. Survival of PTT and anti-PD-1 groups were not statistically significant from the control. The increase in survival from the anti-PD-1 + PTT group is statistically significant from the control ($p < 0.01$, $n = 8$).

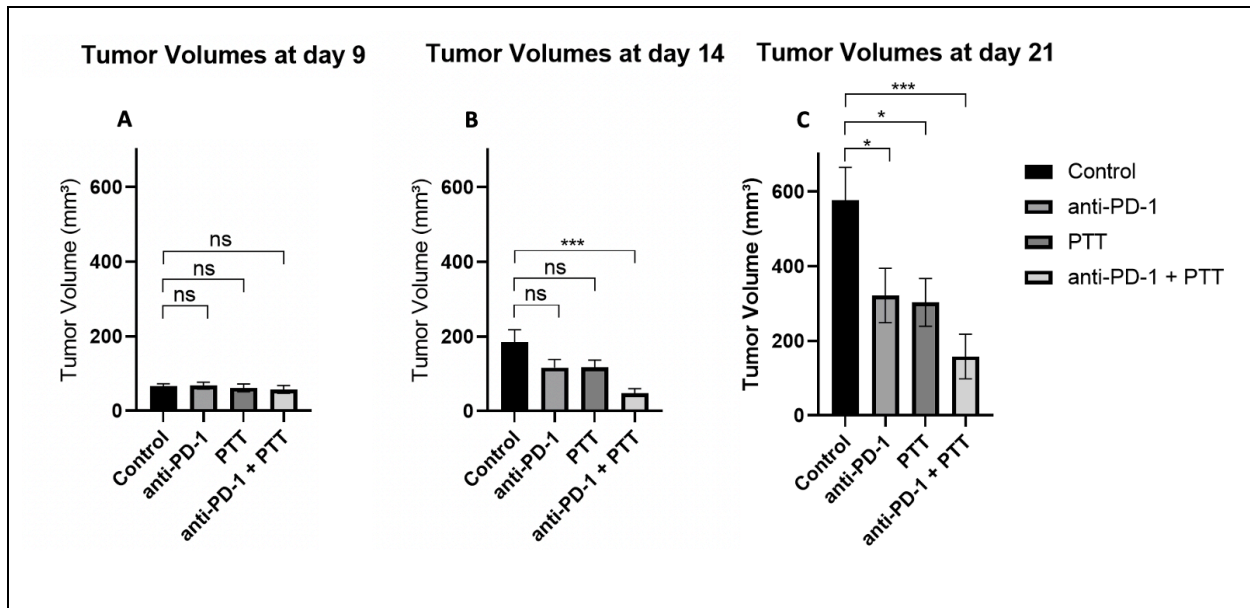


Figure 38: Tumor Volumes on days 9, 14, and 21 after tumor inoculation of combinatorial photothermal therapy (PTT) and checkpoint inhibition (anti-PD-1) in EMT6 tumors. Mice with well-developed orthotopic syngeneic tumors ($d \geq 5$ mm) were administered an IT dose of 1.2 mg/kg SWCNT-ANXA5. Tumors were irradiated with a NIR laser at a power density of 1 W/cm^2 until tumor surface temperature reached

45°C. Select groups received anti-PD-1 (10 mg/kg) on days 8, 11, and 13, while PTT was performed on day 9. Tumor volumes are shown as mean \pm SE (n = 8). Statistical significance was analyzed for the treated groups compared to the untreated control group by one-way ANOVA with Dunnett's multiple comparisons test. Statistical significance is indicated by *p < 0.05 and ***p < 0.001.

Looking at the individual tumor volume graphs in **Figure 38**, on the day of PTT (day 9 – **Figure 38A**), there was no significant difference between the control and other groups, even though two anti-PD-1 injections were performed 1 and 4 days before. Statistical difference from the control group was found on day 21 for the anti-PD-1 group. That is evidence that three injections of anti-PD-1 are necessary to induce an anti-tumoral effect. At day 21 (**Figure 38C**), groups anti-PD-1 alone, and PTT alone temporarily delayed primary tumor growth.

PTT at 45°C alone does not induce tumor recession, which can be seen in the graph tumor volumes on day 14 (5 days after PTT – **Figure 38B**). In previous studies in our lab, the ablation of EMT6 tumors to temperatures up to 54°C was efficient at generating a complete recession within a week of PTT without the combination with checkpoint inhibition; however, it did not increase survival²⁸³. Here, the ablation of EMT6 tumors at a milder temperature of 45°C was not effective at generating a complete tumor recession. Therefore, we hypothesize that even though the PTT at 45°C is more effective at generating an immune response, correlated to the higher levels of pro-inflammatory cytokines (**Figure 36**), this temperature is not sufficient to ablate the whole volume of the primary tumor.

We hypothesize that the combination therapy was efficient in generating a systemic immune response that effectively killed the remaining tumor that the PTT did not efficiently ablate at 45°C. By day 21 (12 days after PTT), four mice in the anti-PD-1 + PTT group had complete tumor recession. Those mice did not undergo tumor regrowth and survived until the end of the study (100 days after tumor inoculation), yielding a 50% survival at 100 days (**Figure 37**).

An immunophenotypical analysis of splenic cells was performed to confirm the hypothesis that the combination therapy induces a systemic immune response. EMT6 tumor-bearing mice were treated using the same protocol used for the long-term survival experiment in **Figure 37**. Fourteen days after PTT, mice were euthanized, their spleens were collected, and splenic cells were stained for immunophenotyping through flow cytometry. The results of this experiment are shown in **Figure 39**.

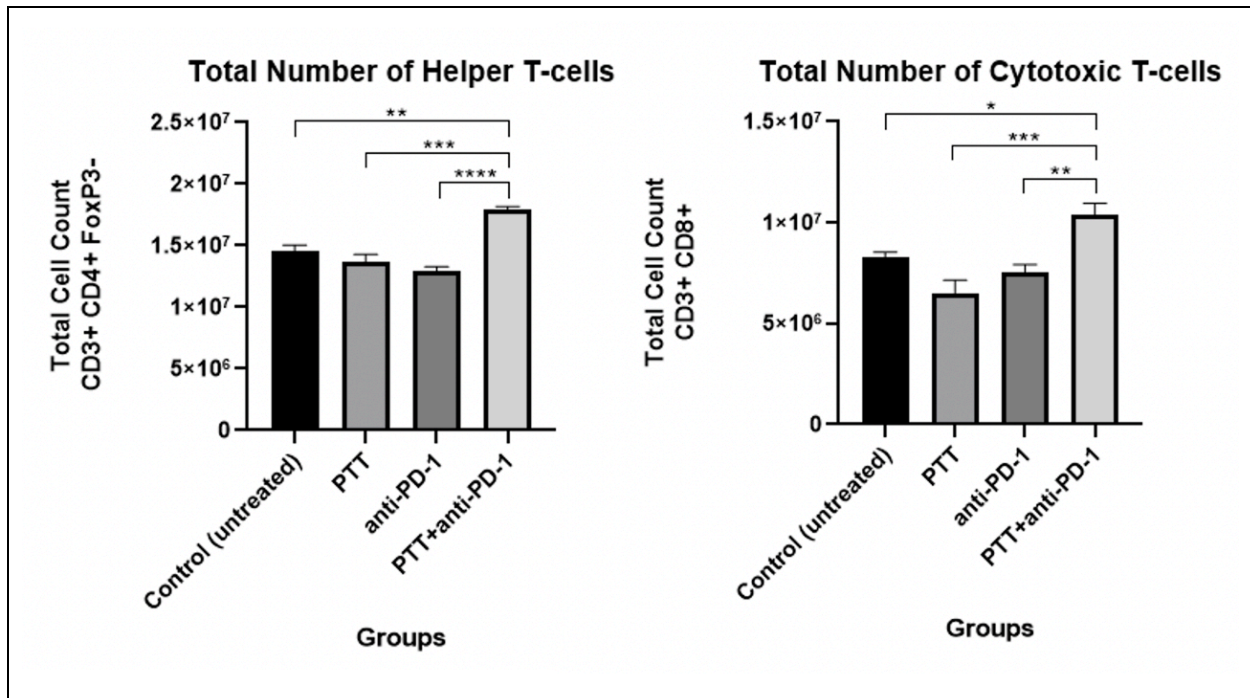


Figure 39: Splenic cell analysis of combinatorial photothermal therapy (PTT) and checkpoint inhibition (anti-PD-1) in EMT6 tumors. Mice with well developed orthotopic syngeneic tumors ($d \geq 5$ mm) were administered an IT dose of 1.2 mg/kg SWCNT-ANXA5. Tumors were irradiated with a NIR laser at a power density of 1 W/cm² until tumor surface temperature reached 45°C. Select groups received anti-PD-1 (10 mg/kg) on days 8, 11, and 16. Spleens were harvested 14 days after PTT after euthanasia. The combination of PTT and anti-PD-1 significantly increased the relative numbers of CD4+, and CD8+ splenocytes observed 2 weeks after PTT compared to control. Splenocyte counts are shown as mean \pm SE ($n = 4$). Statistical significance was analyzed by comparing all the groups to one another by one-way ANOVA with

Tukey's multiple comparisons test. Significance is indicated by *p < 0.05, **p < 0.01, ***p < 0.001, p < 0.0001.

Figure 39 shows that only the combination therapy was effective at increasing the total number of helper T cells (CD4 positive) and cytotoxic T cells (CD8 positive) in the spleen, which introduces an understanding of the mechanism of antitumor immunity. While helper CD4+ T cells assist other immune cells by cytokine stimulation and direct cell-cell contacts, mediating a humoral immune response, cytotoxic CD8+ T lymphocytes are directly responsible for killing tumor cells. Therefore, increased CD4+ and CD8+ cell numbers suggest systemic anti-cancer immune responses.

The results from the combination therapy of anti-PD-1 and PTT at 45°C were encouraging due to the cure of 50% of mice from an EMT6 tumor and evidence of an abscopal effect. Because EMT6 tumor models are known to establish metastatic tumors very early in tumor development, long-term survival is evidence that the combination therapy of PTT and anti-PD-1 elicits a systemic antitumoral response that efficiently suppresses metastatic tumors.

Despite the encouraging results from the long-term survival test in **Figure 37**, we hypothesized that if PTT efficiently ablates the tumor's whole volume, the combination therapy response would be even more effective. For that, longer irradiation times would allow heat transfer from the surface of the tumor, where most of the irradiation reaches, to deeper layers of cancer, and thus promoting heat stress in the totality of the tumor volume. To test that hypothesis, we tested tumor control of a 45°C PTT keeping tumors at that temperature for extended periods (1, 2, and 5 min). EMT6 tumor-bearing mice (~100 mm³ of tumor volume or ~6 mm in size) were injected intratumorally with SWCNT-ANXA5 and treated with 980 nm laser at 1 W/cm² while monitoring the tumor surface temperature by a thermal camera. After reaching 45°C, the laser was cycled on/off to keep the tumor surface temperature at 45°C +/- 3°C. Tumor volumes were assessed for 15 days after irradiation, as shown in **Figure 40**.

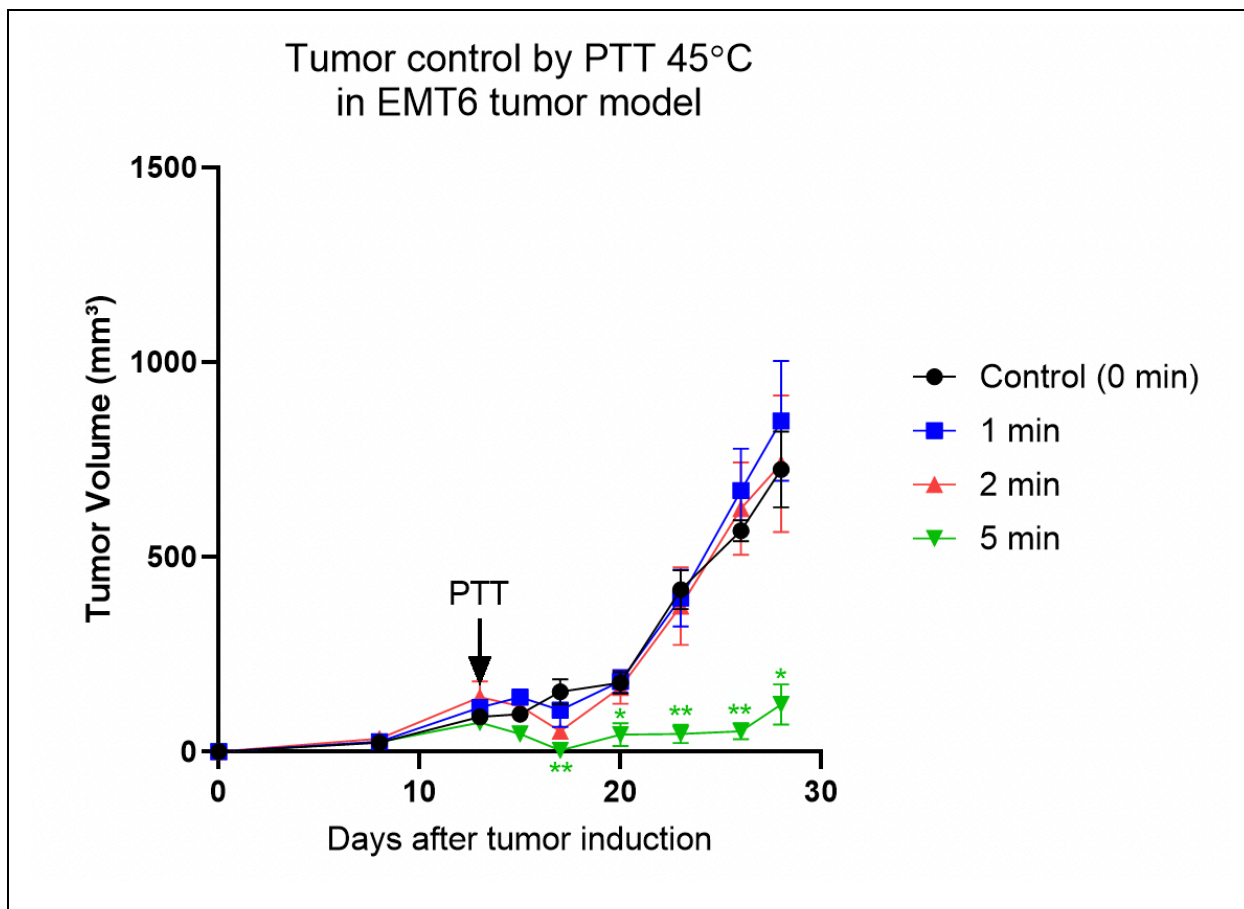


Figure 40: Tumor control from SWCNT-ANXA5 mediated PTT at 45°C for longer irradiation times in EMT6 tumor model: Mice with well-developed orthotopic syngeneic tumors ($d \geq 6$ mm) were administered an IT dose of 1.2 mg/kg SWCNT-ANXA5. Tumors were irradiated with a NIR laser at a power density of 1 W/cm² until tumor surface temperature reached 45°C; then the laser was cycled on/off to keep the surface temperature at 45°C +/- 3°C for periods of 1, 2 and 5 min. The control group was treated with PTT, and irradiation immediately stopped when the tumor surface reached 45°C. Tumor volumes are shown as mean \pm SE (n = 5). Statistical significance was analyzed for groups irradiated for longer compared to the control group by one-way ANOVA with Dunnett's multiple comparisons test. Statistical significance is indicated by *p < 0.05 and **p < 0.01.

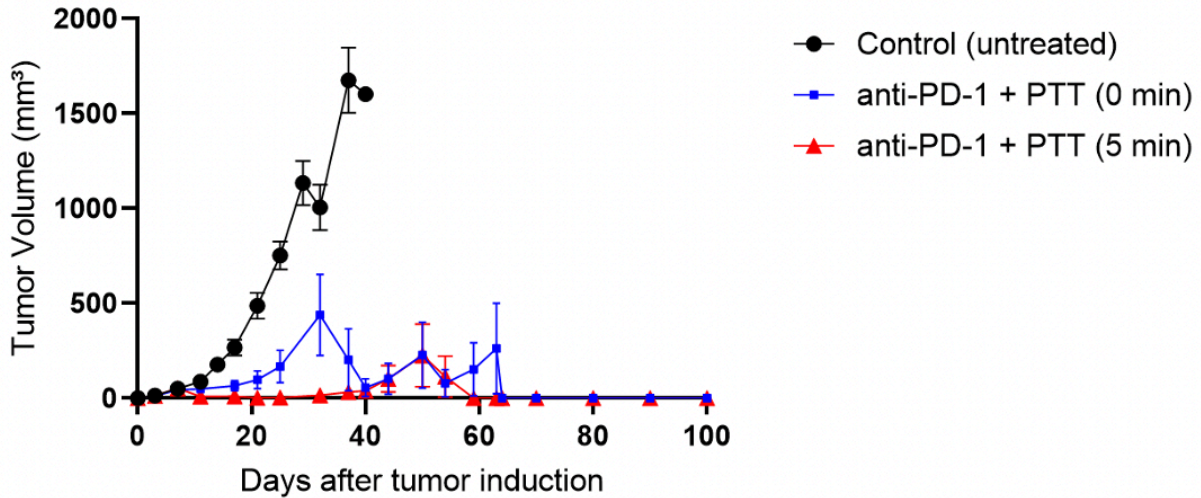
Figure 40 shows the tumor control after irradiation of EMT6 tumors at 45°C for more extended time period. After PTT, the groups 1 min, 2 min, and 5 min were able

to induce a decrease in tumor volume, which did not happen in the control group that was irradiated with PTT at 45°C and immediately stopped, which is an indication of how the mild PTT at 45°C is. Additionally, this result strengthens the hypothesis of a synergistic effect of combination therapy with anti-PD-1, since the PTT at 45°C (0 min) did not induce tumor recession by itself.

PTT for 1 min and 2 min were not efficient maintaining a statistically significant reduction of tumor volumes compared to control, whereas the 5 min irradiation of tumor at 45°C reduced the tumor volumes significantly and maintained that difference until the end of the study 15 days after irradiation. This is evidence that a better tumor control can be achieved with a milder PTT temperature of 45°C in EMT6 tumor, ultimately leading to a safer procedure.

From the previous result, another long-term survival test was performed to analyze the hypothesis that a more efficient ablation of the tumor using 45°C can be achieved by holding the tumor surface temperature for 5 min and increasing the efficiency of the combination therapy of anti-PD-1 and PTT. EMT6 tumor-bearing mice were injected intratumorally with SWCNT-ANXA5 on day 11 after tumor induction. The tumor size at the time was ~ 5 mm. PTT was performed with 1 W/cm² while monitoring tumor surface temperature with a thermal camera. For one treated group [anti-PD-1 + PTT (0 min)], NIR irradiation was immediately stopped when the tumor surface temperature reached 45°C. For the other treated group [anti-PD-1 + PTT (5 min)], NIR irradiation continued for 5 min after reaching 45°C, cycling the laser on/off to keep the tumor surface temperature at 45°C +/- 3°C. The treated groups received three doses of anti-PD-1 injected intraperitoneally on days 7, 10, and 15 after tumor inoculation. The results of treated groups are compared to untreated EMT6 tumor-bearing mice (control). Tumor volumes were monitored every 3 days, and so were the health conditions of the mice. Mice that seemed sick according to the mouse Grimace scale were euthanized or when the tumor size was greater than 15 mm. Results from this experiment are shown in **Figure 41**:

A Tumor Volumes of combination therapy of anti-PD-1 and PTT at 45°C for longer time in EMT6 tumor



B Survival of combination therapy of anti-PD-1 and PTT at 45°C for longer time in EMT6 tumor

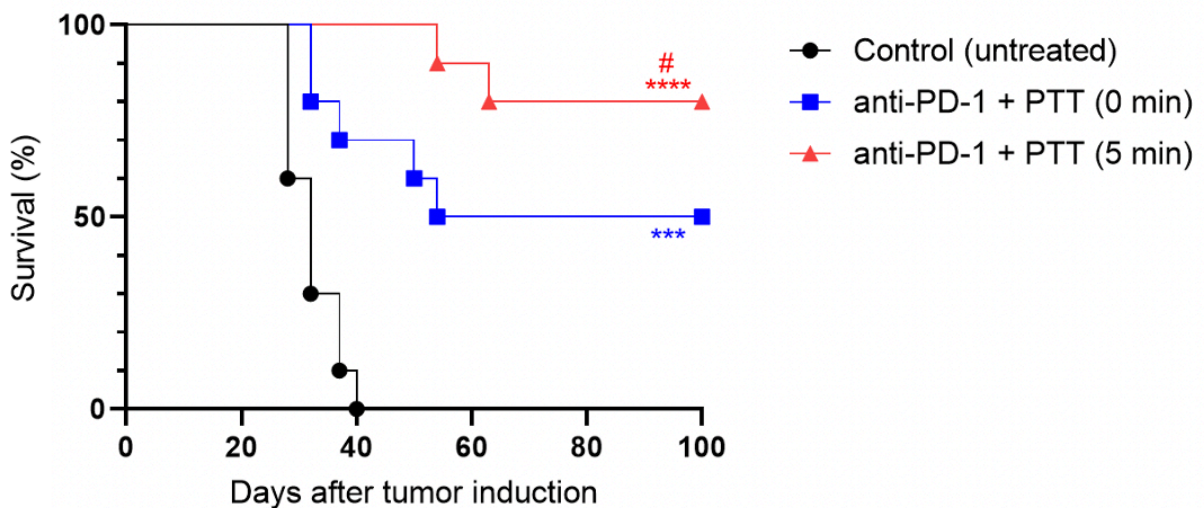


Figure 41: Results of combinatorial therapy of checkpoint inhibition (anti-PD-1) and photothermal therapy (PTT) at 45°C (immediately stopped or kept for 5 min) and in EMT6 tumors. Mice with well-developed orthotopic syngeneic tumors ($d \geq 5$ mm) were administered an IT dose of 1.2 mg/kg SWCNT-ANXA5. Select groups received anti-PD-1 (10 mg/kg) on days 7, 10, and 15. Tumors were irradiated with a NIR laser at a power density of 1 W/cm². Group anti-PD-1 + PTT (0 min) received

irradiation until the tumor surface temperature reached 45°C, whereas group anti-PD-1 + PTT (5 min) received irradiation up to 45°C when the laser was cycled on/off to keep the tumor surface temperature at 45°C for 5 min. A) Tumor volume shown as mean \pm SE (n = 10). Statistical analysis is omitted due to overcrowding of data on the graph (available in Appendix A - **Figure 75**). B) Survival curve of the combination of photothermal therapy and immune checkpoint inhibition. The statistical significance of survival curves was determined by the Mantel–Haenszel log-rank test in GraphPad Prim 8. The increase in survival from the anti-PD-1 + PTT (5 min) group is statistically significant from the control (****p < 0.0001, n = 10). Anti-PD-1 + PTT (0 min) compared to control is significant (**p < 0.001, n = 10). The increase in survival from anti-PD-1 + PTT (5 min) compared to anti-PD-1 + PTT (0 min) is also significant (# p < 0.05, n = 10).

Figure 41 shows that combining checkpoint inhibition of anti-PD-1 to the PTT keeping the tumor at 45 C for 5 min is a more effective treatment for EMT6 tumor than stopping the irradiation immediately after the tumor reaches 45°C. Eighty percent of the mice survived 100 days after PTT, which is evidence of complete cure.

Another experiment was performed to analyze the biodistribution of SWCNT after intratumoral injection. EMT6-tumor-bearing mice were injected with 1.2 mg/kg of SWCNT-ANXA5 intratumorally, treated with PTT at 45°C, and euthanized seven days after. Organs were harvested, weighed, and digested in lysing buffer. The concentration of SWCNT in the tumor, liver, and kidney was determined by relative NIR fluorescence spectroscopy. Tumors had a detectable amount of SWCNT in tissue lysate, while SWCNT could not be detected in the liver and kidneys. In previous studies with intravenous injection of the conjugate, SWCNT tended to accumulate in high percentages in the liver and kidneys and had a slow rate of clearance over a period of months. Therefore, this is evidence that the intratumoral injection of SWCNT-ANXA5 prevents the systemic distribution of the nanotubes, which is beneficial for avoiding accumulation in clearance organs. These results confirm the hypothesis that the SWCNT is too long to diffuse out of the injection site and/or is prevented from leaving the tumor because of being bound to PS on the surface of tumor cells. Accordingly, one of the mice in this

biodistribution study had complete tumor recession due to PTT, and the image of the skin injected with SWCNT-ANXA5 resembled a tattoo. Similar to the ink particles in a tattoo, SWCNT is confined in the tissue.

3.2.2 4T1 tumor model treated with SWCNT-ANXA5-mediated PTT

EMT6 cells and 4T1 cells are non-immunogenic models of triple-negative breast cancer in mouse cell lines. Nonetheless, the 4T1 tumor model is considered more aggressive and invasive^{313,314}. To illustrate that, while we use 1×10^6 for the establishment of an EMT6 tumor in our studies, 4T1 requires a tenth of that number for the tumor establishment (1×10^5), which results in a similar growth rate that tumors are ~5 mm at around day 10-11. Additionally, even though EMT6 is considered a non-immunogenic tumor model compared to other tumor models, 4T1 is even less immunogenic than EMT6³¹⁵. Thus, 4T1 is more challenging tumor model to be treated.

Therefore, to prove that the PTT is still efficient at treating a more challenging tumor model, we repeated the experiment from **Figure 41** in 4T1 tumor, where anti-PD-1 was combined with PTT at 45°C for 5 min. 4T1 tumor-bearing mice were injected intratumorally with SWCNT-ANXA5 on day 11 after tumor induction. The tumor size at the time was ~ 5 mm. PTT was performed with 1 W/cm² while monitoring tumor surface temperature with a thermal camera. For one treated group [anti-PD-1 + PTT (0 min)], NIR irradiation was immediately stopped when the tumor surface temperature reached 45°C. For the other treated group [anti-PD-1 + PTT (5 min)], NIR irradiation continued for 5 min after reaching 45°C, cycling the laser on/off to keep the tumor surface temperature at 45°C +/- 3°C. The treated groups received three doses of anti-PD-1 and were injected intraperitoneally on days 7, 10, and 15 after tumor inoculation. The results of treated groups are compared to untreated 4T1-tumor-bearing mice (control). Tumor volumes were monitored every 3 days, and so were the health conditions of the mice. Mice that seemed sick according to the mouse Grimace scale were euthanized, or when the tumor size was greater than 15 mm. Results from this experiment are shown in **Figure 42**:

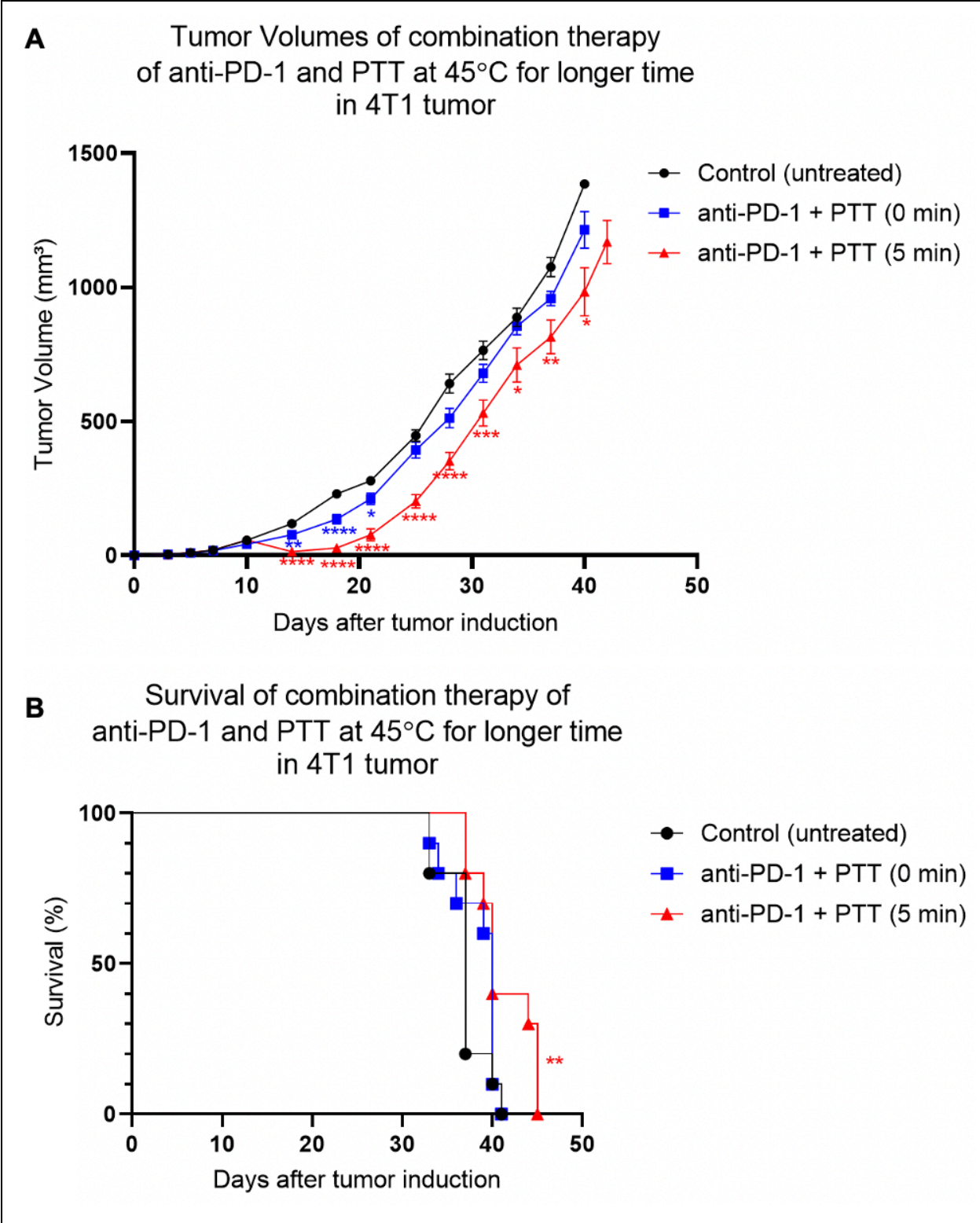


Figure 42: Results of combinatorial therapy of checkpoint inhibition (anti-PD-1) and photothermal therapy (PTT) at 45°C (immediately stopped or kept for 5 min)

in 4T1 tumors. Mice with well-developed orthotopic syngeneic tumors ($d \geq 5$ mm) were administered an IT dose of 1.2 mg/kg SWCNT-ANXA5. Select groups received anti-PD-1 (10 mg/kg) on days 7, 10, and 15. Tumors were irradiated with a NIR laser at a power density of 1 W/cm². Group anti-PD-1 + PTT (0 min) received irradiation until the tumor surface temperature reached 45°C, whereas group anti-PD-1 + PTT (5 min) received irradiation up to 45°C when the laser was cycled on/off to keep the tumor surface temperature at 45°C for 5 min. A) Tumor volumes are shown as mean \pm SE ($n = 10$). Statistical significance was analyzed for treated groups compared to the control group by one-way ANOVA with Dunnett's multiple comparisons test. Statistical significance is indicated by * $p < 0.05$, ** $p < 0.01$, *** $p < 0.001$, **** $p < 0.0001$. B) Survival curves. The statistical significance of survival curves was determined by the Mantel–Haenszel log-rank test in GraphPad Prism 8, compared to untreated control. The increase in survival from the anti-PD-1 + PTT (5 min) group is statistically significant from the control (** $p < 0.01$, $n = 10$).

We have obtained encouraging results with the survival study in which EMT6-tumor-bearing mice were treated with SWCNT-mediated PTT at 45°C for 5 min in combination with checkpoint inhibition using anti-PD-1 (**Figure 41**). The same treatment in a 4T1 tumor model resulted in a statistically significant decrease in tumor volumes in the anti-PD-1 + PTT (5 min) group compared to the control (untreated) for the entire study duration (**Figure 42**). Meanwhile, for the anti-PD-1 + PTT (0 min) group, the statistical significance of tumor volumes compared to control started after PTT day and ended on day 25 (17 days after PTT). Additionally, the combination of anti-PD-1 and PTT for 5 min induced a statistically significant increase in survival ($p < 0.05$) compared to untreated control. On the other hand, the same combination therapy but stopping the PTT immediately after reaching 45°C did not increase survival in 4T1 tumors. These results strengthen the hypothesis that the irradiation of cancer for longer times turning the laser on/off induce a more efficient ablation of the entirety of the tumor volume. More experiments should be done to assess the heat transfer to deeper layers of the tumor during their superficial irradiation.

Even though the combination therapy of anti-PD-1 and PTT at 45°C for 5 min induced an increase in survival compared to the untreated group in 4T1, those results are not as satisfactory as the results from the same therapy in EMT6 tumor models. For the group anti-PD-1 + PTT (5 min), the treatment resulted in an 80% survival 100 days after tumor inoculation for EMT6 tumors. The median survival was 40 days for 4T1 tumors treated with the same therapy. Those comparable results speak for the aggressiveness of 4T1 tumors compared to EMT6 tumors. Additionally, 4T1 tumors are less immunogenic than EMT6 tumors, thus, less responsive to immunotherapy. There is evidence in the literature that the lack of tumor-infiltrating lymphocytes (a.k.a non-immunogenic tumors) correlates to tumors' insufficient response to immunotherapy. Indeed, the effectiveness of checkpoint inhibition in humans has been correlated to tumor-infiltrating lymphocytes. Immunoadjuvants have been shown to increase the presence of tumor-infiltrating lymphocytes.

In immune-oncology, checkpoint inhibition aims to produce effector T cells that have an anti-tumoral response. Even though T cells are considered part of the adaptive immune system, the production of extended protective memory T cells depends upon the interconnection with the innate immune system (see **Figure 43**). The established mechanisms for detecting tumor cells are not specific to that type of cells, but they are thought to be part of the pathogen and damage receptors recognition tools. One example of this connection between the two types of immunity is that antigen-presenting cells (APCs) can induce the action of tumor-specific CD8 T cells³¹⁶.

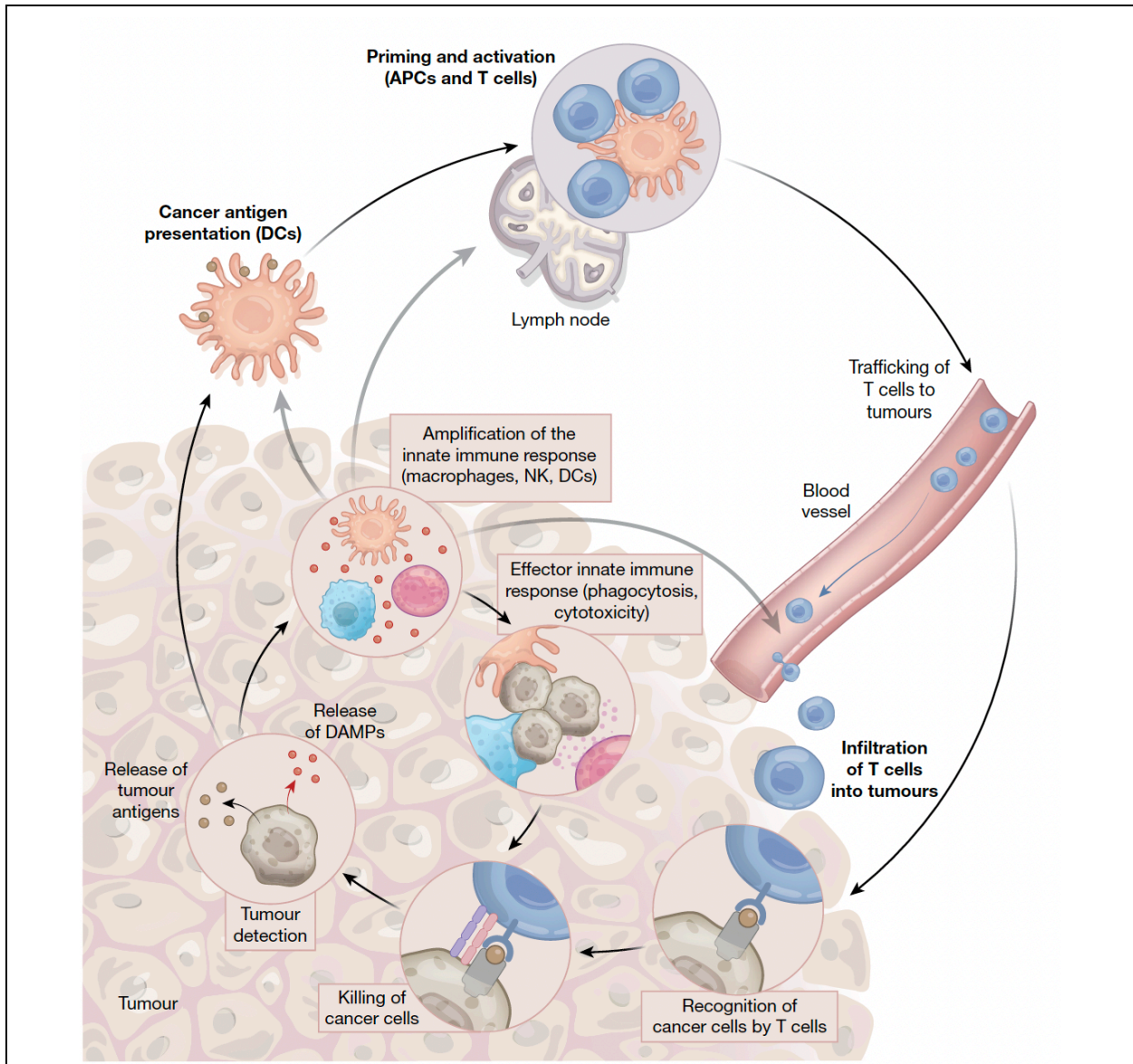


Figure 43: The anti-cancer innate immunity cycle. The cancer-immunity cycle is fully integrated by innate immunity, which is necessary for developing and maintaining adaptive immunity. Innate immune cells become activated in response to tumor detection, encouraging effector activities and tumor cell eradication. Eventually, tumor eradication produces more detection signals, propagating immune responses. Tumor-activated innate immune cells participate in the activation, proliferation, and infiltration of tumor-specific T-cells at the tumor site, contributing to all T-cell production and activity against cancer cells. They also play an essential role in the direct tumoricidal effect. Image from de Maria *et al.*, 2019³¹⁷

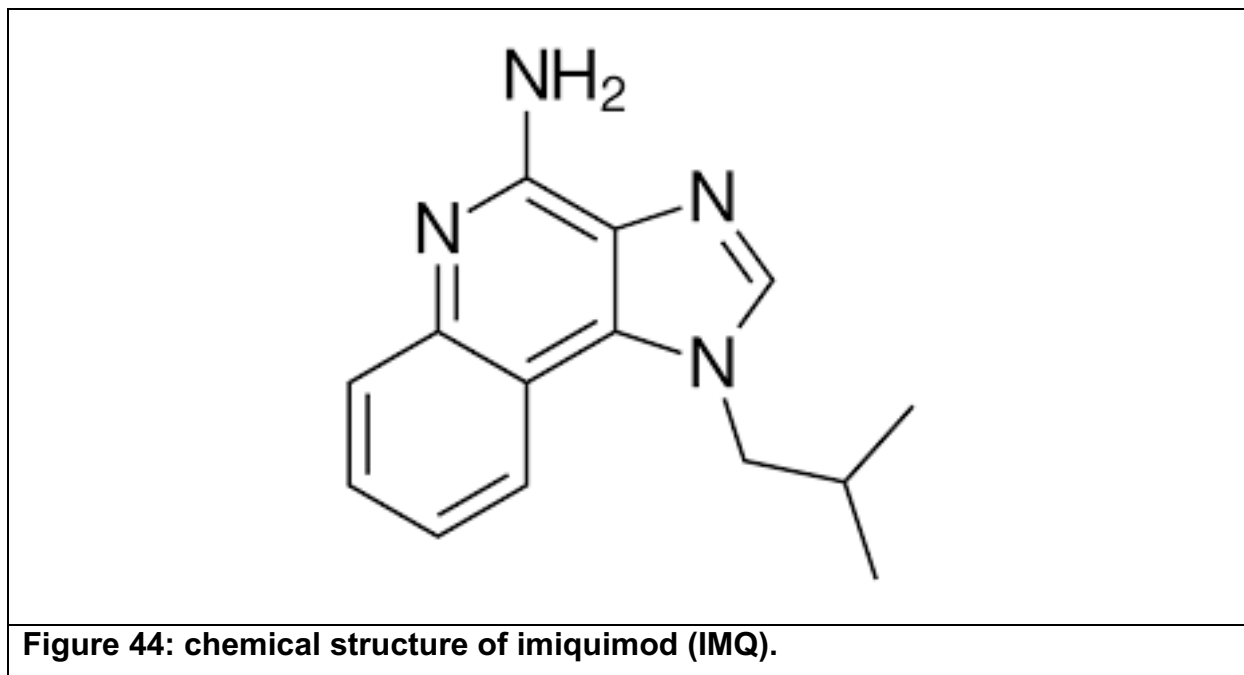
Immunoadjuvants are synthetic molecules that activate the innate immune system by mimicking the chemical moieties usually recognized as pathogen derived. A toll-like receptor (TLR) agonist is a type of immunoadjuvant mainly studied. Although the systemic administration of those chemicals has usually induced inflammatory syndromes, the intratumoral injection of TLR agonists has shown promising results by itself, with a reduction of tumor size and effect on metastatic tumors (abscopal effect)^{318–320}. Additionally, this combination of the checkpoint inhibition by anti-PD-1 antibody to the immunoadjuvant treatment was tested in a clinical trial and improved the efficacy of the treatment, increasing the tumoral infiltration of CD8+ T cells and release of proinflammatory cytokines. For this trial, the overall response rate was 71% for metastatic melanomas³²¹. Other immunoadjuvant types, such as agonists for stimulator of interferon gene (STING) and RIG-I-like receptors (RLRs), have also been studied pre-clinically and clinically in combination with checkpoint inhibition and showed effective results in controlling tumor growth and promotion of CD8+ responses^{322–324}.

Another piece of the puzzle is that the effectiveness of checkpoint inhibition in humans has been correlated to the presence of tumor-infiltrating lymphocytes. Immunoadjuvants have been shown to increase the presence of infiltrating lymphocytes in the tumor environment³²⁵.

Therefore, here we present the strategy of combining the strategy currently being studied in our research group, the targeted SWCNT- mediated PTT and checkpoint inhibition, with the addition of an immunoadjuvant to the cancer treatment strategy. The use of PTT in combination with anti-CTLA-4 and anti-PD-1 has already shown promising results, which have been attributed to the release of tumor antigens and danger signals that the immune system can recognize. The addition of an immunoadjuvant could improve the immunogenicity of the tumor by attracting the innate immune response to the tumor site, consequently transforming an immunogenic cold tumor into a hot tumor by the increase of tumor-infiltrating lymphocytes. This strategy was tested in 4T1 tumors, which are less immunogenic than EMT6.

One of the FDA-approved immunoadjuvants is imiquimod (IMQ), a toll-like receptor 7 agonist used for the treatment of viral warts, basal cell carcinoma, and actinic keratoses. Most of the applications of IMQ require daily applications for extended time

periods of up to months to promote good results^{326–331}, which is attributed to the inherently small molecule size that tends to diffuse out of the application site (see **Figure 44**). Therefore, to improve the effectiveness of the addition of IMQ to the combination, we encapsulated IMQ in hydrogel for the slow release of the small molecule into the tumor.

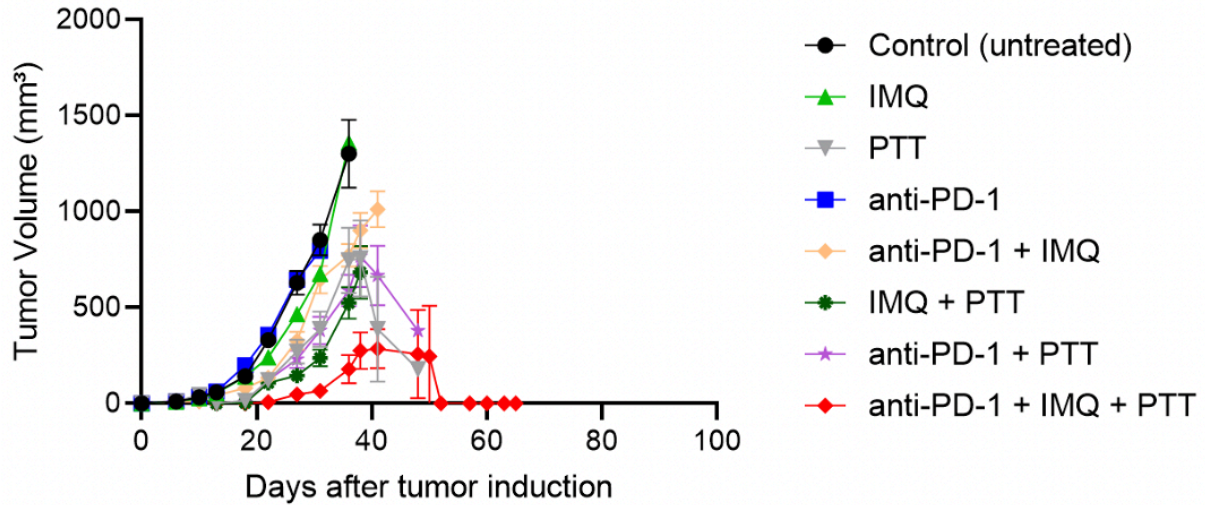


We hypothesize that an intratumoral administration of IMQ would first induce an attraction of lymphocytes to the tumor region, turning the tumor into an immunogenic environment. This attraction occurs due to mimicry of bacterial infection by binding to the toll-like receptor on the surface of immune cells³³². Then, the current combination therapy of PTT and anti-PD-1 (Ab) would efficiently treat the tumor and metastasis.

For that, 4T1 tumor-bearing mice were treated on day 7 after tumor inoculation when the tumor size at the time was ~3 mm. On that day, mice were intratumorally injected with hydrogel-loaded IMQ (50 mg) and intraperitoneally injected with anti-PD-1 (10 mg/kg). On day 10, another injection of checkpoint inhibitor antibody was performed. On day 11, SWCNT-ANXA5 was injected intratumorally, followed by 980 nm laser irradiation at 1 W/cm² while monitoring tumor surface temperature by a thermal camera. The irradiation session ceased when the tumor surface temperature

reached 55°C. Another injection of anti-PD-1 was performed on day 15 after tumor inoculation. The results of treated groups are compared to untreated 4T1 tumor-bearing mice (control), as shown in **Figure 45**. Tumor volumes were monitored every 3 days, and so were the health conditions of the mice. Mice that seemed sick according to the mouse Grimace scale were euthanized or when the tumor size was greater than 15 mm.

A Tumor Volumes of combination therapy of anti-PD-1, IMQ and PTT at 55°C in 4T1 tumor



B Survival of combination therapy of anti-PD-1 + IMQ + PTT in 4T1 tumor

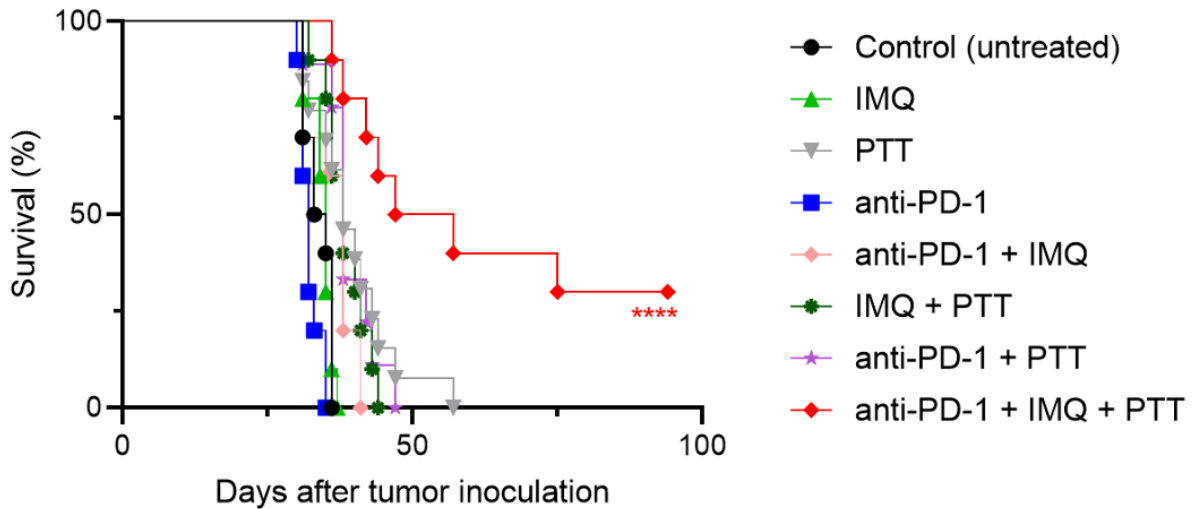


Figure 45: Long term survival study of combinatorial therapy of anti-PD-1, imiquimod-loaded hydrogel and photothermal therapy (PTT) at 55°C in 4T1 tumors. Female Balb c/J mice bearing 4T1 orthotopic syngeneic tumors (d ~ 3 mm) were treated with combinatorial therapy. Selected groups were administered with imiquimod (IMQ)-loaded hydrogel intratumorally (50 mg of IMQ) on day 7 after tumor

inoculation. Select groups also received intraperitoneal injection of anti-PD-1 (10 mg/kg) on days 7, 10, and 15. On day 11, groups were administered with an IT dose of 1.2 mg/kg SWCNT-ANXA5. Tumors were irradiated with a NIR laser at a power density of 1 W/cm² until tumor surface temperature reached 55°C. A) Tumor volume shown as mean ± SE (n = 10). Statistical analysis is omitted due to overcrowding of data on the graph (available in Appendix A - **Figure 76**). B) Survival curves. Statistical significance of survival curves was determined by the Mantel–Haenszel log-rank test in GraphPad Prim 8, compared to untreated control. Increase of survival from complete treatment (anti-PD-1 + IMQ + PTT) is statistically significant from control (****p < 0.0001, n = 10). Three mice in the complete treatment group are alive, healthy, and without tumors on day 94. Study will be terminated at day 100. Statistical significance of other groups compared to control is omitted due to overcrowding of data on the graph (available in Appendix A – **Figure 78**)

In **Figure 45A**, groups in which the PTT was performed showed significantly decreased tumor volumes compared to those that was not. Therefore, a temperature of 55°C is efficient at promoting tumor control. Those results can be confirmed in the graphs of tumor volumes on individual days available in Appendix A. Nonetheless, it was observed that some mice in those groups had no protruding tumors but a tough abdominal area surrounding the primary tumor site. After the death or euthanasia of those mice, it was observed the growth of internal tumors in the abdominal wall. Thus, the PTT at 55°C might still be inefficient at ablating the totality of the tumor volumes due to heat transfer limitations to deeper layers of the tumor.

Despite those limitations in the PTT, the combination therapy of anti-PD-1 + IMQ + PTT efficiently increased the survival of mice bearing 4T1 tumors. It is known that this tumor model is challenging due to aggressiveness and low immunogenicity. Thus, the fact that, at day 94, three mice from the complete treatment group were alive and healthy might while the mice in every other group had died is evidence that they may be cured of cancer. This study will be finalized on day 100.

While these results are promising, the mechanisms of anti-tumoral response need to be assessed to confirm the hypothesis of a systemic immune system

activation against cancer. A set of two experiments were designed to evaluate the immune activation after the treatment. First, pro-inflammatory cytokine levels in serum were quantified by ELISA seven days after PTT. The results of that experiment are in **Figure 46**.

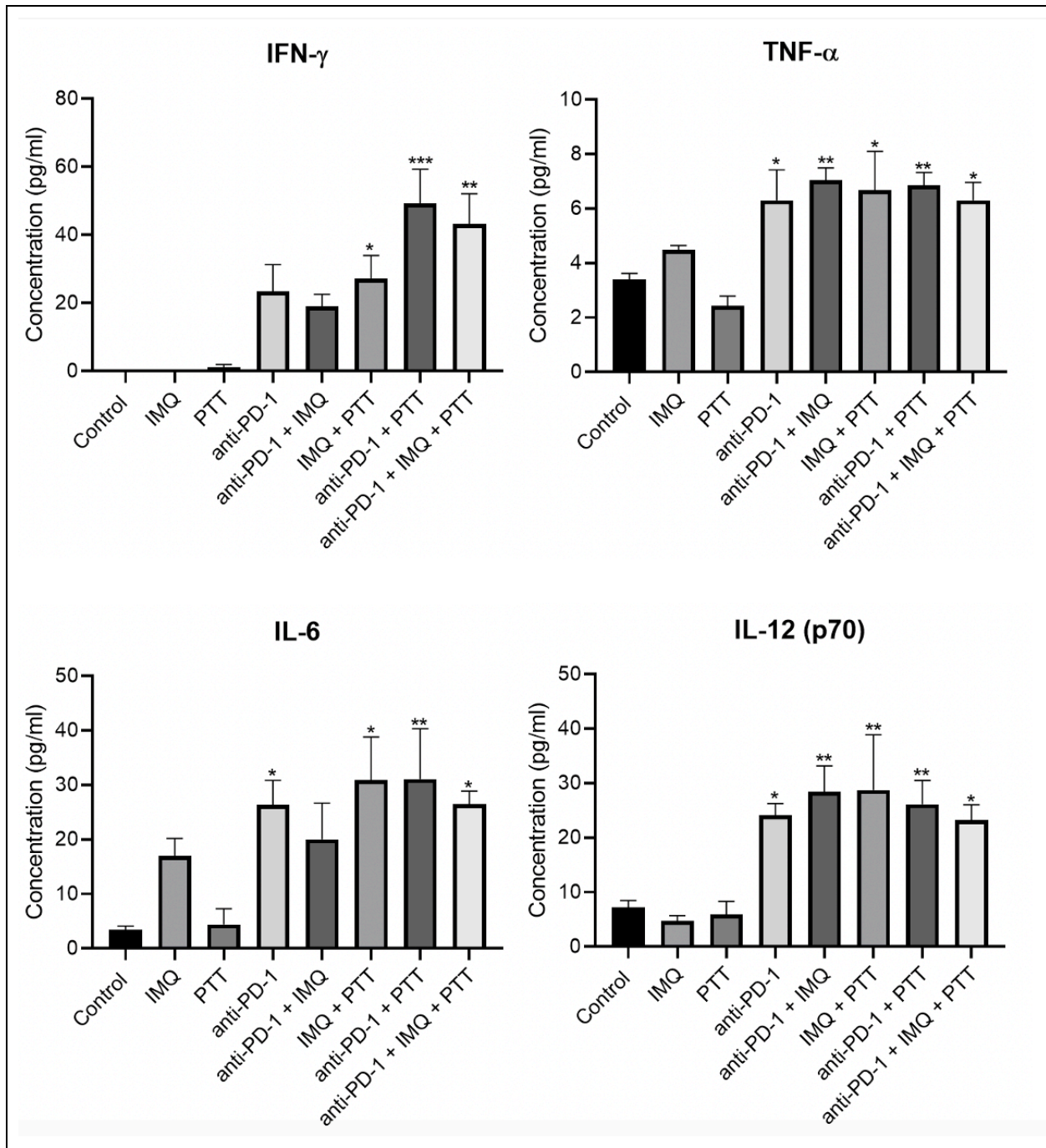


Figure 46: Serum cytokine concentration of combinatorial therapy of anti-PD-1, imiquimod-loaded hydrogel and photothermal therapy (PTT) at 55°C in 4T1 tumors. Female Balb c/J mice bearing 4T1 orthotopic syngeneic tumors (d ~ 3 mm) were treated with combinatorial therapy. Selected groups were administered with imiquimod (IMQ)-loaded hydrogel intratumorally (50 mg) on day 7 after tumor inoculation. Select groups also received intraperitoneal injection of anti-PD-1 (10 mg/kg) on days 7, 10, and 15. On day 11, groups were administered with an IT dose of 1.2 mg/kg SWCNT-ANXA5. Tumors were irradiated with a NIR laser at a power density of 1 W/cm² until tumor surface temperature reached 55°C. Quantification of serum cytokine levels in mouse serum 7 days after PTT showed a significant increase of IFN- γ , TNF- α , IL-6 and IL-12 (p70) levels in mice following PTT. Data are presented as mean \pm SE (n = 5). Statistical significance was analyzed for the treated groups compared to the untreated control group by one-way ANOVA with Dunnett's multiple comparisons test. Statistical significance is indicated by *p < 0.05, **p < 0.01, ***p < 0.001.

Figure 46 shows the levels of proinflammatory cytokines IFN- γ , TNF- α , IL-6, and IL-12 (p70). The groups IMQ + PTT, anti-PD-1 + PTT, and anti-PD-1 + IMQ + PTT increased the levels of the four cytokines studied compared to the untreated control. As previously discussed, those cytokines play a role in innate and adaptive immune response; thus, the increased presence of those molecules in the circulatory system is evidence of a systemic immune response. It is worthwhile mentioning the additional effect of combining therapies. While PTT alone and IMQ alone did not increase the level of any of those cytokines compared to the untreated control, the combination of IMQ + PTT promoted the production of proinflammatory cytokines. Here, the combination of therapies has a positive effect, which is not usually seen in the combination of drugs in chemotherapy. The combination of treatments in the different groups also induced a significant increase in survival compared to untreated control (survival curves of each group compared to control can be seen in Appendix A – **Figure 78**). Nonetheless, only the complete treatment group (anti-PD-1 + IMQ + PTT) had four mice surviving past 50

days after tumor inoculation. This is evidence of the beneficial anti-cancer effect of combinatorial therapies with PTT.

Additionally, by comparing the groups with individual therapies, only the PTT group increased survival (anti-PD-1 alone and IMQ alone did not increase survival – see **Figure 78**). These results demonstrate the synergistic effect of a combination of therapies, in which the results of the joint therapies are superior to the summation of the therapeutic outcome of individual treatment components.

Another experiment was performed to prove the activation of a systemic immune response. 4T1-tumor-bearing mice were treated identically to the survival test and euthanized 15 days after PTT for the immunophenotyping of splenic cells. The results of that experiment are shown in **Figure 47**.

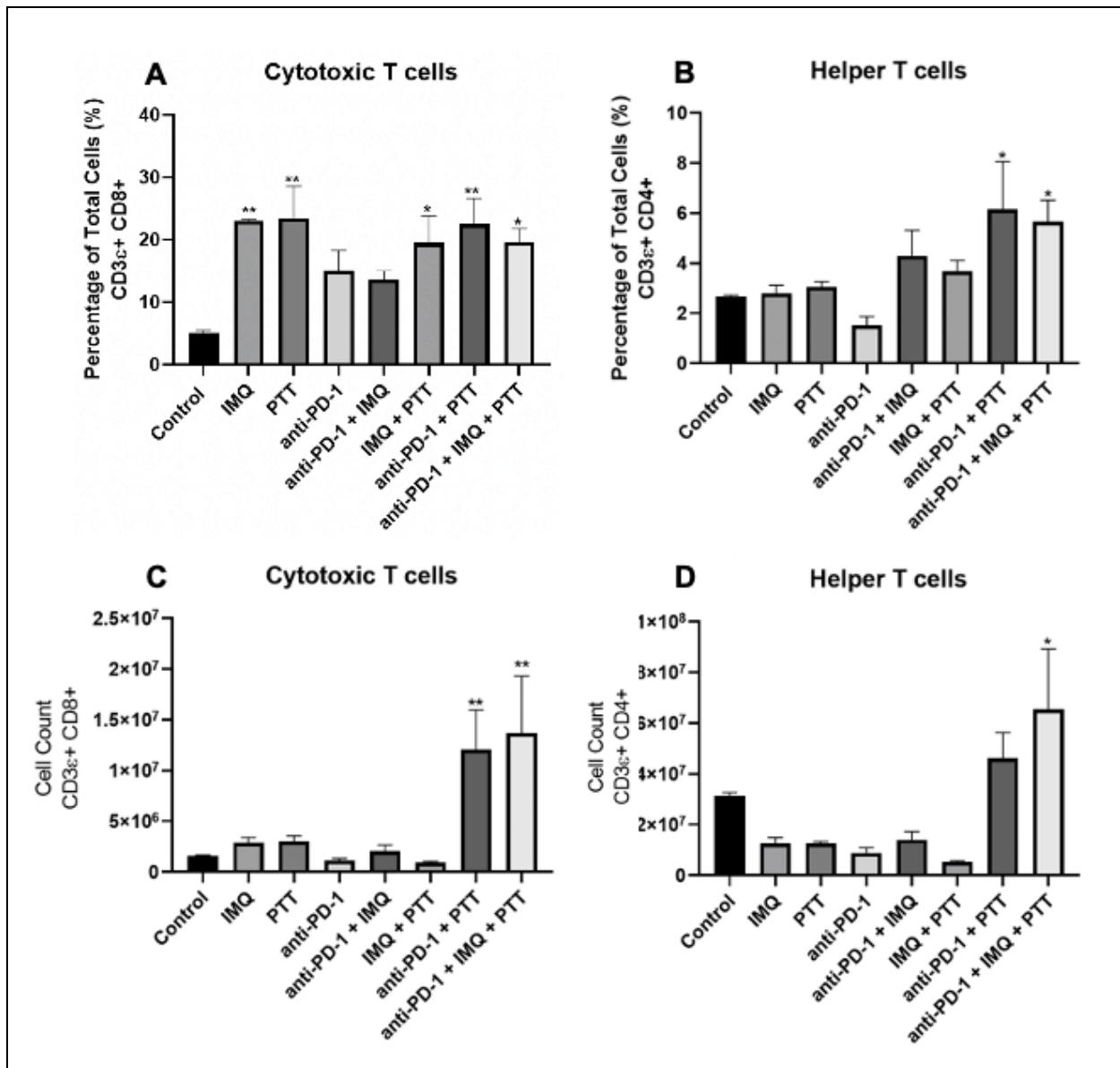


Figure 47: Analysis of splenic cells after combinatorial therapy of anti-PD-1, imiquimod-loaded hydrogel and photothermal therapy (PTT) at 55°C in 4T1 tumors. Female Balb c/J mice bearing 4T1 orthotopic syngeneic tumors (d ~ 3 mm) were treated with combinatorial therapy. Selected groups were administered with imiquimod (IMQ)-loaded hydrogel intratumorally (50 mg) on day 7 after tumor inoculation. Select groups also received intraperitoneal injection of anti-PD-1 (10 mg/kg) on days 7, 10, and 15. On day 11, groups were administered with an IT dose of 1.2 mg/kg SWCNT-ANXA5. Tumors were irradiated with a NIR laser at a power density of 1 W/cm² until tumor surface temperature reached 55°C. Analysis of splenic

cells 15 days after PTT A, B) Percentage of total cells for cytotoxic T cells (A) and helper T cells (B); C,D) Cell count of cytotoxic T cells (C) and helper T cells (D). Data are presented as mean \pm SE (n = 4). Statistical significance was analyzed for the treated groups compared to the untreated control group by one-way ANOVA with Dunnett's multiple comparisons test. Statistical significance is indicated by *p < 0.05, **p < 0.01.

Figure 47A shows an increase in the percentage of cytotoxic T cells in many treatment groups, whereas **Figure 47B** shows the percentage of helper T cells was increase only in the anti-PD-1 + PTT and anti-PD-1 + IMQ + PTT groups. More importantly, the total cell count for those types of cells are shown in **Figure 47 C and D**, where the number of cytotoxic T cells was significantly increased in anti-PD-1 + PTT and anti-PD-1 + IMQ + PTT groups, and the number of helper T cells was significantly increase only for anti-PD-1 + IMQ + PTT group. The difference from the results from percentage of total cells and cell count is due to the enlargement of spleens seen for the groups anti-PD-1 + PTT and anti-PD-1 + IMQ + PTT groups.

Cytotoxic T cells kill target cells and would be essential in eliminating remaining cancerous cells in the primary tumor and metastatic tissue. Helper T cells are required for most adaptive immune responses. The increased splenic cell count of those cell types in the treated groups strengthens the hypothesis of an anti-tumoral immune response.

In conclusion, the complete treatment of intratumoral injection of imiquimod-loaded hydrogel, checkpoint inhibition with anti-PD-1, and targeted photothermal therapy increased tumor control, survival, proinflammatory cytokines in serum, and percentage of cytotoxic T cells and helper T cells and cytotoxic T cell count and helper T cell count in the spleen in the 4T1 tumor model. This evidence supports the effectiveness of combining targeted photothermal therapy, immune checkpoint inhibition, and immunoadjuvant for treating non-immunogenic metastatic breast cancer.

Due to the encouraging pre-clinical results gathered in this work, efforts to translate this treatment strategy to a clinical setting are possible. This translation would involve using a needle-like laser probe to guide the laser into the tumor location, along with an imaging technique to locate the tumor.

Similar to the other laser probes in the market approved for PTT, the use of cooling systems to avoid probe overheating might be necessary for the device design, even though the power output used in this therapy is significantly reduced due to the very efficient transformation of the NIR light into heat from the (6,5) SWCNT. The laser probe should also be coupled with temperature measurement devices to assess the thermal kinetics of the tumoral tissue. All those systems should be controlled by automated control systems that would ensure the maintenance of a suitable heating profile and temperature for efficient ablation of the primary tumor. The intratumoral injection of the SWCNT-ANXA5 conjugate can be performed immediately before the laser irradiation using the same imaging technique. Multifocal cancers would require the ablation of each tumor since the effectiveness of the combination therapy is correlated with the efficient ablation of the primary tumor. Another possibility to achieve therapeutic effects is the ablation of lymph nodes when they are involved in the spread of primary tumors.

It is worthwhile mentioning that primary mammary tumors in humans can surpass sizes of 5 cm in diameter. Due to the limitations regarding NIR light penetration in tissue, the efficient ablation of large primary tumors might require irradiation sessions in different tumor locations. Another feasible approach is placing the laser tip in the center of the tumor and relying on heat transfer to the boundaries, while monitoring the temperature at the boundaries. Heat transfer from the irradiation site to the edges would allow the ablation of the whole tumor volume. A milder temperature at the boundaries would determine when to stop the irradiation (for example, the border is at 45°C for 5 min). Larger tumors are known to be hypoxic; therefore, the lack of blood flow would decrease the heat loss to the circulation. This condition might enhance the conductive heat transfer from the center to the tumor's boundaries, resulting in efficient ablation.

Additionally, the PTT would replace lumpectomy or mastectomy as primary courses of treatment for breast cancer because the tumor surgical removal would hinder the generation of tumor antigens and danger signals required for the synergistic effect of

PTT with the checkpoint inhibition. After the therapeutic effects of the combination therapy are established, mastectomy might be encouraged to avoid cancer recurrence.

3.3 Preliminary *in vitro* and *in vivo* studies with SWCNT-ANXA5 mediated radiofrequency ablation

3.3.1 Preliminary studies with SWCNT-ANXA5 mediated radiofrequency ablation

A series of experiments were performed to study the SWCNT responsivity in the RF field. Most of them were done using SWCNT suspension in surfactant, but others were performed on the SWCNT-ANXA5 conjugate.

First, different carbon nanotubes were suspended in sodium dodecyl sulfate (SDS) using sonication. (6,5) SWCNT used in the PTT was tested in comparison to few-walled CNT (FWCNT) produced by Dr. Daniel Resasco's research group. Suspensions were placed in a square cuvette (1 cm x 1cm x 4 cm), irradiated at 13.56 MHz between parallel plates in a Comdel RF generator and matching networks for 60 s at different power outputs. The temperature was recorded using a type K thermocouple. The results are seen in **Figure 48**.

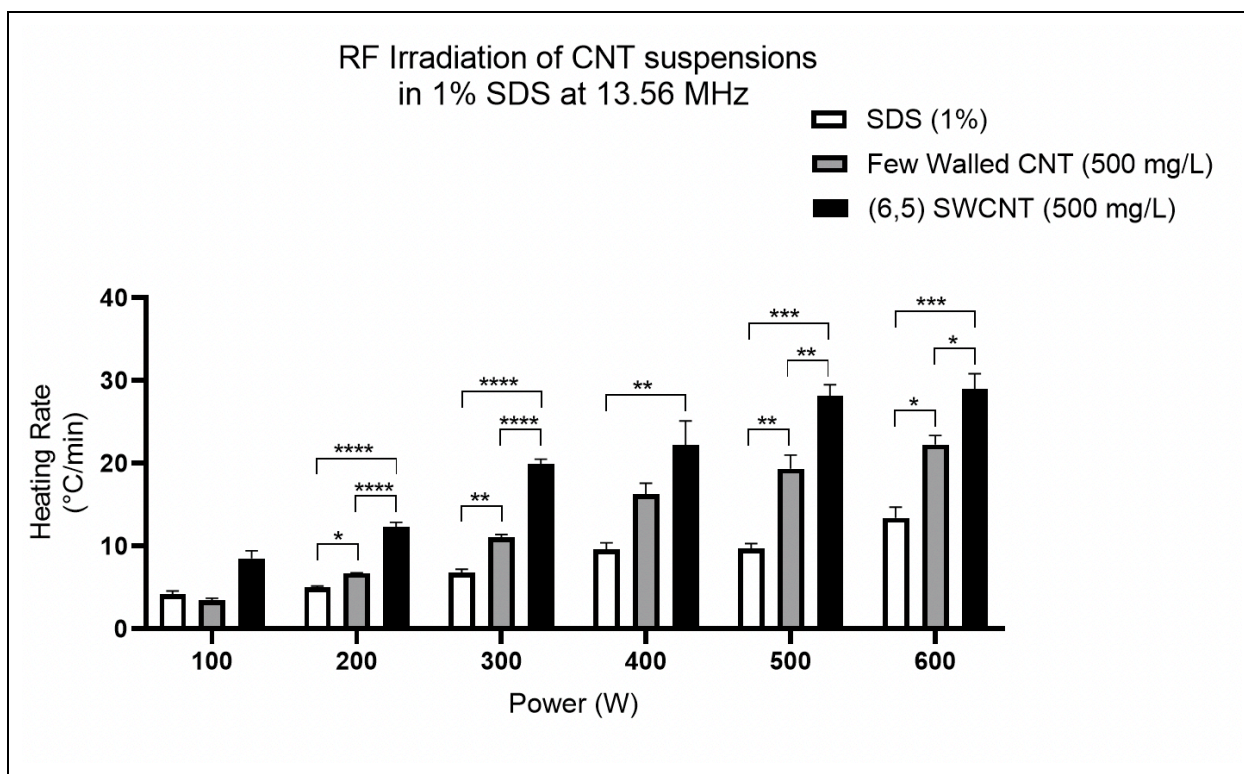


Figure 48: Heating rate of (6,5) SWCNT and few walled CNT suspended in sodium dodecyl sulfate (SDS) in RF field. One ml samples of SDS (1%), (6,5) SWCNT and few-walled CNT placed in the cuvette (1 cm × 1 cm × 4 cm) were irradiated in 13.56 MHz RF field generated between horizontal plates at various power outputs. Initial and final temperatures were measured with a type K thermocouple immersed in the liquid phase. Statistical analysis: one-way ANOVA with Tukey's multiple comparisons test comparing the three groups in each power level (n = 3). *p < 0.05, **p < 0.01, ***p < 0.001, ****p < 0.0001.

In the first experiment (**Figure 48**), the comparison of single-walled to few-walled carbon nanotubes (FWCNT) in SDS surfactant showed that the SWCNT induced a significantly higher heating rate than FWCNT in the RF field for all power levels. Statistical significance was also found between the CNT suspension and surfactant solution. While those results are encouraging, the heating of the surfactant is relevant. It is worthwhile mentioning that the higher the power output, the more significant the difference in heating rate between CNT and surfactant solution. Therefore, it can be

inferred that the responsivity of CNT to the RF increases more rapidly than the surfactant solution as the power output increases. That observation might benefit cancer applications since a lower power output might generate some heat to biological tissue. Still, higher powers might be more efficient at inducing localized heating in the presence of SWCNT.

Similarly, the CNT samples were suspended in a different surfactant. Following the same procedures, (6,5) SWCNT and few-walled CNT were suspended in sodium deoxycholate (SDC) and subjected to RF irradiation. The results are shown in **Figure 49**.

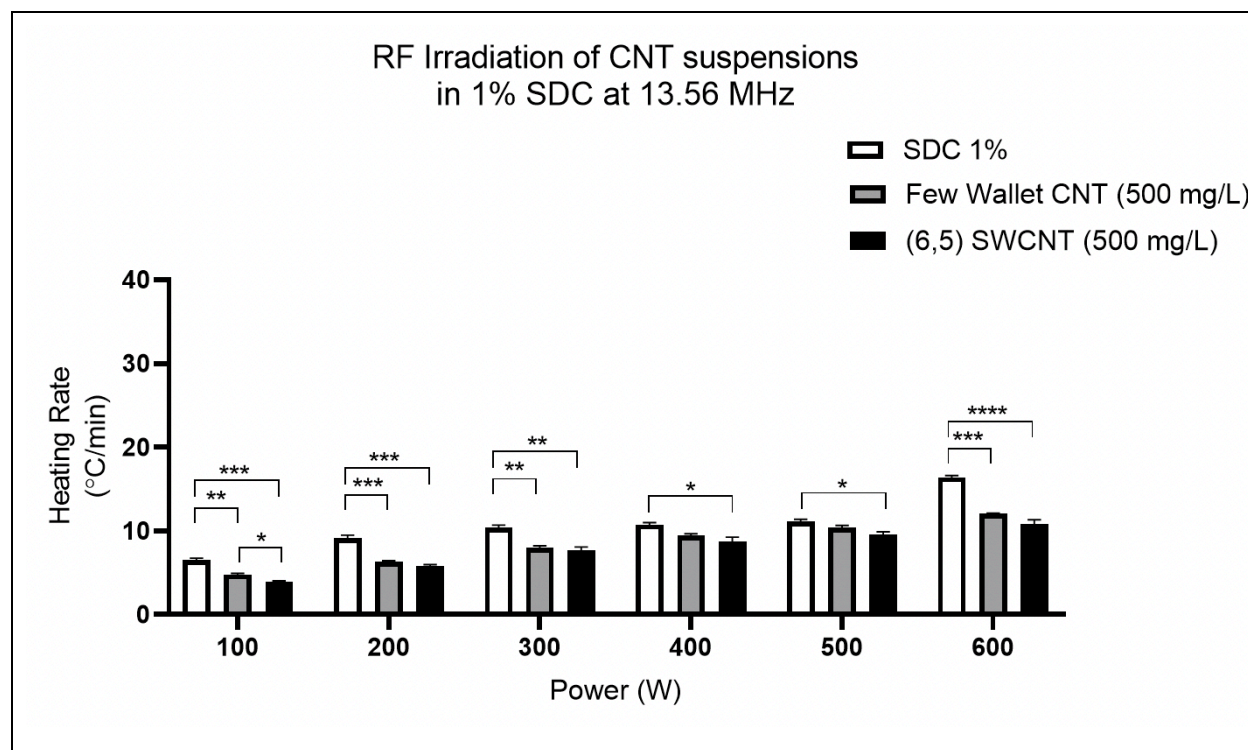


Figure 49: Heating rate of (6,5) SWCNT and few walled CNT suspended in sodium deoxycholate (SDC) in 13,56 MHz RF field. One ml sample of SDC (1%), (6,5) SWCNT and few-walled CNT placed in a cuvette (1 cm × 1 cm × 4 cm) were irradiated in 13.56 MHz RF field generated between horizontal plates at various power outputs. Initial and final temperatures were measured with a type K thermocouple immersed in the liquid phase. Statistical analysis: ordinary one-way ANOVA with Tukey’s multiple

comparisons test comparing the three groups in each power level (n = 3). *p < 0.05, **p < 0.01, ***p < 0.001, ****p < 0.0001.

For the experiment with the carbon nanotubes suspended in SDC, the heating of the surfactant was more effective than the CNT suspension at any power output. Somehow, the interaction of the CNT with the surfactant reduced the surfactant's responsivity and shielded the CNT's responsivity to the RF field. That was important to show that the different interactions between compounds in the system might produce a deleterious effect on the responsivity of the nanoparticles to the RF field. Conversely, in this work, the use of SDC was chosen over SDS as a surfactant for the suspension of CNT in the production of SWCNT-ANXA5 conjugate for photothermal therapy due to the higher availability of (6,5) SWCNT in the samples after sonication pointed out by Dr. Prada Silvy and Dr. Sathish. Therefore, while SDC is a better surfactant for PTT applications, it evokes a deleterious effect in CNT in radiofrequency ablation (RFA) applications.

The effect of other surfactants was also studied compared to SDS and SDC previously showed. The (6,5) SWCNT suspended in different surfactants were subjected to RF irradiation in a cuvette as before, applying different power outputs. SWCNT concentration was 500 mg/L. The results are shown in **Figure 50**.

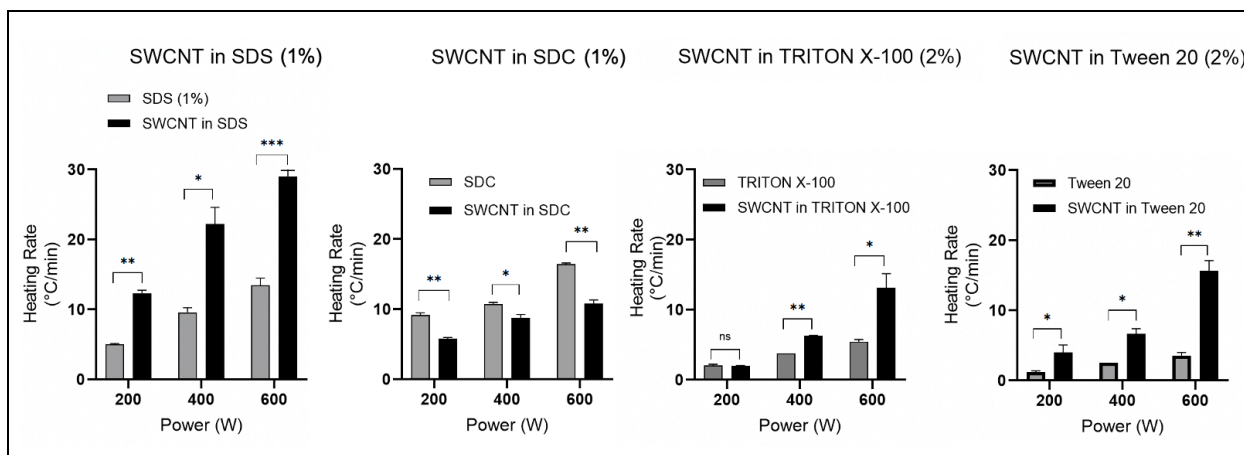


Figure 50: Assessment of radiofrequency responsivity of (6,5) SWCNT suspended in different surfactants. Samples of (6,5) SWCNT were sonicated in different surfactants [SDS (1%), SDC (1%), Triton X-100 (2%), and Tween 20 (2%)] for

1 h. One ml samples were placed in a cuvette (1 cm × 1 cm × 4 cm) and irradiated in 13.56 MHz generated between horizontal plates at different power outputs (200, 400, and 600 W). Initial and final temperatures were measured with a type K thermocouple immersed in the liquid phase. Statistical analysis between surfactant and SWCNT suspension in surfactant was done by unpaired t-test with Welch's correction for assumed different variances. n = 3, *p < 0.05, **p < 0.01, ***p < 0.001.

Comparing the different surfactants, only SDC had a deleterious effect on the responsivity of the SWCNT to the RF field. Additionally, although SWCNT suspension in SDS has a higher heating rate than in other surfactants, the effect of the SDS alone is much more considerable than TRITON X-100 and TWEEN-20. Therefore, it was reasoned that using TWEEN-20 for the following experiments would be more beneficial due to a lower heating “noise” generated by this surfactant. Once again, the molecular environment of the SWCNT influences the heating rate of the samples, which might influence the performance of SWCNT as responsive materials in RF.

Another possibility that was analyzed was the suspension of (6,5) SWCNT in solvent instead of the aqueous surfactant solution. For that, HPLC ethanol was used to suspend the CNT. The responsivity of ethanol to RF was also assessed by 13.56 MHz in a cuvette, as shown in **Figure 51**.

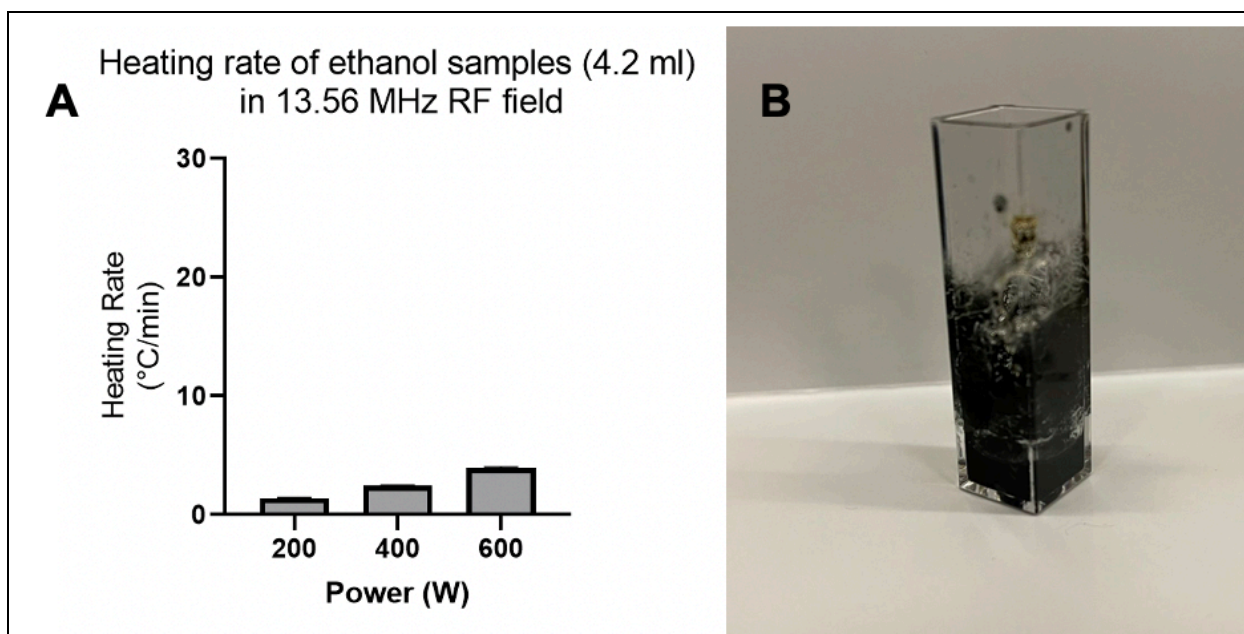


Figure 51: Analysis of the effect of the suspension of (6,5) SWCNT in solvent ethanol. A) Samples of 4.2 ml of ethanol were irradiated with a 13.56 MHz RF field, and the temperature was measured with a type K thermocouple. The heating rate was not very high compared to some surfactant solutions. B) Image of cuvette after a few seconds of irradiation of SWCNT suspended in ethanol. Ignition of the flammable solvent occurred during irradiation; therefore, the heating rate was not measured.

Figure 51 shows that ethanol alone being irradiated with the RF field did not result in a very high heating rate. Nonetheless, the addition of SWCNT to the solvent induces the ignition of the flammable liquid. This is evidence that the SWCNT is very responsive to the RF field, but caution should be used in choosing the method of suspension of CNT. Due to ignition, solvents are not an adequate medium to suspend CNT for RF applications.

From the contradictory effect of surfactants on the heating rate of CNT suspensions subjected to 13.56 MHz irradiation, it can be hypothesized that the molecular environment of the CNT affects the responsiveness of those nanoparticles to RF. Thus, the conjugation of SWCNT to the targeting protein ANXA5 might induce a deleterious effect in the RF due to the change in the molecular environment of CNT. To assess that possibility, SWCNT-ANXA5 conjugate was produced and characterized using the same

procedures described previously for the PTT project. Deionized (DI) water and phosphate buffered saline (PBS) were used as control samples. SWCNT-ANXA5 had a concentration of ~115 mg/L in CNT. Cuvettes holding 1 ml samples were loaded between the plates in the RF system. The bulk temperature of the liquids was assessed with a type K thermocouple before and after 60 s of irradiation. Samples were individually irradiated in the Comdel system. Power output was set to 300 W. Results are shown in **Figure 52**.

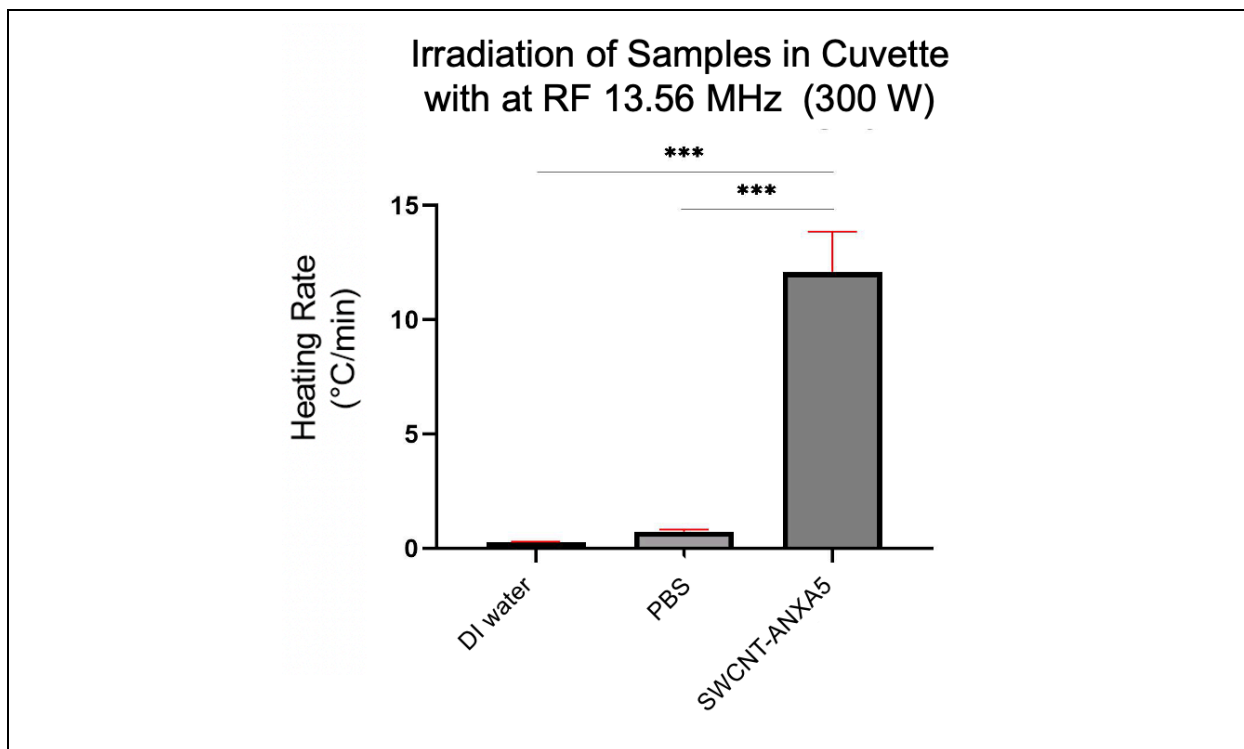


Figure 52: Heating rate of SWCNT-ANXA5 conjugate in 13.56 MHz RF field. One ml samples of deionized (DI) water, phosphate buffered saline (PBS), and (6,5) SWCNT-ANXA5 (~115 mg/L of SWCNT) were placed in a cuvette (1 cm × 1 cm × 4 cm) and irradiated in 13.56 MHz RF field generated between horizontal plates at 300 W power output. Initial and final temperatures were measured with a type K thermocouple immersed in the liquid phase. Statistical Analysis: ordinary one-way ANOVA with Tukey's multiple comparisons test comparing the three groups in each power level (n=3). ***p < 0.001.

In the experiment in **Figure 52**, it can be seen a very statistically significant higher heating rate compared to the controls. Thus, the conjugation of SWCNT to ANXA5

did not produce a deleterious effect on the responsivity of the nanoparticle in the RF field. Additionally, comparing the heating rate of the suspension of SWCNT in SDS and SDC at 300 W to the heating rate of SWCNT-ANXA5, the heating rate of the conjugate is similar to the SWCNT suspended in SDS, even though the concentration of CNT is lower (115 mg/L in SWCNT-ANXA5 compared to 500 mg/L in SDS suspension). The heating rate of the conjugate is also more significant than that seen for SWCNT suspended in SDC, though the concentration in the conjugation is lower. Thus, disregarding the concentration effects, the compared heating rate of the suspension and the conjugate is evidence that the conjugation process did not cause a deleterious effect on the responsiveness of SWCNT to RF. The use of a similar concentration would be beneficial to strengthen this claim. Nonetheless, those are promising results for the biomedical applications of SWCNT-ANXA5-mediated RFA intended in this project. The interactions with biological tissue and fluids might change those results; thus, further studies *in vitro* and *in vivo* are necessary to confirm the preservation of the responsivity in biological systems.

Another aspect that might influence the responsivity of CNT to RF irradiation is the chirality. As previously mentioned, the properties of CNT are correlated to their chirality, the way their carbon atoms assemble in the tube structure. CHASM™ produced and purified SWCNT with different chiral enrichments and provided those samples to our lab. Samples were suspended in SDS (1%) by sonication for 1 h at the concentration of 500 mg/L and subjected to 13.56 MHz RF irradiation following the same protocols as before. Samples were also compared to few-walled carbon nanotubes. Maximum power was used in those experiments (600 W). See results in **Figure 53**.

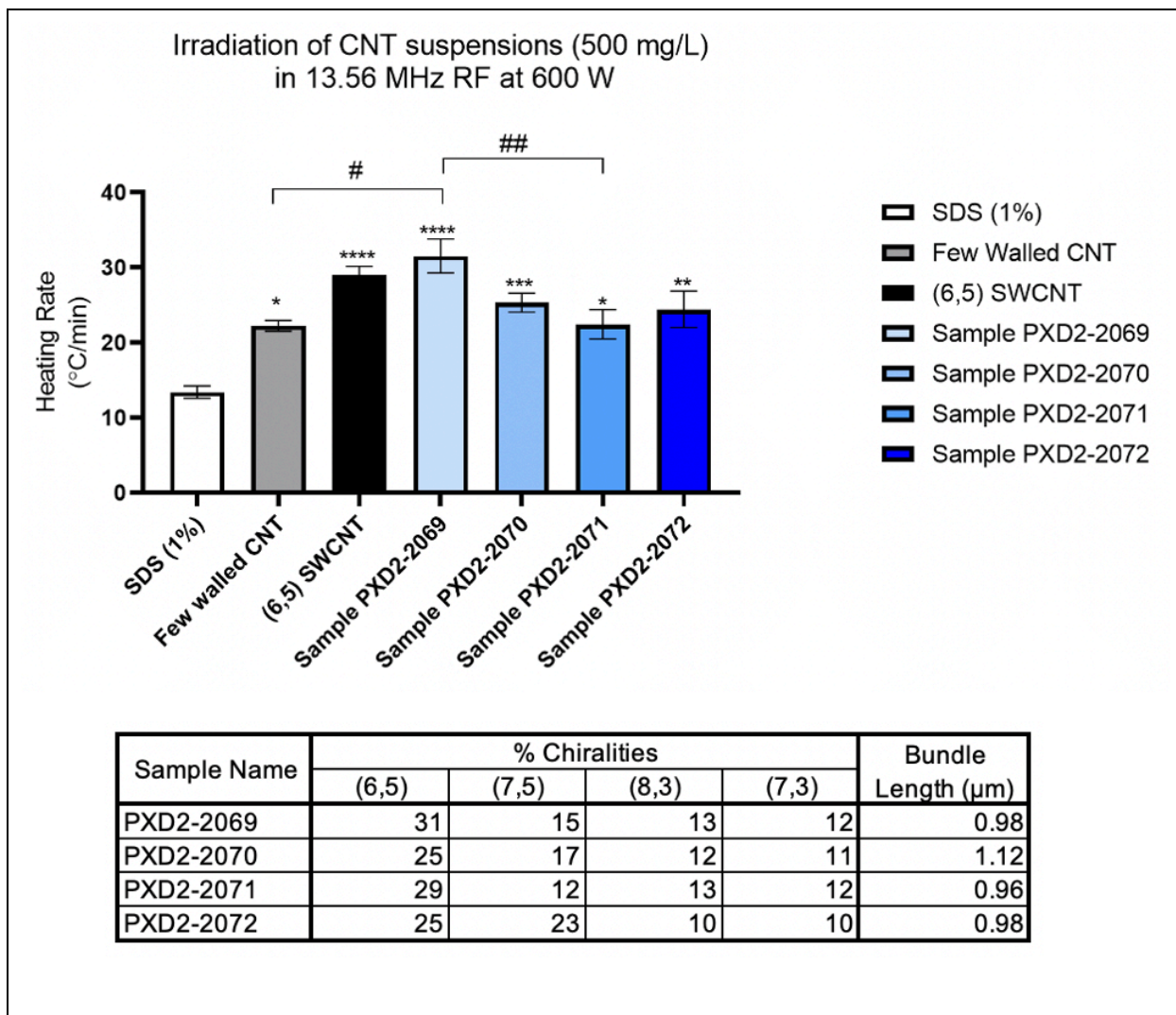


Figure 53: Heating rate of different chiral CNT suspended in sodium dodecyl sulfate (SDS) in 13.56 MHz RF field. One milliliter samples of CNT suspensions presenting different chiral enrichments were placed in a cuvette (1 cm × 1 cm × 4 cm) and irradiated in 13.56 MHz RF field generated between horizontal plates at 600 W power output. Initial and final temperatures were measured with a type K thermocouple immersed in the liquid phase. Statistical Analysis: ordinary one-way ANOVA with Tukey's multiple comparisons test comparing the three groups in each power level (n=5). Statistical analysis: ordinary one-way ANOVA with Tukey's multiple comparisons test comparing groups (n=5). *p < 0.05, **p < 0.01, ***p < 0.001, ****p < 0.0001 compared to SDS 1% (control) and #p < 0.05, ## p < 0.01 between groups.

Based on the heating rate data (**Figure 53**), (6,5) SWCNT and sample PXD2-2069 appear to be more efficient at heating in the RF field. Comparing it with the enrichment data, PXD2-2069 was the sample with the higher proportion of (6,5) chirality. With this result, (6,5) SWCNT might be more RF responsive than the other chiralities studied. Additionally, because no statistical difference was observed between (6,5) SWCNT and sample PXD2-2069, the length of the CNT in the range of micrometers might not influence the responsivity of the nanomaterial to RF since (6,5) SWCNT is 1.5 μm and sample PXD2-2069 is 0.98 μm long. Although a decrease of 500 nm in length does not seem to influence the heating rate, a further reduction of the CNT length to the nanometer range (~ 200 nm) might affect the responsivity, which would need to be confirmed experimentally.

Another parameter evaluated to influence the heating rate of samples was the geometry of the sample. While all the previous experiments were performed using one ml samples in a cuvette, we assessed the heating rate of SWCNT and sample PXD2-2069 suspensions when completely filling out the cuvette with a total volume of 4.2 ml. Temperature rise was measured remotely by a thermal camera with emissivity adjusted to 0.93 (the emissivity of PP, the cuvette material). Results are shown in **Figure 54**.

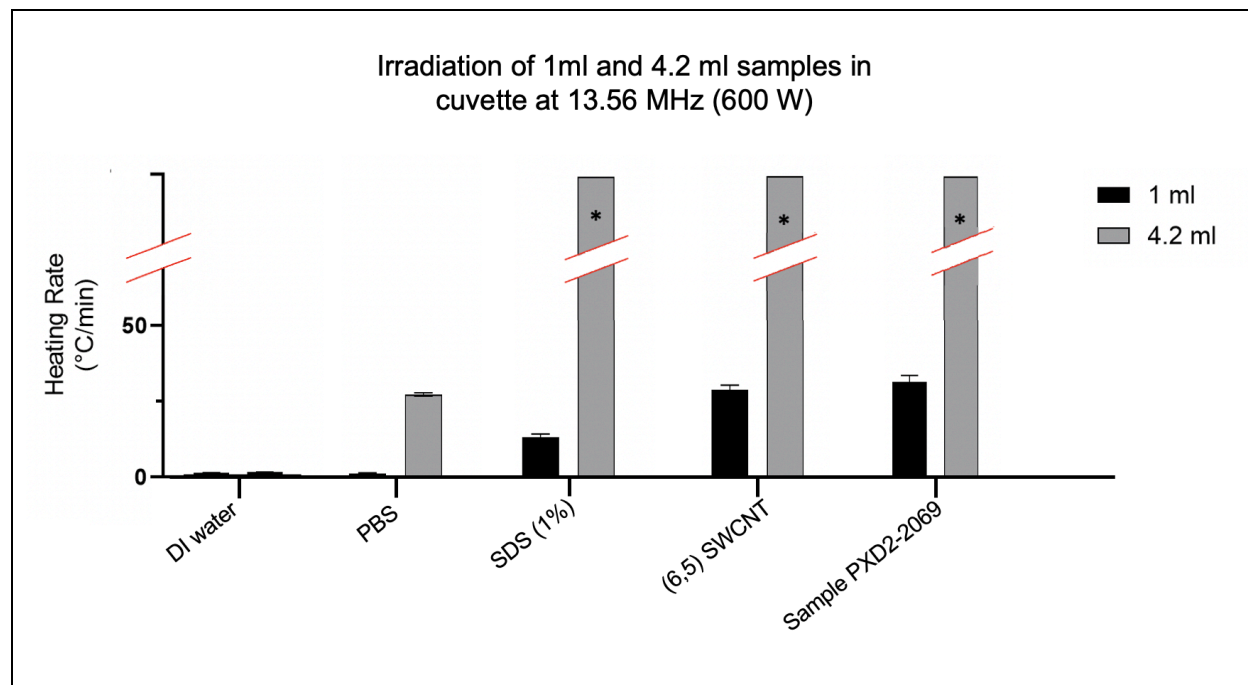


Figure 54: Effect of the geometry of liquid phase on the heating rate of different samples in 13.56 MHz RF field. Either 1 ml or 4.2 ml was sampled into a cuvette (1 cm × 1 cm × 4 cm), creating liquid volumes of 1 cm or 4.2 cm of height. Samples of deionized (DI) water, phosphate buffered saline (PBS), SDS (1%), (6,5) SWCNT suspended in 1% SDS, and sample PXD2-2069 were irradiated with 13.56 MHz Comdel RF system between horizontal plates at 600 W power output. The temperature was measured with a thermal camera. The heating of DI water was not affected by the height of the liquid phase, while PBS presented a significantly greater heating rate when the height of the liquid phase was bigger. The heating rate of 4.2-ml samples of SDS (1%) could not be assessed because boiling started at around 30 s of irradiation, which did not happen to the 1 ml sample. (6,5) SWCNT and sample PXD2-2069 at volume 4.2 ml boiled rapidly after the irradiation (within less than 5 s), and the heating rate was also not assessed. *Indicates inability to measure heating rate due to the boiling of the liquid sample inside the cuvette.

Figure 54 shows that 4.2-ml samples heated much more efficiently than the 1 cm samples. This seems counterintuitive because the power output was the same 600 W used before for all the previous experiments. In standard heat transfer settings, the heating rate is inversely proportional to the object's mass to be heated; thus, it would be expected that the 1 ml samples would heat more efficiently than the 4.2 ml samples. This discrepancy might be explained by how long the path of the RF field through the sample is. The radiofrequency irradiation of samples with a longer path (4.2 cm in 4.2-ml sample) demonstrated a much higher heating rate than those with a shorter path (1 cm in 1 ml samples).

Interestingly, Li *et al.*²⁸⁶ have demonstrated both experimentally and theoretically that the sample holder geometry influences the heating rate of saline samples in a 13.56 MHz RF field. For example, in a vertically aligned RF field in samples saline of ~1 ml, the temperature increase of a petri dish at 10 min of irradiation was undetectable, whereas the temperature increase for a tube holding a similar volume of saline was ~2°C. Li *et al.* argue that a long, thin object parallelly oriented to the field would allow a more efficient penetration of the field compared to a perpendicularly oriented

shape. In our experiment, even though the shape of the sample holder was kept the same between experiments, the shape of the liquid volume varied due to the use of a larger volume. It is believed that the longer path RF field inside the fluid sample induces an increased absorbance of the irradiation. Actually, the geometry of the sample to be irradiated influences the results of the radiofrequency ablation (RFA).

To illustrate how much more efficient the irradiation of the 4.2 ml CNT samples was compared to 1 ml samples, thermal pictures, and photos of those samples were taken in less than 5 s after the beginning of the irradiation and are shown in **Figure 55**.

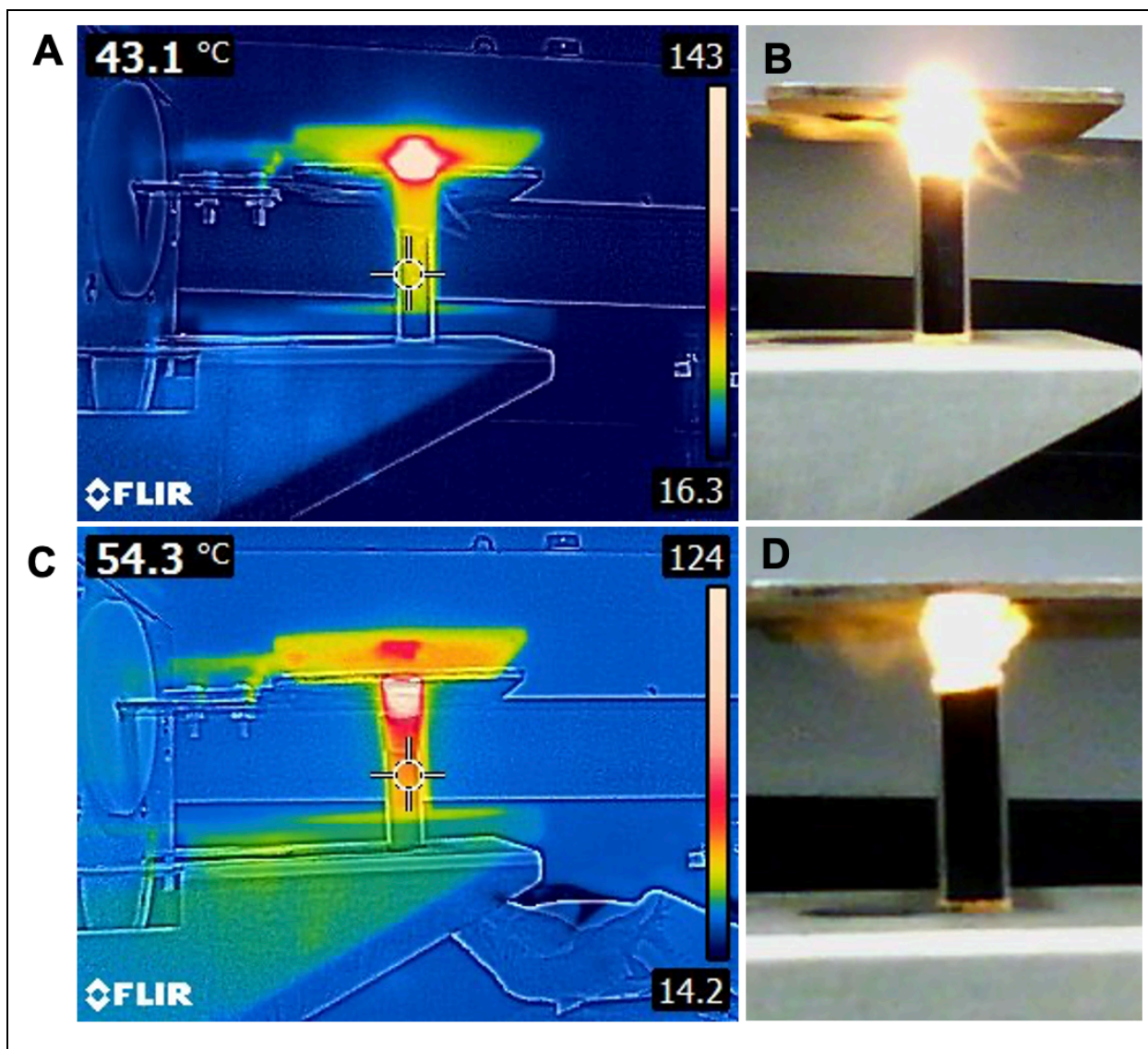


Figure 55: Images of the 13.56 MHz RF field irradiation of (6,5) SWCNT and sample PDX2-2069 in a completely filled cuvette. SWCNT samples (4.2 ml, 500 mg/L) were placed in the cuvette (1 cm × 1 cm × 4 cm) creating 4.2 cm of height. Cuvettes were irradiated with 13.56 MHz RF field between horizontal plates at 600 W power output. A, B) Thermal (A) and photo (B) images of (6,5) SWCNT within less than 5 s of the beginning of irradiation session. C, D) Thermal (C) and photo (D) images of sample PDX2-2069 within less than 5 s of the start of irradiation. Images show the explosive behavior of the suspensions when the height of the liquid volume is longer.

Figure 55 shows an explosive behavior of both (6,5) SWCNT and sample PDX2-2059, both at a concentration of 500 mg/ml. Another observation was that the phenomenon seems to happen at the interface of liquid and air. Therefore, an experiment was performed to avoid the presence of a liquid-air interface. For that, a volume of 0.2 ml of commercial coconut oil was placed on top of the aqueous suspension of (6,5) SWCNT. Before that, the heating rate of samples of coconut oil (4.2 ml) was also evaluated in the 13.56 MHz RF field, and the results are shown in **Figure 56**. It was also hypothesized that the explosive behavior was caused by ionization. Thus, as shown in **Figure 56**, another sample of very high ionic concentration (6 M of NaCl) was also evaluated inside 13.56 MHz.

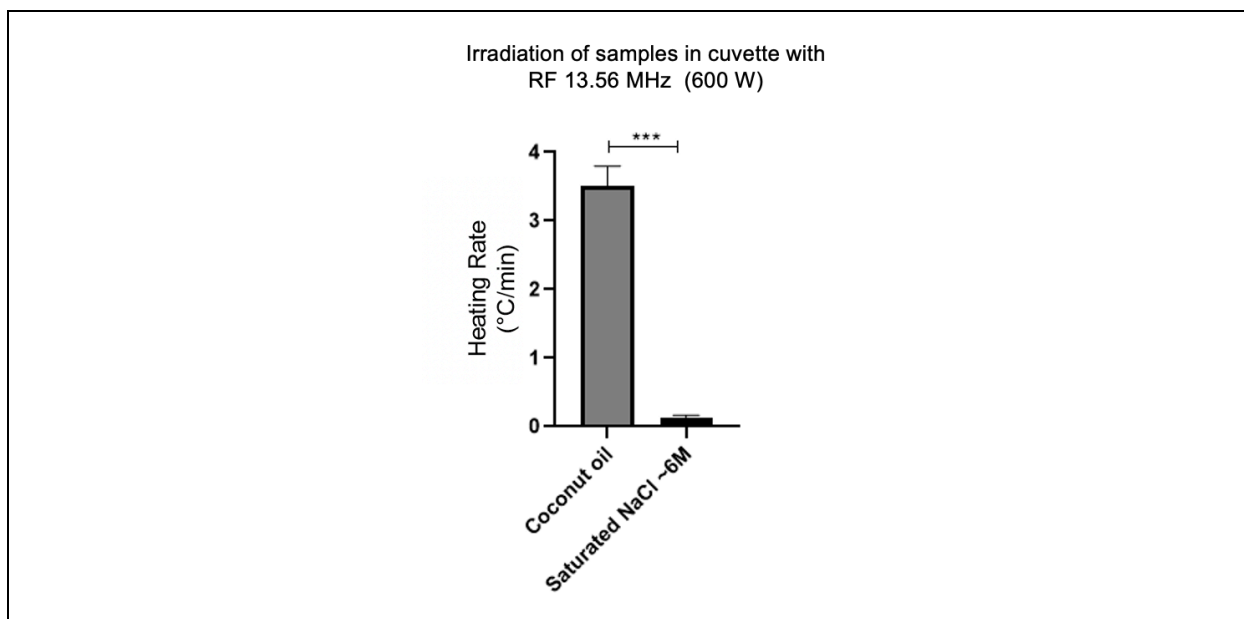


Figure 56: The heating rate of commercially available coconut oil and saturated sodium chloride solution irradiated with 13.56 MHz RF field at 600 W power output. Samples of coconut oil and NaCl (~6 M) were placed in a cuvette (4.2 ml) and irradiated in a Comdel system. The temperature was assessed with a type K thermocouple. Statistical analysis: unpaired t-test with Welch's correction for assumed unequal variances (n = 3). ***p < 0.001.

Figure 56 shows that the heating rate of coconut oil is not very significant compared to the heating rate of CNT suspensions. Additionally, the high concentration of NaCl did not induce a very high heating rate either. Therefore, the hypothesis of ionization was discarded. Subsequent tests of 4.0 ml of (6,5) SWCNT covered with 0.2 ml of coconut oil did not change the results seen in **Figure 55**, with the explosive behavior of the CNT suspension still happening and boiling starting in the aqueous phase. Hence, the explosive behavior of the CNT suspensions can be accredited to the CNT's very efficient absorbance of the 13.56 MHz RF field. More experiments are necessary to fully understand the physical mechanisms involved in this phenomenon.

Another parameter that influences the responsivity of CNT to the RF field is the frequency of the field used for the irradiation. For the laser irradiation of (6,5) SWCNT, a Raman spectrum shows a very high absorption in the near-infrared range and a peak absorption at 980 nm. Therefore, the wavelength of 980 nm was chosen for PTT applications. In the electromagnetic spectrum, wavelength and wave frequency are inversely proportional variables. In the RF range of the spectrum, there should be a wavelength/frequency where the CNT absorbs the most, similar to the peak absorption in the NIR range. That peak absorption would be called the resonance frequency in RF applications.

For that, in collaboration with Dr. Caleb Fulton, from the University of Oklahoma Electrical Engineering Department and Advance Radar Research Center and his student Josh Short, an RF generator and matching network was built to create RF irradiation between plates at different frequencies. Conversely to the Comdel system previously used that only generates the RF at 13.56 MHz, the device developed at the University of Oklahoma was able to change the frequency of the RF field. The power

output from this device was estimated to be ~ 15 W, which is much lower than the maximum power output generated in the Comdel system. Various frequencies were tested by comparing DI water and PEGylated SWCNT. Samples of DI water and (6,5) SWCNT (300 mg/ml) that were PEGylated following the initial part of the protocol for SWCNT-ANXA5 conjugation were placed in a cuvette (1 ml) and irradiated at 35, 40, 45, 55 and 60 MHz. Initial and final temperatures were measured with type K thermocouple immersed in the liquid phase. Samples were irradiated for 8 min. The results are shown in **Figure 57**.

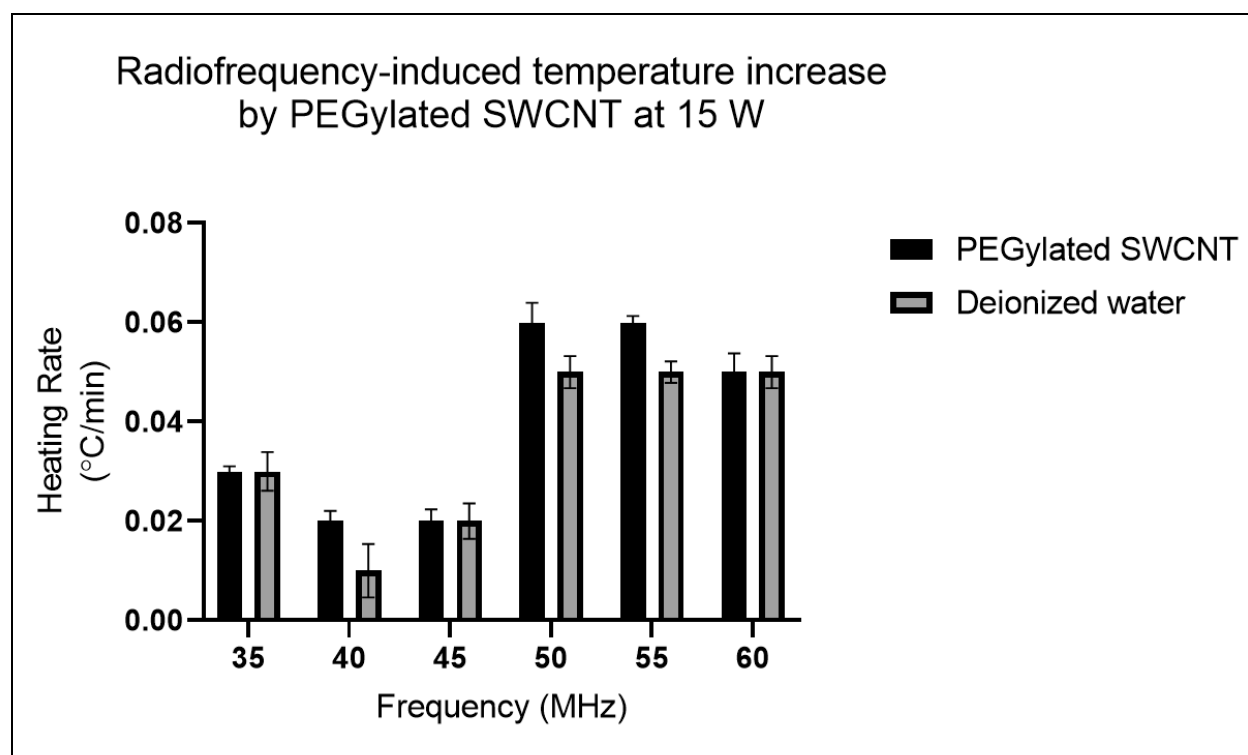


Figure 57: Assessment of the effect of frequency in the responsivity of SWCNT to the RF irradiation at 15 W power output. Dr. Caleb Fulton and student Josh Short designed a radiofrequency generator and matching network to create an RF field between two horizontal plates. For each test, matching conditions were assessed by a network analyzer. One mL samples of deionized water and PEGylated SWCNT (300 mg/mL) were placed in a cuvette and irradiated at different frequencies in the RF range. The temperature was measured by type K thermocouple inside of the liquid phase before and after the 8-min irradiation session. No statistical significance was

found between PEGylated SWCNT suspension and DI water for the rate of temperature increase in the range of 35 – 60 MHz using a power output of 15 W. Statistical analysis: unpaired t-test with Welch's correction for assumed unequal variances (n = 3).

Figure 57 shows no statistical significance between the SWCNT-PEG and control (DI water) was found. Additionally, the heating rates in this experiment are two orders of magnitude smaller than the ones found for SWCNT suspension irradiated with the Comdel system. Indeed, in the results previously depicted in this work, there is a trend of increasing the difference between the heating rate of CNT suspensions and the heating rate of control samples as the power output increases. It is hypothesized that the power output of the system for the experiments on varying the frequency might not be enough to produce significant results. This collaboration with Dr. Fulton is still in place, and there are already efforts to build another RF generator and matching network capable of delivering a higher power output between the plates.

Another set of experiments was designed to determine if the power output of 100 W is enough to generate statistically significant results between CNT suspensions and control. For that, Comdel System outputting 100 W was used. More accurate temperature measurement was achieved using the thermal camera FLIR ThermaCAM S60 and thermal images analysis with ThermaCAM Researcher Pro 2.7 Software. Samples of 1 ml completely filled glass cylindrical sample holder (8 mm radius and 35 mm height). Thermal images were taken before irradiation at 60 s of irradiation. The temperature was defined using analyzer software as the average temperature of superficial area of shell vial visualized by camera (see Appendix A - **Figure 80**). Smaller plates of 2 cm in width were used to concentrate the irradiation. Results are shown in **Figure 58**.

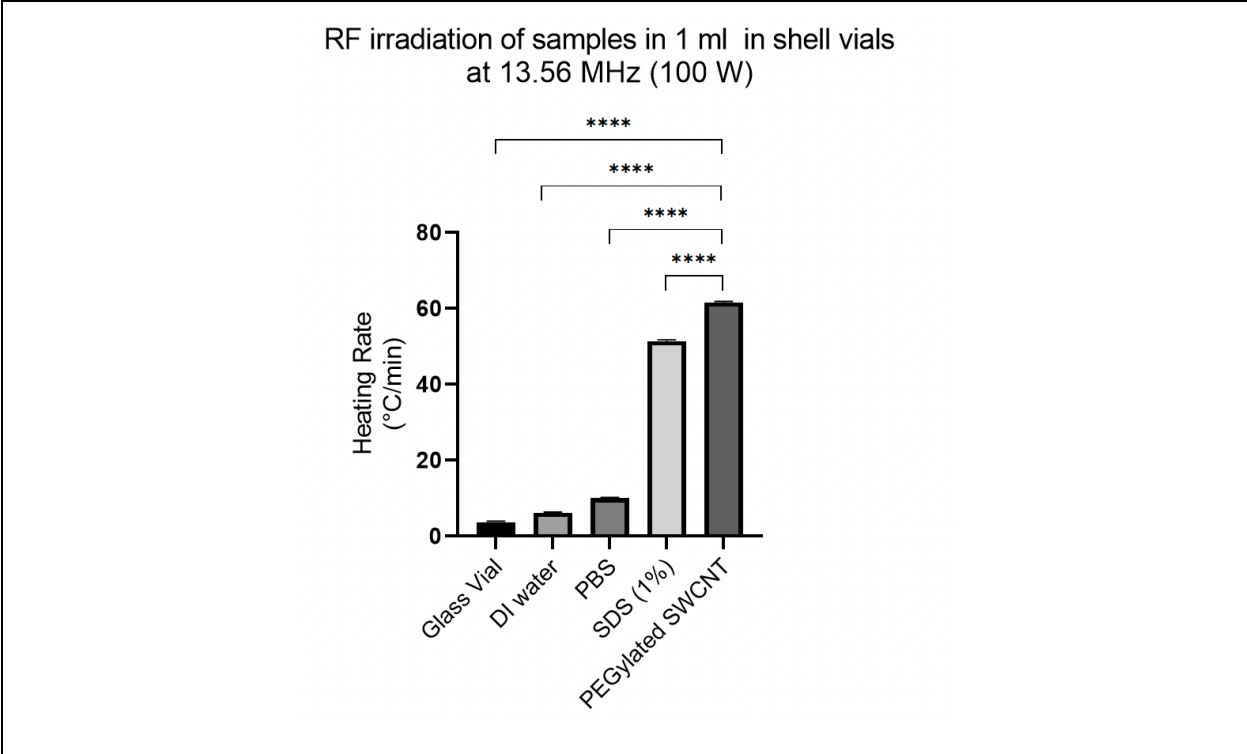


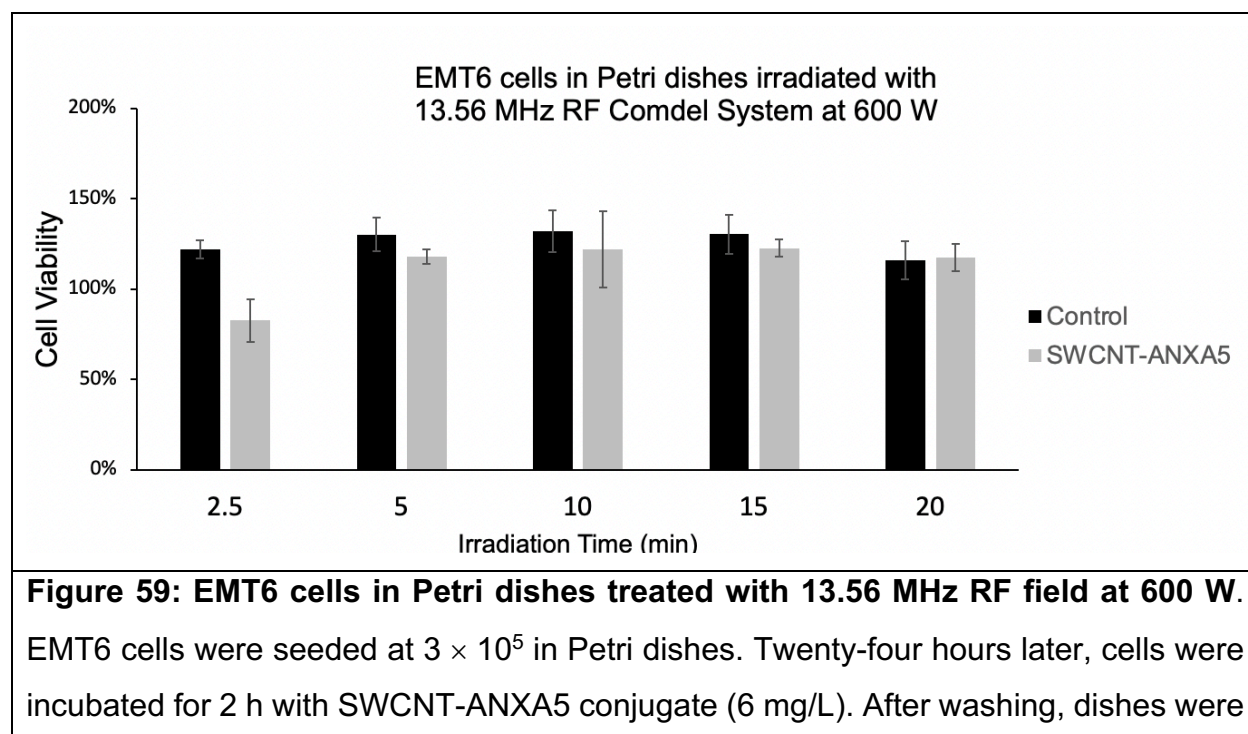
Figure 58: Analysis of statistical significance between samples irradiated with 100 W output power. Smaller irradiation plates designed by Dr. Fulton of 2 cm width were used to concentrate the field. Samples were placed in cylindrical sample holder (~1 ml, 8 mm in diameter and 35 mm height) and irradiated by Comdel System at 13.56 MHz with a power output of 100 W. Temperature was assessed with FLIR ThermaCAM S60 and analyzed with ThermaCAM Researcher Pro 2.7 Software, which measured the average temperature in the radial surface of the sample holder seen by camera. Thermal images were captured before irradiation; RF was turned on simultaneously with the timer. When the timer reached 60 s, another thermal image was captured, and the RF was turned off. Statistical Analysis: ordinary one-way ANOVA with Tukey's Multiple Comparison Test, which compares the mean of each group with the mean of every other group (n = 5). Every pair was considered significant with $p < 0.0001$, even though significance to PEGylated SWCNT was the only one depicted in the figure to avoid overcrowding of data on the graph.

Figure 58 shows that using a more advanced temperature measurement system generated results with lower standard deviations, which ultimately resulted in a

more robust statistical analysis. Even though the temperature of the glass vial is not precisely the temperature of the sample inside the vial, if more accurate results are necessary, that internal temperature can be estimated mathematically. The use of the thermal camera allowed minimization of errors in the measurement. Even the SDS (1%) and CNT were statistically significantly different at 100 W, which was not seen before with thermocouple temperature measurement. Therefore, the design of an RF system that delivers 100 W at various frequencies is supposedly sufficient to define the resonance frequency of (6,5) SWCNT.

3.3.2 SWCNT-ANXA5-mediated radiofrequency ablation in biological system

Attempts to apply the SWCNT-ANXA5-mediated radiofrequency ablation in biological systems were performed. First, EMT6 cells were plated in 35-mm Petri dishes and incubated for 2 hours with SWCNT-ANXA5. After washing with PBS, dishes were irradiated with 13.56 MHz in Comdel System at 600 W for different durations. The Alamar Blue assay was used to assess cell viability. Cells that were not incubated with conjugate were used as control. The results are shown in **Figure 59**.



irradiated with 13.56 MHz RF at 600 W for different durations. Alamar Blue assay assessed the cell viability after treatment. Statistical analysis was performed with an unpaired t-test with Welch's correction for assumed unequal variances (n = 3). No statistical significance was found between SWCNT-ANXA5 and control groups at any irradiation time.

Figure 59 shows that the RF irradiation of cells in Petri dishes did not induce a significant decrease in viability, neither for the cells incubated with SWCNT-ANXA5 nor for the ones in the control group. Even though the irradiation of SWCNT suspensions and SWCNT-ANXA5 have shown impressive results in terms of heating rate in the RF field, those results were not translated into a cytotoxic effect on cells in Petri dishes. We believe that similarly to the impact of geometry observed in this work for the irradiation of SWCNT suspensions (**Figure 54** and **Figure 55**), the positioning of the RF field perpendicularly to the monolayer of cells induces a minimal effect on the system. Those results can also be correlated to the evidence shown in Li *et al.*²⁸⁶, in which a dish with a shape similar to the Petri dish holding saline solution had a non-detectable heating rate in a vertical field of 13.56 MHz RF irradiation. In contrast, a vertical tube containing the same amount of saline had a substantial temperature rise in the same field. Therefore, we believe that the monolayer of cells should be aligned to the RF to induce a cytotoxic effect. The Comdel device lacks the flexibility of rotating the position of the plates in between which the field is generated. For this reason, we were precluded from testing that hypothesis since the rotation of the Petri dishes to align to the field would induce cell media spill and compromise the sterility of the experiment. Indeed, when Gannon *et al.*²⁵⁸ have shown evidence of cell death *in vitro* with the 13.56 MHz irradiation cells pretreated with SWCNT, it is mentioned that the monolayer of cells is aligned to the RF field. In conclusion, design changes in the Comdel system to generate a horizontal field are necessary to test the *in vitro* cytotoxic effect of SWCNT-ANXA5-mediated RFA.

Despite a lack of cytotoxic effect seen with *in vitro* experiments, *in vivo* studies were performed to test the SWCNT-mediated radiofrequency ablation (RFA). The reasoning behind that decision was that the inherent three-dimensional structure of a tumor in a mouse would offset the geometric limitations of the two-dimensional

arrangement of cells grown in Petri dishes. Thus, we first tested 13.56 MHz irradiation of euthanized mice. Euthanized mice were subjected to RF irradiation at 400 W. Surface temperature distribution was assessed with a thermal camera. The results are shown in **Figure 60**.

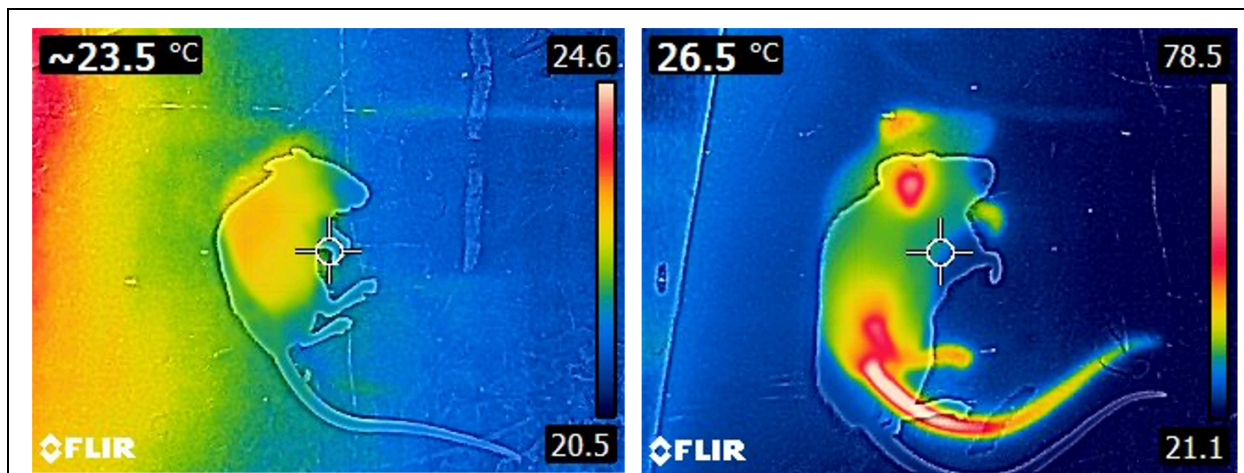


Figure 60: RF irradiation of euthanized mice at 400 W. Left panel: temperature distribution before irradiation; Right panel: temperature distribution after irradiation. Very high heating is observed in pointed parts of the mouse, especially the tail and ears. The temperature in those areas reached around 95° C.

In **Figure 60**, the pointed parts of the mouse received exceedingly high heating. It is important to point out that SWCNT was not used in this experiment. These results are essential for understanding how the geometry of the objects subjected to the RF field influences the heating. It is hypothesized that the pointed areas concentrate charge in the same manner that occurs in the principle related to the functionality of lightning rods. Therefore, we conjectured that, by reengineering the plates to smaller dimensions, the RF field would be concentrated in the abdominal region of the mouse where the tumor is located. With that, irradiating the whole mouse body would be avoided preventing the overheating of the pointed parts.

Accordingly, smaller plates were built by Dr. Fulton and connected to the Comdel system. The width of the new plates was reduced to 2 cm. EMT6-tumor-bearing

mice (> 5 mm) were separated into SWCNT and no SWCNT, where the former was injected with SWCNT-ANXA5 intratumorally and the latter was not. The thermal images of the mice after irradiation are shown in **Figure 61**. Mice were immediately euthanized by CO₂ asphyxiation after pictures were taken. Details of the setup are available in Appendix A – **Figure 81**.

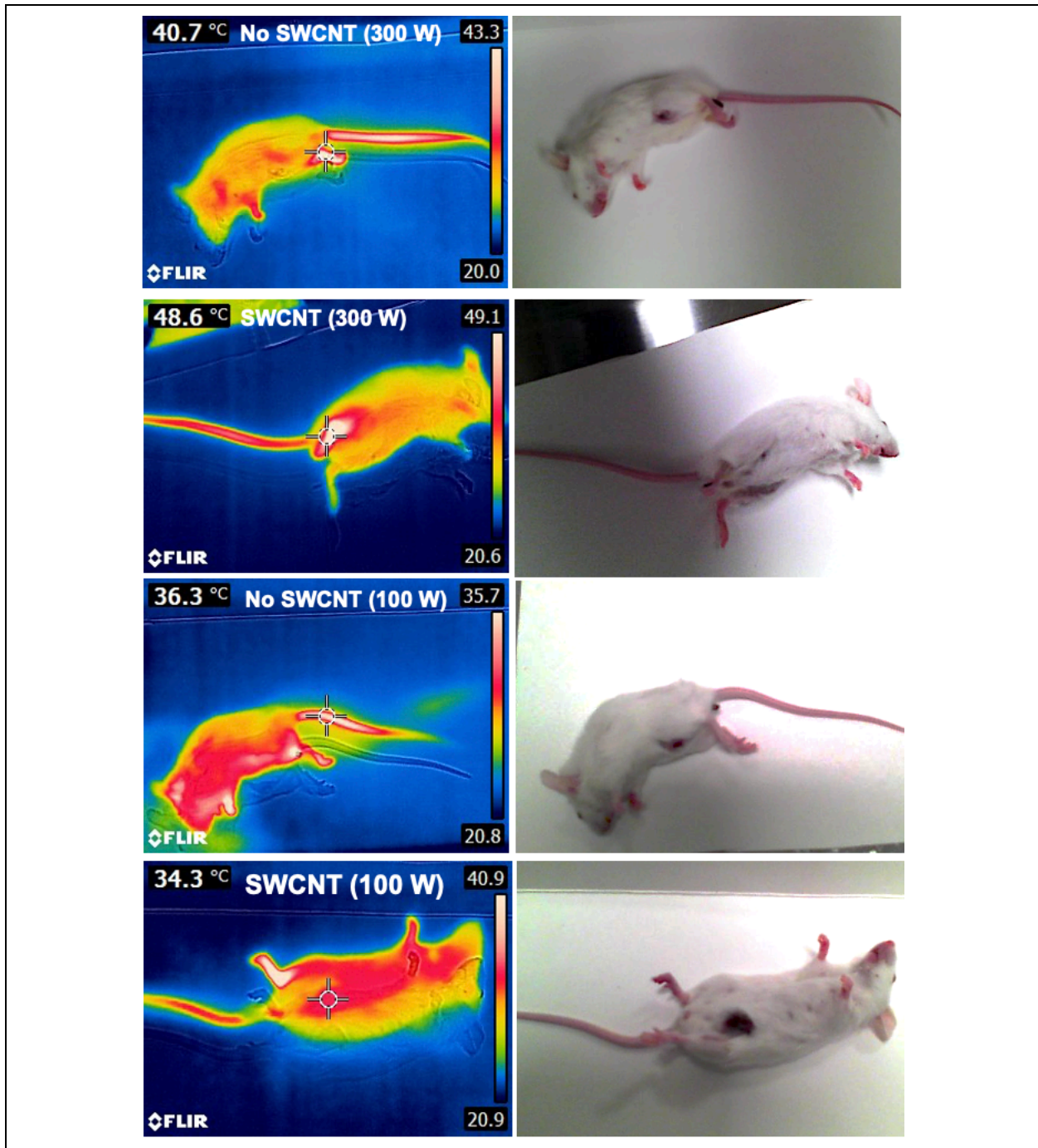


Figure 61: Irradiation of tumor-bearing mice with 13.56 MHz RF field in small plates. EMT6 tumor-bearing mice (> 5 mm) were injected with SWCNT-ANXA5 (1.2 mg/mg) intratumorally and treated with a 13.56 MHz RF field at 300 and 100 W. Mice were placed between RF plates with a width of 2 cm to concentrate the RF field to the abdominal area. Mouse temperature was monitored with FLIR E5xt thermal camera, and the irradiation session ceased when signs of overheating were detected. Thermal pictures were taken after turning off the RF generator. Thermal images on the left and respective photos on the right show the heating of the paws and the tail but no heating of the tumor region, even when the mice were intratumorally injected with conjugate (SWCNT group).

Figure 61 shows the attempt to concentrate the field to the abdominal area of the mice while testing SWCNT-ANXA5 mediated RFA *in vivo*. Even though the paws, tails, and ears were not in between the plates, overheating was observed in those areas, resulting in the irradiation session's ending. It is believed that the mice acted as antennae during irradiation absorbing the RF field more efficiently than the SWCNT. Additionally, live tissue has conductivity; therefore, the absorbed irradiation is concentrated in the paws, tail, and ears of the mouse due to the tendency of charges to build up in pointed objects.

Another attempt was made to avoid overheating those areas in the mouse by connecting the mouse extremities to the ground electrode of the RF machine. For that, aluminum stripes were taped on one side around paws, ears, and tails and on the other side to the ground electrode (see **Figure 82** of the setup in Appendix A). The setup was also not effective at avoiding overheating. Additionally, limitations were found with the grounding of the upper body due to the requirement of nose cone induced burning of the eyes in one mouse that was immediately euthanized. A more efficient grounding technique should be pursued if more experiments are to be performed for the SWCNT-ANXA5 mediated RFA *in vivo*. Some research groups were able to perform the grounding of mice irradiated with RF field between plates^{252,333,334}. Hence, improvements to our setup should be able to be made to achieve better results.

3.4 Gold nanoparticle – annexin A5 – DM1 conjugate

UV-vis spectroscopy was used to confirm the conjugation of DM1 to ANXA5, and the link of ANXA5-DM1 to AuNP. First, a standard curve for DM1 was obtained by endpoint absorption at 288 nm (**Figure 62**).

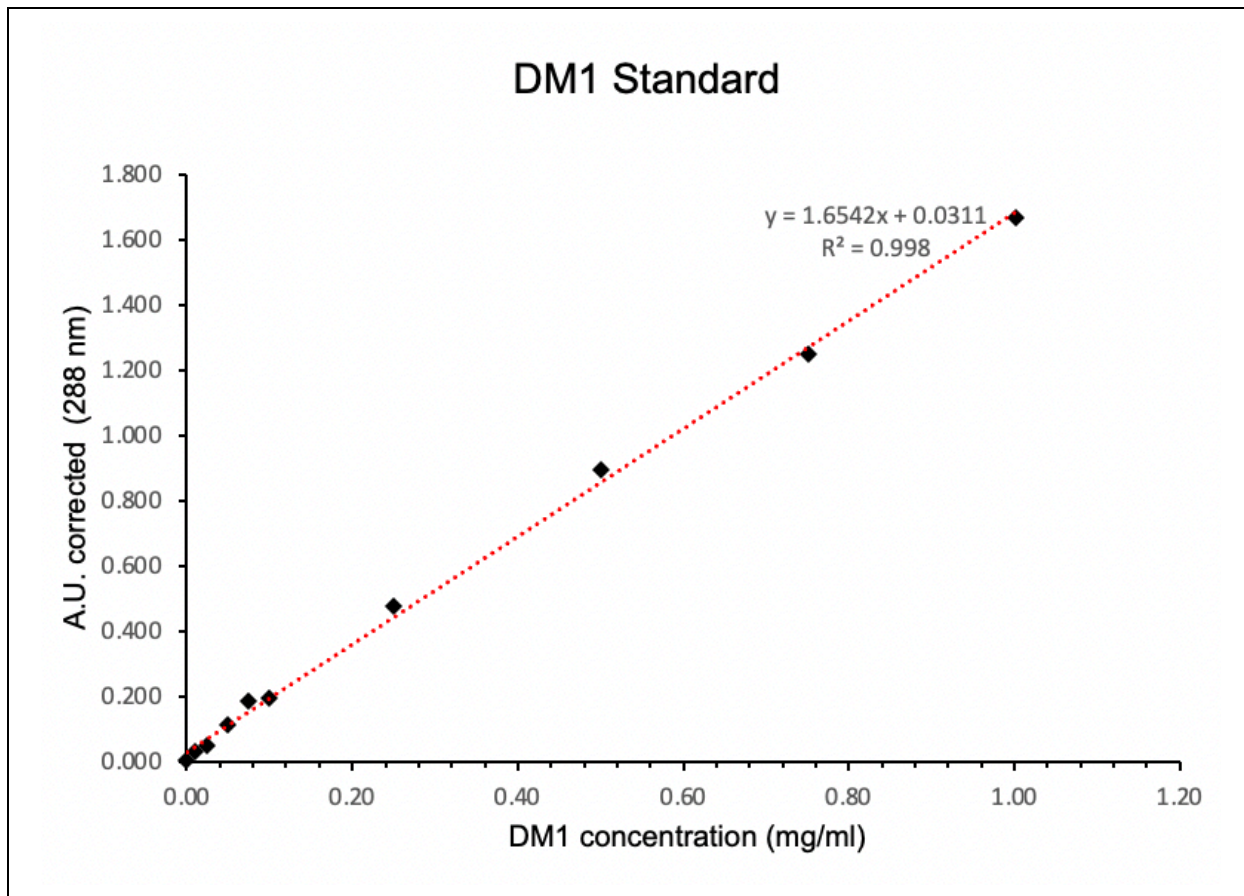


Figure 62: DM1 standard curve. For the standard solution of DM1, 3.0 mg of DM1 was dissolved in 1000 μL of DMSO. Serial dilutions were performed using DMSO. Samples of 100 μL from different concentrations were placed in 96-well plates. Endpoint absorption at 288 nm was measured using DMSO as blank.

The contribution of ANXA5 to the 288 nm signal was also assessed, obtaining a standard curve of ANXA5 in 288 nm, as shown in **Figure 63**.

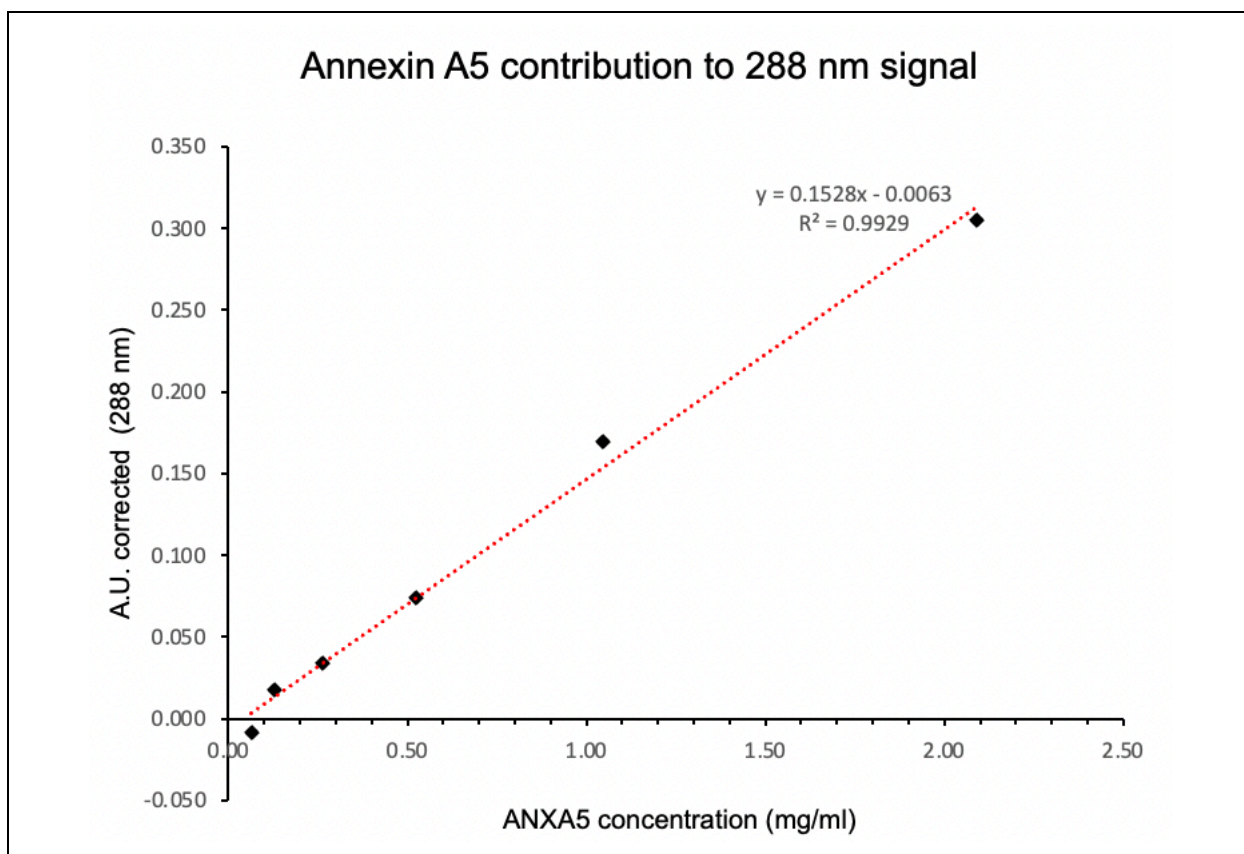


Figure 63: Annexin A5 contribution to 288 nm signal. A sample of ANXA5 with a known concentration was used as a standard solution. Serial dilutions were performed. Samples (100 μ L) were placed in wells in 96-well plates, and endpoint absorption was read at 288 nm using PBS as blank. This protocol is identical to the one used for the DM1 standard curve.

After conjugation, the concentration of ANXA5 in ANXA5-DM1 was assessed with the Bradford assay. The contribution of that ANXA5 concentration to the 288 nm signal was estimated using the standard curve in **Figure 63**. Then, the conjugate endpoint absorption at 288 nm was measured. The concentration of DM1 in the ANXA5-DM1 was calculated by subtracting ANXA5 contribution (**Figure 63**) from the total conjugate absorption at 288 nm and then comparing the subtracted result to the DM1 standard curve in **Figure 62**. The molar ratio of DM1/ ANXA5 was 9. The fact that there is an increase in the absorbance at 288 nm compared to unconjugated protein at the same concentration is evidence that the conjugation was effective.

Second, the ANXA5-DM1 conjugate was analyzed by SDS-PAGE on a 4-20% gradient denaturing gel, as shown in **Figure 64**.

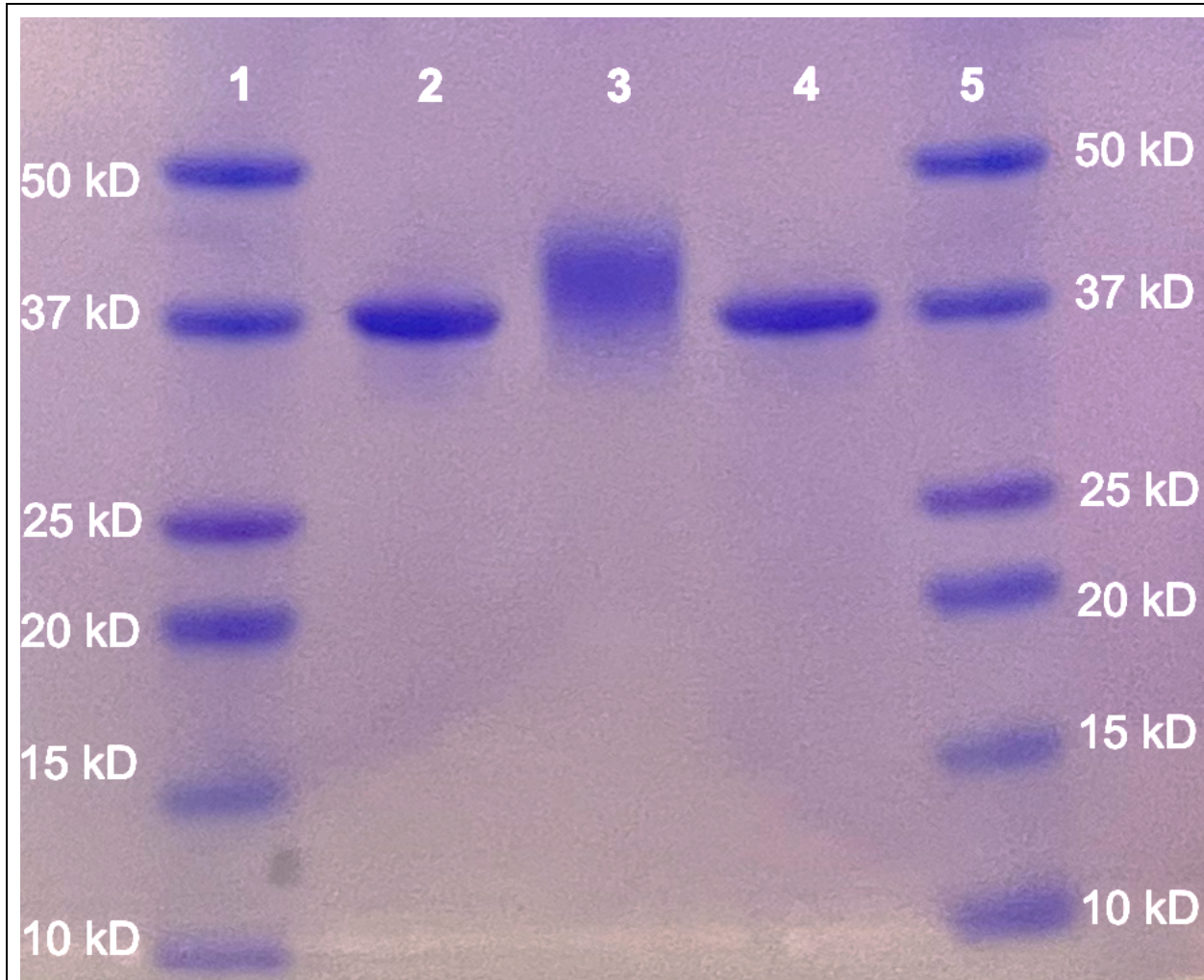


Figure 64: SDS-PAGE gel of ANXA5 and ANXA5-DM1. Samples of 5 μ L of each of the ANXA5 protein (0.4 mg/mL) and ANXA5-DM1 conjugate (0.4 mg/mL) were denatured by boiling with 5 μ L Laemmli sample buffer. The ladder provides molecular weight standards to estimate the size of proteins separated by gel electrophoresis. 1,5) Molecular ladder; 2,4) unconjugated ANXA5; 3) ANXA5-DM1 conjugate. The increase in molecular weight compared to unconjugated ANXA5 is evidence of successful conjugation.

SDS-PAGE electrophoresis separates proteins based on size. An electric potential is applied to the gel, causing proteins to migrate through the gel. Larger proteins are more impeded from moving through the gel than smaller or unconjugated proteins. **Figure 64** shows that the unconjugated protein in lanes two and four migrated farther than ANXA5-DM1. Additionally, the absence of other protein bands confirms the purity of both ANXA5 and ANXA5-DM1 and the lack of protein-protein linkage during conjugation.

UV-vis spectroscopy was also used to prove the linkage of ANXA5-DM1 to AuNP. First, the contribution of AuNP to Bradford Assay at various concentrations of AuNP was used to create a standard curve at 595 nm. Bradford reagent (250 μL) was added to wells in 96-well plates. AuNP samples (5 μL) with known concentrations were added to the Bradford reagent samples. Endpoint absorbance at 595 nm was measured to obtain a standard curve for the contribution of AuNP to the Bradford assay, as shown in **Figure 65**.

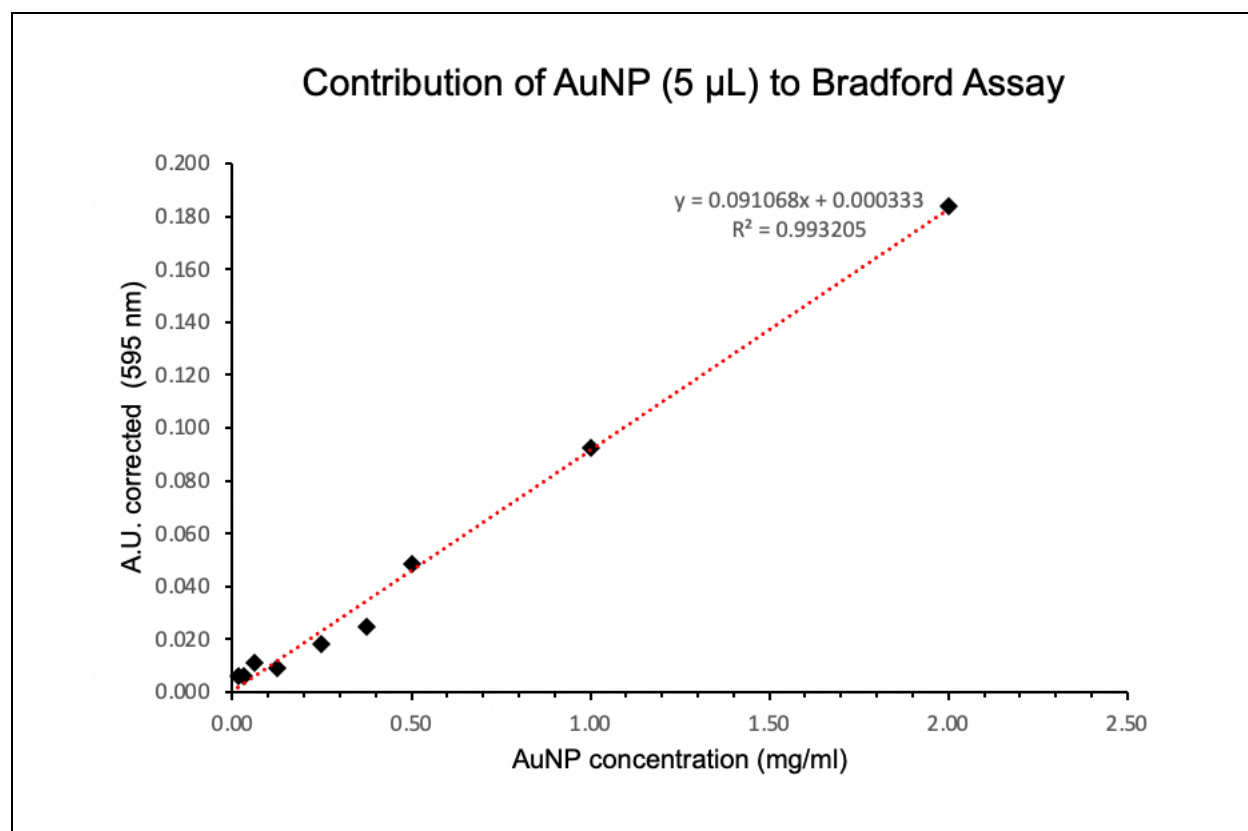


Figure 65: Contribution of AuNP to Bradford assay. A standard curve for AuNP in Bradford Reagent was obtained by adding 5 μL of AuNP samples with a known

concentration in 250 μ L of Bradford reagent. The endpoint absorbance was read at 595 nm. Blank was 5 μ L of PBS + 250 μ L of Bradford reagent. This protocol is identical to the one used for the Bradford assay to measure protein concentration.

After the linkage of AuNP to ANXA5-DM1, the concentration of AuNP was assessed using absorbance at 520 nm and compared to the standard curve previously obtained (available in Appendix A – **Figure 82**). The contribution of the measured AuNP concentration to the Bradford assay in the AuNP-ANXA5-DM1 was estimated using the standard in **Figure 65**. Then, a Bradford assay was performed with the conjugate. The signal obtained from the AuNP was subtracted from the signal obtained from the conjugate in the Bradford assay. The concentration of protein in the AuNP-ANXA5-DM1 was determined using the adjusted signal and compared to the protein concentration standard curve. The presence of protein in AuNP-ANXA5-DM1 assessed by Bradford assay is evidence that the link between AuNP and ANXA5-DM1 was successful.

Additionally, AuNP and AuNP-ANXA5-DM1 were assayed in a horizontal agarose gel electrophoresis. The results are shown in **Figure 66**.

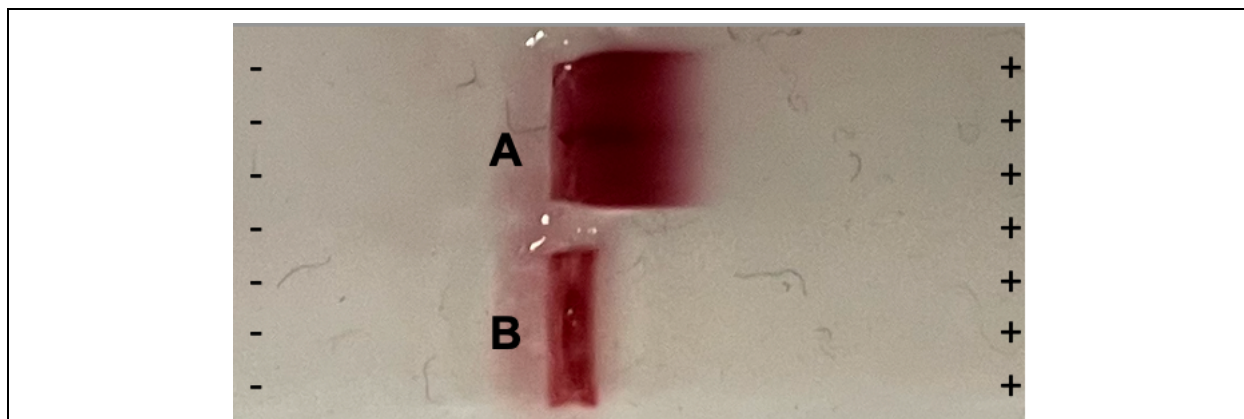


Figure 66: Agarose gel electrophoresis of AuNP and AuNP-ANXA5-DM1 conjugate. Agarose gel was cast with TAE buffer and 1 % agarose. Samples were loaded into the wells at a concentration of \sim 2 mg/ml with 10% glycerol. Samples were run in a horizontal electrophoresis chamber at 80 V for 10 min. A) free AuNP. B) AuNP-ANXA5-DM1. Smaller particles, such as AuNP, move further and fast through the gel,

while larger particles, such as AuNP-ANXA5-DM1, slower down the gel, which confirms conjugation.

An agarose gel allows nanomaterials to move through an electric field based on size. Smaller particles, such as AuNP, travel further down the gel, while larger particles, such as AuNP-ANXA5-DM1, travel slower. As seen in **Figure 66**, AuNP moved the furthest (**Figure 66A**), while AuNP-ANXA5-DM1 did not move for the duration of the assay (**Figure 66B**). This is evidence that the conjugation of ANXA5-DM1 to AuNP.

The concentration of DM1 in AuNP-ANXA5-DM1 was inferred from the concentration of ANXA5 in the conjugate. For that, it was assumed that the molar ratio of DM1/ANXA5 before and after the linkage to AuNP did not change.

After confirming the conjugation, a cytotoxicity assay was performed to compare the toxicity of AuNP-ANXA5-DM1 to ANXA5-DM1 and free DM1. EMT6 cells were treated with different concentrations of DM1 in both conjugates and DM1 alone. After 72 h, cell viability was assessed using the Alamar Blue assay. The results can be seen in **Figure 67**.

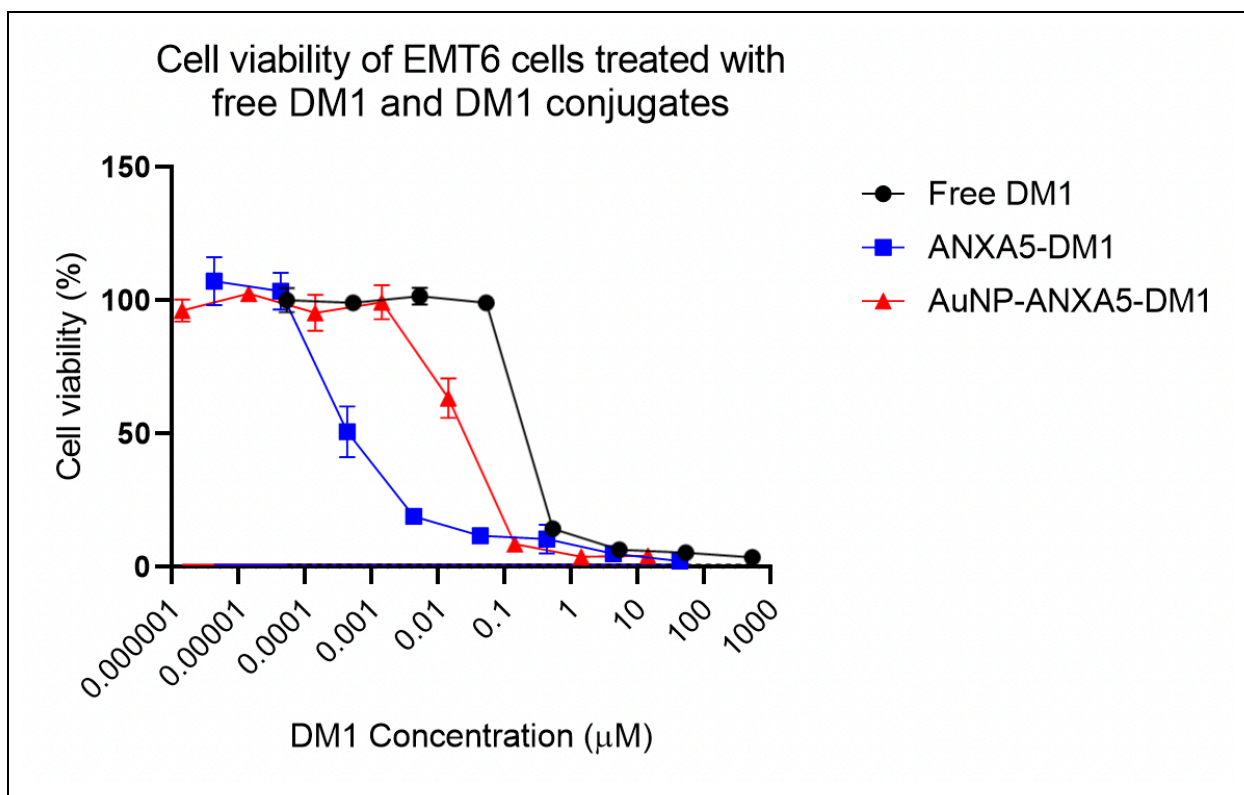


Figure 67: Cell viability of EMT6 cells treated with free DM1 and DM1 conjugates. EMT6 cells were treated for 72 h with free DM1 (black), ANXA5-DM1 (blue), and AuNP-ANXA5-DM1 (red). After treatment, the Alamar Blue assay was performed to assess cell viability.

Figure 67 shows the comparative cytotoxicity of free DM1, ANXA5-DM1, and AuNP-ANXA5-DM1. Half maximal effective concentration (EC₅₀) is the parameter used to compare cytotoxicity curves and indicates the concentration of the drug that induces the killing of 50% of the cells. In this assay, the EC₅₀ of free DM1 was ~0.2 µM, AuNP-ANXA5-DM1 was ~0.02 µM, and ANXA5-DM1 was ~0.0004 µM. Previous students in this lab have reported similar results for free DM1 and ANXA5-DM1, which validates the results found in this work. The conjugation of DM1 to ANXA5 improves the effectiveness of the drug 500 times, while the conjugation of ANXA5-DM1 to AuNP limited the increase of cytotoxic effect to only ten times *in vitro*.

From those results, it is hypothesized that AuNP-ANXA5-DM1 has a limited internalization rate compared to ANXA5-DM1. Various parameters might cause that

limitation. Diffusion is a possible cause of this decrease in effectiveness since the attachment of ANXA5-DM1 to a much larger particle limits the rate of diffusion of the species in solution, thus decreasing the collisions between particle and cell surface. Another explanation might be related to the mechanism of internalization of ANXA5. It is believed that ANXA5 induces non-receptor-mediated internalization due to the formation of a convex crystal lattice from trimers of the protein (as shown in **Figure 10** and **Figure 11**). A particular 3D orientation characterizes crystal lattices. By linking ANXA5-DM1 to AuNP, the protein loses degrees of freedom, which might hinder the possibility of orienting itself to the other neighboring proteins to form the trimer that induces the internalization.

Although those results are not as encouraging as expected, linking ANXA5-DM1 to AuNP might have therapeutic advantages *in vivo*. Because of the limited diffusion of AuNP-ANXA5-DM1, AuNP might be able to lock the conjugate in the site of injection in the case of intratumoral injections. DM1 is a highly toxic drug that induces systemic toxicity and cannot be administered in humans as a free drug. Therefore, hindering the drug diffusion from a site of intratumoral injection to the system might prevent side effects from the protein-drug conjugation. Additionally, our lab has started the experiments *in vivo* with the administration of ANXA5-DM1 intratumorally. One relevant limitation was the immediate release of part of the injected volume outside of the tumor, due to the toughness of the tumors. We believe that the link to AuNP would prevent that phenomenon during injections.

CHAPTER 4 – CONCLUSIONS AND FUTURE
DIRECTIONS

Here, we demonstrate a novel combinatorial treatment modality where we obtain a high survival rate in mice with aggressive metastatic breast cancer, the EMT6 tumor model, using SWCNT-ANXA5-mediated photothermal therapy at lower temperature combined with anti-PD-1-based checkpoint inhibition. The study of the temperature of photothermal therapy is crucial for the safety of the treatment and the potential translation to clinical trials. A lower PTT temperature in a relatively immunogenic tumor would be enough to generate a systemic immune response when combined with checkpoint inhibition. Additionally, the transition from intravenous to intratumoral injection improved immune activation and prevented the accumulation of the SWCNT in major organs. Even though just the original tumor was given radiation treatment, it is interesting to note that mice with metastatic cancer that received combinatorial therapy lived longer. Only the combination of both treatment modalities enhanced the amount of CD4+ helper and CD8+ cytotoxic T cells in the EMT6 tumor model, according to a mechanistic investigation that quantified the splenic antitumor effector cells. According to our hypothesis, this rise in T cells results from an abscopal response, in which antitumoral effector cells prevent tumor spread.

In this work we could compare the response of different tumor models, EMT6 and 4T1, to the combinatorial treatment of anti-PD-1 and SWCNT-ANXA5-mediated PTT. The aggressiveness and non-immunogenicity of 4T1 required a more a belligerent approach to treat this tumor model. The PTT temperature was raised to 55°C and we added the immunoadjuvant IMQ to attract immune cells to the tumor microenvironment. Here, we presented a novel combination therapy of immunoadjuvant, anti-PD-1 checkpoint inhibition, SWCNT-ANXA5-mediated PTT to treat non-immunogenic and metastatic triple negative breast cancer. This therapy was able to increase survival compared to any other treatment. Markers of systemic immune response was also found in this treatment strategy, confirming the hypothesis an abscopal response after the local irradiation of tumor, which combated metastasis.

Future work can be done studying a lower dose of intratumorally injected SWCNT-ANXA5. Here we used a dose previously optimized for the systemic administration of the conjugate. Due to the very high bioavailability of the SWCNT in the tumor, which in 100% of the injection dose is confined to the injection site, a lower dose

of SWCNT-ANXA5 could be efficient at inducing the ablation and promoting favorable thermal kinetics. Additionally, other cancer types that are considered non-immunogenic can be tested for the treatment that was successful at treating 4T1 tumors. ANXA5 is a biomarker in many cancer types, which allows the translation of this strategy to other models.

Here we also demonstrated the responsiveness of SWCNT to the radiofrequency field. Even though the complexity of this response is greater than the NIR-irradiation, there is enough evidence to attribute a highly effective heating of SWCNT in response to the RF field. Design changes in the RF generator, such as flexibility in the orientation of the field generated between plates, could possibly give positive results in biological systems. Additionally, the use of needle-like electrodes for a more localized RF field generated *in vivo*, such as the devices currently used in the clinics for RFA, might be able to avoid the negative results seen in the irradiation of mice between plates. Furthermore, the use of devices that are already approved for humans might facilitate the translation of a CNT-mediated RFA to clinical settings.

In this work, a novel theranostic agent comprised of gold nanoparticles (AuNP), the targeting protein annexin A5 (ANXA5) and the chemotherapeutic agent mertansine (DM1) was developed. Previously published evidence shows increased detection of breast tumors with ANXA5 targeted versus untargeted gold nanoparticles in microCT²⁸¹. Additionally, here we showed results of the cytotoxic effect of the conjugate. Therefore, we have developed a multi-modal nanoparticle for the detection and therapy of breast cancer, which can deliver DM1 to tumors while improving the detection of breast cancer. Future work would include the study of the conjugate *in vivo* to determine if the limitations of the intratumoral injection of ANXA5-DM1 are surpassed by the link to the AuNP. Additionally, the combination of chemotherapy to PTT would be feasible with the irradiation of tumors similarly to the PTT here studied using the AuNP-ANXA5-DM1 conjugate. Nonetheless, adjustments of laser wavelength to 800 nm (AuNP peak absorbance) requires the acquisition of another laser generator device.

Breast cancer is still a challenge worldwide and the development of novel treatment strategies is necessary. This dissertation introduces valuable knowledge that can be used in the translation of pre-clinical research into humans.

REFERENCES

1. Ribatti, D. An historical note on the cell theory. *Experimental Cell Research* **364**, 1–4 (2018).
2. Cooper, G. M. *The cell: a molecular approach*. (Sinauer Associates, an imprint of Oxford University Press, 2019).
3. Rees, D. C., Johnson, E. & Lewinson, O. ABC transporters: the power to change. *Nat Rev Mol Cell Biol* **10**, 218–227 (2009).
4. Catterall, W. A. Ion Channel Voltage Sensors: Structure, Function, and Pathophysiology. *Neuron* **67**, 915–928 (2010).
5. Singer, S. J. & Nicolson, G. L. The Fluid Mosaic Model of the Structure of Cell Membranes. *Science* **175**, 720–731 (1972).
6. Nicolson, G. L. The Fluid—Mosaic Model of Membrane Structure: Still relevant to understanding the structure, function and dynamics of biological membranes after more than 40years. *Biochimica et Biophysica Acta (BBA) - Biomembranes* **1838**, 1451–1466 (2014).
7. Kalappurakkal, J. M., Sil, P. & Mayor, S. Toward a new picture of the living plasma membrane. *Protein Science* **29**, 1355–1365 (2020).
8. Murate, M. *et al.* Transbilayer lipid distribution in nano scale. *Journal of Cell Science* jcs.163105 (2015) doi:10.1242/jcs.163105.
9. van Meer, G., Voelker, D. R. & Feigenson, G. W. Membrane lipids: where they are and how they behave. *Nat Rev Mol Cell Biol* **9**, 112–124 (2008).
10. Bretscher, M. S. Asymmetrical Lipid Bilayer Structure for Biological Membranes. *Nature New Biology* **236**, 11–12 (1972).
11. Verkleij, A. J., Zwaal, R. F. A., Roelofsen, B., Comfurius, P. & Kastelijn, D. THE ASYMMETRIC DISTRIBUTION OF PHOSPHOLIPIDS IN THE HUMAN RED CELL MEMBRANE. 16.

12. Op den Kamp, J. A. F. Lipid Asymmetry in Membranes. *Annu. Rev. Biochem.* **48**, 47–71 (1979).
13. Devaux, P. F. & Morris, R. Transmembrane Asymmetry and Lateral Domains in Biological Membranes: Rafts and Transmembrane Asymmetry. *Traffic* **5**, 241–246 (2004).
14. Son, M. & London, E. The dependence of lipid asymmetry upon polar headgroup structure. *Journal of Lipid Research* **54**, 3385–3393 (2013).
15. Shin, H.-W. & Takatsu, H. Substrates of P4-ATPases: beyond aminophospholipids (phosphatidylserine and phosphatidylethanolamine). *FASEB j.* **33**, 3087–3096 (2019).
16. Murate, M. & Kobayashi, T. Revisiting transbilayer distribution of lipids in the plasma membrane. *Chemistry and Physics of Lipids* **194**, 58–71 (2016).
17. Clarke, R. J., Hossain, K. R. & Cao, K. Physiological roles of transverse lipid asymmetry of animal membranes. *Biochimica et Biophysica Acta (BBA) - Biomembranes* **1862**, 183382 (2020).
18. Zachowski, A. Phospholipids in animal eukaryotic membranes: transverse asymmetry and movement. *Biochemical Journal* **294**, 1–14 (1993).
19. McConnell, H. M. & Kornberg, R. D. Inside-outside transitions of phospholipids in vesicle membranes. *Biochemistry* **10**, 1111–1120 (1971).
20. Hirata, F. & Axelrod, J. Enzymatic synthesis and rapid translocation of phosphatidylcholine by two methyltransferases in erythrocyte membranes. *Proceedings of the National Academy of Sciences* **75**, 2348–2352 (1978).
21. De Kruijff, B., Van Zoelen, E. J. J. & Van Deenen, L. L. M. Glycophorin facilitates the transbilayer movement of phosphatidylcholine in vesicles. *Biochimica et Biophysica Acta (BBA) - Biomembranes* **509**, 537–542 (1978).
22. Nguyen, M. H. L. *et al.* Peptide-Induced Lipid Flip-Flop in Asymmetric Liposomes Measured by Small Angle Neutron Scattering. *Langmuir* **35**, 11735–11744 (2019).
23. Devaux, P. F. Protein Involvement in Transmembrane Lipid Asymmetry. 25.

24. Doktorova, M., Symons, J. L. & Levental, I. Structural and functional consequences of reversible lipid asymmetry in living membranes. *Nat Chem Biol* **16**, 1321–1330 (2020).
25. Ikeda, M., Kihara, A. & Igarashi, Y. Lipid Asymmetry of the Eukaryotic Plasma Membrane: Functions and Related Enzymes. *Biological & Pharmaceutical Bulletin* **29**, 1542–1546 (2006).
26. Kobayashi, T. & Menon, A. K. Transbilayer lipid asymmetry. *Current Biology* **28**, R386–R391 (2018).
27. Shin, H.-W. & Takatsu, H. Phosphatidylserine exposure in living cells. *Critical Reviews in Biochemistry and Molecular Biology* **55**, 166–178 (2020).
28. Seigneuret, M. & Devaux, P. F. ATP-dependent asymmetric distribution of spin-labeled phospholipids in the erythrocyte membrane: relation to shape changes. *Proceedings of the National Academy of Sciences* **81**, 3751–3755 (1984).
29. Morrot, G., Zachowski, A. & Devaux, P. F. Partial purification and characterization of the human erythrocyte Mg²⁺-ATPase A candidate aminophospholipid translocase. *FEBS Letters* **266**, 29–32 (1990).
30. Tang, X., Halleck, M. S., Schlegel, R. A. & Williamson, P. A Subfamily of P-Type ATPases with Aminophospholipid Transporting Activity. *Science* **272**, 1495–1497 (1996).
31. Quazi, F. & Molday, R. S. Differential Phospholipid Substrates and Directional Transport by ATP-binding Cassette Proteins ABCA1, ABCA7, and ABCA4 and Disease-causing Mutants. *Journal of Biological Chemistry* **288**, 34414–34426 (2013).
32. Neumann, J., Rose-Sperling, D. & Hellmich, U. A. Diverse relations between ABC transporters and lipids: An overview. *Biochimica et Biophysica Acta (BBA) - Biomembranes* **1859**, 605–618 (2017).
33. Pomorski, T. G. & Menon, A. K. Lipid somersaults: Uncovering the mechanisms of protein-mediated lipid flipping. *Progress in Lipid Research* **64**, 69–84 (2016).
34. Watanabe, R., Sakuragi, T., Noji, H. & Nagata, S. Single-molecule analysis of phospholipid scrambling by TMEM16F. *Proc Natl Acad Sci USA* **115**, 3066–3071 (2018).

35. Clark, M. R. Flippin' lipids. *Nat Immunol* **12**, 373–375 (2011).
36. Bethel, N. P. & Grabe, M. Atomistic insight into lipid translocation by a TMEM16 scramblase. *Proc Natl Acad Sci USA* **113**, 14049–14054 (2016).
37. Pomorski, T. & Menon, A. K. Lipid flippases and their biological functions. *Cell. Mol. Life Sci.* **63**, 2908–2921 (2006).
38. Suzuki, J., Umeda, M., Sims, P. J. & Nagata, S. Calcium-dependent phospholipid scrambling by TMEM16F. *Nature* **468**, 834–838 (2010).
39. Varga-Szabo, D., Braun, A. & Nieswandt, B. Calcium signaling in platelets. *Journal of Thrombosis and Haemostasis* **7**, 1057–1066 (2009).
40. Bevers, E. M., Comfurius, P., Van Rijn, J. L. M. L. & Hemker, H. C. Generation of Prothrombin-Converting Activity and the Exposure of Phosphatidylserine at the Outer Surface of Platelets. *Eur J Biochem* **122**, 429–436 (1982).
41. Suzuki, J., Denning, D. P., Imanishi, E., Horvitz, H. R. & Nagata, S. Xk-Related Protein 8 and CED-8 Promote Phosphatidylserine Exposure in Apoptotic Cells. *Science* **341**, 403–406 (2013).
42. Nagata, S. Apoptosis and Clearance of Apoptotic Cells. *Annu. Rev. Immunol.* **36**, 489–517 (2018).
43. Savitskaya, M. A. & Onishchenko, G. E. Mechanisms of apoptosis. *Biochemistry Moscow* **80**, 1393–1405 (2015).
44. Hankins, H. M., Baldrige, R. D., Xu, P. & Graham, T. R. Role of Flippases, Scramblases and Transfer Proteins in Phosphatidylserine Subcellular Distribution. *Traffic* **16**, 35–47 (2015).
45. Birge, R. B. *et al.* Phosphatidylserine is a global immunosuppressive signal in efferocytosis, infectious disease, and cancer. *Cell Death Differ* **23**, 962–978 (2016).
46. Lemke, G. How macrophages deal with death. *Nat Rev Immunol* **19**, 539–549 (2019).

47. Sharma, B. & Kanwar, S. S. Phosphatidylserine: A cancer cell targeting biomarker. *Seminars in Cancer Biology* **52**, 17–25 (2018).
48. Riedl, S. *et al.* In search of a novel target — Phosphatidylserine exposed by non-apoptotic tumor cells and metastases of malignancies with poor treatment efficacy. *Biochimica et Biophysica Acta (BBA) - Biomembranes* **1808**, 2638–2645 (2011).
49. Schröder-Borm, H., Bakalova, R. & Andrä, J. The NK-lysin derived peptide NK-2 preferentially kills cancer cells with increased surface levels of negatively charged phosphatidylserine. *FEBS Letters* **579**, 6128–6134 (2005).
50. Vallabhapurapu, S. D. *et al.* Variation in human cancer cell external phosphatidylserine is regulated by flippase activity and intracellular calcium. *Oncotarget* **6**, 34375–34388 (2015).
51. Ran, S., Downes, A. & Thorpe, P. E. Increased Exposure of Anionic Phospholipids on the Surface of Tumor Blood Vessels. 10.
52. Ran, S. & Thorpe, P. E. Phosphatidylserine is a marker of tumor vasculature and a potential target for cancer imaging and therapy. *International Journal of Radiation Oncology*Biophysics* **54**, 1479–1484 (2002).
53. Lima, L. G., Chammas, R., Monteiro, R. Q., Moreira, M. E. C. & Barcinski, M. A. Tumor-derived microvesicles modulate the establishment of metastatic melanoma in a phosphatidylserine-dependent manner. *Cancer Letters* **283**, 168–175 (2009).
54. Liang, P. & Yang, H. Molecular underpinning of intracellular pH regulation on TMEM16F. *Journal of General Physiology* **153**, e202012704 (2021).
55. Xu, J. *et al.* ATP11B inhibits breast cancer metastasis in a mouse model by suppressing externalization of nonapoptotic phosphatidylserine. *Journal of Clinical Investigation* **132**, e149473 (2022).
56. Fadok, V. A., Voelker, D. R., Campbell, P. A., Cohen, J. J. & Henson, P. M. Exposure of phosphatidylserine on the surface of apoptotic lymphocytes triggers specific recognition and removal by macrophages. 11.

57. Albert, M. L., Sauter, B. & Bhardwaj, N. Dendritic cells acquire antigen from apoptotic cells and induce class I-restricted CTLs. *Nature* **392**, 86–89 (1998).
58. Eladl, E. *et al.* Role of CD47 in Hematological Malignancies. *J Hematol Oncol* **13**, 96 (2020).
59. Kim, R., Emi, M. & Tanabe, K. Cancer cell immune escape and tumor progression by exploitation of anti-inflammatory and pro-inflammatory responses. *Cancer Biology & Therapy* **4**, 924–933 (2005).
60. Taylor, A., Verhagen, J., Blaser, K., Akdis, M. & Akdis, C. A. Mechanisms of immune suppression by interleukin-10 and transforming growth factor-beta: the role of T regulatory cells. *Immunology* **117**, 433–442 (2006).
61. Chang, W., Fa, H., Xiao, D. & Wang, J. Targeting phosphatidylserine for Cancer therapy: prospects and challenges. *Theranostics* **10**, 9214–9229 (2020).
62. Kelleher, R. J. *et al.* Extracellular Vesicles Present in Human Ovarian Tumor Microenvironments Induce a Phosphatidylserine-Dependent Arrest in the T-cell Signaling Cascade. *Cancer Immunology Research* **3**, 1269–1278 (2015).
63. Reutelingsperger, C. P. M., Kop, M. M., Hornstra, G. & Hemker, H. C. Purification and characterization of a novel protein from bovine aorta that inhibits coagulation. **8**.
64. Tait, J. F., Gibson, D. & Fujikawa, K. Phospholipid binding properties of human placental anticoagulant protein-I, a member of the lipocortin family. *Journal of Biological Chemistry* **264**, 7944–7949 (1989).
65. Andree, H. A. *et al.* Clustering of lipid-bound annexin V may explain its anticoagulant effect. *Journal of Biological Chemistry* **267**, 17907–17912 (1992).
66. Tait, J. F., Gibson, D. F. & Smith, C. Measurement of the affinity and cooperativity of annexin V–membrane binding under conditions of low membrane occupancy. *Analytical Biochemistry* **329**, 112–119 (2004).
67. Huber, R., Römisch, J. & Paques, E. P. The crystal and molecular structure of human annexin V, an anticoagulant protein that binds to calcium and membranes. *The EMBO Journal* **9**, 3867–3874 (1990).

68. Huber, R., Schneider, M., Mayr, I., Römisch, J. & Paques, E.-P. The Calcium Binding Sites in Human Annexin V by Crystal Structure Analysis at 2.0 Å Resolution. Implications for Membrane Binding and Calcium Channel Activity. *FEBS Lett* **275**, 15–21 (1990).
69. Swairjo, M. A., Concha, N. O., Kaetzel, M. A., Dedman, J. R. & Seaton, B. A. Ca²⁺-bridging mechanism and phospholipid head group recognition in the membrane-binding protein annexin V. *Nat Struct Mol Biol* **2**, 968–974 (1995).
70. Kenis, H. *et al.* Cell Surface-expressed Phosphatidylserine and Annexin A5 Open a Novel Portal of Cell Entry. *Journal of Biological Chemistry* **279**, 52623–52629 (2004).
71. Oling, F. *et al.* Structure of Membrane-bound Annexin A5 Trimers: A Hybrid Cryo-EM - X-ray Crystallography Study. *Journal of Molecular Biology* **304**, 561–573 (2000).
72. Oling, F., Bergsma-Schutter, W. & Brisson, A. Trimers, Dimers of Trimers, and Trimers of Trimers Are Common Building Blocks of Annexin A5 Two-Dimensional Crystals. *Journal of Structural Biology* **133**, 55–63 (2001).
73. van Genderen, H. O., Kenis, H., Hofstra, L., Narula, J. & Reutelingsperger, C. P. M. Extracellular annexin A5: Functions of phosphatidylserine-binding and two-dimensional crystallization. *Biochimica et Biophysica Acta (BBA) - Molecular Cell Research* **1783**, 953–963 (2008).
74. van Heerde, W. L., Poort, S., van 't Veer, C., Reutelingsperger, C. P. M. & de Groot, P. G. Binding of recombinant annexin V to endothelial cells: effect of annexin V binding on endothelial-cell-mediated thrombin formation. *Biochemical Journal* **302**, 305–312 (1994).
75. Mallat, Z. *et al.* Shed Membrane Microparticles With Procoagulant Potential in Human Atherosclerotic Plaques: A Role for Apoptosis in Plaque Thrombogenicity. *Circulation* **99**, 348–353 (1999).
76. Gidon-Jeangirard, C. *et al.* Annexin V delays apoptosis while exerting an external constraint preventing the release of CD4⁺ and PrP^c membrane particles in a human T lymphocyte model. *J Immunol* **162**, 5712–5718 (1999).

77. Mari, C. *et al.* Detection of focal hypoxic-ischemic injury and neuronal stress in a rodent model of unilateral MCA occlusion/reperfusion using radiolabeled annexin V. *European Journal of Nuclear Medicine and Molecular Imaging* **31**, 733–739 (2004).
78. van Genderen, H. O., Kenis, H., Hofstra, L., Narula, J. & Reutelingsperger, C. P. M. Extracellular annexin A5: Functions of phosphatidylserine-binding and two-dimensional crystallization. *Biochimica et Biophysica Acta - Molecular Cell Research* **1783**, 953–963 (2008).
79. Sung, H. *et al.* Global Cancer Statistics 2020: GLOBOCAN Estimates of Incidence and Mortality Worldwide for 36 Cancers in 185 Countries. *CA A Cancer J Clin* **71**, 209–249 (2021).
80. Bray, F., Laversanne, M., Weiderpass, E. & Soerjomataram, I. The ever-increasing importance of cancer as a leading cause of premature death worldwide. *Cancer* **127**, 3029–3030 (2021).
81. Torre, L. A., Siegel, R. L., Ward, E. M. & Jemal, A. Global Cancer Incidence and Mortality Rates and Trends—An Update. *Cancer Epidemiol Biomarkers Prev* **25**, 16–27 (2016).
82. Luzzati, T., Parenti, A. & Rughi, T. Economic Growth and Cancer Incidence. *Ecological Economics* **146**, 381–396 (2018).
83. Bray, F. *et al.* Global cancer statistics 2018: GLOBOCAN estimates of incidence and mortality worldwide for 36 cancers in 185 countries. *CA: A Cancer Journal for Clinicians* **68**, 394–424 (2018).
84. Podlaha, O., Riester, M., De, S. & Michor, F. Evolution of the cancer genome. *Trends in Genetics* **28**, 155–163 (2012).
85. Hanahan, D. & Weinberg, R. A. Hallmarks of Cancer: The Next Generation. *Cell* **144**, 646–674 (2011).
86. Hanahan, D. Hallmarks of Cancer: New Dimensions. *Cancer Discovery* **12**, 31–46 (2022).
87. Witsch, E., Sela, M. & Yarden, Y. Roles for Growth Factors in Cancer Progression. *Physiology* **25**, 85–101 (2010).

88. Bhowmick, N. A., Neilson, E. G. & Moses, H. L. Stromal fibroblasts in cancer initiation and progression. *Nature* **432**, 332–337 (2004).
89. Vélez-Cruz, R. & Johnson, D. The Retinoblastoma (RB) Tumor Suppressor: Pushing Back against Genome Instability on Multiple Fronts. *IJMS* **18**, 1776 (2017).
90. Tiwari, B., Jones, A. E. & Abrams, J. M. Transposons, p53 and Genome Security. *Trends in Genetics* **34**, 846–855 (2018).
91. Hernández Borrero, L. J. & El-Deiry, W. S. Tumor suppressor p53: Biology, signaling pathways, and therapeutic targeting. *Biochimica et Biophysica Acta (BBA) - Reviews on Cancer* **1876**, 188556 (2021).
92. Mota, M. & Shevde, L. A. Merlin regulates signaling events at the nexus of development and cancer. *Cell Commun Signal* **18**, 63 (2020).
93. Hezel, A. F. & Bardeesy, N. LKB1; linking cell structure and tumor suppression. *Oncogene* **27**, 6908–6919 (2008).
94. Shaw, R. J. Tumor Suppression by LKB1: SIK-ness Prevents Metastasis. *Sci. Signal.* **2**, (2009).
95. Adams, J. M. & Cory, S. The Bcl-2 apoptotic switch in cancer development and therapy. *Oncogene* **26**, 1324–1337 (2007).
96. Lowe, S. W., Cepero, E. & Evan, G. Intrinsic tumour suppression. *Nature* **432**, 307–315 (2004).
97. Evan, G. & Littlewood, T. A Matter of Life and Cell Death. *Science* **281**, 1317–1322 (1998).
98. Junttila, M. R. & Evan, G. I. p53 — a Jack of all trades but master of none. *Nat Rev Cancer* **9**, 821–829 (2009).
99. Galluzzi, L. & Kroemer, G. Necroptosis: A Specialized Pathway of Programmed Necrosis. *Cell* **135**, 1161–1163 (2008).

100. Gong, Y. *et al.* The role of necroptosis in cancer biology and therapy. *Mol Cancer* **18**, 100 (2019).
101. Grivennikov, S. I., Greten, F. R. & Karin, M. Immunity, Inflammation, and Cancer. *Cell* **140**, 883–899 (2010).
102. Dewhurst, S. M. Chromothripsis and telomere crisis: engines of genome instability. *Current Opinion in Genetics & Development* **60**, 41–47 (2020).
103. Calcinotto, A. *et al.* Cellular Senescence: Aging, Cancer, and Injury. *Physiological Reviews* **99**, 1047–1078 (2019).
104. Blasco, M. A. Telomeres and human disease: ageing, cancer and beyond. *Nat Rev Genet* **6**, 611–622 (2005).
105. Pańcyszyn, A., Boniewska-Bernacka, E. & Goc, A. The role of telomeres and telomerase in the senescence of postmitotic cells. *DNA Repair* **95**, 102956 (2020).
106. De Vitis, M., Berardinelli, F. & Sgura, A. Telomere Length Maintenance in Cancer: At the Crossroad between Telomerase and Alternative Lengthening of Telomeres (ALT). *IJMS* **19**, 606 (2018).
107. Artandi, S. E. & DePinho, R. A. Mice without telomerase: what can they teach us about human cancer? *Nat Med* **6**, 852–855 (2000).
108. Raynaud, C. M. *et al.* DNA Damage Repair and Telomere Length in Normal Breast, Preneoplastic Lesions, and Invasive Cancer. *American Journal of Clinical Oncology* **33**, 341–345 (2010).
109. Chin, K. *et al.* In situ analyses of genome instability in breast cancer. *Nat Genet* **36**, 984–988 (2004).
110. De Sanctis, F., Ugel, S., Faccioponte, J. & Facciabene, A. The dark side of tumor-associated endothelial cells. *Seminars in Immunology* **35**, 35–47 (2018).
111. Loh, C.-Y. *et al.* The E-Cadherin and N-Cadherin Switch in Epithelial-to-Mesenchymal Transition: Signaling, Therapeutic Implications, and Challenges. *Cells* **8**, 1118 (2019).

112. Su, S.-C. *et al.* Cancer metastasis: Mechanisms of inhibition by melatonin. *J. Pineal Res.* **62**, e12370 (2017).
113. Seyfried, T. N. & Huysentruyt, L. C. On the Origin of Cancer Metastasis. *37* (2014).
114. Pavlova, N. N. & Thompson, C. B. The Emerging Hallmarks of Cancer Metabolism. *Cell Metabolism* **23**, 27–47 (2016).
115. Vander Heiden, M. G., Cantley, L. C. & Thompson, C. B. Understanding the Warburg Effect: The Metabolic Requirements of Cell Proliferation. *Science* **324**, 1029–1033 (2009).
116. Vajdic, C. M. & van Leeuwen, M. T. Cancer incidence and risk factors after solid organ transplantation. *Int. J. Cancer* **125**, 1747–1754 (2009).
117. Teng, M. W. L., Swann, J. B., Koebel, C. M., Schreiber, R. D. & Smyth, M. J. Immune-mediated dormancy: an equilibrium with cancer. *Journal of Leukocyte Biology* **84**, 988–993 (2008).
118. Britt, K. L., Cuzick, J. & Phillips, K.-A. Key steps for effective breast cancer prevention. *Nat Rev Cancer* **20**, 417–436 (2020).
119. Fitzmaurice, C. & Global Burden of Disease Cancer Collaboration. Global, regional, and national cancer incidence, mortality, years of life lost, years lived with disability, and disability-adjusted life-years for 29 cancer groups, 2006 to 2016: A systematic analysis for the Global Burden of Disease study. *JCO* **36**, 1568–1568 (2018).
120. Menarche, menopause, and breast cancer risk: individual participant meta-analysis, including 118 964 women with breast cancer from 117 epidemiological studies. *The Lancet Oncology* **13**, 1141–1151 (2012).
121. Rödström, K. *et al.* Evidence for a secular trend in menopausal age: a population study of women in Gothenburg: *Menopause* **10**, 538–543 (2003).
122. Jatoi, I. & Miller, A. B. Why is breast-cancer mortality declining? *The Lancet Oncology* **4**, 251–254 (2003).

123. Malhotra, G. K., Zhao, X., Band, H. & Band, V. Histological, molecular and functional subtypes of breast cancers. *Cancer Biology & Therapy* **10**, 955–960 (2010).
124. Waks, A. G. & Winer, E. P. Breast Cancer Treatment: A Review. *JAMA* **321**, 288 (2019).
125. Kaufman, C. S. Increasing Role of Oncoplastic Surgery for Breast Cancer. *Curr Oncol Rep* **21**, 111 (2019).
126. Aebi, S. *et al.* Chemotherapy for isolated locoregional recurrence of breast cancer (CALOR): a randomised trial. *The Lancet Oncology* **15**, 156–163 (2014).
127. Hon, J. D. C. *et al.* Breast cancer molecular subtypes: from TNBC to QNBC. 9.
128. Loibl, S., Poortmans, P., Morrow, M., Denkert, C. & Curigliano, G. Breast cancer. *The Lancet* **397**, 1750–1769 (2021).
129. Kumar, P. & Aggarwal, R. An overview of triple-negative breast cancer. *Arch Gynecol Obstet* **293**, 247–269 (2016).
130. Barnard, M. E., Boeke, C. E. & Tamimi, R. M. Established breast cancer risk factors and risk of intrinsic tumor subtypes. *Biochimica et Biophysica Acta (BBA) - Reviews on Cancer* **1856**, 73–85 (2015).
131. Polyak, K. Heterogeneity in breast cancer. *J. Clin. Invest.* **121**, 3786–3788 (2011).
132. Russo, J. & Russo, I. H. The role of estrogen in the initiation of breast cancer. *The Journal of Steroid Biochemistry and Molecular Biology* **102**, 89–96 (2006).
133. Hammond, M. E. H. *et al.* American Society of Clinical Oncology/College of American Pathologists Guideline Recommendations for Immunohistochemical Testing of Estrogen and Progesterone Receptors in Breast Cancer. *JCO* **28**, 2784–2795 (2010).
134. Shagufta & Ahmad, I. Tamoxifen a pioneering drug: An update on the therapeutic potential of tamoxifen derivatives. *European Journal of Medicinal Chemistry* **143**, 515–531 (2018).
135. Riggs, B. L. Selective Estrogen-Receptor Modulators — Mechanisms of Action and Application to Clinical Practice. *The New England Journal of Medicine* **13** (2003).

136. Kharb, R., Haider, K., Neha, K. & Yar, M. S. Aromatase inhibitors: Role in postmenopausal breast cancer. *Arch Pharm* **353**, 2000081 (2020).
137. Early Breast Cancer Trialists' Collaborative Group (EBCTCG). Relevance of breast cancer hormone receptors and other factors to the efficacy of adjuvant tamoxifen: patient-level meta-analysis of randomised trials. *The Lancet* **378**, 771–784 (2011).
138. Francis, P. A. *et al.* Tailoring Adjuvant Endocrine Therapy for Premenopausal Breast Cancer. *N Engl J Med* **379**, 122–137 (2018).
139. Early Breast Cancer Trialists' Collaborative Group (EBCTCG). Comparisons between different polychemotherapy regimens for early breast cancer: meta-analyses of long-term outcome among 100 000 women in 123 randomised trials. *The Lancet* **379**, 432–444 (2012).
140. Hanker, A. B., Sudhan, D. R. & Arteaga, C. L. Overcoming Endocrine Resistance in Breast Cancer. *Cancer Cell* **37**, 496–513 (2020).
141. Wolff, A. C. *et al.* Recommendations for Human Epidermal Growth Factor Receptor 2 Testing in Breast Cancer: American Society of Clinical Oncology/College of American Pathologists Clinical Practice Guideline Update. *JCO* **31**, 3997–4013 (2013).
142. Piccart-Gebhart, M. J. *et al.* Trastuzumab after Adjuvant Chemotherapy in HER2-Positive Breast Cancer. *The New England Journal of Medicine* **14** (2005).
143. Mitsogianni, M. *et al.* The changing treatment of metastatic her2-positive breast cancer (Review). *Oncol Lett* **21**, 287 (2021).
144. Fink, M. Y. & Chipuk, J. E. Survival of HER2-Positive Breast Cancer Cells: Receptor Signaling to Apoptotic Control Centers. *Genes & Cancer* **4**, 187–195 (2013).
145. Richard, S. *et al.* Pertuzumab and trastuzumab: the rationale way to synergy. *An. Acad. Bras. Ciênc.* **88**, 565–577 (2016).
146. Tolaney, S. M. *et al.* Seven-Year Follow-Up Analysis of Adjuvant Paclitaxel and Trastuzumab Trial for Node-Negative, Human Epidermal Growth Factor Receptor 2–Positive Breast Cancer. *JCO* **37**, 1868–1875 (2019).

147. von Minckwitz, G. *et al.* Adjuvant Pertuzumab and Trastuzumab in Early HER2-Positive Breast Cancer. *N Engl J Med* **377**, 122–131 (2017).
148. von Minckwitz, G. *et al.* Trastuzumab Beyond Progression in Human Epidermal Growth Factor Receptor 2–Positive Advanced Breast Cancer: A German Breast Group 26/Breast International Group 03-05 Study. *JCO* **27**, 1999–2006 (2009).
149. Hortobagyi, G. N., Edge, S. B. & Giuliano, A. New and Important Changes in the TNM Staging System for Breast Cancer. *American Society of Clinical Oncology Educational Book* 457–467 (2018) doi:10.1200/EDBK_201313.
150. Coleman, C. Early Detection and Screening for Breast Cancer. *Seminars in Oncology Nursing* **33**, 141–155 (2017).
151. Yin, L., Duan, J.-J., Bian, X.-W. & Yu, S. Triple-negative breast cancer molecular subtyping and treatment progress. *Breast Cancer Res* **22**, 61 (2020).
152. Siegel, R. L., Miller, K. D. & Jemal, A. Cancer statistics, 2019. *CA: A Cancer Journal for Clinicians* **69**, 7–34 (2019).
153. Costa, R. L. B. & Gradishar, W. J. Triple-Negative Breast Cancer: Current Practice and Future Directions. *Journal of Oncology Practice* **13**, 301–303 (2017).
154. Plevritis, S. K. *et al.* Association of screening and treatment with breast cancer mortality by molecular subtype in US women, 2000-2012. *JAMA - Journal of the American Medical Association* **319**, 154–164 (2018).
155. Guarneri, V. *et al.* Prognostic value of pathologic complete response after primary chemotherapy in relation to hormone receptor status and other factors. *Journal of Clinical Oncology* **24**, 1037–1044 (2006).
156. Liedtke, C. *et al.* Response to neoadjuvant therapy and long-term survival in patients with triple-negative breast cancer. *Journal of Clinical Oncology* **26**, 1275–1281 (2008).
157. Mustacchi, G. & De Laurentiis, M. The role of taxanes in triple-negative breast cancer: literature review [Corrigendum]. *Drug Design, Development and Therapy* 5669 (2015) doi:10.2147/dddt.s97778.

158. Poggio, F. *et al.* Platinum-based neoadjuvant chemotherapy in triple-negative breast cancer: a systematic review and meta-analysis. *Annals of Oncology* **29**, 1497–1508 (2018).
159. den Brok, W. D. *et al.* Homologous Recombination Deficiency in Breast Cancer: A Clinical Review. *JCO Precision Oncology* 1–13 (2017) doi:10.1200/PO.16.00031.
160. Bianchini, G., Balko, J. M., Mayer, I. A., Sanders, M. E. & Gianni, L. Triple-negative breast cancer: challenges and opportunities of a heterogeneous disease. *Nat Rev Clin Oncol* **13**, 674–690 (2016).
161. Partridge, A. H. *et al.* Chemotherapy and Targeted Therapy for Women With Human Epidermal Growth Factor Receptor 2–Negative (or unknown) Advanced Breast Cancer: American Society of Clinical Oncology Clinical Practice Guideline. *JCO* **32**, 3307–3329 (2014).
162. Lehmann, B. D. *et al.* Identification of human triple-negative breast cancer subtypes and preclinical models for selection of targeted therapies. *J. Clin. Invest.* **121**, 2750–2767 (2011).
163. Masuda, H. *et al.* Differential Response to Neoadjuvant Chemotherapy Among 7 Triple-Negative Breast Cancer Molecular Subtypes. *Clinical Cancer Research* **19**, 5533–5540 (2013).
164. Bianchini, G., De Angelis, C., Licata, L. & Gianni, L. Treatment landscape of triple-negative breast cancer — expanded options, evolving needs. *Nat Rev Clin Oncol* **19**, 91–113 (2022).
165. Bryant, H. E. *et al.* Specific killing of BRCA2-deficient tumours with inhibitors of poly(ADP-ribose) polymerase. **434**, 6 (2005).
166. Robson, M. *et al.* Olaparib for Metastatic Breast Cancer in Patients with a Germline *BRCA* Mutation. *N Engl J Med* **377**, 523–533 (2017).
167. Litton, J. K. *et al.* Talazoparib in Patients with Advanced Breast Cancer and a Germline *BRCA* Mutation. *N Engl J Med* **379**, 753–763 (2018).
168. Lord, C. J. & Ashworth, A. PARP inhibitors: Synthetic lethality in the clinic. *Science* **355**, 1152–1158 (2017).

169. Tung, N. M. *et al.* TBCRC 048: Phase II Study of Olaparib for Metastatic Breast Cancer and Mutations in Homologous Recombination-Related Genes. *JCO* **38**, 4274–4282 (2020).
170. Cubas, R., Zhang, S., Li, M., Chen, C. & Yao, Q. Trop2 expression contributes to tumor pathogenesis by activating the ERK MAPK pathway. *Mol Cancer* **9**, 253 (2010).
171. Bardia, A. *et al.* Sacituzumab Govitecan in Metastatic Triple-Negative Breast Cancer. *N Engl J Med* **384**, 1529–1541 (2021).
172. Taylor, K. M. *et al.* The Emerging Role of the LIV-1 Subfamily of Zinc Transporters in Breast Cancer. *Mol Med* **13**, 396–406 (2007).
173. Rizzo, A., Cusmai, A., Acquafredda, S., Rinaldi, L. & Palmiotti, G. Ladiratumab vedotin for metastatic triple negative cancer: preliminary results, key challenges, and clinical potential. *Expert Opinion on Investigational Drugs* **31**, 495–498 (2022).
174. Pascual, J. & Turner, N. C. Targeting the PI3-kinase pathway in triple-negative breast cancer. *Annals of Oncology* **30**, 1051–1060 (2019).
175. Sinkala, M., Nkhoma, P., Mulder, N. & Martin, D. P. Integrated molecular characterisation of the MAPK pathways in human cancers reveals pharmacologically vulnerable mutations and gene dependencies. *Commun Biol* **4**, 9 (2021).
176. Bertucci, F. *et al.* Genomic characterization of metastatic breast cancers. *Nature* **569**, 560–564 (2019).
177. Logue, J. S. & Morrison, D. K. Complexity in the signaling network: insights from the use of targeted inhibitors in cancer therapy. *Genes Dev.* **26**, 641–650 (2012).
178. Lu, Q. *et al.* Bicalutamide plus Aromatase Inhibitor in Patients with Estrogen Receptor-Positive/Androgen Receptor-Positive Advanced Breast Cancer. *The Oncologist* **25**, 21-e15 (2020).
179. Traina, T. A. *et al.* Enzalutamide for the Treatment of Androgen Receptor–Expressing Triple-Negative Breast Cancer. *JCO* **36**, 884–890 (2018).

180. Lehmann, B. D. *et al.* PIK3CA mutations in androgen receptor-positive triple negative breast cancer confer sensitivity to the combination of PI3K and androgen receptor inhibitors. *Breast Cancer Res* **16**, 406 (2014).
181. Xiang, J. *et al.* Antigen-Loaded Upconversion Nanoparticles for Dendritic Cell Stimulation, Tracking, and Vaccination in Dendritic Cell-Based Immunotherapy. *ACS Nano* **9**, 6401–6411 (2015).
182. Doughty, A. C. V. *et al.* Nanomaterial applications in photothermal therapy for cancer. *Materials* **12**, (2019).
183. de Melo-Diogo, D., Pais-Silva, C., Dias, D. R., Moreira, A. F. & Correia, I. J. Strategies to Improve Cancer Photothermal Therapy Mediated by Nanomaterials. *Advanced Healthcare Materials* **6**, (2017).
184. Tang, J. Effect of hyperthermia on invasion ability and TGF- β 1 expression of breast carcinoma MCF-7 cells. *Oncol Rep* (2011) doi:10.3892/or.2011.1240.
185. Hsiao, C.-W. *et al.* Photothermal tumor ablation in mice with repeated therapy sessions using NIR-absorbing micellar hydrogels formed in situ. *Biomaterials* **56**, 26–35 (2015).
186. Richter, K., Haslbeck, M. & Buchner, J. The Heat Shock Response: Life on the Verge of Death. *Molecular Cell* **40**, 253–266 (2010).
187. Knavel, E. M. & Brace, C. L. Tumor Ablation: Common Modalities and General Practices. *Techniques in Vascular and Interventional Radiology* **16**, 192–200 (2013).
188. Goldman, L. A review: Applications of the laser beam in cancer biology. *Int. J. Cancer* **1**, 309–318 (1966).
189. Sultan, R. A. Tumour ablation by laser in general surgery. *Laser Med Sci* **5**, 185–193 (1990).
190. Rai, P. *et al.* Development and applications of photo-triggered theranostic agents. *Advanced Drug Delivery Reviews* Preprint at <https://doi.org/10.1016/j.addr.2010.09.002> (2010).
191. Hu, J. J., Cheng, Y. J. & Zhang, X. Z. Recent advances in nanomaterials for enhanced photothermal therapy of tumors. *Nanoscale* **10**, 22657–22672 (2018).

192. Hussein, E. A., Zagho, M. M., Nasrallah, G. K. & Elzatahry, A. A. Recent advances in functional nanostructures as cancer photothermal therapy. *International Journal of Nanomedicine* **13**, 2897–2906 (2018).
193. Kim, T. H. *et al.* Evaluation of Temperature-Sensitive, Indocyanine Green-Encapsulating Micelles for Noninvasive Near-Infrared Tumor Imaging. *Pharm Res* **27**, 1900–1913 (2010).
194. Zhou, J. *et al.* NIR photothermal therapy using polyaniline nanoparticles. *Biomaterials* **34**, 9584–9592 (2013).
195. Yoon, H.-J., Lee, H.-S., Lim, J.-Y. & Park, J.-H. Liposomal Indocyanine Green for Enhanced Photothermal Therapy. *ACS Appl. Mater. Interfaces* **9**, 5683–5691 (2017).
196. Du, C. *et al.* Polymeric photothermal agents for cancer therapy: recent progress and clinical potential. *J. Mater. Chem. B* **9**, 1478–1490 (2021).
197. Li, Y., Lu, W., Huang, Q., Li, C. & Chen, W. Copper sulfide nanoparticles for photothermal ablation of tumor cells. *Nanomedicine* **5**, 1161–1171 (2010).
198. Shao, J. *et al.* Biodegradable black phosphorus-based nanospheres for in vivo photothermal cancer therapy. *Nat Commun* **7**, 12967 (2016).
199. Fernandes, N., Rodrigues, C. F., Moreira, A. F. & Correia, I. J. Overview of the application of inorganic nanomaterials in cancer photothermal therapy. *Biomater. Sci.* **8**, 2990–3020 (2020).
200. Vines, J. B., Yoon, J.-H., Ryu, N.-E., Lim, D.-J. & Park, H. Gold Nanoparticles for Photothermal Cancer Therapy. *Front. Chem.* **7**, 167 (2019).
201. Saha, R. N., Vasanthakumar, S., Bende, G. & Snehalatha, M. Nanoparticulate drug delivery systems for cancer chemotherapy. *Molecular Membrane Biology* **27**, 215–231 (2010).
202. Yu, B., Tai, H. C., Xue, W., Lee, L. J. & Lee, R. J. Receptor-targeted nanocarriers for therapeutic delivery to cancer. *Molecular Membrane Biology* **27**, 286–298 (2010).
203. Li, X., Lovell, J. F., Yoon, J. & Chen, X. Clinical development and potential of photothermal and photodynamic therapies for cancer. *Nat Rev Clin Oncol* **17**, 657–674 (2020).

204. Zhao, Y. *et al.* Combination of phototherapy with immune checkpoint blockade: Theory and practice in cancer. *Front. Immunol.* **13**, 955920 (2022).
205. Muz, B., de la Puente, P., Azab, F. & Azab, A. K. The role of hypoxia in cancer progression, angiogenesis, metastasis, and resistance to therapy. *HP* **83** (2015) doi:10.2147/HP.S93413.
206. Lal, S., Clare, S. E. & Halas, N. J. Nanoshell-Enabled Photothermal Cancer Therapy: Impending Clinical Impact. *Acc. Chem. Res.* **41**, 1842–1851 (2008).
207. Rastinehad, A. R. *et al.* Gold nanoshell-localized photothermal ablation of prostate tumors in a clinical pilot device study. *Proc. Natl. Acad. Sci. U.S.A.* **116**, 18590–18596 (2019).
208. Stern, J. M. *et al.* Initial Evaluation of the Safety of Nanoshell-Directed Photothermal Therapy in the Treatment of Prostate Disease. *Int J Toxicol* **35**, 38–46 (2016).
209. Monaco, H., Yokomizo, S., Choi, H. S. & Kashiwagi, S. Quickly evolving near-infrared photoimmunotherapy provides multifaceted approach to modern cancer treatment. *VIEW* **3**, 20200110 (2022).
210. Hansen, G. & Sundset, A. Transbronchial laser ablation of benign and malignant tumors. *Minimally Invasive Therapy & Allied Technologies* **15**, 4–8 (2006).
211. Wenger, H., Yousuf, A., Oto, A. & Eggener, S. Laser ablation as focal therapy for prostate cancer. *Current Opinion in Urology* **24**, 236–240 (2014).
212. Gough-Palmer, A. L. & Gedroyc, W. M. W. Laser ablation of hepatocellular carcinoma-A review. *WJG* **14**, 7170 (2008).
213. Arienti, V. *et al.* Complications of Laser Ablation for Hepatocellular Carcinoma: A Multicenter Study. *Radiology* **246**, 947–955 (2008).
214. Vogl, T. J., Straub, R., Eichler, K., Söllner, O. & Mack, M. G. Colorectal Carcinoma Metastases in Liver: Laser-induced Interstitial Thermotherapy—Local Tumor Control Rate and Survival Data. *Radiology* **230**, 450–458 (2004).
215. Lagman, C. *et al.* Laser neurosurgery: A systematic analysis of magnetic resonance-guided laser interstitial thermal therapies. *Journal of Clinical Neuroscience* **36**, 20–26 (2017).

216. Chen, M. *et al.* Interstitial Laser Ablation as Alternative to Surgical Treatment of Benign Breast Tumors. *Journal of the American College of Surgeons* **227**, e83 (2018).
217. Schwartzberg, B. *et al.* Phase 2 Open-Label Trial Investigating Percutaneous Laser Ablation for Treatment of Early-Stage Breast Cancer: MRI, Pathology, and Outcome Correlations. *Ann Surg Oncol* **25**, 2958–2964 (2018).
218. Li, X. *et al.* Preliminary safety and efficacy results of laser immunotherapy for the treatment of metastatic breast cancer patients. *Photochem. Photobiol. Sci.* **10**, 817 (2011).
219. Braun, C. L. & Smirnov, S. N. Why is water blue? *Journal of Chemical Education* **70**, 612–614 (1993).
220. Weissleder, R. A clearer vision for in vivo imaging. *Nature Biotechnology* **19**, (2001).
221. Kastner, J. *et al.* Resonance Raman and infrared spectroscopy of carbon nanotubes. *Chemical Physics Letters* **221**, 53–58 (1994).
222. Hyochol Ahn, Michael Weaver, Debra Lyon, Eunyoung Choi, R. & Roger B. Fillingim. Dual Wavelength Stimulation of Polymeric Nanoparticles for Photothermal Therapy. *Lasers Surg Med* **176**, 139–148 (2017).
223. Fuchs, Y. & Steller, H. Programmed Cell Death in Animal Development and Disease. *Cell* **147**, 742–758 (2011).
224. Tang, D., Kang, R., Berghe, T. V., Vandenabeele, P. & Kroemer, G. The molecular machinery of regulated cell death. *Cell Res* **29**, 347–364 (2019).
225. Galluzzi, L., Buqué, A., Kepp, O., Zitvogel, L. & Kroemer, G. Immunogenic cell death in cancer and infectious disease. *Nat Rev Immunol* **17**, 97–111 (2017).
226. Chen, D. S. & Mellman, I. Oncology Meets Immunology: The Cancer-Immunity Cycle. *Immunity* **39**, 1–10 (2013).
227. Palucka, A. K. & Coussens, L. M. The Basis of Oncoimmunology. *Cell* **164**, 1233–1247 (2016).

228. Galluzzi, L. *et al.* Consensus guidelines for the definition, detection and interpretation of immunogenic cell death. *J Immunother Cancer* **8**, e000337 (2020).
229. Hou, W. *et al.* Strange attractors: DAMPs and autophagy link tumor cell death and immunity. *Cell Death Dis* **4**, e966–e966 (2013).
230. Krysko, D. V. *et al.* Immunogenic cell death and DAMPs in cancer therapy. *Nat Rev Cancer* **12**, 860–875 (2012).
231. Shang, T., Yu, X., Han, S. & Yang, B. Nanomedicine-based tumor photothermal therapy synergized immunotherapy. *Biomater. Sci.* **8**, 5241–5259 (2020).
232. Maruoka, Y., Wakiyama, H., Choyke, P. L. & Kobayashi, H. Near infrared photoimmunotherapy for cancers: A translational perspective. *EBioMedicine* **70**, 103501 (2021).
233. Kobayashi, H. & Choyke, P. L. Near-Infrared Photoimmunotherapy of Cancer. *Acc. Chem. Res.* **52**, 2332–2339 (2019).
234. Abbott, M. & Ustoyev, Y. Cancer and the Immune System: The History and Background of Immunotherapy. *Seminars in Oncology Nursing* **35**, 150923 (2019).
235. Russell, S. J., Peng, K.-W. & Bell, J. C. Oncolytic virotherapy. *Nat Biotechnol* **30**, 658–670 (2012).
236. Mastelic-Gavillet, B., Balint, K., Boudousquie, C., Gannon, P. O. & Kandalaf, L. E. Personalized Dendritic Cell Vaccines—Recent Breakthroughs and Encouraging Clinical Results. *Front. Immunol.* **10**, 766 (2019).
237. Dranoff, G. *et al.* Vaccination with irradiated tumor cells engineered to secrete murine granulocyte-macrophage colony-stimulating factor stimulates potent, specific, and long-lasting anti-tumor immunity. *Proc. Natl. Acad. Sci. U.S.A.* **90**, 3539–3543 (1993).
238. Zitvogel, L., Galluzzi, L., Kepp, O., Smyth, M. J. & Kroemer, G. Type I interferons in anticancer immunity. *Nat Rev Immunol* **15**, 405–414 (2015).

239. Zhang, Y. & Zhang, Z. The history and advances in cancer immunotherapy: understanding the characteristics of tumor-infiltrating immune cells and their therapeutic implications. *Cell Mol Immunol* **17**, 807–821 (2020).
240. Pardoll, D. M. The blockade of immune checkpoints in cancer immunotherapy. *Nat Rev Cancer* **12**, 252–264 (2012).
241. Dermani, F. K., Samadi, P., Rahmani, G., Kohlan, A. K. & Najafi, R. PD-1/PD-L1 immune checkpoint: Potential target for cancer therapy. *J Cell Physiol* **234**, 1313–1325 (2019).
242. Liu, Y. & Zheng, P. How Does an Anti-CTLA-4 Antibody Promote Cancer Immunity? *Trends in Immunology* **39**, 953–956 (2018).
243. Alsaab, H. O. *et al.* PD-1 and PD-L1 Checkpoint Signaling Inhibition for Cancer Immunotherapy: Mechanism, Combinations, and Clinical Outcome. *Front. Pharmacol.* **8**, 561 (2017).
244. Linette, G. P. & Carreno, B. M. Tumor-Infiltrating Lymphocytes in the Checkpoint Inhibitor Era. *Curr Hematol Malig Rep* **14**, 286–291 (2019).
245. Noguchi, E., Shien, T. & Iwata, H. Current status of PD-1/PD-L1 blockade immunotherapy in breast cancer. *Japanese Journal of Clinical Oncology* **51**, 321–332 (2021).
246. Naylor, M. F., Chen, W. R., Teague, T. K., Perry, L. A. & Nordquist, R. E. *In situ* photoimmunotherapy: a tumour-directed treatment for melanoma: ISPI: a tumour-directed treatment for melanoma. *British Journal of Dermatology* **155**, 1287–1292 (2006).
247. Maruoka, Y., Wakiyama, H., Choyke, P. L. & Kobayashi, H. Near infrared photoimmunotherapy for cancers: A translational perspective. *EBioMedicine* **70**, 103501 (2021).
248. Friedman, M. *et al.* Radiofrequency Ablation of Cancer. *CVIR* **27**, (2004).
249. Spliethoff, J. W. *et al.* Monitoring of tumor radio frequency ablation using derivative spectroscopy. *J. Biomed. Opt* **19**, 097004 (2014).

250. Izzo, F. *et al.* Radiofrequency Ablation and Microwave Ablation in Liver Tumors: An Update. *The Oncol* **24**, (2019).
251. De Filippo, M. *et al.* Radiofrequency ablation of osteoid osteoma. *Acta Biomedica Atenei Parmensis* **89**, 175–185 (2018).
252. Glazer, E. S. *et al.* Noninvasive Radiofrequency Field Destruction of Pancreatic Adenocarcinoma Xenografts Treated with Targeted Gold Nanoparticles. *Clinical Cancer Research* **16**, 5712–5721 (2010).
253. Rejinold, N. S., Jayakumar, R. & Kim, Y.-C. Radio frequency responsive nano-biomaterials for cancer therapy. *Journal of Controlled Release* **204**, 85–97 (2015).
254. Cherukuri, P., Glazer, E. S. & Curley, S. A. Targeted hyperthermia using metal nanoparticles. *Advanced Drug Delivery Reviews* **62**, 339–345 (2010).
255. Garcia-Sanchez, D. *et al.* Mechanical Detection of Carbon Nanotube Resonator Vibrations. *Phys. Rev. Lett.* **99**, 085501 (2007).
256. Jensen, K., Weldon, J., Garcia, H. & Zettl, A. Nanotube Radio. *Nano Lett.* **7**, 3508–3511 (2007).
257. Hüttel, A. K. *et al.* Carbon Nanotubes as Ultrahigh Quality Factor Mechanical Resonators. *Nano Lett.* **9**, 2547–2552 (2009).
258. Gannon, C. J. *et al.* Carbon nanotube-enhanced thermal destruction of cancer cells in a noninvasive radiofrequency field: Nanotube Heating Kills Cancer Cells. *Cancer* **110**, 2654–2665 (2007).
259. Iijima, S. Helical microtubules of graphitic carbon. *Nature* **354**, 56–58 (1991).
260. Treacy, M. M. J., Ebbesen, T. W. & Gibson, J. M. Exceptionally high Young's modulus observed for individual carbon nanotubes. *Nature* **381**, 678–680 (1996).
261. Kataura, H. *et al.* Optical properties of single-wall carbon nanotubes. *Synthetic Metals* **103**, 2555–2558 (1999).

262. Pop, E., Mann, D., Wang, Q., Goodson, K. & Dai, H. Thermal Conductance of an Individual Single-Wall Carbon Nanotube above Room Temperature. *Nano Lett.* **6**, 96–100 (2006).
263. Koziol, K. K., Janas, D., Brown, E. & Hao, L. Thermal properties of continuously spun carbon nanotube fibres. *Physica E: Low-dimensional Systems and Nanostructures* **88**, 104–108 (2017).
264. Hodge, S. A., Bayazit, M. K., Coleman, K. S. & Shaffer, M. S. P. Unweaving the rainbow: a review of the relationship between single-walled carbon nanotube molecular structures and their chemical reactivity. *Chem. Soc. Rev.* **41**, 4409 (2012).
265. Dresselhaus, M. S., Dresselhaus, G., Saito, R. & Jorio, A. Raman spectroscopy of carbon nanotubes. *Physics Reports* **409**, 47–99 (2005).
266. Zhang, W. *et al.* Chirality dependence of the thermal conductivity of carbon nanotubes. *Nanotechnology* **15**, 936–939 (2004).
267. Resasco, D. E. *et al.* A Scalable Process for Production of Single-walled Carbon Nanotubes (SWNTs) by Catalytic Disproportionation of CO on a Solid Catalyst. 6.
268. Bachilo, S. M. *et al.* Narrow (n,m)-Distribution of Single-Walled Carbon Nanotubes Grown Using a Solid Supported Catalyst. *J. Am. Chem. Soc.* **125**, 11186–11187 (2003).
269. Lolli, G. *et al.* Tailoring (n , m) Structure of Single-Walled Carbon Nanotubes by Modifying Reaction Conditions and the Nature of the Support of CoMo Catalysts. *J. Phys. Chem. B* **110**, 2108–2115 (2006).
270. Komatsu, N. & Wang, F. A Comprehensive Review on Separation Methods and Techniques for Single-Walled Carbon Nanotubes. *Materials* **3**, 3818–3844 (2010).
271. Janas, D. Towards monochiral carbon nanotubes: a review of progress in the sorting of single-walled carbon nanotubes. *Mater. Chem. Front.* **2**, 36–63 (2018).
272. Agboola, A. E., Pike, R. W., Hertwig, T. A. & Lou, H. H. Conceptual design of carbon nanotube processes. *Clean Techn Environ Policy* **9**, 289–311 (2007).

273. Rafique, M. M. A. & Iqbal, J. Production of Carbon Nanotubes by Different Routes-A Review. *JEAS* **01**, 29–34 (2011).
274. Resasco, D. E. *et al.* A Scalable Process for Production of Single-walled Carbon Nanotubes (SWNTs) by Catalytic Disproportionation of CO on a Solid Catalyst. *Journal of Nanoparticle Research* **4**, 131–136 (2002).
275. Kwon, I. K., Lee, S. C., Han, B. & Park, K. Analysis on the current status of targeted drug delivery to tumors. *Journal of Controlled Release* **164**, 108–114 (2012).
276. Abolmaali, S. S., Tamaddon, A. M. & Dinarvand, R. A review of therapeutic challenges and achievements of methotrexate delivery systems for treatment of cancer and rheumatoid arthritis. *Cancer Chemother Pharmacol* **71**, 1115–1130 (2013).
277. Lopus, M. *et al.* Maytansine and Cellular Metabolites of Antibody-Maytansinoid Conjugates Strongly Suppress Microtubule Dynamics by Binding to Microtubules. *Molecular Cancer Therapeutics* **9**, 2689–2699 (2010).
278. Prota, A. E. *et al.* A new tubulin-binding site and pharmacophore for microtubule-destabilizing anticancer drugs. *Proc. Natl. Acad. Sci. U.S.A.* **111**, 13817–13821 (2014).
279. Rosenthal, S., Harris, D. T., Horton, J. & Glick, J. H. Phase II study of maytansine in patients with advanced lymphomas: an Eastern Cooperative Oncology Group pilot study. *Cancer Treat Rep* **64**, 1115–1117 (1980).
280. Franklin, R. *et al.* A phase I-II study of maytansine utilizing a weekly schedule. *Cancer* **46**, 1104–1108 (1980).
281. Virani, N. A. *et al.* Enhanced computed tomography imaging of breast cancer via phosphatidylserine targeted gold nanoparticles. *Biomed. Phys. Eng. Express* **5**, 065019 (2019).
282. Neves, L. F. F. *et al.* Targeting single-walled carbon nanotubes for the treatment of breast cancer using photothermal therapy. *Nanotechnology* **24**, 375104 (2013).

283. McKernan, P. *et al.* Targeted Single-Walled Carbon Nanotubes for Photothermal Therapy Combined with Immune Checkpoint Inhibition for the Treatment of Metastatic Breast Cancer. *Nanoscale Research Letters* **16**, 9 (2021).
284. Liu, Z. *et al.* Circulation and long-term fate of functionalized, biocompatible single-walled carbon nanotubes in mice probed by Raman spectroscopy. *Proc. Natl. Acad. Sci. U.S.A.* **105**, 1410–1415 (2008).
285. Li, J. *et al.* In situ injectable hydrogel-loaded drugs induce anti-tumor immune responses in melanoma immunochemotherapy. *Materials Today Bio* **14**, 100238 (2022).
286. Li, D. *et al.* The Effect of Sample Holder Geometry on Electromagnetic Heating of Nanoparticle and NaCl Solutions at 13.56 MHz. *IEEE Trans. Biomed. Eng.* **59**, 3468–3474 (2012).
287. Hainfeld, J. F. *et al.* Micro-CT enables microlocalisation and quantification of Her2-targeted gold nanoparticles within tumour regions. *BJR* **84**, 526–533 (2011).
288. Takae, S. *et al.* Ligand Density Effect on Biorecognition by PEGylated Gold Nanoparticles: Regulated Interaction of RCA₁₂₀ Lectin with Lactose Installed to the Distal End of Tethered PEG Strands on Gold Surface. *Biomacromolecules* **6**, 818–824 (2005).
289. Ba, H., Rodríguez-Fernández, J., Stefani, F. D. & Feldmann, J. Immobilization of Gold Nanoparticles on Living Cell Membranes upon Controlled Lipid Binding. *Nano Lett.* **10**, 3006–3012 (2010).
290. Fisher, J. W. *et al.* Photothermal Response of Human and Murine Cancer Cells to Multiwalled Carbon Nanotubes after Laser Irradiation. *Cancer Research* **70**, 9855–9864 (2010).
291. Yi, W. *et al.* Enhanced response of tamoxifen toward the cancer cells using a combination of chemotherapy and photothermal ablation induced by lentinan-functionalized multi-walled carbon nanotubes. *International Journal of Biological Macromolecules* **120**, 1525–1532 (2018).

292. Alexandru S. Biris *et al.* Nanophotothermolysis of multiple scattered cancer cells with carbon nanotubes guided by time-resolved infrared thermal imaging. *J Biomed Opt* **14**, (2009).
293. Raffa, V., Ciofani, G., Vittorio, O., Riggio, C. & Cuschieri, A. Physicochemical properties affecting cellular uptake of carbon nanotubes. *Nanomedicine* **5**, 89–97 (2010).
294. Kenis, H. *et al.* Cell Surface-expressed Phosphatidylserine and Annexin A5 Open a Novel Portal of Cell Entry. *Journal of Biological Chemistry* **279**, 52623–52629 (2004).
295. Kraus, J. J., De Crescenzo, O. & Harrison, R. G. Purine Nucleoside Phosphorylase Targeted by Annexin V to Breast Cancer Vasculature for Enzyme Prodrug Therapy. *PLoS ONE* **8**, e76403 (2013).
296. Xiao, Y. *et al.* Anti-HER2 IgY antibody-functionalized single-walled carbon nanotubes for detection and selective destruction of breast cancer cells. *BMC Cancer* **9**, 351 (2009).
297. Shao, N., Lu, S., Wickstrom, E. & Panchapakesan, B. Integrated molecular targeting of IGF1R and HER2 surface receptors and destruction of breast cancer cells using single wall carbon nanotubes. *Nanotechnology* **18**, (2007).
298. Kam, N. W. S., O'Connell, M., Wisdom, J. A. & Dai, H. Carbon nanotubes as multifunctional biological transporters and near-infrared agents for selective cancer cell destruction. *Proceedings of the National Academy of Sciences of the United States of America* **102**, 11600–11605 (2005).
299. Marches, R. *et al.* The importance of cellular internalization of antibody-targeted carbon nanotubes in the photothermal ablation of breast cancer cells. *Nanotechnology* **22**, (2011).
300. Wang, C. H., Huang, Y. J., Chang, C. W., Hsu, W. M. & Peng, C. A. In vitro photothermal destruction of neuroblastoma cells using carbon nanotubes conjugated with GD2 monoclonal antibody. *Nanotechnology* **20**, (2009).
301. Iancu, C. *et al.* Enhanced laser thermal ablation for the in vitro treatment of liver cancer by specific delivery of multiwalled carbon nanotubes functionalized with human serum albumin. *International Journal of Nanomedicine* **6**, 129–141 (2011).

302. Chou, H. T., Wang, T. P., Lee, C. Y., Tai, N. H. & Chang, H. Y. Photothermal effects of multi-walled carbon nanotubes on the viability of BT-474 cancer cells. *Materials Science and Engineering C* **33**, 989–995 (2013).
303. Katt, M. E., Placone, A. L., Wong, A. D., Xu, Z. S. & Searson, P. C. In vitro tumor models: Advantages, disadvantages, variables, and selecting the right platform. *Frontiers in Bioengineering and Biotechnology* **4**, (2016).
304. Moon, H. K., Lee, S. H. & Choi, H. C. In vivo near-infrared mediated tumor destruction by photothermal effect of carbon nanotubes. *ACS Nano* **3**, 3707–3713 (2009).
305. Burke, A. *et al.* Long-term survival following a single treatment of kidney tumors with multiwalled carbon nanotubes and near-infrared radiation. *Proceedings of the National Academy of Sciences of the United States of America* **106**, 12897–12902 (2009).
306. Ghosh, S. *et al.* Increased heating efficiency and selective thermal ablation of malignant tissue with DNA-encased multiwalled carbon nanotubes. *ACS Nano* **3**, 2667–2673 (2009).
307. Huang, N. *et al.* Single-wall carbon nanotubes assisted photothermal cancer therapy: Animal study with a murine model of squamous cell carcinoma. *Lasers in Surgery and Medicine* **42**, 638–648 (2010).
308. Zhou, F. *et al.* Antitumor immunologically modified carbon nanotubes for photothermal therapy. *Biomaterials* **33**, 3235–3242 (2012).
309. Zhou, F., Wu, S., Wu, B., Chen, W. R. & Xing, D. Mitochondria-targeting single-walled carbon nanotubes for cancer photothermal therapy. *Small* **7**, 2727–2735 (2011).
310. Wang, C. *et al.* Immunological responses triggered by photothermal therapy with carbon nanotubes in combination with anti-CTLA-4 therapy to inhibit cancer metastasis. *Advanced Materials* **26**, 8154–8162 (2014).
311. Dong, X., Sun, Z., Wang, X. & Leng, X. An innovative MWCNTs/DOX/TC nanosystem for chemo-photothermal combination therapy of cancer. *Nanomedicine: Nanotechnology, Biology, and Medicine* **13**, 2271–2280 (2017).

312. Li, Y. *et al.* Phototherapy using immunologically modified carbon nanotubes to potentiate checkpoint blockade for metastatic breast cancer. *Nanomedicine: Nanotechnology, Biology, and Medicine* **18**, 44–53 (2019).
313. Ouzounova, M. *et al.* Monocytic and granulocytic myeloid derived suppressor cells differentially regulate spatiotemporal tumour plasticity during metastatic cascade. *Nat Commun* **8**, 14979 (2017).
314. Erin, N. *et al.* Bidirectional effect of CD200 on breast cancer development and metastasis, with ultimate outcome determined by tumor aggressiveness and a cancer-induced inflammatory response. *Oncogene* **34**, 3860–3870 (2015).
315. Ravindranathan, S. *et al.* Tumor-derived granulocyte colony-stimulating factor diminishes efficacy of breast tumor cell vaccines. *Breast Cancer Res* **20**, 126 (2018).
316. Broz, M. L. *et al.* Dissecting the Tumor Myeloid Compartment Reveals Rare Activating Antigen-Presenting Cells Critical for T Cell Immunity. *Cancer Cell* **26**, 638–652 (2014).
317. Demaria, O. *et al.* Harnessing innate immunity in cancer therapy. *Nature* **574**, 45–56 (2019).
318. Marabelle, A. *et al.* Depleting tumor-specific Tregs at a single site eradicates disseminated tumors. *J. Clin. Invest.* **123**, 2447–2463 (2013).
319. Houot, R. & Levy, R. T-cell modulation combined with intratumoral CpG cures lymphoma in a mouse model without the need for chemotherapy. *Blood* **113**, 3546–3552 (2009).
320. Sagiv-Barfi, I. *et al.* Eradication of spontaneous malignancy by local immunotherapy. *Sci. Transl. Med.* **10**, eaan4488 (2018).
321. Ribas, A. *et al.* SD-101 in Combination with Pembrolizumab in Advanced Melanoma: Results of a Phase Ib, Multicenter Study. *Cancer Discov* **8**, 1250–1257 (2018).
322. Sivick, K. E. *et al.* Magnitude of Therapeutic STING Activation Determines CD8+ T Cell-Mediated Anti-tumor Immunity. *Cell Reports* **25**, 3074-3085.e5 (2018).
323. Corrales, L. *et al.* Direct Activation of STING in the Tumor Microenvironment Leads to Potent and Systemic Tumor Regression and Immunity. *Cell Reports* **11**, 1018–1030 (2015).

324. Demaria, O. *et al.* STING activation of tumor endothelial cells initiates spontaneous and therapeutic antitumor immunity. *Proc Natl Acad Sci USA* **112**, 15408–15413 (2015).
325. Adams, S. Toll-like receptor agonists in cancer therapy. *Immunotherapy* **1**, 949–964 (2009).
326. Adams, S. *et al.* Immunization of Malignant Melanoma Patients with Full-Length NY-ESO-1 Protein Using TLR7 Agonist Imiquimod as Vaccine Adjuvant. *J Immunol* **181**, 776–784 (2008).
327. Adams, S. *et al.* Topical TLR7 Agonist Imiquimod Can Induce Immune-Mediated Rejection of Skin Metastases in Patients with Breast Cancer. *Clinical Cancer Research* **18**, 6748–6757 (2012).
328. Dewan, M. Z. *et al.* Synergy of Topical Toll-like Receptor 7 Agonist with Radiation and Low-Dose Cyclophosphamide in a Mouse Model of Cutaneous Breast Cancer. *Clinical Cancer Research* **18**, 6668–6678 (2012).
329. Lu, H. *et al.* Treatment Failure of a TLR-7 Agonist Occurs Due to Self-Regulation of Acute Inflammation and Can Be Overcome by IL-10 Blockade. *J.I.* **184**, 5360–5367 (2010).
330. Nerurkar, L., McColl, A., Graham, G. & Cavanagh, J. The Systemic Response to Topical Aldara Treatment is Mediated Through Direct TLR7 Stimulation as Imiquimod Enters the Circulation. *Sci Rep* **7**, 16570 (2017).
331. Redondo, P. *et al.* Imiquimod Enhances the Systemic Immunity Attained by Local Cryosurgery Destruction of Melanoma Lesions. *Journal of Investigative Dermatology* **127**, 1673–1680 (2007).
332. Scarfi, F. *et al.* The role of topical imiquimod in melanoma cutaneous metastases: A critical review of the literature. *Dermatologic Therapy* **33**, (2020).
333. Lapin, N. A., Krzykawska-Serda, M., Ware, M. J., Curley, S. A. & Corr, S. J. Intravital microscopy for evaluating tumor perfusion of nanoparticles exposed to non-invasive radiofrequency electric fields. *Cancer Nano* **7**, 5 (2016).

334. Lapin, N. A. *et al.* The effects of non-invasive radiofrequency electric field hyperthermia on biotransport and biodistribution of fluorescent [60]fullerene derivative in a murine orthotopic model of breast adenocarcinoma. *Journal of Controlled Release* **260**, 92–99 (2017).

APPENDIX A – Supplemental data

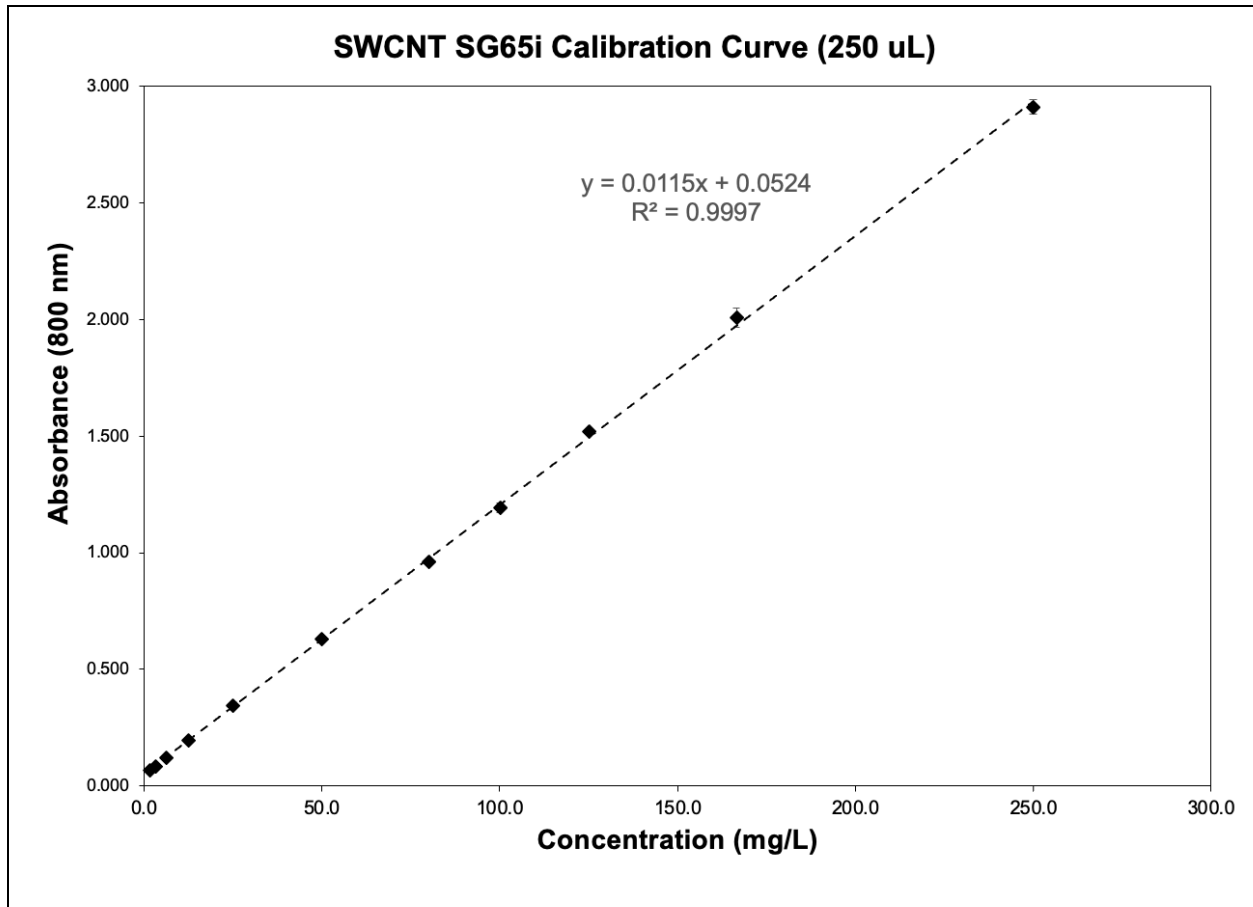


Figure 68: Standard curve for low concentration SWCNT suspension using 250 μL samples in 96-well plates.

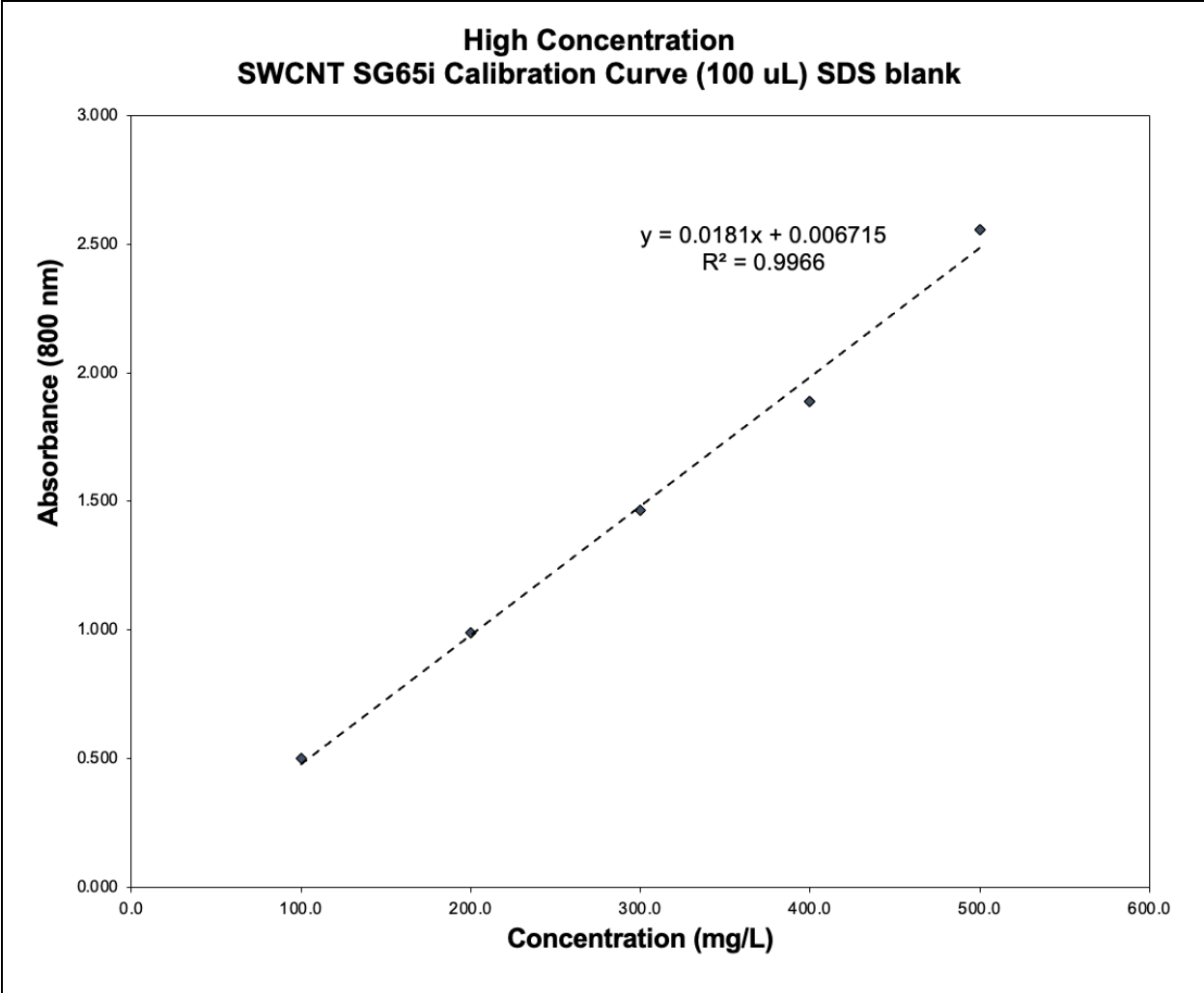


Figure 69: Standard curve for high concentration SWCNT suspension using 100 μ L samples in 96-well plates.

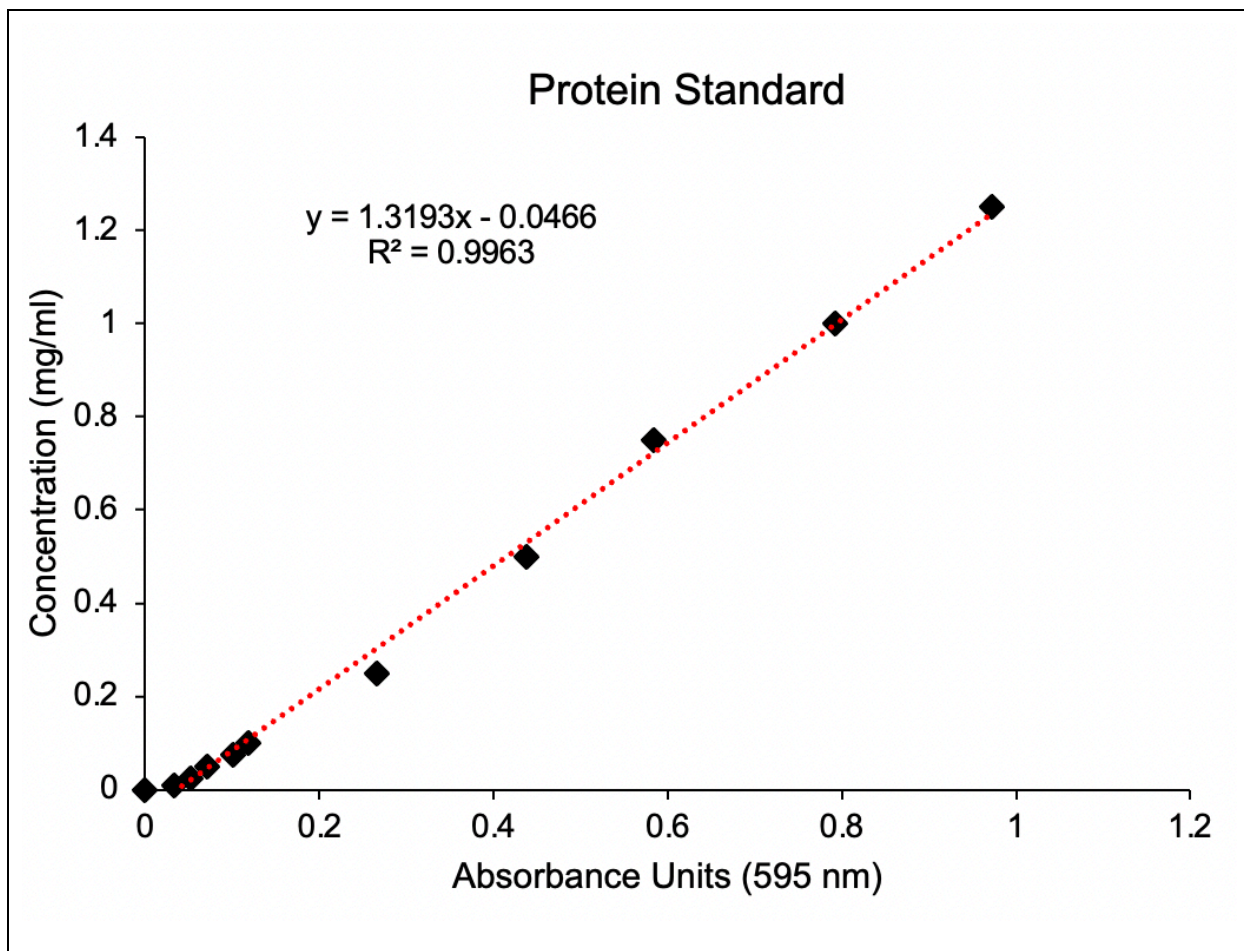


Figure 70: Protein standard for Bradford assay. The standard is made with bovine serum albumin (BSA) to create the standard solution, and it is used to assess the concentration of annexin A5 in solutions and conjugations. For that, 250 μL of Bradford reagent and 5 μL of protein solution is used. PBS in Bradford reagent is used as blank.

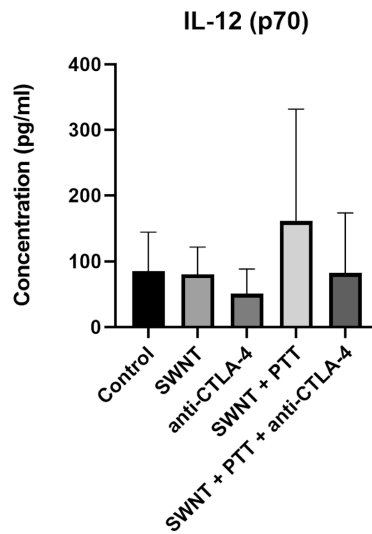


Figure 71: IL-12 p70 concentration in serum 7 days after PTT in mice treated with combination therapy of SWCNT-ANXA5 mediated PTT and anti-CTLA-4: Levels of TNF- α , IL-6, IFN- γ and IL-12 p70 were measured in the serum of mice treated with IV injections of conjugate, anti-CTLA-4 injection alone, IV injections of conjugate combined with PTT, IV injections of conjugate combined with PTT and anti-CTLA-4 injection, or untreated mice as a control. Laser wavelength was 980 nm and power density 1.0 W/cm² for 175 seconds. Blood samples were collected 7 days after photothermal therapy. For each treatment compared to the control, one-way ANOVA and Dunnett's multiple comparisons were carried out on the GraphPad Prism 8. No statistical significance was found between groups for IL-12 p70.

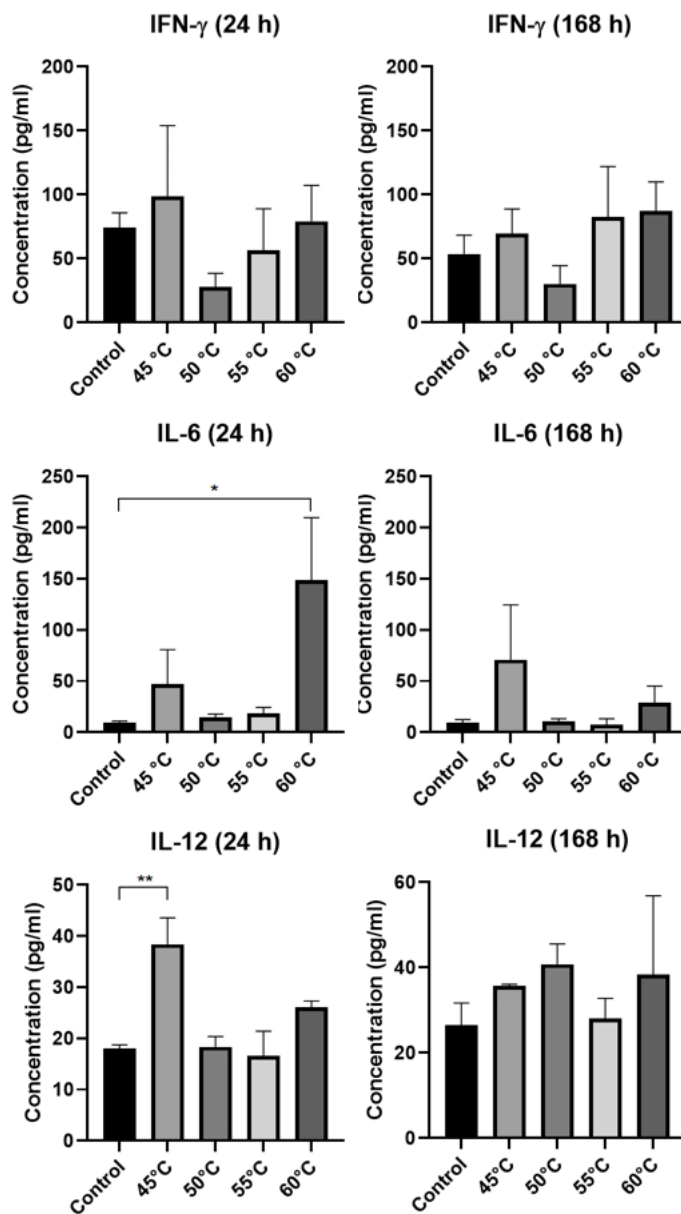


Figure 72: Extra data from cytokine concentrations in serum 1 day (24 h) and 7 days (168 h) after PTT with different final temperatures in EMT6 tumors. The diagrams show the level of IFN- γ , IL-6 and IL-12(p70) in the serum of mice treated with 980 nm-laser at power density 1.0 W/cm² after IT injection of SWCNT-ANXA5 conjugate. Blood samples were collected 1 day and 7 days after PTT, and the levels of TNF- α IFN- γ , IL-6 and IL-12(p70) in the serum were analyzed by ELISA compared to untreated control (injected intratumorally with SWCNT-ANXA5 but not treated with

PTT). Photothermal therapy was performed until reaching final temperatures of 45, 50, 55, or 60°C for each group. Data are presented as mean \pm SE (n = 4–5). Statistical significance was analyzed for the treated groups compared to the untreated control group by one-way ANOVA with Dunnett's multiple comparisons test. Statistical significance is indicated by *p < 0.05 and **p < 0.01.

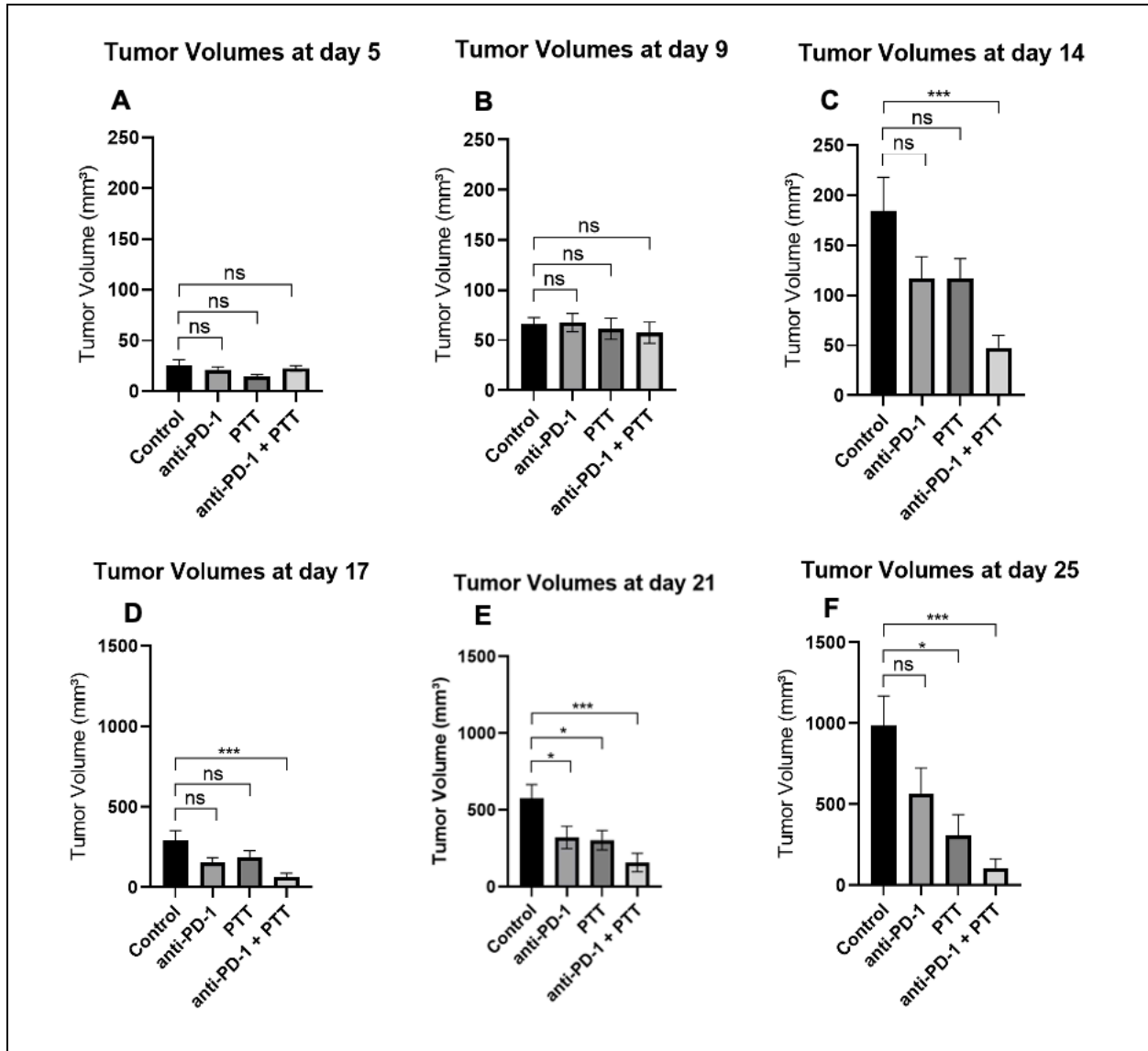


Figure 73: Tumor volumes from combinatorial photothermal therapy (PTT) and checkpoint inhibition (anti-PD-1) in EMT6 tumors from days 5 to 25. Mice with well-developed orthotopic syngeneic tumors (d \geq 5 mm) were administered an IT dose of

1.2 mg/kg SWCNT-ANXA5. Tumors were irradiated with an NIR laser at a power density of 1 W/cm² until the tumor surface temperature reached 45°C. Select groups received anti-PD-1 (10 mg/kg) on days 8, 11, and 16. Tumor volume is shown as mean ± SE (n = 7). Statistical analysis was performed comparing each treatment group to the untreated control. One-way ANOVA and Dunnett's multiple comparisons were carried out on GraphPad Prism 8. (ns = non-significant, *p < 0.05, ***p < 0.001)

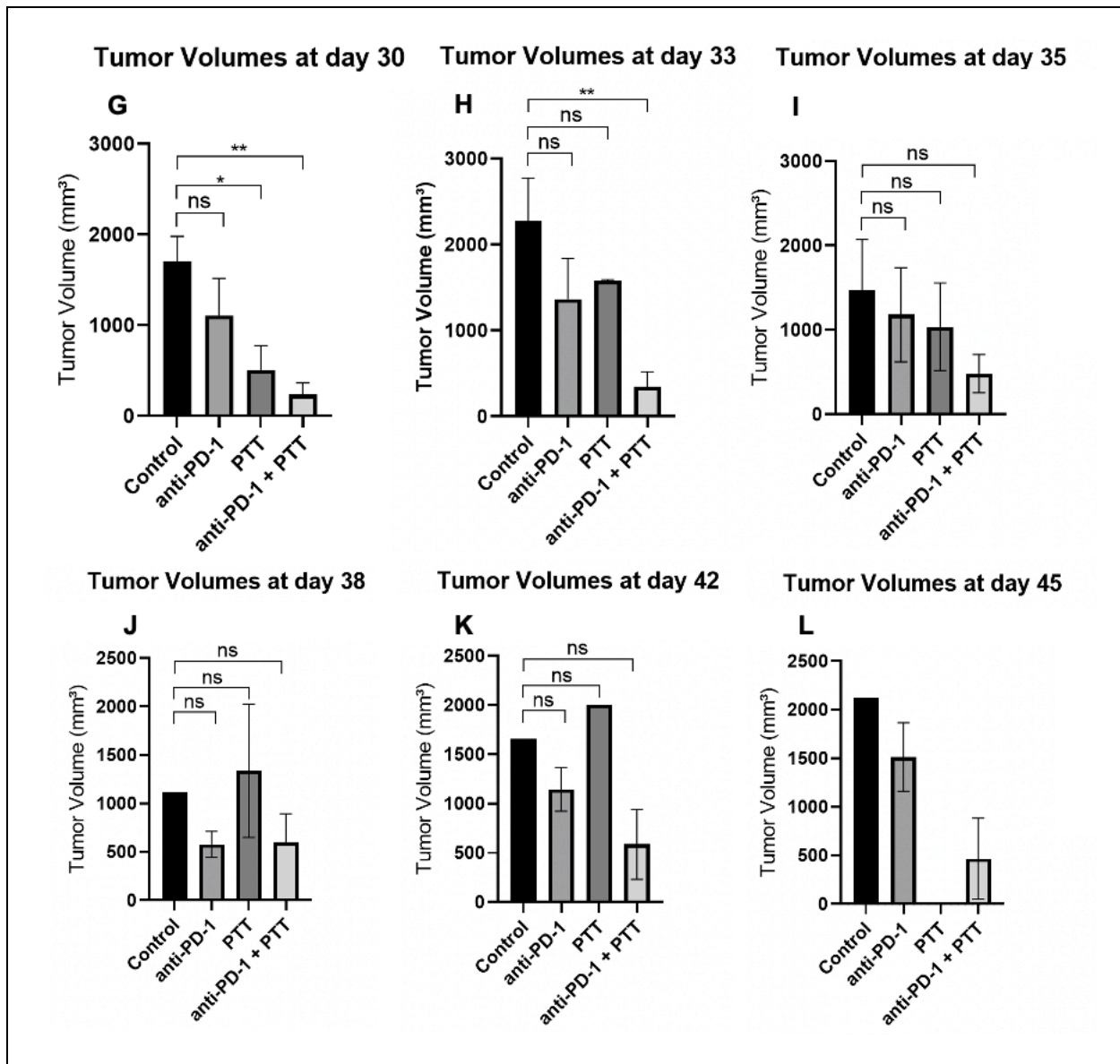


Figure 74: Tumor volumes from combinatorial photothermal therapy (PTT) and checkpoint inhibition (anti-PD-1) in EMT6 tumors from days 30 to 45. Mice with well-developed orthotopic syngeneic tumors ($d \geq 5$ mm) were administered an IT dose of 1.2 mg/kg SWCNT-ANXA5. Tumors were irradiated with an NIR laser at a power density of 1 W/cm² until the tumor surface temperature reached 45°C. Select groups received anti-PD-1 (10 mg/kg) on days 8, 11, and 16. Tumor volume is shown as mean \pm SE (n = 7). Statistical analysis was performed comparing each treatment group to the untreated control. One-way ANOVA and Dunnett's multiple comparisons were carried out on GraphPad Prism 8. (ns = non-significant, *p < 0.05, ***p < 0.001)

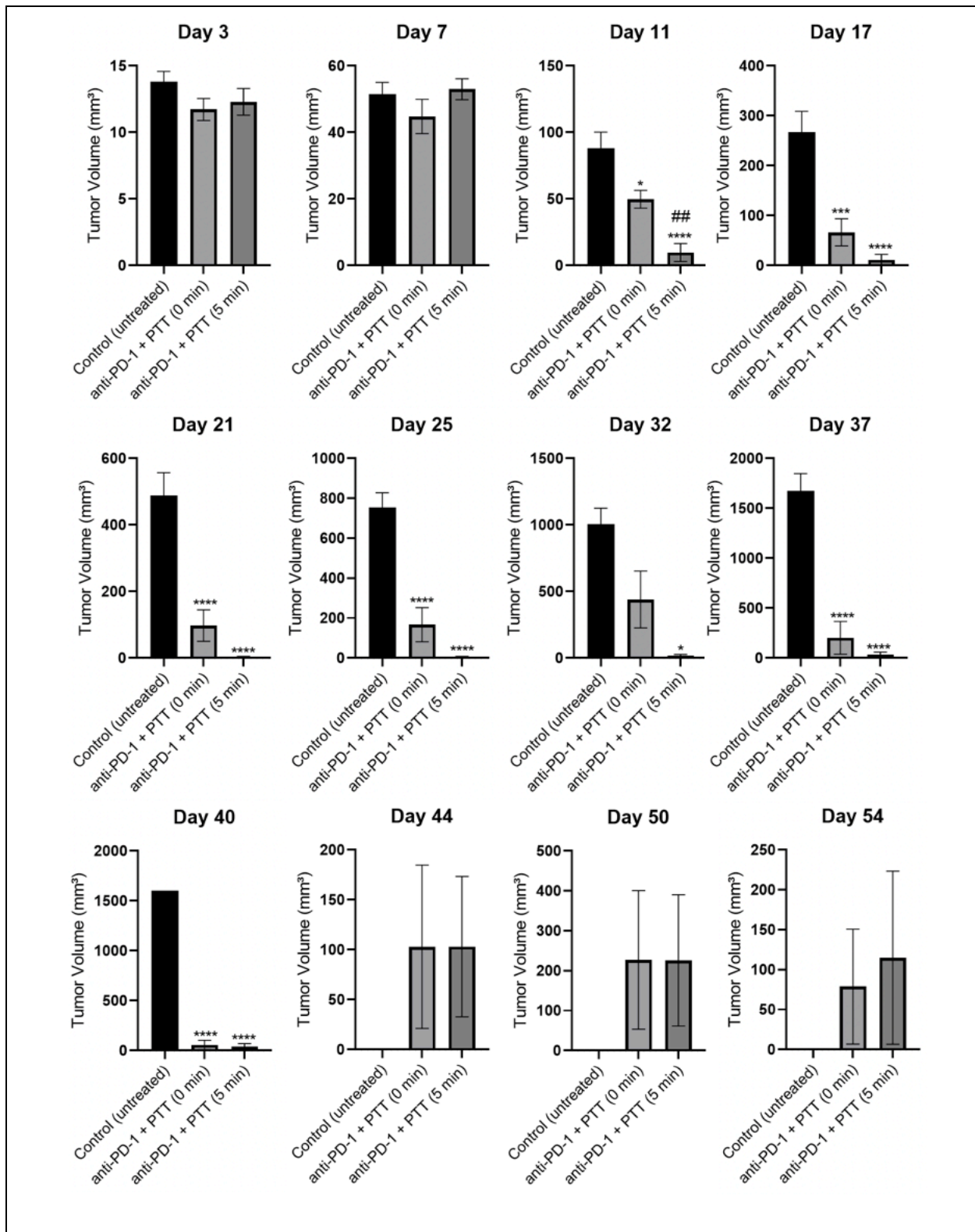


Figure 75: Tumor volumes at various days for combinatorial therapy of checkpoint inhibition (anti-PD-1) and photothermal therapy (PTT) at 45°C

(immediately stopped or kept for 5 min) and in EMT6 tumors. Mice with well-developed orthotopic syngeneic tumors ($d \geq 5$ mm) were administered an IT dose of 1.2 mg/kg SWCNT-ANXA5. Select groups received anti-PD-1 (10 mg/kg) on days 7, 10, and 15. Tumors were irradiated with an NIR laser at a power density of 1 W/cm². The anti-PD-1 + PTT (0 min) group received irradiation until the tumor surface temperature reached 45°C, whereas the anti-PD-1 + PTT (5 min) group received irradiation up to 45°C when the laser was cycled on/off to keep the tumor surface temperature at 45°C for 5 min. Tumor volumes are shown as mean \pm SE (n = 10). Statistical analysis was performed by one-way ANOVA and Tukey's multiple comparisons were carried out on GraphPad Prism 8, comparing the mean of each group with the mean of every other group. Statistical significance from treated groups to control untreated is shown by *p < 0.05, ***p < 0.001 and ****p < 0.0001. Statistical significance between anti-PD-1 + PTT (0 min) anti-PD-1 + PTT (5 min) is shown by ##p < 0.01.

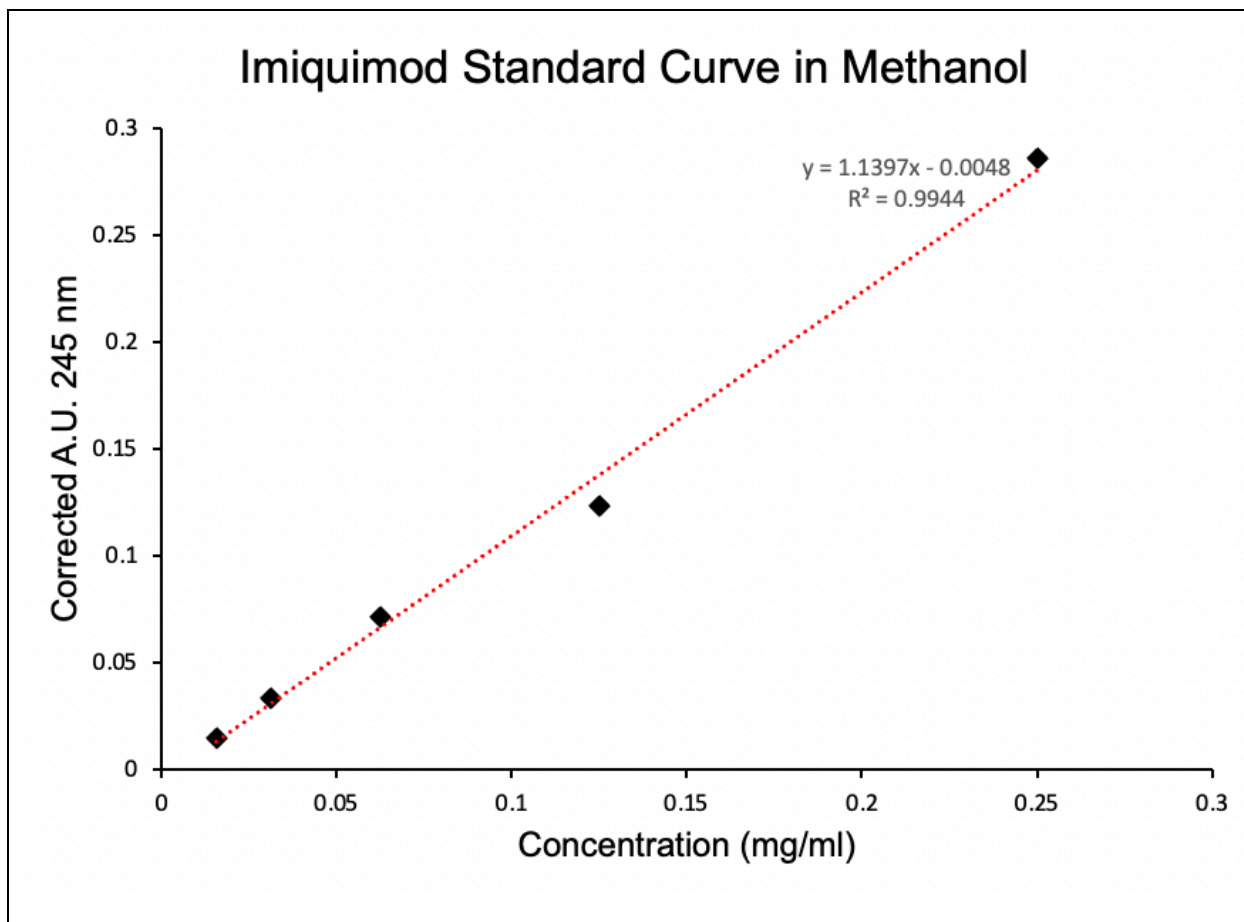


Figure 76: Standard curve of imiquimod (IMQ) in methanol. The standard solution was prepared by dissolving 3.0 mg of IMQ in 3.0 ml of methanol. Serial dilutions were performed in methanol. One hundred milliliter samples were placed in triplicate in 96-well plates, and endpoint absorbance was read at 245 nm.

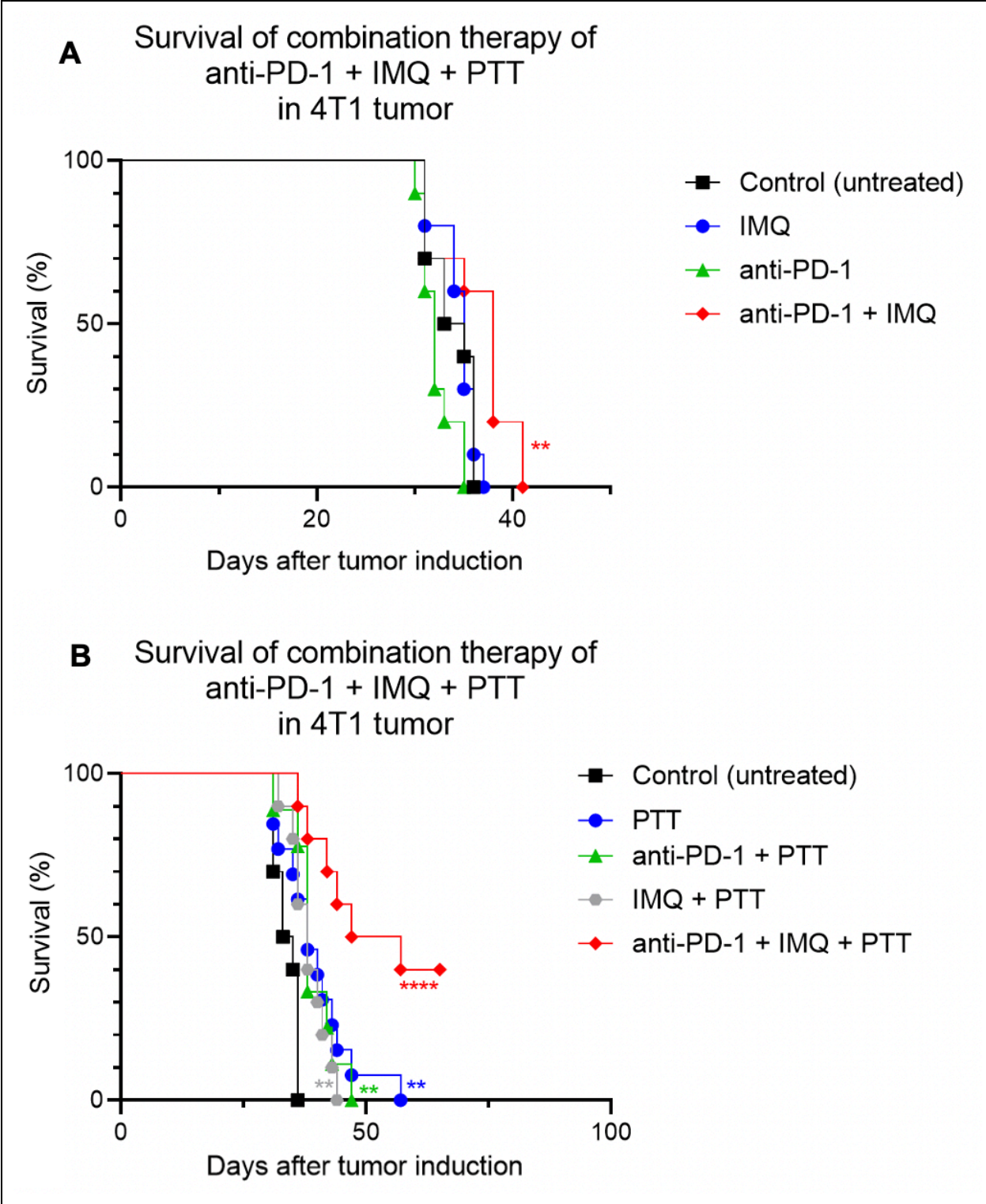


Figure 77: Long-term survival study of combinatorial therapy of anti-PD-1, imiquimod-loaded hydrogel and photothermal therapy (PTT) at 55°C in 4T1 tumors. Female Balb c/J mice bearing 4T1 orthotopic syngeneic tumors (d ~ 3 mm)

were treated with combinatorial therapy. Selected groups were administered with imiquimod (IMQ)-loaded hydrogel intratumorally (50 mg of IMQ) on day 7 after tumor inoculation. Select groups also received intraperitoneal injection of anti-PD-1 (10 mg/kg) on days 7, 10, and 15. On day 11, groups were administered with an IT dose of 1.2 mg/kg SWCNT-ANXA5. Tumors were irradiated with a NIR laser at a power density of 1 W/cm² until tumor surface temperature reached 55°C. A) Survival curves of treated groups that did not involve PTT. B) Survival curves of treated groups that did not involve PTT. Statistical significance of survival curves was determined by the Mantel–Haenszel log-rank test in GraphPad Prim 8, compared to untreated control. Increase of survival from complete treatment (anti-PD-1 + IMQ + PTT) is statistically significant from control (****p < 0.0001, n = 10). Four mice in the complete treatment group are alive, healthy, and without tumors on day 65. Study will be terminated at day 100.

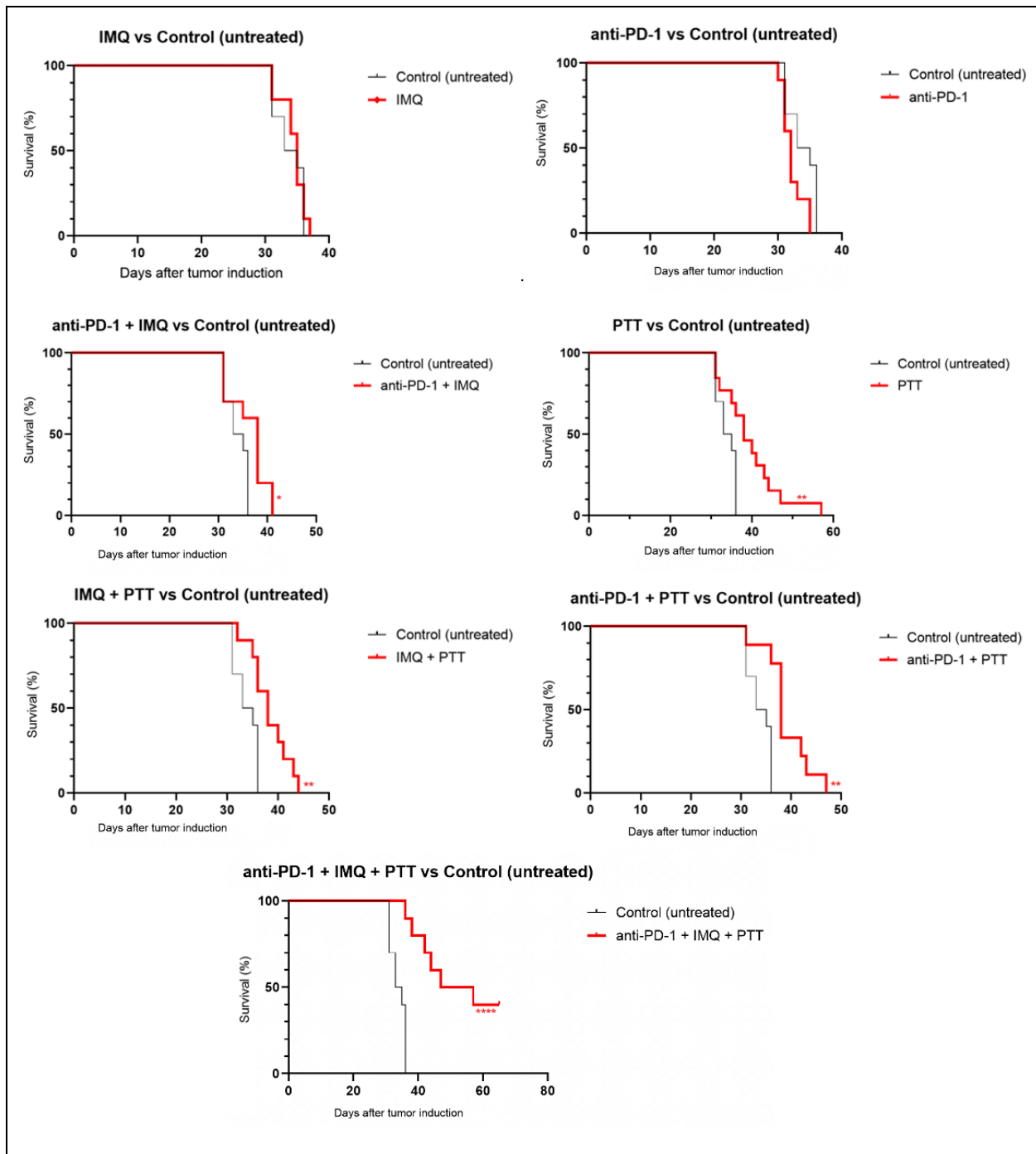


Figure 78: Survival curves of individual groups compared to control in long-term survival study of combinatorial therapy of anti-PD-1, imiquimod-loaded hydrogel and photothermal therapy (PTT) at 55°C in 4T1 tumors. Female Balb c/J mice bearing 4T1 orthotopic syngeneic tumors (d ~ 3 mm) were treated with combinatorial therapy. Selected groups were administered with imiquimod (IMQ)-loaded hydrogel intratumorally (50 mg of IMQ) on day 7 after tumor inoculation. Select groups also

received intraperitoneal injection of anti-PD-1 (10 mg/kg) on days 7, 10, and 15. On day 11, groups were administered with an IT dose of 1.2 mg/kg SWCNT-ANXA5. Tumors were irradiated with an NIR laser at a power density of 1 W/cm² until the tumor surface temperature reached 55°C. Statistical significance of survival curves was determined by the Mantel–Haenszel log-rank test in GraphPad Prim 8, compared to untreated control. *p < 0.05, **p < 0.01 ****p < 0.0001, n = 10. Three mice in the complete treatment group were alive, healthy, and without tumors on day 94. Study will be terminated at day 100.

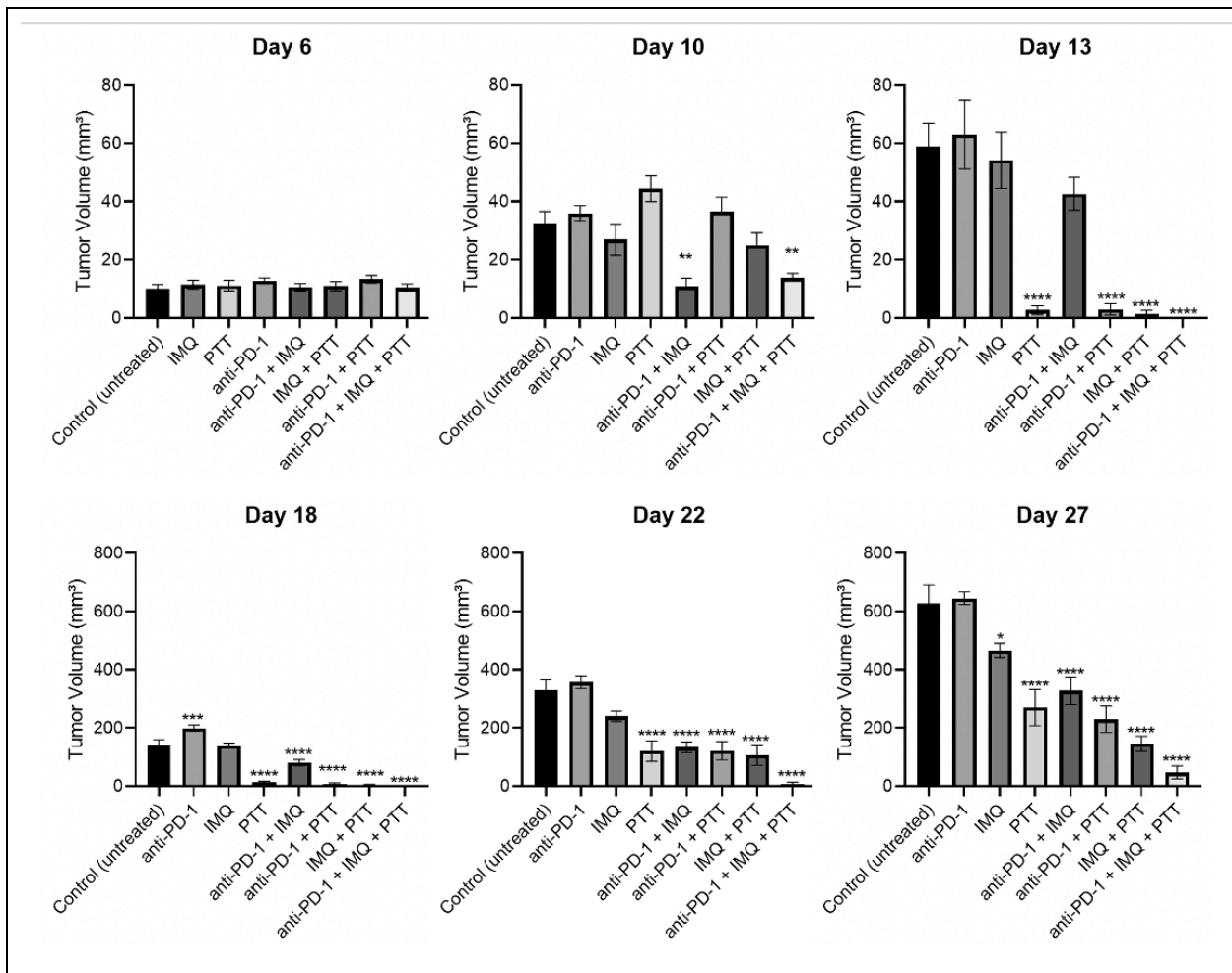


Figure 79: Tumor volumes from days 6 to 27 in long-term survival study of combinatorial therapy of anti-PD-1, imiquimod-loaded hydrogel and photothermal therapy (PTT) at 55°C in 4T1 tumors. Female Balb c/J mice bearing

4T1 orthotopic syngeneic tumors (d ~ 3 mm) were treated with combinatorial therapy. Selected groups were administered with imiquimod (IMQ)-loaded hydrogel intratumorally (50 mg of IMQ) on day 7 after tumor inoculation. Select groups also received intraperitoneal injection of anti-PD-1 (10 mg/kg) on days 7, 10, and 15. On day 11, groups were administered with an IT dose of 1.2 mg/kg SWCNT-ANXA5. Tumors were irradiated with an NIR laser at a power density of 1 W/cm² until the tumor surface temperature reached 55°C. Tumor volume is shown as mean ± SE (n = 10). Statistical analysis was performed comparing each treatment group to the untreated control. One-way ANOVA and Dunnett's multiple comparisons were carried out on GraphPad Prism 8. (*p < 0.05, **p < 0.01, ***p < 0.001, ****p < 0.001)

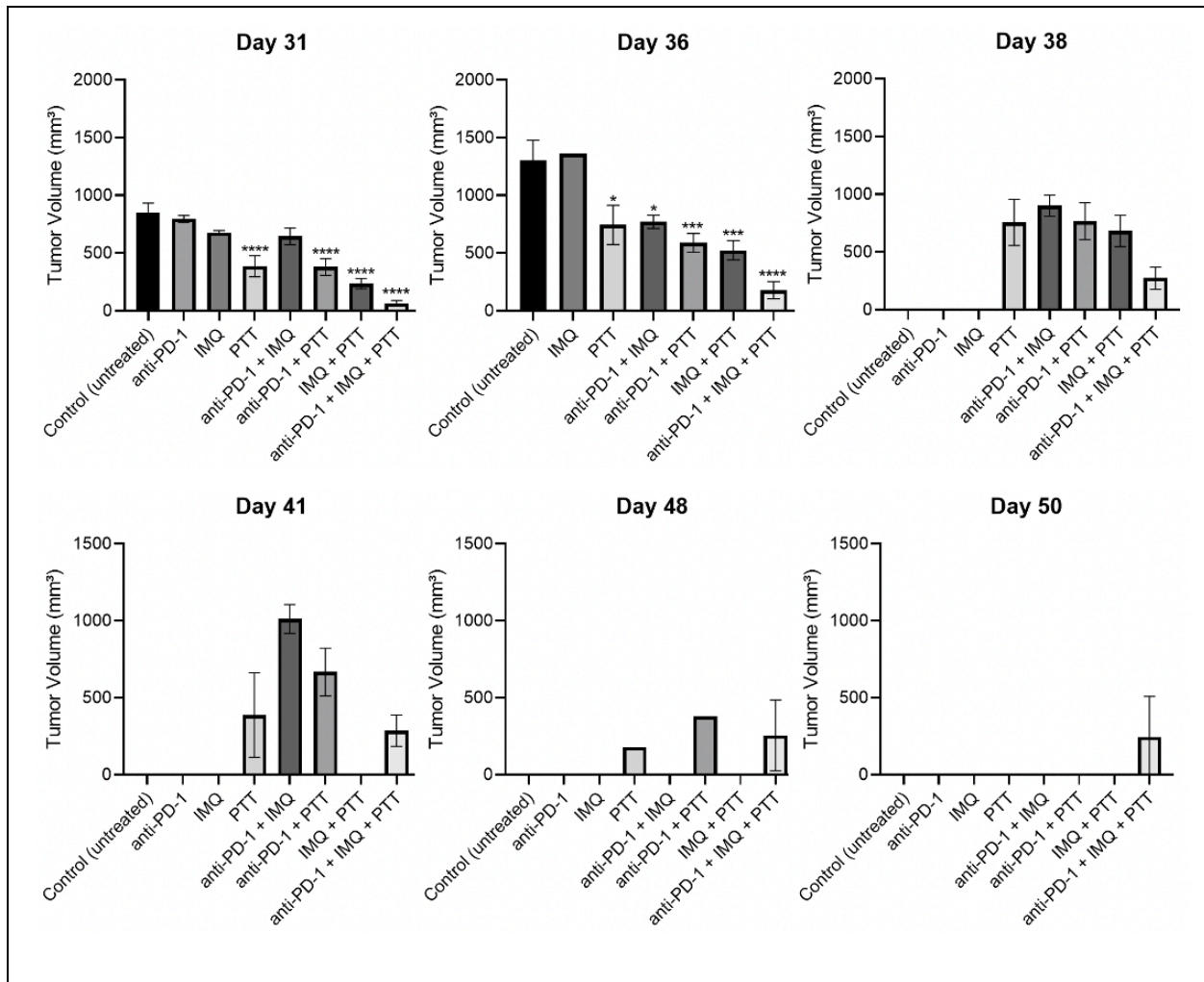


Figure 80: Tumor volumes from days 31 to 50 in long-term survival study of combinatorial therapy of anti-PD-1, imiquimod-loaded hydrogel and photothermal therapy (PTT) at 55°C in 4T1 tumors. Female Balb c/J mice bearing 4T1 orthotopic syngeneic tumors (d ~ 3 mm) were treated with combinatorial therapy. Selected groups were administered with imiquimod (IMQ)-loaded hydrogel intratumorally (50 mg of IMQ) on day 7 after tumor inoculation. Select groups also received intraperitoneal injection of anti-PD-1 (10 mg/kg) on days 7, 10, and 15. On day 11, groups were administered with an IT dose of 1.2 mg/kg SWCNT-ANXA5. Tumors were irradiated with an NIR laser at a power density of 1 W/cm² until the tumor surface temperature reached 55°C. Tumor volume is shown as mean ± SE (n = 10). Statistical analysis was performed comparing each treatment group to the untreated control. One-way ANOVA and Dunnett's multiple comparisons were carried out on GraphPad Prism 8. (*p < 0.05, **p < 0.01, ***p < 0.001, ****p < 0.0001).

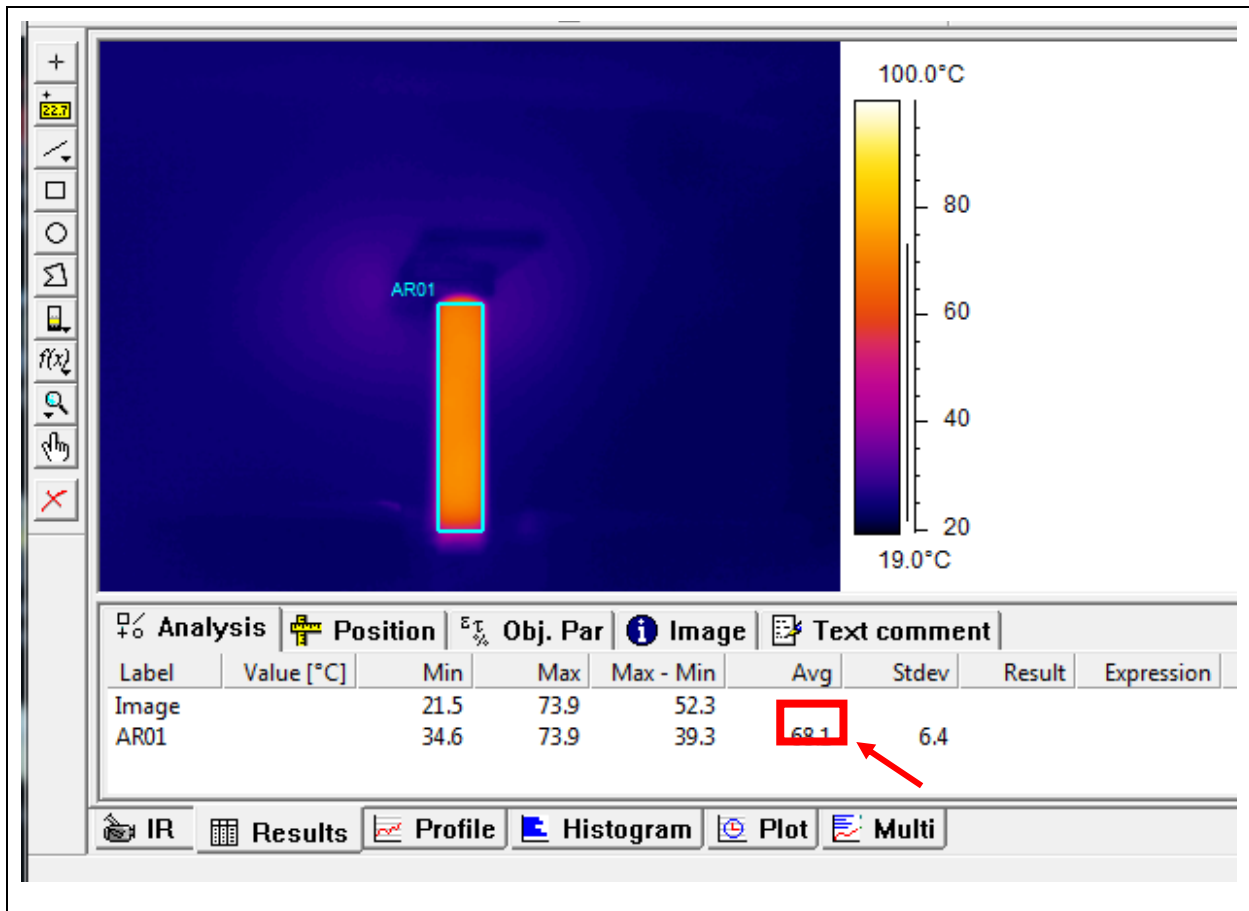


Figure 81: Thermal image analysis with ThermaCAM Researcher Pro 2.7 Software for experiment shown in Figure 58. Arrow indicates the average temperature evaluated by the software in area AR01, which was set up to capture the lateral area of cylindrical sample holder (shell vial) with samples being irradiated with a 13.56 MHz RF field.



Figure 82: Details of the setup to concentrate the RF field to the abdominal area of the mouse with smaller plates. Plates with width of 2 cm were built by Dr. Caleb Fulton. Styrofoam was used to isolate lower plate. Cardboard was placed to avoid leaking of the field. This setup was not efficient to avoid overheating of regions outside of the irradiation area, which can be seen in **Figure 61**.

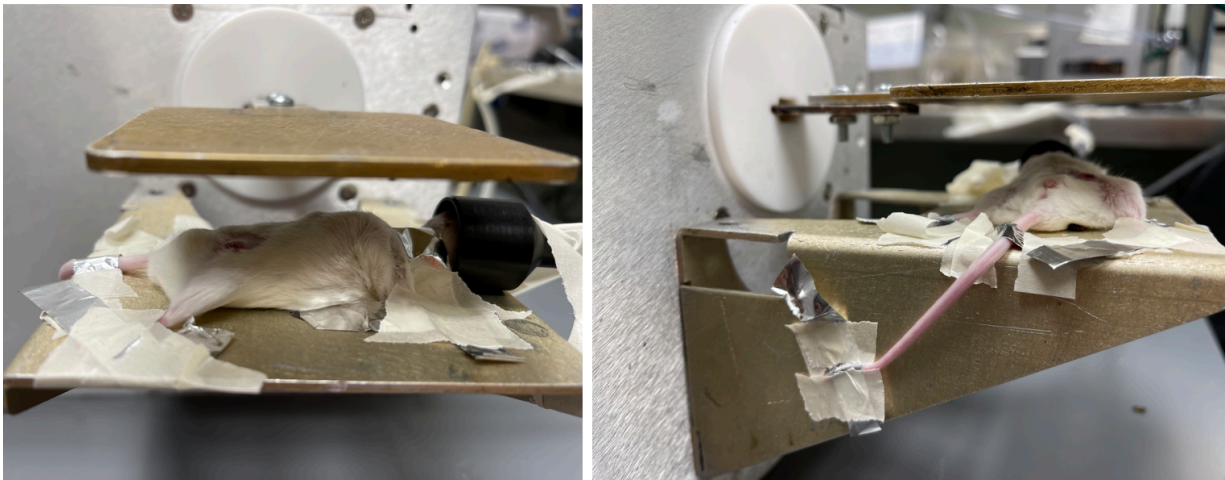


Figure 83: Details of the setup to ground excess charges built up from RF irradiation on mouse extremities. Aluminum stripes were wrapped around front and back paws, tail, and ears from one end and connected to the ground electrode from the RF Comdel system. This setup was not effective at avoiding overheating, especially in the head area because of the limitations of the grounding due to presence of the nose cone.

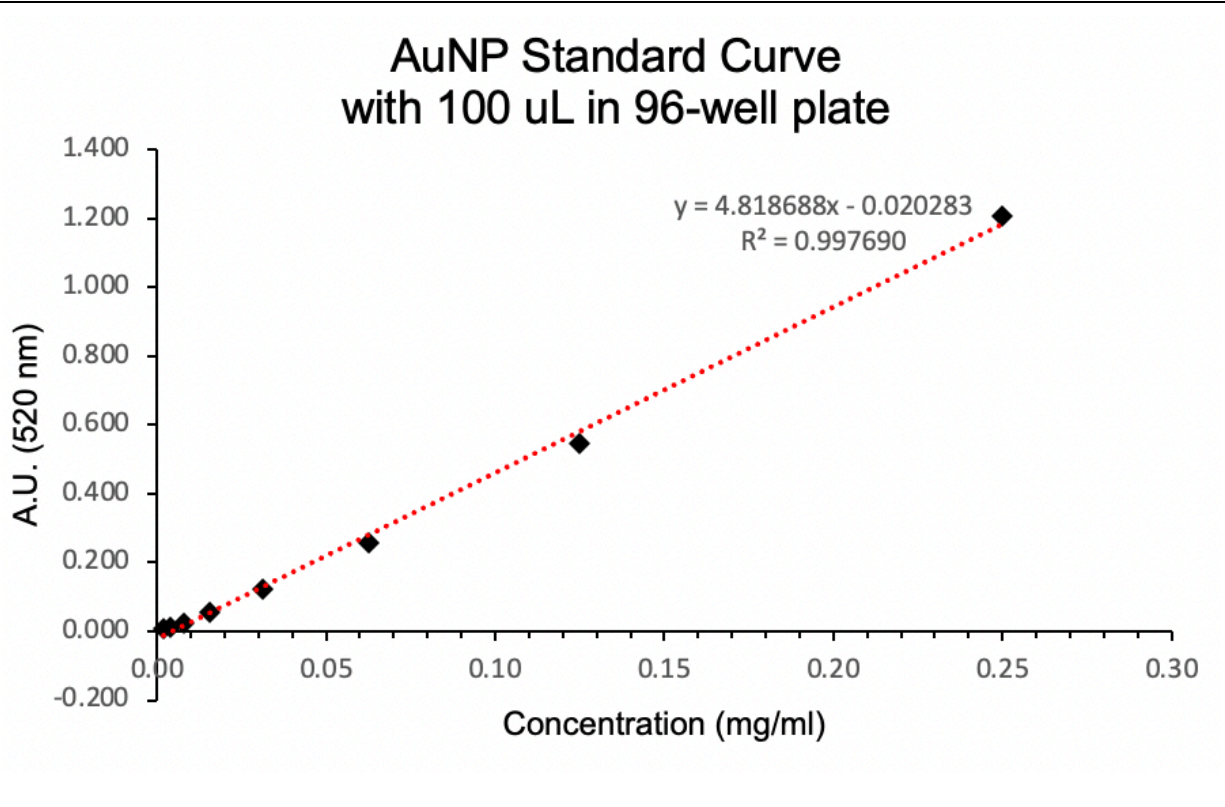


Figure 84: Standard curve of AuNP. After serial dilutions from the standard solution, samples (100 μL) were placed in individual wells in a 96-well plate. PBS was used as blank. Endpoint absorbance was read at 520 nm.

APPENDIX B – Protein Protocols

B1. Annexin production using LB media

Day before starting, autoclave the following items:

- 1 liter LB medium
- 4 x 1 liter Erlenmeyer flask (with aluminum foil on top)
- 125 ml Erlenmeyer flask (with aluminum foil on top)
- 100 ml beaker (with aluminum foil on top)
- All size tips
- 1.5 ml centrifuge tubes (100)
- 1 liter DI water

Protein Expression

Day 1

1. Culture 5 μ l of *E. coli*/BL21(DE3) harboring pET303CT with the fusion gene ANXA5 in 10 ml of LB medium containing 35 μ g/ml kanamycin in a 125 ml Erlenmeyer flask overnight at 37°C with shaking at 200 rpm. $OD_{600} = 0.5$
 - LB medium: 1 liter DI H₂O + 10 g tryptone + 5 g yeast extract + 5 g NaCl.
 - Add 35 mg kanamycin to the 1 L of LB medium before taking out the 10 ml for the initial culture.
 - Incubate.

Day 2

2. Add 10 ml of the cell culture to 1 liter of fresh culture medium+ kanamycin and incubate at 37°C with shaking (200 rpm). Take 1.5 mL of medium before adding the bacteria, as a blank. This cell culture was grown to mid-log phase => $OD_{600} = 0.5$.
 - Take a 1.5 ml sample of just the LB medium. Label 1.5 ml tube 'LB.'
 - Transfer 10 mL of bacteria to 1 L LB medium.
 - Transfer entire volume of medium to 4 x 1 L flasks.
 - Put in shaker at 37° C at 200 rpm.

- After 1.5 hrs of shaking, measure optical density at 600 nm (absorbance) using a clear 96 well plate and microtiter plate reader of sample vs LB medium => using 250 µl samples of each. When $OD_{600nm} = 0.5$ (between .5 and .8 is good), then proceed to next step.
3. Add isopropyl β -D-thiogalactopyranoside (IPTG - stored @ -20°C top shelf) to a final concentration of 0.4 mM (96 mg IPTG total – 24 mg per flask) to solutions in 4 x 1 L flasks and incubate at 30°C with shaking (180 rpm) for 5 h to induce protein expression.
 - Take 750 ml sample of solution before adding IPTG. Label it 'BI.'
 - Add 24 mg IPTG to each flask.
 - Put back in shaker at 30°C for 5 hours.
 - IPTG stimulates the production of fusion protein. (IPTG activates the promoter in the plasmid that will start the transcription of the gene that follows the promoter =>Annexin V gene.)
 4. Harvest the cells by centrifugation for 10 min at 1000 x g, at 4°C.
 - Take 750 ml sample before centrifuge. Label sample 'BC.'
 - Centrifuge at 1000xg = ~3000 rpm (centrifuge uses rpm – consult table on machine). Only 4 – 50 ml centrifuge tubes at a time, temp 4°C, 10 mins.
 - After first centrifuge, pour out supernatant, add more culture to same 4 tubes. Bacteria will be stuck to side of tubes so inverting to pour out is not a problem.
 - Can put the 4 tubes in -20°C freezer for overnight storage.

Day 3

5. Resuspend the cell pellet in 40 ml of sonication buffer.
 - Add ~10 ml to each of the 4 centrifuge tubes.
 - Vortex to resuspend cell pellets.
 - Pour contents of the 4 tubes back into the 100 ml beaker.
 - Sonication Buffer
 - 0.05 mM N- *p*-tosyl-L-phenylalanine chloromethyl ketone (TPCK) - (-20°C) => 0.704 mg.
 - 1 mM phenylmethylsulfonyl fluoride (PMSF) - (shelf) =>6.968 mg.
 - 1% HPLC ethanol - (flammables) => 400 µl.
 - 0.01% β -mercaptoethanol – (bench top) => 4 µl.
 - 0.02 M sodium phosphate dibasic – (shelf) => 113.6 mg.
 - 40 mL DI

- Dissolve TPCK and PMSF in ethanol in microcentrifuge tube, then add to beaker.
 - Make this buffer in the 100 ml beaker.
 - Correct to pH 7.4 – using HCl
6. Lyse the cells by sonication at 4°C for 30 sec at 4.5 watts then allow it to cool for 30 sec on ice. This cycle was repeated 4 times (= 5 times total) for a total sonication time of 2.5 min on power level 4.
- Clean sonicator tip w/ ethanol before use.
 - Put beaker in tub w/ ice while sonicating.
7. Centrifuge the lysate obtained at 12,000 x g for 30 min to remove the cell debris and take the supernatant.
- Pour beaker contents into 1 purple VWR 50 ml centrifuge tube.
 - Centrifuge at 12000xg for 30 mins => this equals ~10,000 rpm.
 - Take 750 µl sample after centrifuging. Label sample 'SS.' The proteins will be in the supernatant and the cell debris will be at bottom of tube.

Protein Purification

Day 4

8. After taking supernatant sample, add imidazole (40 mM) and NaCl (500 mM) to the lysate to reduce non-specific protein binding.
- 40 mM imidazole => use 0.0817 g
 - 500 mM NaCl => use 1.168 g
9. Equilibrate a 5 ml HisTrap chromatography column with immobilized Ni²⁺ using Wash Buffer 1.
- Feed wash buffer thru column until the output reaches baseline, then feed lysate thru at -8.00 ↶
 - Turn on detector.
 - Turn on drop former – mode 0, rack 1, size 2, last tube 100, min 4, delay 0.
 - WASH BUFFER 1 (500 mL) (- 30 min)
 - 20 mM sodium phosphate dibasic => use 1.42 g
 - 40 mM imidazole => use 1.362 g
 - 500 mM NaCl => use 14.61 g
 - Correct this to pH 7.4

10. Feed the soluble protein fraction into the column. Collect flow through and label 'F1-1.'
11. Wash the column with 70 column volumes of Wash Buffer 2 to remove unwanted proteins and endotoxin (250 ml).
- Collect flow thru – contains unwanted proteins
 - Label sample 'F1-2.'
 - WASH BUFFER 2 (300 mL) (- 1.5 hours)
 - 20 mM sodium phosphate dibasic =>use 0.8517 g
 - 40 mM imidazole =>use 0.817 g
 - 500 mM NaCl=> use 8.766 g
 - 0.1% Triton X-114 => 3 ml
 - Correct this to pH 7.4
12. Wash the column with 20 column volumes of Wash Buffer 1 to wash the protein until the pen reaches the baseline (100 ml). (- 40 min)
- Collect flow thru – contains unwanted proteins (take 800 µl sample)
 - Label sample 'F1-3.'
 - Look at graph paper from previous run to understand when/what to collect.
13. Elute the protein using elution buffer.
- Collect the elution – contains our FP (take 800 µl sample)
 - Label the sample 'E1.'
 - Look at graph paper from previous run to understand when/what to collect.
 - ELUTION BUFFER (300 mL)
 - 20 mM sodium phosphate dibasic =>use 0.8517 g
 - 500 mM imidazole => use 10.212 g
 - 500 mM NaCl => use 8.766 g
 - Correct this to pH 7
14. Dialyze eluted protein for 3 hours against 2 liters of dialysis buffer containing 20 mM sodium phosphate at pH 7.4 to remove NaCl and imidazole from the protein solution and make it suitable for C-terminal His-tag cleavage.
- DIALYSIS 1 BUFFER (2 L) – *Used 2 dialysis because collected 40 mL of protein -> 20 mL for each dialysis*
 - 20 mM sodium phosphate dibasic =>5.678 g
 - Adjust to pH 7.4
 - After dialysis, put back in a 50 ml centrifuge tube. Take a 750 µl sample. Label the sample 'AD1.'

15. Before continuing, need to regenerate the column using this procedure:
- 25 ml of 1 M KCl => make 200 ml, so use 14.91 g
 - 25 ml of 1 M NaOH => make 200 ml, so use 8.0 g
 - 25 ml of DI water
 - 25 ml of 1 M HPLC Grade Ethanol => 1.46 ml ethanol + 23.54 ml DI Water
16. Measure the concentration of protein (Bradford protein assay). *2.81 mg/mL measured in 40 mL -> total is 112.4 mg*
- Add 30 ml DI Water to tube w/ cell pellet. Take 750 μ l sample. Label sample '**SP.**'
17. Cleave the C-terminal His-tag by adding HRV 3C protease at 10 U/mg of protein with the recommended 10X buffer provided (stored @ -20°C). Incubate for 16 h at 4°C at 30 rpm.
- Add HRV 3C protease. HRV 3C protease comes as 2 U/ μ l, and we want to use it at 10 U/mg protein.
 - *We have ~112 mg protein (10.17.11), but will only cleave ~30 mg (112 mg / 40 mL -> ~10.8 mL)*
 - *~30 mg * 10 U/mg = 300 U*
 - *300 U * 1 μ l/2U = 150 μ l HRV 3C protease.*
 - *12 mL reaction: 10.8 mL protein, 1.2 mL buffer, 150 μ L HRV 3C*
 - Take 750 μ l sample after cleavage is complete.
 - Label sample '**AC.**'

Day 5

18. Equilibrate the HisTrap column with Wash Buffer 1. Change chromatography sensitivity to 0.2 (otherwise set to 1.0).
- Feed thru the column until baseline is reached.
19. Add imidazole (40 mM) and NaCl (500 mM) to the cleaved protein solution (depends on particular volume after overnight cleavage incubation).
- 40 mM imidazole => use _____ g
 - *11.25 mL so .031 g*
 - *(15.25 mL so .042 g)*
 - 500 mM NaCl => use _____ g
 - *11.25 mL so .329 g*
 - *(15.25 mL so .446 g)*

20. Feed the solution to the HisTrap column.
 - Collect first peak solution from the column (flow-thru) is solution to dialyze. This contains our protein.
 - Take a 750 µl sample of flow-thru and label it 'F2.'
 - Flowthrough has 26 ml.

21. Feed Wash Buffer 1 into column to pull out all cleaved protein before proceeding forward.

22. Elute uncleaved protein with imidazole.
 - Collect elution. Take 750 µl sample and label it 'E2.'

23. Dialyze purified protein for 3 hours against 2 liters of dialysis buffer.
 - DIALYSIS 2 BUFFER
 - 20 mM sodium phosphate dibasic => use 5.5678 g
 - 100 mM NaCl => use 11.688 g
 - Adjust to pH 7.4
 - Take 750 µl sample after dialysis. Label it 'AD2.'

24. Regenerate the column as above.

25. (IF NECESSARY) Concentrate the protein using a 10 kDa, 20 ml protein concentrator (Millipore #89921).

26. Aliquot purified protein into cryovials and put in the liquid nitrogen tank prior to freeze-drying. (Friday - 930am)

27. Perform an SDS-PAGE on samples
 - Suspend 50 µl of sample + 50 µl loading buffer (95% Laemmli sample buffer + 5% β-mercaptoethanol).
 - For BI, centrifuge for resuspend in 100 µl of loading buffer.

B2. Annexin production using TB media

Day before starting, **autoclave** the following items:

- 1 liter TB medium
 - TB medium nutrients
 - 12 g tryptone
 - 24 g yeast extract
 - 4 mL glycerol
 - 900 mL DI water
 - TB Medium Buffering
 - 2.31 g KH_2PO_4
 - 12.54 g K_2HPO_4
 - 100 mL DI water
- 4 x 1 liter Erlenmeyer flask (with aluminum foil on top)
- 125 ml Erlenmeyer flask (with aluminum foil on top)
- 100 ml beaker (with aluminum foil on top)
- All size tips
- 1.5 ml centrifuge tubes (like 100)
- 1 liter DI water

Protein Expression

Day 1

1. Culture 5 μl of *E. coli*/BL21(DE3) harboring pET303CT with the fusion gene ANXA5 in 10 ml of LB medium containing 35 $\mu\text{g/ml}$ kanamycin in a 125 ml Erlenmeyer flask overnight at 37°C with shaking at 200 rpm. $\text{OD}_{600} = 0.5$
 - **Add 35 mg kanamycin to the 1 L of TB medium before taking out the 10 ml for the initial culture.**
 - Incubate.

2. Add 10 ml of the cell culture to 1 liter of fresh culture medium+ kanamycin and incubate at 37°C with shaking (200 rpm). Take 1.5 mL of medium before adding the bacteria, as a blank. This cell culture was grown to mid-log phase => **$\text{OD}_{600} = 1.2$** .
 - Take a 1.5 ml sample of just the TB medium. Label 1.5 ml tube '**TB.**'
 - Transfer 10 mL of bacteria to 1 L TB medium.
 - Transfer entire volume of medium to 4 x 1 L flasks.

- Put in shaker at 37° C at 200 rpm.
- After 1.5 hrs of shaking, measure optical density at 600 nm (absorbance) using a clear 96 well plate and microtiter plate reader of sample vs LB medium => using 250 µl samples of each. When $OD_{600nm} = 1.2$, then proceed to next step.

Day 2

3. Add isopropyl β-D-thiogalactopyranoside (IPTG - stored @ -20°C top shelf) to a final concentration of 0.4 mM (96 mg IPTG total – 24 mg per flask) to solutions in 4 x 1 L flasks and incubate at 30°C with shaking (180 rpm) for 5 h to induce protein expression.
 - Take 750 ml sample of solution before adding IPTG. Label it 'BI.'
 - Add 24 mg IPTG to each flask.
 - Put back in shaker at 30°C for 5 hours.
 - IPTG stimulates the production of fusion protein. (IPTG activates the promoter in the plasmid that will start the transcription of the gene that follows the promoter =>Annexin V gene.)

Day 4

4. Harvest the cells by centrifugation for 10 min at 1000 x g, at 4°C.
 - Take 750 ml sample before centrifuge. Label sample 'BC.'
 - Centrifuge at 1000xg = ~3000 rpm (centrifuge uses rpm – consult table on machine). Only 4 – 50 ml centrifuge tubes at a time, temp 4°C, 10 mins.
 - After first centrifuge, pour out supernatant, add more culture to same 4 tubes. Bacteria will be stuck to side of tubes so inverting to pour out is not a problem.
 - Can put the 4 tubes in -20°C freezer for overnight storage.

Day 5

5. Resuspend the cell pellet in 80 ml of sonication buffer.
 - Add ~10 ml to each of the 4 centrifuge tubes.
 - Vortex to resuspend cell pellets.
 - Pour contents of the 4 tubes back into the 100 ml beaker.
 - **Sonication Buffer**
 - 0.05 mM N- p-tosyl-L-phenylalanine chloromethyl ketone (TPCK) - (-20°C) => 1.408 mg.
 - 1 mM phenylmethylsulfonyl fluoride (PMSF) - (shelf) =>13.936mg.
 - 1% HPLC ethanol - (flammables) => 800 µl.

- 0.01% β -mercaptoethanol – (bench top) => 8 μ l.
 - 0.02 M sodium phosphate dibasic – (shelf) => 227.2 mg.
 - 80 mL DI
 - **Dissolve TPCK and PMSF in ethanol in microcentrifuge tube, then add to beaker.**
 - **Make this buffer in the 100 ml beaker.**
 - **Correct to pH 7.4 – using HCl**
6. Lyse the cells by sonication at 4°C for 30 sec at 4.5 watts then allow it to cool for 30 sec on ice. This cycle was repeated 4 times (= 5 times total) for a total sonication time of 2.5 min on power level 4.
- Clean sonicator tip w/ ethanol before use.
 - Put beaker in tub w/ ice while sonicating.
7. Centrifuge the lysate obtained at 4000 x g for 1:30 h to remove the cell debris and **take the supernatant.**
- Pour beaker contents into 2 VWR 50 ml centrifuge tube.
 - Centrifuge at 4000xg for 1:30 h => this equals ~10,000 rpm.
 - Confirm that there is no debris in suspension. Debris clogs the HisTrap chromatography column.
 - Take 750 μ l sample after centrifuging. Label sample '**SS.**' The proteins will be in the supernatant and the cell debris will be at bottom of tube.

Protein Purification

8. After taking supernatant sample, add imidazole (40 mM) and NaCl (500 mM) to each of the lysate to reduce non-specific protein binding.
- 40 mM imidazole => use 0.0817 g
 - 500 mM NaCl => use 1.168 g
9. Equilibrate a 5 ml HisTrap chromatography column with immobilized Ni²⁺ using Wash Buffer 1.
- Feed wash buffer thru column until the output reaches baseline, then feed lysate through at -8.00
 - Turn on detector.
 - Turn on drop former – mode 0, rack 1, size 2, last tube 100, min 4, delay 0.
 - **WASH BUFFER 1** (500 mL) (- 30 min)
 - 20 mM sodium phosphate dibasic => use 1.42 g
 - 40 mM imidazole => use 1.362 g

- 500 mM NaCl => use 14.61 g
 - **Correct this to pH 7.4**
10. Feed the soluble protein fraction into the column.
11. Wash the column with 70 column volumes of Wash Buffer 2 to remove unwanted proteins and endotoxin (250 ml).
- Collect flow thru – contains unwanted proteins
 - Label sample 'F1-2.'
 - **WASH BUFFER 2** (500 mL) (- 1.5 hours)
 - 20 mM sodium phosphate dibasic =>use 1.4195 g
 - 40 mM imidazole =>use 1.3616 g
 - 500 mM NaCl=> use 14.61g
 - 0.1% Triton X-114 => 5 ml
 - **Correct this to pH 7.4**
12. Wash the column with 20 column volumes of Wash Buffer 1 to wash the protein until the pen reaches the baseline (100 ml). (- 40 min)
- Collect flow through – contains unwanted proteins (take 800 µl sample)
 - Look at graph paper from previous run to understand when/what to collect.
13. Elute the protein using elution buffer.
- Collect the elution – contains our FP (take 800 µl sample)
 - Look at graph paper from previous run to understand when/what to collect.
 - **ELUTION BUFFER** (300 mL)
 - 20 mM sodium phosphate dibasic =>use 0.8517 g
 - 500 mM imidazole => use 10.212 g
 - 500 mM NaCl => use 8.766 g
 - **Correct this to pH 7.0**
14. Dialyze eluted protein for 3 hours against 2 liters of dialysis buffer containing 20 mM sodium phosphate at pH 7.4 to remove NaCl and imidazole from the protein solution and make it suitable for C-terminal His-tag cleavage.
- **DIALYSIS 1 BUFFER** (2 L) – *Used 2 dialysis because collected 40 mL of protein -> 20 mL for each dialysis*
 - 20 mM sodium phosphate dibasic =>5.678 g
 - Adjust to pH 7.4
 - After dialysis, put back in a 50 ml centrifuge tube.
15. Before continuing, need to regenerate the column using this procedure:

- 25 ml of 1 M KCl => make 200 ml, so use 14.91 g
- 25 ml of 1 M NaOH => make 200 ml, so use 8.0 g
- 25 ml of DI water
- 25 ml of 1 M HPLC grade ethanol => 1.46 ml ethanol + 23.54 ml DI Water

16. Measure the concentration of protein (Bradford protein assay). *2.81 mg/mL measured in 40 mL -> total is 112.4 mg*

17. Add 30 ml DI Water to tube w/ cell pellet. Cleave the C-terminal His-tag by adding HRV 3C protease at 10 U/mg of protein with the recommended 10X buffer provided (stored @ -20°C). Incubate for 16h at 4°C at 30 rpm.

- Add HRV 3C protease. HRV 3C protease comes as 2 U/μl and we want to use it at 10 U/mg protein.
 - *We have ~112 mg protein (10.17.11), but will only cleave ~30 mg (112 mg / 40 mL -> ~10.8 mL)*
 - *~30 mg * 10 U/mg = 300 U*
 - *300 U * 1 μl/2U = 150 μl HRV 3C protease.*
 - *12 mL reaction: 10.8 mL protein, 1.2 mL buffer, 150 μL HRV 3C*
- Take 750 μl sample after cleavage is complete.
- Label sample 'AC.'

Day 6

18. Equilibrate the HisTrap column with Wash Buffer 1. Change chromatography sensitivity to 0.2 (otherwise set to 1.0).

- Feed thru the column until baseline is reached.

19. Add imidazole (40 mM) and NaCl (500 mM) to the cleaved protein solution (depends on particular volume after overnight cleavage incubation).

- 40 mM imidazole => use _____ g
 - *11.25 mL so .031 g*
 - *(15.25 mL so .042 g)*
- 500 mM NaCl => use _____ g
 - *11.25 mL so .329 g*
 - *(15.25 mL so .446 g)*

20. Feed the solution to the HisTrap column.

- Collect first peak solution from the column (flow-thru) is solution to dialyze. This contains our protein.

- Take a 750 µl sample of flow-thru and label it 'F2.'
 - Flow-thru has 26 ml.
21. Feed Wash Buffer 1 into column to pull out all cleaved protein before proceeding forward.
22. Elute uncleaved protein with imidazole.
- Collect elution. Take 750 µl sample and label it 'E2.'
23. Dialyze purified protein for 3 hours against 2 liters of dialysis buffer.
- DIALYSIS 2 BUFFER
 - 20 mM sodium phosphate dibasic => use 5.5678 g
 - 100 mM NaCl => use 11.688 g
 - Adjust to pH 7.4
 - Take 750 µl sample after dialysis. Label it 'AD2.'
24. Regenerate the column as above.
25. Pass the sample thru a 0.2 µm cellulose-acetate filter.
26. (IF NECESSARY) Concentrate the protein using a 150kDa, 20 ml protein concentrator (Millipore #89921).
27. Aliquot purified protein into cryovials and put in the liquid nitrogen for fresh freezing.
28. Perform an SDS-PAGE on samples.
- Suspend 50 µl of sample + 50 µl loading buffer (95% Laemmli sample buffer + 5% β-mercaptoethanol).
 - For BI, centrifuge for resuspend in 100 µl of loading buffer.

B3. Bradford protein assay

Standard Preparation

1. The standard protocol can be performed in a 250 µL microplate assay. Remove the 1x dye reagent from 4°C storage, aliquot it, and let it warm to ambient temperature. Invert the 1x dye reagent a few times before use.

2. Prepare a 2 mg/ml bovine serum albumin (BSA) standard solution in phosphate buffer saline (PBS 1X).
3. Perform serial dilutions of the standard BSA using PBS as diluent.
4. Assay 5 μL of each different protein concentration into 250 μL of Bradford dye reagent 1X. Blank samples are 5 μL of PBS in 250 μL of Bradford dye reagent 1X.
5. Incubate at room temperature for at least 5 min. Samples should not be incubated longer than 1 h at room temperature.
6. Set the spectrophotometer to 595 nm. Measure the absorbance of the standards and blanks.
7. Create a standard curve by plotting the 595 nm values (y-axis) versus their concentration in $\mu\text{g/ml}$ (x-axis). The average blank value should be subtracted from the average standard samples.

Assessment of concentration of unknown concentration protein sample

1. Following the same protocol for the standard curve sample preparation, assay 5 μL of different protein concentration into 250 μL of Bradford dye reagent 1X in triplicates.
2. Blank (PBS) should also be assayed in different wells.
3. Read endpoint absorbance at 595 nm.
4. Determine the unknown sample concentration using the standard curve prepared before.
5. If absorbance unit is greater than the maximum absorbance in the standard curve, then dilute sample by a known dilution factor.
6. If the samples were diluted, adjust the final concentration of the unknown samples by multiplying by the dilution factor used.

B4. SDS-page electrophoresis

Sample preparation

1. Mix 5 μL of protein sample to 20 μL of Laemmli running buffer in a small microcentrifuge tube
 - a. Protein sample should not be too concentrated because the band at the end will be too thick. Aim for a protein concentration in the sample of ~ 0.4 mg/ml.

- b. Perform dilution if necessary.
2. Heat sample for 5 min at 100°C in boiling water bath.
3. Let sample cool to room temperature.

Setting up gel and electrophoresis chamber

1. Take pre-casted gel from the fridge and remove the green slab from the bottom.
2. Place gel and another plate in the back in assembly module. Close the wings to firmly hold gel and plate in place.
3. Fill up gap between gel the other plate in the gel holder with the Tris buffer
 - a. Make sure that there is no leakage through the gap between gel and gasket
4. Load 10 µL of the prepared protein sample in of the wells of the precasted gels.
5. Load 5 µL of the ladder (protein standard) in a well closeby.
6. Place gel holder in electrophoresis chamber, mathing the colors of the sides of the holder which the color of the chamber (black on black, red on red).
7. Fill up electrophoresis chamber at the marked minimum level (2 gels)
8. Connect electrophoresis chamber to power generator also respecting color pattern.
9. Run gel for approximately 45 min at 150 V.
 - a. Run it until the coloring band reaches the bottom of the gel.
 - b. The more separated the bands, the more resolution of the results you get.
 - c. Samples can run out of the gel if running time is too long.

Staining and Destaining the gel

1. Remove gel from chamber and holder.
2. Carefully break the sides of the plastic plates that secure the gel.
3. Carefully remove gel from the plastic plates and place it into a staining dish.
4. Wash Tris buffer from gel
 - a. Add DI water to the dish until it covers the gel, place flask on shaker for 5 min.
 - b. Replace DI water.
 - c. Repeat washing 2 more times (3 X total).
5. Remove DI water and cover gel with Imperial stain, place it on shaker for 1 h.
6. Remove Imperial stain and add DI water to dish to destain gel for at least 1 h.
7. Check for purity by confirming the presence of only 1 band in the gel.

B5. SWCNT-ANXA5 conjugation

Materials:

- SDS
- SWCNT
- DSPE-PEG-MAL linker
- 2 kD dialysis membrane
- L-cysteine
- 100 kD dialysis membrane

1. Prepare 1% SDS solution.
 - a. Prepare 1% SDS stock.
 - i. 0.5 g SDS in 50 mL DI water.
2. Prepare SWCNT suspensions. (2 hours and 45 minutes store in the fridge)
 - a. Sonicate the SWCNT solution for 30 minutes. (6 mg SWCNT in 5 ml 1% SDS)
 - a. Use SG65i from 5/13/2013.
 - b. Make solution in a glass vial.
 - c. Sonicate it with (make sure probe does not touch the glass vial).
 - d. Place vial in water bath to prevent it from overheating.
 - b. Centrifuge the SWCNT solution for 30 min at 13,000 rpm.
 - a. Store supernatant.
 - b. Aggregates will drop to the bottom of solution.
 - c. Transfer SWCNTs supernatant solution to new tube and **repeat steps a and b.**
3. Dissolve DSPE-PEG-maleimide linker (MW 4368 Da) at 1.5 mg/ml in 1% SDS.
 - a. Dissolve 1.5 mg of linker in 1 mL 1% SDS. Rounds of water bath sonication and vortexing helps with dissolution.
 - b. Store linker at -20°C under nitrogen.
4. Add 1 ml of linker to 5 ml of SWCNT suspension.
5. Mix at RT for 30 min with gentle shaking on shaker with stir bar.

6. Dialyze SWCNT-linker for 8 hr against 2 L of DI water. Change the dialysate after 4 hr. Use a 2 kD dialysis membrane. Do not allow this dialysis to go too long (more than 8 h).
7. Reconstitute 5 mg of annexin A5 protein with 1 ml of DI water.
 - a. Conduct a Bradford assay to confirm protein concentration.
 - b. Protein concentration should approach 5 mg/ml. If protein concentration is lower than that, use protein concentrators (10 kDa) to increase concentration.
8. Take 2 ml of SWCNT-linker suspension and add 5 mg of ANXA5 to it. (annexin:linker molar ratio= 1.05:1).
9. Mix the SWCNT-linker and ANXA5 at room temperature for 2 h with gentle shaking on shaker (3 ml total volume).
10. Block unreacted linker sites with 0.166 mg of L-cysteine and mix at RT for 1 hr with gentle shaking. (The molar ratio of L-cys:linker is 4:1). Add 33.2 μ L of a 5 mg/ml solution of L-cysteine.
11. Dialyze the SWCNT-annexin A5 conjugate for 8 h against 2 L of 20 mM sodium phosphate buffer at pH 7.4 (8.61 g of sodium phosphate/ 3 L DI water). Change the dialysate after 4 hr. Use a 100kD dialysis membrane. Do not allow this dialysis to go too long)
12. Centrifuge the resulting SWCNT-annexin A5 conjugate at 15,680g for 1 h to remove aggregates.
 - a. Keep supernatant.
13. Measure the SWCNT and protein concentrations.
 - a. Run Bradford assay for protein concentration.
 - b. Measure SWCNT absorbance at 800 nm and compare it to SWCNT standard curve.
14. Store conjugate at 4°C.
15. Use prepared sample within 1 week after the end of preparation.

B6. SWCNT standard curve preparation

- 1- Sonicate 6 mg of SWCNTs in 5 ml of 1% SDS for 1 h.

- 2- Immediately, **without centrifuging**, make serial dilutions using 1% SDS and transfer 250 μL -samples to a 96-well plate
- 3- Measure the absorbance at 800 nm using microtiter plate reader to make a curve of SWCNT concentration versus absorbance.

Making the Standards: Serial Dilutions

1. Make a concentrated stock solution of the standard. Typically, the compound is accurately weighed out and then **quantitatively transferred** into a **volumetric flask**. Add some solvent, mix so the sample dissolves, then fill to the line with the proper solvent.
2. Perform serial dilutions. Take another volumetric flask and pipette the amount of standard needed for the dilution, then fill to the line with solvent and mix. A two-fold dilution is typically made, so for a 10-mL volumetric flask, add 1 mL of the previous dilution.
3. Continue as needed for more dilutions, pipetting from the previous solution to dilute it to make the next sample. For a good calibration curve, at least 5 concentrations are needed.

Run the samples for the calibration curve and the unknown samples

1. Run the samples with the UV-Vis spectrophotometer to determine the instrumental response needed for the calibration curve.
2. Take the reading with the first sample. It is a good idea to run the samples in random order (*i.e.* not highest to lowest or lowest to highest) in case there are any systematic errors. In order to get an estimate of noise, repeat the reading on any given sample 3–5x.
3. Run the additional standard samples, repeating the measurements for each sample to get an estimate of noise. Record the data to make a plot later.
4. Run the unknown sample(s). Use as similar conditions to running the standards as possible. Thus, the sample matrix or buffer should be the same, the pH should be the same, and the concentration should be in the range of the standards run.

B7. AuNP-annexin A5-DM1 conjugation

First day

ANXA5-DM1 preparation

1. Completely dissolve 12 mg of sulfo-SMCC in 2000 μL of DI water.
 - a. This is a 100x molar ratio to 1 mg/mL annexin, about 10x molar ratio for the available lysine residues on annexin.
 - b. If necessary, heat up sulfo-SMCC in water bath at 60°C to help it solubilize. Wait it to cool down to room temperature before adding it to ANXA5.
2. Add all of the sulfo-SMCC solution to 10 mg of annexin
3. Allow the mixture to react at 4 °C for **1 hour**.
4. Completely dissolve 10.0 mg of DM1 in 1500 μL of DMSO
 - a. This is a 50x molar ratio to 10 mg/mL annexin, the degree of sulfo-SMCC conjugation determines the number of available maleimide reaction sites
2. Add all of the DM1 solution in DMSO to the prepared annexin-SMCC conjugate
3. Allow the mixture to react at 4 °C **overnight**.

PEGylating AuNP

- 1- Dilute AuNPs to (20 mg·ml⁻¹, 0.1 M) in PBS.
 - a. AuroVistTM-15 nm initially at 200 mg ml⁻¹ PBS.
 - b. Final volume 0.5 ml.
 - c. 50 μL of 200 mg ml⁻¹ solution in 450 μL ml of PBS.
- 2- Dilute 61.2 mg (0.36 M) HS-PEG-NH₂ spacer in 0.5 ml of PBS (4:1 weight ratio spacer:AuNPs).
 - a. Sonicate spacer solution for 15 min in water bath sonicator.
 - b. Add HS-PEG-NH₂ solution dropwise to AuNPs solution and place on rotator.
 - c. Let solution stir **overnight** on rotator (speed 1.5) at 4°C.

Second day

ANXA5-DM1 preparation and purification

- 1- Block unreacted maleimide by adding cysteine to the ANXA5-DM1 conjugation vial, and let it react for **2 h** in 4°C.
- 2- Centrifuge conjugate if there is precipitate at the bottom.
- 3- Dialyze for **4 h** against 2 L of 20 mM phosphate buffer, pH 7.4

- a. Membrane MWCO should be between 1 and 10 kDa
- 4. Determine the product protein concentration by Bradford assay
- 5. Determine the extent of DM1 conjugation by reading absorbance at 288 nm of the conjugate and a blank of unconjugated annexin at the same concentration.
 - a. Calculate the DM1/ANXA5 ratio for the conjugate.

Purification of PEGylated AuNP

1. Wash excess linker away
 - a. Pipette solution into ultracentrifuge tube. Wash tube with PBS and place wash buffer with nanoparticles. Fill remaining ultracentrifuge tube space with PBS.
 - b. Centrifuge tubes at 16,000g for 20 min.
 - c. Remove supernatant and redisperse in sulfo-SMCC PBS buffer with water bath/probe sonicator for **10-15min**
 - i. Add 10 mg Sulfo-SMCC in 0.5 ml PBS

Preparation of AuNP-ANXA5-DM1

- 1- Adding maleimide groups to NH₂ functionalized AuNPs
 - a. Add 10 mg sulfo-SMCC solution to AuNP-PEG-NH₂.
 - b. Let reaction stir for 30 min under on rotator at room temperature.
- 2- Purifying AuNP-SMCC solution:
 - a. Wash excess crosslinker away:
 - i. Pipette solution into ultracentrifuge tube. Wash tube with PBS and place wash buffer with nanoparticles. Fill remaining ultracentrifuge tube space with PBS.
 - ii. Centrifuge tubes at 16,000g for 20 min.
 - iii. Remove supernatant and redisperse in 0.5 ml PBS buffer with water bath/probe sonicator until total dispersion.
- 3- Adding ANXA5-DM1 to maleimide functionalized AuNPs:
 - a. Add 5 mg of ANXA5-DM1 previously prepared and purified.
 - b. Let reaction shake **18 h** under moderate speed at 4°C.
 - i. Vial should be stabilized in a Styrofoam box and parallel to ensure proper circulation.
- 4- Blocking leftover maleimide groups on AuNP-ANXA5-DM1:
 - a. Dissolve 15mg L-cysteine in 1mL PBS.
 - i. Vortex for a minute to dissolve
 - b. Add 10 μL L-cysteine solution to AuNP-ANXA5
 - c. Let shake 1 h under moderate speed at 4°C.
- 5- Dialyze it against PBS overnight in 100 kDa dialysis membrane
 - a. Unbound ANXA5-DM1 and other components will be washed away

Third Day

- 1- Measure concentration of AuNP and ANXA5 in final product.
 - b. AuNP concentration is measure through absorbance at 520 nm and compared to standard curve.
 - c. Protein concentration is measured by Bradford assay, reading absorbance of the suspension at 595 nm, and subtracting the contribution of AuNP at that wavelength.
 - i. It might be necessary to use a low concentration standard curve to measure protein concentration (10-100 $\mu\text{g/ml}$).
 - d. The absorbance of AuNP in the solution should be subtracted from the absorption of the conjugate
 - i. After measuring the concentration of AuNP in the suspension, dilute stock solution to the concentration of the suspension and measure it with Bradford reagent parallel to the measurement of the protein concentration in the suspension.
 - e. Calculate the ANXA5/AuNP ratio.
- 6- Store it in 4°C fridge

B8. Nanoparticle protein conjugates sterilization and assessment of sterility

- 1- Place the suspension in a small petri dish, to allow the formation of a thin layer of the fluid.
- 2- Subject the petri dish to a direct UV (UV-C, shortwave UV at 254 nm) irradiation for 30 min in a sterile environment - sterilized in a regular laminar flow hood equipped with a Philips UV-C lamp (30 Watts).
- 3- Store the samples in an aseptic vial.
- 4- To confirm sterility, plate tap water, non-sterile, and sterile SWCNTs suspensions in an agar plate enriched with LB medium.

B9. AuNP-ANXA5-DM1 conjugate quantification

After conjugating DM1 to ANXA5, quantify the extent of conjugation:

- 1- Perform Bradford assay and determine ANXA5 concentration.
- 2- Utilize the standard curve of ANXA5 concentration vs absorbance at 288 nm to determine ANXA5 contribution to 288 nm signal (ANXA5 A.U.).
- 3- Determine the contribution of ANXA5-DM1 conjugate to 288 nm signal by reading the endpoint absorption of the conjugate (100 μ L sample): conjugate A.U.
- 4- Calculate the contribution of DM1 to the 288 nm signal (DM1 A.U.) as shown in the equation below:

$$(DM1 \text{ A.U. at } 288 \text{ nm}) = (\text{conjugate A.U. at } 288 \text{ nm}) - (\text{ANXA5 A.U. at } 288 \text{ nm})$$

- 5- Compare DM1 A.U. at 288 nm to the DM1 standard curve in DMSO at 288 nm to determine DM1 concentration in the conjugate.
- 6- Convert mass concentrations to molar concentrations for both DM1 and ANXA5, and determine molar ratio of DM1/ANXA5.
- 7- Perform SDS-page electrophoresis to confirm conjugation.

After purification of AuNP-ANXA5-DM1, determine the concentrations of both ANXA5 and AuNP in the conjugate:

- 1- Determine the concentration of AuNP in the conjugate by reading endpoint absorption at 520 nm.
- 2- Utilize the standard curve of 5 μ L of AuNP in 250 μ L of Bradford reagent read at 595 nm to determine the contribution of AuNP to the 595 nm signal of the conjugate.
- 3- Determine the contribution of AuNP-ANXA5-DM1 conjugate to the Bradford assay (reading at 595 nm of samples of 5 μ L of the conjugate in 250 μ L of Bradford).
- 4- Calculate the contribution of ANXA5 to the 595 nm signal (ANXA5 A.U. at 595 nm in Bradford) as shown in the equation below.

$$\begin{aligned} (\text{ANXA5 in Bradford A.U. at } 595 \text{ nm}) \\ = (\text{conjugate in Bradford A.U. at } 595 \text{ nm}) \\ - (\text{AuNP in Bradford A.U. at } 595 \text{ nm}) \end{aligned}$$

- 5- Use ANXA5 in Bradford A.U. at 595 nm to determine the ANXA5 concentration in the nanoparticle conjugate.

- 6- Infer the concentration of DM1 in AuNP-ANXA5-DM1 concentration by multiplying the molar concentration of ANXA5 to the molar ratio DM1/ANXA5.

APPENDIX C – Cell Culture Protocols

Source: Freshney, Culture of Animal Cells, 2010.

C1. Aseptic technique in vertical laminar flow

Outline

Clean and swab down work area, and bring bottles, pipettes, and other instruments. Carry out preparative procedures first (preparation of media and other reagents), followed by culture work. Finally, tidy up and wipe over surface with 70% alcohol.

Materials

Sterile (placed in hood):

Culture medium

Pipettes, graduated, and plugged, in an assortment of sizes, 1, 5, 10, 25 mL

Culture flasks

Nonsterile:

- Pipette controller or bulb in hood
- 70% alcohol in spray bottle in hood
- Lint-free swabs or wipes beside hood
- Absorbent paper tissues beside hood
- Pipette cylinder containing water and disinfectant on floor beside hood
- Waste bin (for paper waste, swabs, and packaging) on floor beside hood on opposite side from pipette cylinder
- Suction line to aspirator below hood or waste beaker in hood (both with disinfectant)
- Scissors
- Marker pen with alcohol-insoluble ink
- Notebook, pen, protocols

Procedure

1. Swab down the work surface and all other inside surfaces of laminar-flow hood, including inside of the front screen, with alcohol and a lint-free swab or tissue.
2. Bring medium and reagents from cold store, water bath, or otherwise thawed from freezer; swab bottles with alcohol, and place those that you will need first in the hood.
3. Collect pipettes, and place at one side of the back of work surface in an accessible position.

- 4.** Open pipette cans and place lids on top or alongside, with the open side down, or stack individually wrapped pipettes, sorted by size, on a rack or in cans.
- 5.** Collect any other glassware, plastics, and instruments that you will need, and place them close by (e.g., on a cart or an adjacent bench).
- 6.** Slacken, but do not remove, caps of all bottles about to be used.
- 7.** Remove the cap of the flask into which you are about to pipette, and the bottles that you wish to pipette from, and place the caps open side uppermost on the work surface, at the back of the hood and behind the bottle, so that your hand will not pass over them. Alternatively, if you are handling only one cap at a time, grasp the cap in the crook formed between your little finger and the heel of your hand, and replace it when you have finished pipetting.
- 8.** Select a pipette:
 - (a)** For glass pipettes or bulk-wrapped plastic
 - (i) Take a pipette from the can, lifting it parallel to the other pipettes in the can and touching them as little as possible, particularly at the tops (if the pipette that you are removing touches the end of any of the pipettes still in the can, discard it).
 - (ii) Insert the top end of the pipette into a pipette controller or bulb, pointing the pipette away from you, and holding it well above the graduations, so that the part of the pipette entering the bottle or flask will not be contaminated.
 - (b)** If pipettes individually wrapped plastic:
 - (i) Open the pack at the top.
 - (ii) Peel the ends back, turning them outside in.
 - (iii) Insert the end of the pipette into the bulb or pipette controller.
 - (iv) Withdraw the pipette from the wrapping without it touching any part of the outside of the wrapping, or the pipette touching any nonsterile surface.
 - (v) Discard the wrapping into the waste bin.
- 9.** The pipette in the bulb or pipette controller will now be at right angles to your arm. Take care that the tip of the pipette does not touch the outside of a bottle or the inner surface of the hood; always be aware of where the pipette is. Following this procedure is not easy when you are learning aseptic technique, but it is an essential requirement for success and will come with experience.
- 10.** Tilt the medium bottle toward the pipette so that your hand does not come over the open neck, withdraw 5 mL of medium, and transfer it a flask, also tilted.
- 11.** Discard the pipette into the pipette cylinder containing disinfectant. Plastic pipettes can be discarded into double-thickness autoclavable biohazard bags.
- 12.** Recap the flask.
- 13.** Replace the cap on the medium bottle and flasks.

Bottles may be left open while you complete a particular maneuver, but should always be closed if you leave the hood for any reason.

Note. In vertical laminar flow, do not work immediately above an open vessel. In horizontal laminar flow, do not work behind an open vessel.

14. On completion of the operation, tighten all caps, and place flasks in incubator.

Note. If shortage of space requires you to stack flasks in the incubator you may need to release the pressure in the flasks after they have been in the incubator for about 30 min as the flasks may distort due to expansion of the gas phase, particularly with larger flasks.

15. Remove all solutions and materials no longer required from the work surface, and swab down.

C2. Feeding a monolayer culture in flasks

Examine the culture by eye and on an inverted microscope. If indicated (e.g. by a fall in pH), remove the spent medium and add fresh medium. Return the culture to the incubator.

Materials

Sterile:

- Cell cultures
- Growth medium
- Pipettes, graduated, and plugged in an assortment of sizes, 1, 5, 10, 25 mL, in a square pipette can (glass pipettes will have been sterilized in the can; individually wrapped plastic pipettes can also be placed in a can for protection and convenience)
- Unplugged pipettes for aspirating medium if pump or vacuum line is available

Nonsterile:

- Pipette controller or bulb
- Tubing to receiver connected to vacuum line or to receiver via peristaltic pump
- Alcohol, 70%, in spray bottle
- Lint-free swabs or wipes
- Absorbent paper tissues
- Cylinder or jar containing water and disinfectant for pipette disposal
- Marker pen with alcohol-insoluble ink
- Notebook, pen, protocols

Procedure

1. Prepare the hood by ensuring it is clear and swabbing it with 70% alcohol.
2. Bring the reagents and materials necessary for the procedure, swab bottles with 70% alcohol, and place items required immediately in the hood.
3. Examine the culture carefully for signs of contamination or deterioration.

4. Check the previously described criteria—pH and cell density or concentration—and based on your knowledge of the behavior of the culture, decide whether or not to replace the medium. If feeding is required, proceed as follows.
 5. Take the culture to the sterile work area.
 6. Uncap the flask.
 7. Take a sterile pipette and insert it into a bulb or pipetting aid, or select an unplugged pipette and connect it to a vacuum line or pump.
 8. Withdraw the medium, and discard it into a waste beaker or aspirate the medium via a suction line.
 9. Discard the pipette.
 10. Uncap the medium bottle.
 11. Take a fresh pipette and add the same volume of fresh medium as was removed, prewarmed to 37°C if it is important that there be no check in cell growth, and recap the bottle.
 12. Discard the pipette.
- See the necessity of washing the plate with PBS.*
For the 15 cm² flask, use 10-15 mL of media.
13. Recap the flask and the medium bottle.
- Note.** If the culture is maintained under 5% CO₂ use a permeable cap for a CO₂ incubator or gas the air space in the flask with 5% CO₂ for around 10 s before recapping for regular incubators or hot room.
14. Return the culture to the incubator (CO₂ or not as appropriate).
 15. Complete the record of observations and feeding on a record sheet or lab book.
 16. Clear away all pipettes, glassware, and other movable items, and swab down the work surface

C3. Subculture of monolayer cells

Materials

Sterile:

- _ Monolayer culture at late log phase (just reaching confluence)
- _ Growth medium
- _ Trypsin, 0.25% at 4°C with 1 mM EDTA
- _ Pipettes, graduated, and plugged in an assortment of sizes, 1, 5, 10, 25 mL, in a square pipette can
- _ Unplugged pipettes for aspirating medium if pump or vacuum line is available
- _ Universal containers or 50-mL centrifuge tubes

_ Culture flasks

Nonsterile:

- _ Pipette controller or bulb
- _ Waste beaker or tubing to receiver connected to vacuum line or to receiver via peristaltic pump
- _ Alcohol, 70%, in spray bottle
- _ Lint-free swabs or wipes
- _ Absorbent paper tissues
- _ Pipette cylinder or jar containing water and disinfectant
- _ Marker pen with alcohol-insoluble ink
- _ Notebook, pen, protocols
- _ Hemocytometer or electronic cell counter

Procedure

1. Prepare the hood, and bring the reagents and materials to the hood
 2. Examine the cultures carefully for signs of deterioration or contamination
 3. Check the criteria and based on your knowledge of the behavior of the culture, decide whether or not to subculture. If subculture is required, proceed as follows.
 4. Take the culture flasks to a sterile work area, and remove and discard the medium (see Protocol 12.1, steps 7–9). Handle each cell line separately, repeating this procedure from this step for each cell line handled.
 5. Add PBS to the side of the flasks opposite the cells so as to avoid dislodging cells, rinse the prewash over the cells, and remove by pipette. This step is designed to remove traces of serum that would inhibit the action of the trypsin and deplete the divalent cations, which contribute to cell adhesion.
 6. Add trypsin to the side of the flasks opposite the cells. Turn the flasks over and lay them down. Ensure that the monolayer is completely covered. Leave the flasks stationary for 15 to 30 s. (A shorter exposure may be necessary if the trypsin is at room temperature.)
 7. Tilt the flasks to remove the trypsin from the monolayer and quickly check that the monolayer is not detaching. Using trypsin at 4°C helps to prevent premature detachment, if this turns out to be a problem.
 8. Withdraw all but a few drops of the trypsin.
 9. Incubate, with the flasks lying flat, until the cells round up; now when the bottle is tilted, the monolayer should slide down the surface. (This usually occurs after 5–15 min at 37°C.) Do not leave the flasks longer than necessary, but do not force the cells to detach before they are ready to do so, or else clumping may result.
- Note.** In each case the main dissociating agent, be it trypsin or EDTA, is present only briefly, and the incubation is performed in the residue after most of the dissociating

agent has been removed. If you encounter difficulty in getting cells to detach and, subsequently, in preparing a single-cell suspension, you may employ alternative procedures.

10. Add medium (0.1–0.2 mL/cm²), and disperse the cells by repeated pipetting over the surface bearing the monolayer.

11. Finally, pipette the cell suspension up and down a few times, with the tip of the pipette resting on the bottom corner of the bottle, taking care not to create foam. The degree of pipetting required will vary from one cell line to another; some cell lines disperse easily, whereas others require vigorous pipetting in order to disperse them. Almost all cells incur mechanical damage from shearing forces if pipetted too vigorously. Primary suspensions and early-passage cultures are particularly prone to damage, partly because of their greater fragility and partly because of their larger size, but continuous cell lines are usually more resilient and require vigorous pipetting for complete disaggregation. Pipette the suspension up and down sufficiently to disperse the cells into a single-cell suspension. If this step is difficult, apply a more aggressive dissociating agent or DNase.

Note. A single-cell suspension is desirable at subculture to ensure an accurate cell count and uniform growth on reseeded. It is essential if quantitative estimates of cell proliferation or of plating efficiency are being made and if cells are to be isolated as clones.

12. Count the cells with a hemocytometer or an electronic counter, and record the cell counts.

13. Dilute the cell suspensions to the appropriate seeding concentration:

(a) By adding the appropriate volume of cell suspension to a premeasured volume of medium in a culture flask or

(b) By diluting the cells to the total volume required and distributing that volume among several flasks.

Note. Procedure (a) is useful for routine subculture when only a few flasks are used and precise cell counts and reproducibility are not critical, but procedure (b) is preferable when setting up several replicates, because the total number of manipulations is reduced and the concentrations of cells in each flask will be identical.

14. If the cells are grown in elevated CO₂ in a regular incubator or hot room, gas the flask by blowing the correct gas mixture (usually 5% CO₂) from a premixed cylinder, or a gas blender, through a filtered line into the flask above the medium. Do not bubble gas through the medium, as doing so will generate bubbles, which can denature some constituents of the medium and increase the risk of contamination. Alternatively, if culture will be in a CO₂ incubator, use a gas-permeable cap. If the normal gas phase is air, as with Eagle's medium with Hanks's salts, no or minimal gassing is required and the flask is sealed.

15. Cap the flasks, and return them to the incubator. Check the pH after about 1 h. If the pH rises in a medium with a gas phase of air, then return the flasks to the aseptic area and gas the culture briefly (1–2 s) with 5% CO₂. As each culture will behave predictably in the same medium, you eventually will know which cells to gas when they are reseeded, without having to incubate them first. If the pH rises in medium that already has a 5% CO₂ gas phase, either increase the CO₂ to 7% or 10% or add sterile 0.1 M HCl.

Note. The procedure in step 15 should not become a long-term solution to the problem of high pH after subculture. If the problem persists, then reduce the pH of the medium at the time it is made up, and check the pH of the medium in the incubator or in a gassed flask.

16. As the expansion of air inside plastic flasks causes larger flasks to swell and prevents them from lying flat, the pressure should be released by briefly slackening the cap 30 min after placing the flask in the incubator. Alternatively, this problem may be prevented by compressing the top and bottom of large flasks before sealing them (care must be taken not to exert too much pressure and crack the flasks). Incubation restores the correct shape as the gas phase expands. If working in 5% CO₂, using permeable caps will avoid this problem.

C4. Endothelial cell culture

Materials:

- Endothelial cells (HAAE-1) were purchased from ATCC (Manassas, VA) (Cat. # CRL-2472) and Coriell Institute Medical Research (Camden, NJ) (Cat. # AG09799).
- Cell media Ham's F12K (supplemented)
 - Antibiotics penicillin and streptomycin
 - Heparin
 - Endothelial cell growth supplement
 - Fetal bovine serum
- T-75 flasks
- Porcine gelatin
- Trypsin
- PBS
- Pippetes, centrifuge tubes

The cell medium used was Ham's F12K cell medium with 2 mM L-glutamine adjusted to contain 1.5 g/L sodium bicarbonate and supplemented with 0.1 mg/ml heparin and 0.03 mg/ml endothelial cell growth supplement, 90 %; fetal bovine serum, 10 %. The antibiotics penicillin and streptomycin were also included in the medium at 100 U/ml and 100 µg/ml, respectively.

Cell Culturing

- 1- Add a layer of 0.1% porcine gelatin to the bottom of the T-75 flask to create a thin layer.
- 2- Leave the gelatin for 10 minutes in the flask.
- 3- Aspirate the excess of gelatin by aspirating it using a pipette connected to a vacuum system.
- 4- Add media to the flask.
 - a. Warm up cell media prior to use to avoid temperature shock
- 5- Add the cells to the T-75 flask.
- 6- Keep the cells in the controlled environment (37 °C, 5 % CO₂) in an incubator.
- 7- Keep the cells in the T-75 flask to allow the cells to increase their number.
 - a. Change media when necessary (color of the media is related to pH indicator).
- 8- When the cells reach 75 to 85 % confluency, perform cell passage (subculturing)
 - a. The confluency level defines the ratio between the surface area occupied by the cells and the surface area of the flask.
 - b. When that ratio percentage is almost 100 %, the cells enter in a quasi-steady mode, where they basically stop or dramatically reduce their replication rates. Don't let the cells reach 100% confluency.
 - c. Subculturing is the transfer of the cells from one set of culture flasks to another. This cell transfer is required in order to increase the available surface area required by the cells to replicate more.

Subculturing

- 1- Remove cell media using Pasteur pipets connected to the vacuum system.
 - a. Generally, human endothelial cells reach confluence after approximately 3 to 4 days.
- 2- Rinse the flask with 3 ml of phosphate buffer saline (PBS).
 - a. This step is required and very important, because it allows for the complete removal of the F12K medium which has in its composition an trypsin inhibitor.
- 3- Gently shake the flask and aspirate PBS.
- 4- Add 3 mL of trypsin to each T-75 flask and incubate it for 10 minutes at 37 °C.

- 5- Add 3 ml of gelatin to the new T-75 flasks and incubate it for 10 minutes at 37 °C.
 - a. The gelatin constitutes an adhesion support for the cells that will further attach to it and consequently to the surface of the plate.
- 6- Visualize the cells under optical microscope after the 10 minutes incubation. Prior to visualization it is recommend to shake the flask in order to have the cells slightly moving.
 - a. Under the microscope it is expected to see all of the cells floating in suspension. The majority must be detached from the surface at this point, and their morphology should look different with a rounded appearance, instead of the traditional elongated shape. If this does not happen, there was something that did not work properly and the assay must be restarted. If the majority of the cells are floating, it means that the action of the enzymes was successful.
- 7- Add 7 ml of warm F12K medium and mix the cells 3 or 4 times with the pipettor.
 - a. The medium was added to the cells in order to inhibit the action of the accutase/trypsin.
- 8- Transfer the that solution to a 15 ml centrifuge tube. Centrifuge the tube for **5 minutes at 1,100 rpm using a Mistral / MSE 3000 E centrifuge (Leicestershire, England)**.
- 9- Carefully remove 9 ml of the solution and leave 1 ml in the bottom of the tube.
- 10-Add 8 ml of medium to the tube, and pipette the solution several times in order to resuspend all of the cells and allow for obtaining a homogeneous cell suspension.
 - a. A failure on this step can result in transfer of unequal number of cells per flask.
- 11-Assuming a 1:3 cell passage, each T-75 flask received 3 ml of the cells' solution.
 - a. The desired number of cells to add to each T-75 flask after cell passage must be approximately equal to 5×10^4 cells.
- 12-Incubate the cells at 37 °C, 5 % CO₂ in the incubator.

C5. Counting cells with hemocytometer

Materials

Sterile:

- PBS
- Crude trypsin, 0.25%

- Growth medium
- Yellow pipettor tips

Nonsterile:

- Pipettor, 20 μ L or adjustable 100 μ L
- Hemocytometer (Improved Neubauer)
- Tally counter
- Microscope, preferably with phase contrast optics

Procedure

1. Sample the cells:

(a) For a monolayer,

(i) Trypsinize the monolayer as for routine subculture and resuspend in medium to give an estimated 1×10^6 /mL. Where samples are being counted in a growth experiment, the trypsin need not be removed and the cells can be dispersed in the trypsinate and counted directly, or after diluting 50:50 with medium containing serum if the cells tend to reaggregate.

(ii) Mix the suspension thoroughly to disperse the cells, and transfer a small sample (~1 mL) to a vial or universal container.

Aspirate the media

Wash it with PBS (2-3 mL)

Use 2 mL of trypsin for the big flask (75 cm²)

Check on microscope the if the cells have detached from plate.

Gentle agitation and pipetting up and down helps the cells to detach.

Centrifuge for 5 min if the cell concentration is low.

Aspirate the media.

Resuspend the cells in 3 ml of media. Make sure to agitate to make it homogenous.

Take 40 μ L of the suspension and transfer to a microvial.

(b) For a suspension culture,

(i) Mix the suspension thoroughly to disperse any clumps.

(ii) Transfer 1 mL of the suspension to a vial or universal container. A minimum of approximately 1×10^6 cells/mL is required for this method, so the suspension may need to be concentrated by centrifugation (at 100 g for 2 min) and resuspension it in a measured smaller volume.

Centrifuge for 5 min if the cell concentration is low at 1100 rpm (centrifuge in D211).

Aspirate the media.

Resuspend the cells in 3 ml of media. Make sure to agitate to make it homogenous.

2. Prepare the slide:

(a) Clean the surface of the slide with 70% alcohol, taking care not to scratch the semisilvered coating.

(b) Clean the coverslip, and wetting the edges very slightly, press it down over the grooves and semi silvered counting area with the edges of the coverslip extending

beyond the outermost grooves. The appearance of interference patterns (“Newton’s rings”—rainbow colors between the coverslip and the slide, like the rings formed by oil on water) indicates that the coverslip is properly attached, thereby determining the depth of the counting chamber.

Add Trypan Blue solution 0.4% (Sikavitsas’ Lab over the microscope) in a 1:1 volume to the cell suspension.

Rinse the hemocytometer gently with DI water and dry it with paper towel

3. Mix the cell sample thoroughly, pipetting vigorously to disperse any clumps, and collect 20 μL into the tip of a pipettor.

4. Transfer the cell suspension immediately to the edge of the hemocytometer chamber, expel the suspension, and let it be drawn under the coverslip by capillarity. Do not overfill or underfill the chamber, or else its dimensions may change, due to alterations in the surface tension; the fluid should run only to the edges of the grooves.

Pipette 20 μL of cell-Trypan Blue suspension into the hemocytometer

5. Mix the cell suspension, reload the pipettor, and fill the second chamber if there is one.

6. Blot off any surplus fluid (without drawing from under the coverslip), and transfer the slide to the microscope stage.

7. Select a 10 \times objective, and focus on the grid lines in the chamber. If phase contrast is not available and focusing is difficult because of poor contrast, close down the field iris, or make the lighting slightly oblique by offsetting the condenser.

8. Move the slide so that the field you see is the central area of the grid and is the largest area that you can see bounded by three parallel lines. This area is 1 mm^2 . With a standard 10 \times objective this area will almost fill the field, or the corners will be slightly outside the field, depending on the field of view.

9. Count the cells lying within this 1- mm^2 area, using the subdivisions (also bounded by three parallel lines) and single grid lines as an aid for counting. Count cells that lie on the top and left-hand lines of each square, but not those on the bottom or right-hand lines, to avoid counting the same cell twice. For routine subculture, attempt to count between 100 and 300 cells; the more cells that are counted, the more accurate the count becomes. For more precise quantitative experiments, 500 to 1000 cells should be counted.

(a) If there are very few cells (<100/ mm^2), count one or more additional squares (each 1 mm^2) surrounding the central square mm^2 .

(b) If there are too many cells (>1000/ mm^2), count only five small squares (each 0.04 mm^2 and bounded by three parallel lines) across the diagonal of the larger (1 mm^2) square, giving a total of 0.2 mm^2 .

10. If the slide has two chambers, move to the second chamber and do a second count. If not, rinse the slide and repeat the count with a fresh sample.

With the hemocytometer we have in the lab, the cell concentration is the average of counting in each of the 4 squares \times Dilution rate Trypan Blue) $\times 10000$ cells/mL

C6. Freezing cells

Grow the culture to late log phase, prepare a high concentration cell suspension in medium with a cryoprotectant, aliquot into ampoules, and freeze slowly.

Materials

Sterile or aseptically prepared:

- _ Culture to be frozen
- _ If monolayer: 0.25% crude trypsin
- _ Growth medium (serum improves survival of the cells after freezing; up to 50%, or even pure, serum has been used. If serum is being used with serum free cultures, it should be washed off after thawing)
- _ Cryoprotectant, free of impurities (see above):
DMSO in a glass or polypropylene vial, or glycerol, fresh, and in a universal container
- _ Syringe, 1 to 5 mL, for dispensing glycerol if used (because it is viscous)
- _ Plastic ampoules, 1.2 mL, pre-labeled with the cell line designation and the date of freezing

Procedure

1. Make sure the culture satisfies the criteria for freezing, and check by eye and on microscope for:
 - (a) Healthy appearance.
 - (b) Morphological characteristics.
 - (c) Phase of growth cycle (should be late log phase before entering plateau.
 - (d) Freedom from contamination.
2. Grow the culture up to the late log phase, and if you are using a monolayer, trypsinize and count the cells. If you are using a suspension, count and centrifuge the cells (.
3. Resuspend at 2×10^6 to 2×10^7 cells/mL.
4. Dilute one of the cryoprotectants in growth medium to make freezing medium:
 - (a) Add dimethyl sulfoxide (DMSO) to between 10% and 20%

Safety Note. DMSO can penetrate many synthetic and natural membranes, including *skin* and rubber gloves [Horita & Weber, 1964]. Consequently any potentially harmful substances in regular use (e.g., carcinogens) may well be carried into the circulation through the skin and even through rubber gloves. DMSO should always be handled with caution, particularly in the presence of any toxic substances.
5. Dilute the cell suspension 1:1 with freezing medium to give approximately 1×10^6 to 1×10^7 cells/mL and 5% to 10% DMSO (or 10–15% glycerol). It is not necessary to place

ampoules on ice in an attempt to minimize deterioration of the cells. A delay of up to 30 min at room temperature is not harmful when using DMSO

6. Dispense the cell suspensions into prelabeled ampoules, and cap the ampoules with sufficient torsion to seal the ampoule without distorting the gasket.

7. Place the ampoules on canes for canister storage

8. Freeze the ampoules at 1°C/min.

With the insulated container methods, this will take a minimum of 4 to 6 h after placing them at -70°C if starting from a 20°C ambient temperature, but preferably leave the ampoules in the container at -70°C overnight.

9. When the ampoules have reached -70°C or lower, check the freezer record before removing the ampoules from the -70°C freezer or controlled rate freezer, and identify a suitable location for the ampoules.

10. Transfer the ampoules to the liquid nitrogen freezer, preferably not submerged in the liquid, placing the cane and tube into the predetermined canister or individual ampoules into the correct spaces in the predetermined drawer. This transfer must be done quickly (<2 min), as the ampoules will reheat at about 10°C/min, and the cells will deteriorate rapidly if the temperature rises above -50°C.

☐☐ **Safety Note.** Protective gloves and a face mask should be used when placing ampoules in or near liquid nitrogen.

11. When the ampoules are safely located in the freezer, complete the appropriate entries in the freezer index.

C7. Alamar Blue assay

1. Remove cultures from incubator into laminar flow hood or other sterile work area.

2. Add resazurin dye solution in an amount equal to 10 % of the culture medium volume.

3. Return cultures to incubator for 2-4 hours depending on cell type and maximum cell density. (An incubation period of 2 hours is generally adequate but may be lengthened for low cell densities or cells with lower metabolic activity.) Incubation times should be consistent when making comparisons.

4. Gentle mixing in a gyratory shaker will enhance distribution of the dye.

5. Samples can be measured spectrophotometrically by monitoring the decrease in absorbance at a wavelength of 600 nm. Measure the absorbance of multiwell plates at a reference wavelength of 690 nm and subtract from the 600 nm measurement. Alternatively, samples can be measured fluorometrically by monitoring the increase in fluorescence at a wavelength of 590 nm using an excitation wavelength of 560 nm. **NOTE:** Fluorometric detection is much more sensitive than spectrophotometric detection, and the number of cells used in the assay should be reduced proportionally.

6. Tests performed in multiwell plates can be read using an appropriate type of plate reader or the contents of individual wells may be transferred to appropriate size cuvettes for fluorometric or spectrophotometric measurement.

C8. SWCNT-annexin A5 laser treatment with temperature measurement

Assembly of the laser treatment system

- 1- Place the laser tip over a distance from the bottom of the working area.
- 2- Place the Zap-it[®] paper over the working area.
- 3- Position the 24-well plate over the Zap-it[®] paper.
- 4- Turn on the laser and wait for the paper to burn and show the area affected by the laser.
- 5- Adjust the laser distance from the bottom.
- 6- Repeat steps 4 and 5 until the laser area matches the bottom area of the 24-well plate
- 7- Measure the diameter of the affected area with a caliper and calculate the respective area.

Measuring power attenuation

- 1- Don't change the system assembly.
- 2- Position the power meter over the working area.
- 3- Position a 24-well plate with a correspondent volume of media and the cover on top of the power meter.
 - a. The 24-well plate with a layer of media and the cover of the well plate is used to measure the power attenuation in the whole system.
- 4- Turn on the laser and measure the power with the power meter.
- 5- Adjust the power generated by the laser to get a 1 W/cm².

(I am assuming that once the power generator is set in certain level, the generated power will not change)

Laser Treatment of Endothelial Cells with SWCNT-annexin V on the Cell Surface

Groups:

- Controls (100% viability)
 - Untreated non-confluent HAAE-1 (n=3)

- Untreated 4T1(n=3)
 - Untreated EMT6 (n=3)
 - Laser: Temperature measurement (non-sterile)
 - Non-confluent HAAE-1 (n=3)
 - 4T1(n=3)
 - EMT6 (n=3)
 - Laser: Viability Assay (sterile)
 - Non-confluent HAAE-1 (n=3)
 - 4T1(n=3)
 - EMT6 (n=3)
- 1- Grow non-confluent endothelial cells (HAAE-1), 4T1 and EMT6 cell lines in T-75 flasks.
 - a. Each cell line has their own cell media and protocol for cell culturing.
 - 2- Seed cells into 24-well microtiter plates for 48h.
 - a. 20-50k cells per plate. Make this number consistent through cells types and wells.
 - 3- Incubate the cells with cell medium containing 2 mM CaCl₂ and **sterile** SWCNT-annexin A5 suspension at a concentration of 6 mg/L
 - a. Perform sterilization of SWCNT-Annexin V suspension before incubation
 - b. Place the suspension in a small petri dish, which allows the entire suspension to form a thin layer uniformly distributed.
 - c. Subject the suspension was then subjected to a direct UV (UV-C, shortwave UV at 254 nm) irradiation for 30 min in a sterile environment. The samples were sterilized in a regular laminar flow hood equipped with a Philips UV-C lamp (30 Watts).
 - 4- Wash the plates 4x with 300µl in PBS.
 - 5- Incubate the cells using cell medium supplemented with 2 mM CaCl₂.
 - 6- Submit each plate to the different laser treatments (200s at 1W/cm² = energy density of 200J/cm²) using the Diodevet-50 NIR laser at 980 nm.

Temperature measurements

- 1- Insert the thermometer probe inside of the vial immediately after the laser treatment.
- 2- Repeat the procedure to more 2 vials at the same energy density (triplicate).
- 3- Measure the temperature for all the energy densities.
 - a. Before changing the energy density, apply the laser treatment to vials that will be subject to the Alamar blue assay (n = 3).
 - i. The viability assay cannot be performed on the same plates that the temperature was measure because maintaining sterility in the cell culture is crucial for the viability assay.

- b. For each new energy density, repeat the steps for measuring power attenuation.

Cell viability measurements

- 1- For the same energy densities studied at the temperature measurement assay, submit the 24-well plates to laser treatment in triplicate.
 - a. To avoid greater variability, apply the laser treatment to the sterile vials right after measuring the temperature in non-sterile vials.
- 2- Add 10% of Alamar blue reagent to the well and incubate for 4 h at 37°C
- 3- After incubation, transfer 250 μL of cell media + 10% Alamar blue reagent to wells in an opaque 96-well plate.
- 4- Measure fluorescence with an excitation wavelength of 530 nm and emission wavelength of 590 nm using a microtiter plate reader.

APPENDIX D – Protocols for *in vivo* studies

D1. EMT6 tumor induction in mice

Materials

- EMT6 Cells
- Waymouth's media
- FBS (15% enrichment)
- Antibiotic-antimitotic (1% enrichment)
- PBS
- Trypsin (0.25%) EDTA (1X)
- Sterile pipette tips and Pasteur pipettes
- T-25 and T-75 flask treated
- Matrigel
- Trypan Blue
- 4-week BALB/c female mice
- Isoflurane
- Cotton balls
- 25-gauge needle
- Scalpel for shaving the mice

Preparation

- Cell culturing in T-25 and T-75 flasks following sterile technique in sterile hood.
- Order mice and wait the adaptation time to the new environment.
- On the day before, shave the lower left side of the abdomen of the mice that will be inoculated with cancer cells.

Cells Culture and Injection Preparation

- 1- Culture EMT6 cells in Waymouth's Media (15% FBS and 1% anti-anti) in incubator that provides 5% CO₂ and 37°C.
- 2- At 75% confluency passage cells and discard culture medium.
- 3- Wash cells with 5 ml of fresh PBS.
- 4- Add 2 ml of 0.25% trypsin/mM EDT solution. Let sit for 5 min or until all cells have been lifted from the plate.
- 5- Add 6 ml of fresh Waymouth's media and transfer to 15 ml- conical tube
- 6- Centrifuge cells at 1100 X G for 5 minutes and resuspend it in fresh media
- 7- Count cells with hemocytometer

- 8- Discard supernatant and resuspend cells so that in 50 μ L of 50% PBS and 50% Matrigel there are 50,000 cells.
 - a. Keep cells on ice.
- 9- Load 50 μ L of cells into 1 ml-syringe without needle to prevent shearing.
 - a. Remove air bubbles.
- 10- Add 25-gauge needle and allow the cells to pass through syringe.

Mice short term anesthesia

- 11-Embed a cotton ball with isoflurane.
- 12-Place the cotton ball inside of a bel jar below the ceramic platform.
- 13-Place the mice over the platform and close the lid of the bel jar.
- 14-Wait for the clear anesthetic effect and proceed to tumor cell injection.

Cell injection

- 15-Secure a 6-week-old female BALB/c mouse with one hand by grasping behind the ears using the index finger and thumb. Stretch the mouse body across the hand to expose the abdomen. Secure the tail against the hand using the last two digits of the same hand that secures the neck.
- 16-Inoculate the mouse with EMT6 tumor cells subcutaneously in the 4th mammary fat pad by gently penetrating the skin, with the bevel of the needle facing up and depressing the syringe to the appropriate volume

D2. NIR-irradiation of mice

1. Cover all the surfaces that might reflect the laser, including metallic benchtops and glass surfaces to prevent reflection of laser into the eyes of the operators.
2. Assemble the laser tip inside of an opaque tube to control the area of irradiation pointing down to the benchtop where irradiation will occur.
3. Use the power meter to adjust the power density to 1 W/cm² knowing the area of the opaque tube.
 - a. Adjust height of the laser tip and the power output in the laser generator to obtain desired power density.
 - b. Turn off the light in the procedure room so the red light from the laser can be visualized (red light is emitted when the laser generator is put in standby, but this is not NIR irradiation, so you can look at it)
4. Induce anesthesia placing mice in nose cone at the end of isoflurane .vaporizer connected to the O₂ gas line.
 - a. Level of isoflurane should be 3% for PTT.

- b. Pressure output should be around 2 atm.
5. Irradiate each mouse after confirming anesthesia.
 - a. Safety glasses should be always worn during irradiation session. **NIR-light can cause severe damage to sight!**
 - b. Thermal camera can be used to monitor temperature of the tumor
6. Remove mice from anesthesia and monitor behavior for signs of discomfort.

D3. RF irradiation of mice

1. Set up radiofrequency machine.
 - a. Connect RF matching network to RF generator.
 - b. Connect input water in matching network to faucet and let the output water to drip into the sink.
2. Induce anesthesia placing mice in nose cone at the end of isoflurane vaporizer connected to the O₂ gas line.
 - a. Level of isoflurane should be 3% for PTT.
 - b. Pressure output should be around 2 atm.
3. Adjust power level for the experiment.
4. Monitor the body temperature, including extremities, with thermal camera.
5. Remove mice from anesthesia and monitor behavior for signs of discomfort.

D4. Euthanasia for blood collection

Materials

- Autoclaved microcentrifuge tubes
- 3 ml syringes
- Short needles
- Surgical scissors
- Biohazard plastic bag
- Oxygen
- Isoflurane
- Ultracentrifuge

1. Anesthetize mouse with nose cone apparatus
 - a. Set up Isoflurane at 3% from oxygen gas source.
 - b. Make sure that mouse is completely asleep before proceeding.
 - c. Turn on the IR lamp to keep the mouse warm under anesthesia.

- d. Confirm anesthesia by firmly pinching a toe.
2. Perform a bilateral thoracotomy until you have a good visualization of the chest cavity.
3. Proceed to open the chest cavity and expose the heart.
 - a. Act quickly after opening the chest cavity.
4. Use the 3 ml syringe with a short needle to perforate the heart while sucking the blood.
 - a. Try to collect the most amount of blood from this procedure.
 - b. It is necessary at least 500 μL of blood to get enough serum to run ELISAs for 4 different cytokines.
 - c. Blood spilled into the rib cage can be collected with 100 μL pipette.
5. Immediately transfer the collected blood to microcentrifuge tube.
6. Check mouse for vital signs. Only remove the cone when death is confirmed. Cut the heart to ensure death.
7. Dispose the mouse in biohazard bag
8. Proceed to next mouse
9. Monitor the amount of time that is spent from the beginning of the procedure.
 - a. Blood coagulates at RT naturally. The coagulation time should be between 30 min and no more than 1 h. So, if the first mouse was euthanized 40 min before, stop the procedures, take the older samples and centrifuge it.
10. Empty cages should be placed in trash, while feeders are left on animal room so they can be washed by vivarium personnel.

Serum collection

1. Centrifuge samples for 15 min at 16,000g.
2. Take supernatant: that's the serum.
3. Place serum samples in -80°C freezer for later ELISA analysis

D5. Spleen collection and splenic cells staining for flow cytometry

Tissue Collection:

1. Euthanize animal with CO_2 inhalation.
2. Collect blood and place in heparin tube. Spin tube to separate plasma from blood and store at -20°C .
3. Collect lymph node and spleen and place in 5 ml of cold RPMI-1640 medium. Place samples on ice and transport to Norman.
4. Collect remaining tissue (liver, kidney, heart, lungs, intestine, and tumor) place in 10% neutral buffered formalin (NBF).

Flow Cytometry Buffer Preparation:

1. Flow cytometry staining buffer (SB): 1X PBS + 0.5% BSA + 0.05% sodium azide.
2. Foxp3 fixation/permeabilization working solution: Dilute the fixation/permeabilization concentrate (1 part) with fixation/permeabilization diluent (3 parts). You will need 1 mL of the fixation/permeabilization working solution for each sample, if staining in tubes.
3. Permeabilization buffer: Dilute the 10X concentrate with distilled water prior to use.

All following procedures with cells should be conducted on ice.

Flow cytometry sample preparation:

1. Tease apart tissue (lymph node and spleen) into a single-cell suspension by pressing with the plunger of a 3-mL syringe with 1 ml of SB into a petri dish. Wash plunger 2X with 1 ml SB each time.
2. Place a cell strainer on top of a 50-ml conical tube. Pass cells from the petri culture dish through the cell strainer to eliminate clumps and debris. Wash petri dish and stainer 2X with 1 ml SB each time.
3. Centrifuge cell suspension at 300-400g for 4-5 min at 2-8°C. Discard the supernatant.
4. Resuspend the cell pellet in a 1 ml volume of SB and perform a cell count and viability analysis.
 - a. Add 10 µl of Trypan Blue + 10 µL of diluted cell suspension (1:100 dilution) and count live and total cells.
5. Centrifuge cells as in step 3 and resuspend in appropriate volume of SB so that the final cell concentration is 1×10^7 cells ml⁻¹.

Flow Cytometry Staining

1. Add 100 µL of cell stock to a 2 mL microvial.
2. **Add mouse Fc Block (CD16/CD32 purified)**
3. Spin primary antibody tubes to pull solution to bottom of vial.
4. Prepare antibody cocktail.
5. Add stock antibody cocktail (Table 1) and bring final volume to 50 µL with SB.
6. Incubate for at least 60 minutes at 2-8°C or on ice. Protect from light.
7. Wash the cells by adding SB. Use 2 ml tube⁻¹. Centrifuge at 400-600g for 5 min at room temperature. Discard supernatant.
8. Repeat previous wash step.
9. Add 1 ml of fixation/permeabilization working solution to each tube and pulse vortex.

10. Incubate for 60 min at room temperature. Protect samples from light.
11. Wash the cells by adding 1X permeabilization buffer to each tube. Use 1 ml tube¹. Centrifuge at 400-600g for 5 min at room temperature. Discard supernatant.
12. Repeat previous wash step.
13. Resuspend pellet in 100 μ L of 1X permeabilization Buffer. This is typically the residual volume after decanting.
14. Block with 2% BSA by adding 2 μ L directly to the cells.
15. Incubate for 15 min at room temperature.
16. Without washing, add either 2.5 μ L of PE-Foxp3 antibody or SB to cells.
17. Incubate for at least 30 minutes at room temperature. Protect samples from light.
18. Wash the cells by adding 1X permeabilization buffer to each tube. Use 1 ml/tube. Centrifuge at 400-600g for 5 min at room temperature. Discard supernatant.
19. Repeat previous wash step.
20. Resuspend cells in an appropriate volume of SB.
21. Analyze samples by flow cytometry.

D6. Preparation of tissue lysate for SWCNT detection after biodistribution study

Lysis buffer: 1% SDS, 1% Triton X-100, 40 mM Tris acetate, 10 mM EDTA, 10 mM DTT
 To make 1 L of that buffer:

- Take 1 L of DI water
- Add 7.248 g of tris acetate
- Add 1.543 g of DTT
- Add 10 ml of Triton X-100
- Add 10 g of SDS

Procedures

- 1- Thaw the frozen vial that had cataloged organ/tissue.
 - a. The weight of the sample should have been recorded during collection of organs.
- 2- Cut the organ/tissue in smaller pieces
- 3- Place tissue into tissue grinder and add a small volume of lysis buffer to it (~3 ml).
- 4- Grind tissue.
- 5- Transfer the contents of the tissue grinder to a 15 ml Falcon tube.

- 6- Complete volume to 15 ml of total solution.
- 7- Place vial in incubator at 70°C and leave it for 2 h.
 - a. At the end of this procedure, a clear homogenate tissue solutions should be obtained for Raman measurement.
- 8- Send sample for analysis.

D7. Preparation of injectable hydrogel

- 1- Dissolve 156.25 mg of four-arm polyethylene glycol thiol (PEGSH, 95%, MW 5000) in 500 μ L of PBS
- 2- Dissolve 43.75 mg of poly (ethylene glycol) diacrylate (PEGDA, MW 700) in 500 μ L of PBS
- 3- Mixture both solutions to obtain hydrogel.
- 4- Confirm gelation by tube inversion.

Preparation of imiquimod (IMQ)-loaded injectable hydrogel

- 1- Dissolve 3 mg IMQ with 1 mL DMSO (dimethyl sulfoxide) to get a 3 mg/mL R837 solution.
- 2- Add 66.7 μ L 3 mg/mL R837 solution were added in 500 μ L PEGDA solution (without solid precipitation).
 - a. That gives a 10 μ g/mL imiquimod final concentration in the hydrogel.
- 3- Mixture both solutions to obtain hydrogel.
- 4- Confirm gelation by tube inversion

Injection of imiquimod-loaded injection hydrogel in mice

- 1- Prepare the IMQ loaded PEGDA solution, sterilize by sterile filtering with 0.2 μ m filter.
- 2- Prepare PEGSH solution, sterilize it too.
- 3- Add PEGSH solution to first one in an EP tube and mix it thoroughly under sterile conditions in a location close to where the mice to be injected is located.
- 4- Rapidly suction the mixture into a syringe for quick injection in less than 1 min to avoid gelation.

APPENDIX E – Other Protocols

E1. RF measurements using network analyser

- Open “Network Analyser Application”
- Click on “Response”, Click “Call”, select the third option, select 1 port, set up the “Start” value at 10 M Hz, set up the “Stop” value at 150 M Hz, set up the number of “point” at 804, click “OK”.
- Link the system with the cable, use your hand at first to tighten the grip, and then the adjustable wrench.
- Put on your wrist the bracelet linked to an earthing-cable to be able to touch the system.
(Do not touch the system without this bracelet as it could interfere with the system).
- Set up the oscilloscope on channel 3 and run it by pressing the “Run/Stop” button.
- On the Network Analyser, click “Marker Analysis”, click “Marker”, click “Marker” again, set up at 35 M Hz (or the experimental frequency you want to work with), click “OK”.
- Adjust inductance to match the center of the screen by screwing / unscrewing the inductors.
- Adjust capacitance to match the center of the screen by pressing and turning the capacitors.
(Try to be as close as possible of a resistance of 50 Ohm).
- When the system is adjusted correctly, turn off the oscilloscope and unplug it from the outlet.
- Carry the oscilloscope next to the generator and plug it again.
- Unplug the system and carry it next to the generator. (Be careful not to spill the glass bowl containing the nanotubes or the blank).
- Plug the system to the generator.
- Be sure the oscilloscope is set up on channel 3 and run it by pressing the “Run/Stop” button.
- Press “Voltage” on the oscilloscope and select the last option at the bottom.
- Set up the oscilloscope on “Frenquecing” mode.
- On the generator, set the frequency at 35 M Hz (or the experimental frequency you want to work with), and turn RF “ON”.
- Press “Auto” on the oscilloscope and run the generator + amplifier.
(Step forward to not interfere with the system during the exposure to radiofrequencies).
After 8 minutes, measure the temperature using the thermocouple.

E2. Agarose gel casting and running horizontal electrophoresis

Materials:

- Nanoparticle samples
- 1x Tris-borate-EDTA (TBE)–89 mM tris (pH 7.6), 89 mM boric acid, 2 mM EDTA
 - 10x stock (1 liter)–dissolve in 600 ml distilled water:
 - 108 g Tris base (FW = 121)
 - 55 g boric acid (FW = 61.8)
 - 40 ml 0.5 M EDTA (pH 8.0)
 - Fill to a final volume of 1 liter with distilled water
- Agarose
- Horizontal electrophoresis chamber and power source
- Casting apparatus
- Microwave

Preparation

To make a gel, first figure out what volume you want. You can pour water into the tray and when the wells look deep enough, you can record the volume and make your gel using that volume.

For a 7X7 cm gel tray:

Gel Thickness	0.25 cm	0.5 cm	0.75 cm	1.0 cm
Base	10 ml	20 ml	30 ml	40 ml
Tray	10 ml	20 ml	30 ml	40ml

1. Dilute TBE (Tris-borate-EDTA) buffer to a 1x or 0.5x concentration.
 - a. Place the diluted buffer in a beaker or flask that can hold 2-4 times the volume of agarose to be prepared.
2. Weigh out the agarose and add it to the flask/beaker containing the buffer.
 - a. For example, for a 1% agarose gel, add 1 g agarose to 100 ml buffer.
 - b. Allow the agarose to sit in solution for a few minutes before swirling the flask/beaker and suspending it in the solution. Higher percentage gels (> 1.5%) should hydrate for longer than lower percentage gels. Use a stir bar and stirring plate to rapidly mix the solution.
 - c. Note: Remember to remove the stir bar before microwaving.
3. Cover the mouth of the flask/beaker with plastic wrap and make a small hole in the top to allow the solution to vent.

4. Heat the flask/beaker in the microwave. After 30 seconds, remove and swirl to mix well. Repeat every 30 seconds until all the agarose has dissolved.
 - a. Note: If solid agarose or gel pieces remain, return the flask to the microwave and continue heating in 30-second intervals until all product is in solution. This may take a few minutes, depending on the gel concentration you are making and the power of the microwave.
5. Remove the flask/beaker from the microwave and very gently swirl.
 - a. WARNING: The microwaved solution can become superheated and foam over quickly when agitated. Wear appropriate protection and use caution.
6. Cool the solution to 55-60°C.
7. Cast the gel following the instructions provided for your casting apparatus.

Casting the gel

1. Level the cell using the leveling bubble provided.
2. Place the UVTP tray on the gel stage. (see picture below)
3. Slide the gel casting gates into the slots at opposite ends of the GT gel stage.
 - a. Insure that the gates are evenly seated in the slots and the gates uniformly contact all edges of the UVTP tray. The weight of the gates provides a tight seal to prevent any leakage problems during gel casting
 - b. Note: If leakage occurs while pouring the gel on the casting tray atop the stage, chill the casting gates in the freezer for 2-3 minutes. Place the casting gates into the slots when ready to pour the gel. The chilled casting gates will prevent the gel solution from leaking out of the tray and into the chambers.
4. Place the comb(s) into the appropriate slot(s) of the trays.
5. Prepare the desired concentration and amount of agarose in 1x electrophoresis buffer. When the agarose solution has cooled to 50—60°C, pour the molten agarose between the gates.
 - a. Warning: Hot agarose (>60°C) may cause the tray to warp or craze and will decrease the lifetime of the tray. Warping may also result in sample wells of uneven depth.
6. Allow 20—40 minutes for the gel to solidify at room temperature.
7. Carefully remove the comb from the solidified gel. Remove the gel casting gates
8. Submerge the gel beneath 2 to 6 mm of 1x electrophoresis buffer. Use greater depth overlay (more buffer) with increasing voltages to prevent pH and heat effect

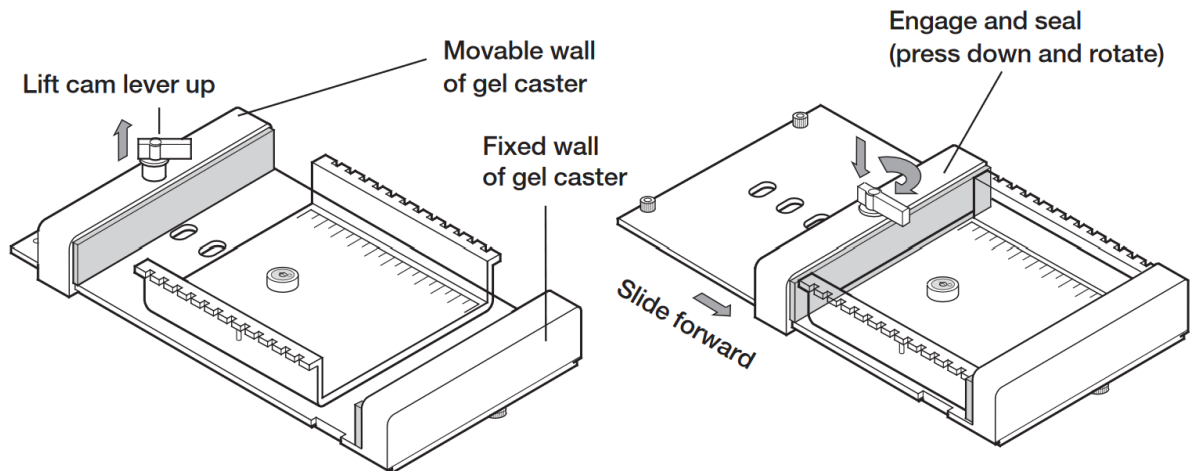


Figure 85: Horizontal electrophoresis gel casting.

Sample loading and running electrophoresis

1. Prepare samples for gel loading.
 - a. Before loading the gel with the PEGylated nanoparticle sample, a small amount of loading buffer (30% D(+)-sucrose in 0.5x TBE-buffer) is added to the sample.
2. Load the samples into the wells using standard pipets
 - a. 10 μ L sample is loaded into one well of the gel.
3. Place the lid on the electrophoresis chamber carefully. Do not disturb the samples. The Sub-Cell GT system lids attach to the base in only one orientation. To attach the lid correctly, match the red and black banana jacks on the lid with the red and black banana plugs of the base.
4. Adjust power input to 150 V in the power source.
5. Run electrophoresis for adequate amount of time (30 - 45 min)